

School of Civil and Mechanical Engineering

**Development of an Innovative Meta-Panel Sandwich Core for Structure
Protection against Blast and Impact Loads**

Hoang Nhi Vo

ORCID: 0000-0001-5649-0270

**This thesis is presented for the Degree of
Doctor of Philosophy
of
Curtin University**

July 2022

Declaration

To the best of my knowledge and belief, this thesis contains no material previously published by any other person except where due acknowledgement has been made.

This thesis contains no material which has been accepted for the award of any other degree or diploma in any university.

Signature:

(HOANG NHI VO)

Data: 11/07/2022

ABSTRACT

According to the Australian Business Roundtable, the total annual cost caused by natural disasters in Australia, e.g. hail, storms, floods, earthquakes, and bushfires, will reach \$39 billion by 2050. Similarly, manmade disasters could also result in massive loss of lives and economy. For instance, nearly 3,000 people perished in the 9/11 terrorist attack which also caused a direct economic loss of approximately US\$135 billion. A large amount of ammonium nitrate accidentally exploded in Beirut's port in August 2020, killing at least 218 lives, wounding more than 7,000 and causing municipal services totalling US\$15 billion in losses. For effective life and economy protection, the construction industry has been confronting an increased challenge of the escalating demands to protect structures against blast loads and fragment impacts from explosions. The common approaches for structural protection are based mainly on the properties of materials, e.g. energy absorption and strength, which usually lead to cumbersome and bulky structures. Furthermore, such protective structures absorb incident energy due to large irreversible plastic deformation, thus, they are incapable of resisting multiple attacks. Therefore, it is necessary to propose a new type of protective structures for better structural protection.

The concept of local resonant meta-materials and meta-structures has recently been proposed for mitigating dynamic loading effects on structures. Intensive research has been devoted to developing meta-materials, e.g., meta-concrete made by completely or partially replacing natural aggregates with engineered aggregates, i.e., local resonators. It has been demonstrated that the local resonators can be designed to have the desired frequency bandgaps in which the stress waves could not propagate through, therefore achieving the objective of structural protection. Although this mechanism has been examined in recent years, most previous works have concentrated on investigating the performance of meta-materials. Very limited study has investigated the performance of meta-structures, and no experimental work has been undertaken to validate the mitigation performance of dynamic loading effects of meta-structures subjected to impulsive loading. This research develops a novel protective structure with the meta-truss bars, named "meta-panel" for mitigation of blast/impact loading effects. The proposed meta-structure consists of local resonators which convert and trap blast and/or impact energy to kinetic energy through local vibrations of the resonators, hence reducing the loading energy transmission to the protected structures. This proposed design opens a door for a new approach to structural protections from the traditional means of either strengthening and/or

energy absorption through large plastic deformations of sacrificial structures. Additionally, under extremely intensive loading, more energy can be absorbed through the combined mechanisms of plastic deformation and the local vibrations, therefore enhancing the protective effectiveness of the proposed structure.

This dissertation comprising eight chapters investigates the structural performances of the proposed meta-panel subjected to blast and impact loads. In particular, Chapter 1 presents an overview of research objectives and methodologies while a theoretical reinvestigation of the bandgap formation in meta-materials associated with the effective negative mass and stiffness is presented in Chapter 2. This chapter discusses contemporary research gaps and provides insightful interpretations regarding the inconsistencies in the literature. The influences of the critical parameters on the bandgap characteristics of the meta-truss bar are studied in Chapter 3. The shear stiffness of all multilayers, which is usually neglected in most previous studies, is considered to predict the bandgaps of the meta-truss bar with higher accuracy. Chapter 4 investigates the impact mitigation capacity of a proposed meta-panel with single resonators utilized as a protective structure. The primary objective is to minimize the applied force to be transmitted to the protected structures. Compared to the conventional panels, the meta-panel exhibits superior performance with an increased impact energy absorption capacity and a substantial reduction in the deflection of the facesheets and the transmitted force.

To increase the width of the bandgap of the meta-panel for more robust blast loading mitigations, Chapter 5 proposes a new design of meta-panel by combining multi-types of resonators. It is revealed that a wide bandgap can be achieved through the combination of the bandgaps of multi-types of resonators, resulting in a significant blast-resistant enhancement of the proposed meta-panel. To further improve the bandwidth and hence enhance the protective effectiveness, a new dual-resonator meta-panel is proposed in Chapter 6. The dual-meta panel has the capability of generating wider bandgaps compared to the single-resonator type, leading to higher effectiveness in dynamic loading mitigation. In Chapter 7, the bandgap of the meta-truss bar and the impact mitigation effectiveness of the proposed meta-panel are experimentally verified. It was experimentally proven that the meta-panel exhibited superior impact resistance compared to the conventional sandwich panels. Finally, the key findings and recommendations for further research needed for practical applications of the proposed meta-panel for structural protections against blast/impact loads are summarized in Chapter 8.

ACKNOWLEDGMENT

First and foremost, I would like to express my heartfelt gratitude and respect to my supervisor John Curtin Distinguished Professor Hong Hao and my co-supervisor Dr Thong Pham for their enlightening guidance, invaluable advice, and persevering support throughout my PhD journey. I am so grateful to have had the opportunity to join the Center for Infrastructural Monitoring and Protection (CIMP). The enthusiasm of the CIMP members for science was a constant source of my inspiration.

Secondly, my sincere thanks also go to the Research Training Program (RTP) scholarship from Curtin University, School of Civil and Mechanical Engineering. Also, I want to thank the financial support from the Australian Research Council Laureate Fellowships FL180100196 for the funding of my experiments and other research involvement.

I would like to express appreciation to A/Prof. Kaiming Bi, A/Prof. Wensu Chen, and Dr. San Ha for their suggestions and recommendations in my study at Curtin University. I would also like to extend my appreciation to all the lab technicians in Civil Engineering Laboratory at Curtin University including Mr. Kevin Reilly, Mr. Loz Brady, and Ms. Alicia Farrelly for their assistance in my experimental lab work. I would like to send special gratefulness to the lab manager, Mr. Mark Whittaker, who responded promptly to my experimental arrangements.

I am truly grateful to all the students, research associates, and staff members in Professor Hong Hao's group at Curtin University for their enormous support during PhD program, especially Dr. Tung Tran, Dr. Tuan Ngo, Mr. Duong Tran, Mr. Emad Pournasiri, Mr. Zhixing Li, and Dr. Zhijie Huang for the strong friendships and great share of knowledge.

Lastly, I would like to express my special gratitude to my family for their unconditional love and eternal encouragement. I am highly indebted to my parents and my sister because of their tremendous sacrifices to bring the best education for me and encourage me to pursue the academic life.

LIST OF PUBLISHED WORK

This thesis contains a series of published papers and submitted manuscripts with the full bibliographic details and where they appear in the dissertation, as outlined below.

Chapter 2

N.H. Vo, T.M. Pham, H. Hao, K. Bi, W. Chen. A reinvestigation of the spring-mass model for metamaterial bandgap prediction. *International Journal of Mechanical Sciences*. 2022; 221:107219.

<https://doi.org/10.1016/j.ijmecsci.2022.107219>

Chapter 3

N.H. Vo, T.M. Pham, H. Hao, K. Bi. Model for analytical investigation on meta-lattice truss for low-frequency spatial wave manipulation. *Wave Motion*. 2021; 103:102735.

<https://doi.org/10.1016/j.wavemoti.2021.102735>

Chapter 4

N.H. Vo, T. M. Pham, H. Hao, K. Bi, W. Chen. Impact Load Mitigation of Meta-panels with Single Local Resonator. *Engineering Structures*. 2022; 265: 114528.

<https://doi.org/10.1016/j.engstruct.2022.114528>

Chapter 5

N.H. Vo, T.M. Pham, H. Hao, K. Bi, W. Chen, N.S. Ha. Blast resistant enhancement of meta-panels using multiple types of resonators. *International Journal of Mechanical Sciences*. 2022; 215:106965.

<https://doi.org/10.1016/j.ijmecsci.2021.106965>

Chapter 6

N.H. Vo, T.M. Pham, H. Hao, K. Bi, W. Chen. Stress Wave Mitigation Properties of Dual-meta Panels against Blast Loads. *International Journal of Impact Engineering*. 2021; 154:103877.

<https://doi.org/10.1016/j.ijimpeng.2021.103877>

Chapter 7

N.H. Vo, T.M. Pham, H. Hao, K. Bi, W. Chen. Experimental and Numerical Validation of Impact Mitigation Capability of Meta-panels. *International Journal of Mechanical Sciences*. 2022; 231:107591.

<https://doi.org/10.1016/j.ijmecsci.2022.107591>

STATEMENT OF CONTRIBUTION OF OTHERS

The research presented in this thesis was analytically derived, numerically simulated, experimentally conducted, analysed and written by the first author (Hoang Nhi Vo) of each publication. Contributions by others are described as follows. Prof. Hong Hao supervised the research scheme with feasible research methodologies and supported the research funding. As a co-supervisor, Dr. Thong Pham significantly contributed to the conceptualization, as well as the approaching methods for each publication. After the first drafts of manuscripts were prepared by the first author, Prof. Hong Hao and Dr. Thong Pham then provided additional intellectual input towards data processing, analysis in the discussions of the results and revised the manuscript. In addition, Dr. Kaiming Bi, Dr. Wensu Chen, and Dr. San Ha also provided intellectual input and useful suggestions in the manuscripts. The signed contribution form is attached in the appendix.

LIST OF RELEVANT ADDITIONAL PUBLICATIONS

The additional publications which are relevant to the dissertation but not forming part of it with the bibliographical details are listed below.

Journal papers

1. S.N. Ha, T.M. Pham, **N.H. Vo**, H. Hao, Dynamic crushing characteristics of bio-inspired minimal surface primitive structures, *International Journal of Solids and Structures*; Under review.

TABLE OF CONTENTS

ABSTRACT	i
ACKNOWLEDGMENT	iii
LIST OF PUBLISHED WORK	iv
STATEMENT OF CONTRIBUTION OF OTHERS	vi
LIST OF RELEVANT ADDITIONAL PUBLICATIONS	vii
TABLE OF CONTENTS	viii
LIST OF FIGURES	xiv
LIST OF TABLES	xxii
CHAPTER 1. INTRODUCTION	1
1.1 Preamble.....	1
1.2 Research objectives	4
1.3 Research outlines.....	5
CHAPTER 2. A REINVESTIGATION OF SPRING-MASS MODEL FOR META-MATERIAL BANDGAP PREDICTION	8
Abstract	8
2.1. Introduction	9
2.2. Analytical model	13
2.2.1 Spring-mass model for meta-concrete rod	13
2.2.1.1 Conventional analysis	13
2.2.1.2 Comprehensive analysis	16
2.2.1.2.1 Identification of the effective parameters.....	17
2.2.1.2.2 Wave dispersive analysis.....	17
2.2.1.2.3 Wave transmission.....	18
2.2.2 Spring-mass model for meta-truss bar	19
2.3. Verification and discussion of mechanisms for bandgap generation	21

2.3.1 Spring-mass model for predicting bandgaps of meta-concrete.....	22
2.3.2 Spring-mass model for predicting bandgaps of meta-truss bar.....	27
2.3.3 Discussions.....	32
2.4. Conclusions.....	33
Appendix.....	35
A. Design guide for meta-truss bars with targeted bandgap regions.....	35
B. Determination of the Starting and Cutoff frequencies of a corresponding bandgap ...	37
C. Worked-out example.....	39
D. Determination of axial and shear stiffness of the analytical model.....	44
CHAPTER 3. MODEL FOR ANALYTICAL INVESTIGATION ON META-TRUSS BAR FOR LOW-FREQUENCY SPATIAL WAVE MANIPULATION.....	45
Abstract.....	45
3.1. Introduction.....	46
3.2. Design of the dual-resonator model.....	48
3.3. Analytical models.....	50
3.3.1 Conventional spring-mass model of meta-truss bar.....	51
3.3.2 Proposed spring-mass spring model of meta-truss bar.....	53
3.4. Numerical simulation.....	57
3.4.1 Numerical model development.....	57
3.4.2 Numerical model verification.....	58
3.4.3 Accuracy of the proposed analytical model.....	59
3.5. Sensitivity of the bandgap characteristics to mass and stiffness based on the proposed analytical model.....	61
3.5.1 Effect of mass on bandwidth and bandgap position.....	61
3.5.2 Effect of stiffness on the bandwidth and bandgap position.....	65
3.6. Transient response of meta-truss bar based on numerical simulation.....	67
3.6.1 Transient response to sweep excitation.....	67
3.6.2 Transient response to a single frequency inside the passband.....	70

3.7. Conclusions	72
CHAPTER 4. IMPACT LOAD MITIGATION OF META-PANELS WITH SINGLE LOCAL RESONATORS	74
Abstract	74
4.1. Introduction	75
4.2. Geometric configuration	77
4.3. Analytical predictions of the bandgaps	78
4.4. Numerical modeling	82
4.4.1 Numerical model calibrations	83
4.4.1.1 Constitutive material models	83
4.4.1.2 Modelling contacts and boundary conditions.....	85
4.4.1.3 Impactor	86
4.4.2 Mesh convergence study	86
4.4.3 Model validation	87
4.4.4 Results and discussions	89
4.4.4.1 Deformation analysis.....	90
4.4.4.2 Energy absorption characteristics.....	92
4.4.4.3 Reaction force and Von Mises stress response	94
4.4.5 Parametric studies	96
4.4.5.1 Effect of the outer tube thickness	96
4.4.5.2 Effects of meta-core properties	98
4.4.5.2.1 Effect of coating modulus (E_c)	99
4.4.5.2.2 Effect of core density (ρ_c).....	102
4.4.5.3 Effect of impact velocity	103
4.5. Concluding remarks	106
CHAPTER 5. BLAST RESISTANT ENHACEMENT OF META-PANELS USING MULTIPLE TYPES OF RESONATORS.....	108
Abstract	108

5.1. Introduction	109
5.2. Meta-panel configurations.....	111
5.3. Programmable negative properties.....	113
5.4. Blasting wave characteristics	114
5.5. Comprehensive numerical investigations.....	116
5.5.1 Model development and verification.....	116
5.5.2 Parametric studies	119
5.5.2.1 Influence of inclusion arrangement.....	119
5.5.2.1.1 Influence of multiple types of meta-core material.....	120
5.5.2.1.2 Influence of multiple types of meta-core size	128
5.5.2.2 Influence of inclusion shape.....	133
5.6. Conclusions	138
CHAPTER 6. STRESS WAVE MITIGATION PROPERTIES OF DUAL-META PANELS AGAINST BLAST LOADS	140
Abstract	140
6.1. Introduction	141
6.2. Design of the Dual-meta panel.....	143
6.3. Analytical method	144
6.4. Numerical approach	148
6.4.1 Model development.....	148
6.4.1.1 Constitutive material models.....	148
6.4.1.2 Constraint and initial conditions	149
6.4.1.3 Blast load modeling.....	150
6.4.2 Mesh convergence test	151
6.4.3 Model validation	151
6.4.4 Results and discussions	153
6.4.5 Parametric investigations	160

6.4.5.1 Effect of the thicknesses of the facesheets	160
6.4.5.2 Effect of boundary conditions	162
6.4.5.3 Effects of blast loading duration and intensity	164
6.5. Conclusions	168
CHAPTER 7. EXPERIMENTAL AND NUMERICAL VALIDATION OF IMPACT MITIGATION CAPABILITY OF META-PANELS	170
Abstract	170
7.1. Introduction	171
7.2. Experimental campaign	173
7.2.1 Testing programs	173
7.2.2 Fabrication process	173
7.2.2.1 Meta-truss bars	173
7.2.2.2 Meta-panels	174
7.2.2.3 Material properties	175
7.2.3 Experimental setup	176
7.2.3.1 Instrumented hammer impact test on meta-truss bars	176
7.2.3.2 Gas gun impact test on meta-panels	177
7.3. Theoretical analysis	178
7.4. Numerical simulation	181
7.5. Results and discussions	183
7.5.1 Experimental verification of the bandgaps in meta-truss bar	183
7.5.2 Transient responses of the meta-panel	185
7.5.2.1 Impact response description	186
7.5.2.2 Deformation analysis	188
7.5.2.3 Reaction forces	191
7.5.2.4 Energy absorption characteristics	193
7.5.3 Effect of impact velocity	196

7.5.3.1 Impact response.....	196
7.5.3.2 Deformation, reaction force and energy absorption.....	198
7.6. Conclusions	200
CHAPTER 8. CONCLUDING REMARKS	202
8.1 Findings.....	202
8.2 Recommendation for future directions.....	204
REFERENCES.....	206
APPENDIX I. STATEMENTS OF CONTRIBUTION OF CO-AUTHORS	216
APPENDIX II. COPYRIGHT CLEARANCE	218
BIBLIOGRAPHY DISCLAIMER	221

LIST OF FIGURES

Figure 1-1. The devastation of buildings due to (a) blast explosion [3] and (b) hail storm impact [4]	2
Figure 2-1. Schematic view of meta-materials utilizing (a) Bragg scattering mechanism [66] and (b) local resonant mechanism [67]	10
Figure 2-2. Schematic view of the discrete spring-mass model adopted for meta-concrete and meta-truss bar in the meta-panel functioning as sacrificial cladding to protect the main structures from blast loading	11
Figure 2-3. Schematic view of the simplified spring-mass model for meta-concrete.....	14
Figure 2-4. Experimental transmission coefficient of the meta-concrete exhibits a high-frequency bandgap not predicted by the conventional approach.	16
Figure 2-5. Schematic view of the simplified spring-mass model for meta-truss bar	20
Figure 2-6. Schematic view of a meta-concrete rod used for modal analysis.....	22
Figure 2-7. Effective parameters of the spring-mass model to show the theoretical bandgap regions of meta-concrete	24
Figure 2-8. Complex frequency band structure of the dispersion curves of the spring-mass model to show the theoretical bandgap regions of meta-concrete	25
Figure 2-9. Bandgaps obtained from experimental test, prediction considering both the effective mass and effective stiffness, and prediction considering only the effective mass	26
Figure 2-10. Schematic view of the meta-truss bar used for modal analysis.....	27
Figure 2-11. Effective parameters of the spring-mass model with shear stiffness to show the theoretical bandgap regions of meta-concrete.....	29
Figure 2-12. Complex frequency band structure of the dispersion curves of the spring-mass model with shear stiffness to show the theoretical bandgap regions of meta-concrete	30
Figure 2-13. Transmission coefficient between numerical and analytical results	31
Figure 2-14. FFT spectra of the input and output displacements at center points of two ends of the meta-truss bar	32
Figure 2-15. Flowchart of the meta-structure design.	36

Figure 2-16. Typical bandgap determination based on the dispersion curves is divided into three regions including $[0-f_{11}]$ for the 1 st bandgap, $[f_{21}-f_{22}]$ for the 2 nd bandgap, and $[>f_{31}]$ for the 3 rd bandgap	37
Figure 2-17. Peak impact force time history of the simulated impact loading	39
Figure 2-18. FFT spectrum of the impact force time history of the simulated impact loading	40
Figure 2-19. Estimated bandgap widths of the designed meta-truss bar.....	40
Figure 2-20. Dispersion curve of the designed meta-truss bar.....	42
Figure 2-21. Design of meta-panel including the schematic view of the meta-panel.....	43
Figure 2-22. Comparison of reaction force of the three panels under impact loading.....	43
Figure 2-23. Outline model utilized for the calculation of (a) k_{s1} and k_{s2} , and (b) k_{a1} and k_{a2} ..	44
Figure 3-1. (a) Schematic view of 3D meta-truss bar, (b) single unit cell and (c) dimension of the single unit cell	50
Figure 3-2. (a) Schematic microstructure of the infinite conventional model of meta-truss bar and (b) Equivalent effective spring-mass model.....	51
Figure 3-3. (a) Schematic microstructure of the proposed model of meta-truss bar and (b) Equivalent effective mass-spring model	54
Figure 3-4. Transmittance profiles of meta-truss bar obtained by the proposed model, conventional model, and numerical simulation model.....	59
Figure 3-5. (a) Displacement time histories and (b) FFT spectrum of the input and output of the meta-truss bar	61
Figure 3-6. Non-dimensionalized dispersion curves obtained by the proposed analytical model	62
Figure 3-7. Effect of the internal mass m_2 on the bandgap characteristics (a) effective mass and (b) effective stiffness.....	63
Figure 3-8. Effect of the internal mass m_1 on the bandgap characteristics (a) effective mass and (b) effective stiffness.....	65
Figure 3-9. Dispersion relations of meta-truss bar embedded with the resonator with varied values of k_{s2}	66
Figure 3-10. Sweep excitation input profiles in time-domain.....	67

Figure 3-11. Snapshots of the interaction displacement (a) 3D meta-truss bar, (b) cross section of unit 1 at $t = 4.299$ ms, and (c) cross section of unit 1 at $t = 6.449$ ms	68
Figure 3-12. Stress waves time histories at different sections of the meta-truss bar at (a) outer mass aluminium and (b) outer coating	69
Figure 3-13. Transient response profiles of the output displacement obtained by the CWT method in the time-frequency domain under the sweep excitation.....	70
Figure 3-14. Stress waves time histories at different sections of the meta-truss bar subjected to harmonic excitation with frequency in the passband at (a) lead core and (b) inner coating	71
Figure 3-15. Transient response profiles of the output displacement obtained by the CWT method under the excitation with a single frequency of 500 Hz.....	72
Figure 4-1. Schematic illustration of the protection of meta-panels against impact loading ...	77
Figure 4-2. Schematic diagrams of (a) the meta-panel under impact loads, (b) meta-truss bar, and (c) unit cell.....	78
Figure 4-3. Equivalent effective spring-mass model	79
Figure 4-4. (a) Dispersion curve and (b) effective parameters of the meta-truss bar	82
Figure 4-5. (a) Time history of impact force and (b) frequency domain	86
Figure 4-6. Mesh convergence analysis	87
Figure 4-7. Analytical and numerical transmission coefficients of the meta-truss bar.....	88
Figure 4-8. (a) Displacement-time histories and (b) FFT spectra at the center points of the meta-truss bar	89
Figure 4-9. Schematic diagram of panels comprising of (a) solid-truss bar and (b) hollow-truss bar.....	90
Figure 4-10. Displacements of the back facesheet (a) time histories, (b) frequency spectra...	91
Figure 4-11. Displacement contour of the back facesheets (a) solid-truss panel, (b) hollow-truss panel, (c) meta-panel, and (d) deformation pattern of the meta-panel.....	92
Figure 4-12. (a) kinetic energy, and (b) internal energy, and (c) total energy of meta-panels	93
Figure 4-13. Energy absorption of the three panels	94
Figure 4-14. Reaction force of the three panels (a) time histories, (b) frequency spectra	95

Figure 4-15. Von Mises stress contours at the back facesheets of (a) solid-truss panel, (b) hollow-truss panel, (c) meta-panel, and (d) plastic deformation of the meta-panel.....	96
Figure 4-16. Schematic diagram of various thickness configurations of the outer tube of meta-truss bar	97
Figure 4-17. Effects of the outer tube thickness (a-b) displacement of back facesheet in time histories and FFT spectra, (c-d) reaction force in time histories and FFT spectra, and (e-f) displacement of front facesheet and energy absorption	98
Figure 4-18. Dynamic responses of core 1 (a-b) displacement of core 1 in time histories and FFT spectra, and (c-d) velocity of core 1 in time histories and FFT spectra	100
Figure 4-19. Effects of the coating modulus (a-b) displacement of back facesheet in time histories and FFT spectra, (c-d) reaction force in time histories and FFT spectra, and (e-f) displacement of front facesheet and energy absorption	101
Figure 4-20. Transmission coefficients of the meta-truss bar with different core densities ..	102
Figure 4-21. Impact loading with various velocities, (a) time-histories, and (b) FFT	104
Figure 4-22. Undeformed and deformed contour of the meta-panel under various impact velocities.....	105
Figure 5-1. Schematic diagram of the meta-panel functions as a sacrificial cladding.....	111
Figure 5-2. (a) Schematic view of the meta-panel, (b) a unit cell, and (c) meta-truss bar.....	112
Figure 5-3. The simplified spring-mass model	113
Figure 5-4. Effective parameters of the spring-mass model to show the theoretical bandgap regions of the meta-truss bar	114
Figure 5-5. Peak reflected pressure profile of the simulated blast loading generated by 0.4 kg TNT at 0.35m stand-off distance (a-b) in time history and its FFT spectrum	115
Figure 5-6. Schematic of the finite element model	117
Figure 5-7. Comparison of the transmission coefficients of the meta-truss bar including the analytical solution and the numerical result	118
Figure 5-8. Input prescribed displacement is excited at one end of the meta-truss bar while the output displacement is captured at the other end	119
Figure 5-9. Schematic diagrams of the meta-panel with different arrangements of resonators (a) combination of Aluminium and Tungsten, (b) Tungsten, and (c) Aluminium	120

Figure 5-10. Analytical transmission coefficient profile of two zones of the meta-truss bar	121
Figure 5-11. Displacement-time history at three points, i.e. the input point (A), the middle point (B), and the output point (C) in the meta-truss bar with two types of resonators	122
Figure 5-12. FFT spectrum of displacement at the three considered points	123
Figure 5-13. Scalograms of displacement in the time-frequency domain at different points (a) point A, (b) point B, and (c) point C	124
Figure 5-14. Diagrams showing deformed meta-panel and the deformation of the back facesheet of three meta-panels with different meta-truss bar (a) aluminium and tungsten resonators and (b-c) uniform tungsten and aluminium, respectively	125
Figure 5-15. Comparison of reaction force-time history curves between the three meta-panels	126
Figure 5-16. Comparison of energy absorptions of different parts of the three meta-panels	127
Figure 5-17. Schematic diagram of meta-truss bars with different sizes of resonators (a) non-uniform resonator meta-truss bar with two sizes of resonators and (b-c) are uniform resonators meta-truss bar with the core radius of 7 mm and 4 mm, respectively.....	128
Figure 5-18. Analytical transmission coefficient profile of two zones of the meta-truss bar with two types of resonators with the radii of 7 mm and 4 mm.....	129
Figure 5-19. Displacement-time history at the three points, i.e. the input point (A), the middle point (B), and the output point (C) in the meta-truss bar with two resonator sizes	130
Figure 5-20. FFT spectrum of displacement at the three points, i.e. the input point (A), the middle point (B), and the output point (C) in the meta-truss bar with two resonator sizes ...	131
Figure 5-21. Scalograms for displacement in the time-frequency domain at different points (a) point A, (b) point B, and (c) point C	132
Figure 5-22. Comparison of displacement-time history curves of the back facesheet between the three meta-panels.....	133
Figure 5-23. Representation and dimensions of meta-unit cells with various inclusion shapes including (a) cylinder, (b) cuboid, (c) pentagonal prism, and (d) hexagonal prism.....	134
Figure 5-24. Frequency band structures of the meta-truss bar with different inclusion shapes	135

Figure 5-25. Effect of inclusion shape on blast energy percentage in the passband of the meta-truss bar	136
Figure 5-26. Comparison of displacements and reaction forces between four meta-panels..	137
Figure 5-27. Comparison of energy absorption of the meta-panel embedded with various inclusion shapes under blast loading	138
Figure 6-1. Schematic diagram of the Dual-meta panel.....	143
Figure 6-2. (a) Schematic view of the dual-meta panel, (b) unit cell, and c) meta-truss bar .	144
Figure 6-3. (a) Schematic microstructure of infinite dual-core meta-materials, (b) Equivalent effective mass-spring model.....	145
Figure 6-4. Analytical solution of the bandgaps range for meta-truss bar (a) dispersion curve, (b) effective mass, and (c) effective stiffness.....	147
Figure 6-5. Peak reflected pressure profile (a) Time history, and (b) FFT spectrum	150
Figure 6-6. Effect of mesh sensitivity on the maximum displacement of the back facesheet	151
Figure 6-7. Transmission profiles of meta-truss bar under sweep frequency input: analytical analysis vs numerical simulation.....	152
Figure 6-8. Input and Output displacement at the center points of two ends of the meta-truss bar (a) time histories and (b) FFT spectra	153
Figure 6-9. Schematic view of the panels with (a) Solid-truss bars and (b) Hollow-truss bars	154
Figure 6-10. Time histories of central displacement of the back facesheet of the three panels	155
Figure 6-11. Energy time histories of each component of the dual-meta panel (a) total energy, (b) kinetic energy, (c) internal energy, and (d) displacement contour	156
Figure 6-12. Energy absorption of the three panels	157
Figure 6-13. Comparison of the reaction force time histories of the three panels under blast loading.....	158
Figure 6-14. (a) Stress contours of 3D dual-meta panel and stress contours at the back facesheet of (b) Dual-meta panel, (c) Hollow truss panel, and (d) Solid truss panel.....	159
Figure 6-15. Effects of the facesheet thickness (a-b) displacements of the back and front facesheets, (c) reaction force, and (d) energy absorption.....	161

Figure 6-16. Effects of the boundary conditions (a-b) displacements of the back and front facesheets (c) reaction force, and (d) energy absorption.....	163
Figure 6-17. Blast loading with different duration, (a) Time histories and (b) FFT spectra..	165
Figure 6-18. Blast loading profiles with different duration and intensities (a) Time histories, and (b) FFT spectra	167
Figure 7-1. Schematic view of the meta-panel comprised of two thin facesheets and the meta-truss bars under impact loading.....	172
Figure 7-2. Schematic diagram of the meta-truss bars (a) meta-truss bar, (b) outer tube, (c) meta-cores with coating.....	174
Figure 7-3. Schematic diagram of the meta-panel fabrication in which the two facesheets were bonded to the meta-truss bars by 3M impact-resistant adhesive.....	175
Figure 7-4. Schematic diagram of the meta-panel fabrication in which the two facesheets were bonded to the meta-truss bars by 3M impact-resistant adhesive.....	176
Figure 7-5. Setup of the instrumented hammer impact test	177
Figure 7-6. Setup of the gas gun test.....	178
Figure 7-7. Illustration of the idealized spring-mass model for an infinite long meta-truss bar	179
Figure 7-8. Theoretical bandgap regions of the meta-truss bar are determined by (a) dispersion curve and (b) effective parameters	181
Figure 7-9. Schematic of finite element model used to investigate the dynamic response of the meta-panel in the impact test.....	182
Figure 7-10. Input and output acceleration time histories at two ends of the meta-truss bar	184
Figure 7-11. Comparison of the bandgaps based on wave transmission ratio of (a) analytical, (b) numerical and (c) experimental results.....	185
Figure 7-12. Schematic diagram of the referenced panels including (a) hollow-truss panel and (b) solid-truss panel.....	186
Figure 7-13. Impact force and impact velocity of the projectile under gas gun impact test of (a) meta-panel and (b) three different panels.....	187
Figure 7-14. FFT spectrum of the impact force of the meta-panel recorded in the impact test	188

Figure 7-15. Comparison of deformation process of the meta-panel from (a) experimental results and numerical predictions	189
Figure 7-16. Displacement time histories of the back facesheet of the three panels	190
Figure 7-17. Deformed shapes with the maximum residual deformation of the back facesheet of (a) meta-panel, (b) hollow-truss panel, and (c) solid-truss panel	191
Figure 7-18. Measured reaction force time histories of the three considered panels	192
Figure 7-19. FFT spectra of the measured reaction forces of the three considered panels	192
Figure 7-20. Time histories of energy compositions in the meta-panel (FEM)	193
Figure 7-21. Energy absorption of each component of the meta-panel (FEM)	194
Figure 7-22. Energy absorption of different panels (FEM)	195
Figure 7-23. Impact force time histories with various impact velocities	197
Figure 7-24. FFT spectra of impact forces with various impact velocities	198
Figure 7-25. Effects of the impact velocity on the central displacement of the back facesheet and the reaction force of the meta-panel	199

LIST OF TABLES

Table 2-1. Elastic material properties for all components	22
Table 2-2. Elastic material properties for all components of the meta-truss bar [41].....	28
Table 3-1. Elastic material properties used in the numerical simulation [111].....	50
Table 3-2. Johnson-Cook material parameters for aluminium [111].....	58
Table 3-3. Equation of state for aluminium used in the numerical simulation [113]	58
Table 3-4. Plastic kinematic material parameters for lead [114]	58
Table 3-5. Meta-truss bar characteristics with varied stiffness k_{a1} , k_{a2} , and k_{s1}	66
Table 4-1. Elastic material properties used in the numerical simulation [111].....	78
Table 4-2. Material properties in the numerical model	84
Table 4-3. Equation of state for aluminium [113].....	85
Table 4-4. Effect of core density on displacements, reaction force, and energy absorptions	103
Table 4-5. Proportion of impact energy with various velocities in the bandgaps.....	105
Table 4-6. Effect of impact velocities on the transient response of the meta-panels.....	106
Table 5-1. Material properties of the meta-panel [111]	113
Table 5-2. Johnson-Cook material parameters for aluminium [111].....	117
Table 5-2. Influence of non-uniform inclusion on reaction force and energy absorption	133
Table 6-1. Elastic material properties used in the numerical simulation [111], [84].....	143
Table 6-2. Johnson-cook material parameters for aluminium [111].....	149
Table 6-3. Equation of state for aluminium used in the numerical simulation [113]	149
Table 6-4. Plastic kinematic material parameters for lead [114]	149
Table 6-5. Proportion of blast loading energy with different duration falling in the bandgaps of the single meta-truss bar.....	166
Table 6-6. Effect of blast loading duration on displacements, reaction force, and energy absorption	166
Table 6-7. Proportion of blast loading energy with different duration and intensities falling in the bandgaps of the single meta-truss bar	168

Table 6-8. Effects of blast loading duration and intensities on displacements, reaction force, and energy absorption	168
Table 7-1. Material properties of silicone rubber.....	176
Table 7-2. Material parameters of aluminium alloy 1060 for Johnson-Cook model [113] ...	183
Table 7-3. Proportion of impact energy with different velocities falling in the bandgaps of the meta-truss bar.	198
Table 7-4. Effect of impact velocities on energy absorption (FEM).	200

CHAPTER 1. INTRODUCTION

1.1 Preamble

Human nature is incredibly intelligent and resilient, and more importantly, humans are unique. Thousands of novel ideas, products and magnificent projects are established globally every day - genuinely owing to human creativity. The instinct of humans to feel safe and protected is one of the fundamental necessities for human creativity to occur. Thus, although global non-violence is the fundamental prerequisite of human life and ideal heaven, increasing risks of terrorist activities and unpredictable natural disasters have caused tragic consequences in fatalities and economic losses in recent decades. For instance, the years 2014-2016 witnessed more casualties reported by terrorist attacks in Europe than in previous years. The deadliest attack of this period was the November 2015 Paris attack, among which 130 people were killed [1]. The immediate costs of terrorist acts include not only the property destruction and the short-term economic depression, but also the costs related to the continuing risk of terrorism and psychological trauma. As reported, over 18 years from 2000 to 2018, terrorism has cost approximately \$855 billion to the global economy [2]. The exposure to blast threats has extended beyond the war zones to civilians due to the use of carry-on explosive detonation on civilian targets by terrorism. Similarly, accidental explosions, for example the accidental explosion occurred in Tianjin, China (Figure 1-1a) in the August of 2015 owing to an overheated container of nitrocellulose claimed 173 human lives and injured hundreds of others and caused more than \$15 billion economic losses [3].

Apart from the high-intensity pressure generated when an explosion is detonated, the explosion also results in substantial fragments and flying debris, i.e. window glass, bricks, and rock. These high-velocity flying fragments are also a major cause of structural damage, which potentially induce wall penetration, window breaking, structure collapse and can fatally inflict human injuries. Besides, other typical examples of impact-induced damage, e.g. hail storms and impacts from runway debris, have also been alarming concerns for the safety of humans and structures. These impact events are known to cause considerable loss of livelihoods, and are one of the significant contributors to total damage to economic assets, unemployment and financial crisis (Figure 1-1b). For example, a devastating hail storm wrecked a significant number of warehouse buildings and caused serious structural failures in Sydney, in April 2015

[4] while another hail storm in 2019 ravaged a large amount of damage to roofs and vehicles, resulting in subsequent harm to the societies.



(a)



(b)

Figure 1-1. The devastation of buildings due to (a) blast explosion [3] and (b) hail storm impact [4]

From the aforementioned issues, it is, therefore, deemed necessary to develop protective structures to protect the structural members exposed to these disastrous threats. Absorbing incident energy from blast/impact events through large deformation, hence minimizing transmitted energy to the protected structure is the primary approach of the conventional protective structures, which nevertheless has the inherent problems that the largely deformed protective structures lose their ability to resist the subsequent attacks. The evolution of engineering structures and materials has indicated a different trend toward enhancing the performance and adaptability of the current generation of protective structures. The key route to achieving these protective design of structures is the employment of innovative materials, geometric and functional hierarchies. The conventional applications by adopting thick solid monolithic structures [5] and porous materials [6] exhibit some limitations since they are bulky and cannot resist multiple loads effectively.

Hence, the utilization of sandwich panels for impact and blast protection has currently been a promising solution due to its lightweight characteristics. Sandwich structures were used as sacrificial claddings that are installed outside the existing structures for protection [7]. In this engineering application, the back facesheet of the panel is attached to the protected structure while the whole panel deforms under the applied loading to absorb energy and thus, the internal forces transferred to the protected structure are mitigated. In particular, a sandwich panel is a combination of two thin facesheets made of metal or composite laminates and lightweight cellular foam or lattice cores. Sacrificial structures have been proven not only light in weight with ease of installation but also of being efficient energy absorbers. It was indicated that

advanced sandwich structures have superior characteristics of absorbing blast/impact energy over monolithic plates. For demonstration, the overviews of dynamic responses of sandwich structures were investigated by Yuen et al. [8] while Xue and Hutchinson [9] examined the influences of core geometries on the performance of metallic sandwich panels. In brief, sandwich structures are classified by the core topologies, namely cellular material cores (e.g. polymer foams or hexagonal honeycombs) and periodic lattice cores (e.g. tetrahedral hollow truss or pyramidal solid truss). The primary energy absorption mechanism of these sandwich panels depends significantly on plastic deformation to mitigate dynamic damage. Recent developments in the fabrication process have led to the exploration of numerous core topologies for blast/impact-resistant sandwich structures. However, these conventional sandwich panels exhibit one major drawback, i.e. excessive plastic deformation under incident loading makes them unusable for repeated loads.

To overcome the limitation of the conventional sandwich panels which leverages the deformation mechanism, some scholars have attempted to solve the problem in an innovative approach, which attenuates stress wave propagation using the locally resonant mechanism, hence leading to the loading mitigation. The stress wave filtering efficiency is primarily affected by the dominant frequencies of the incident loading. Various types of loading have very different frequency contents, therefore it is ideal to design a structure which can effectively filter stress waves with a broad range of frequency. For instance, the dominant frequencies of impact load are usually less than 5 kHz [10], while those of blast loading are normally up to 50 kHz [11]. In recent decades, the revolution of man-made materials having the capability of manipulating wave propagation due to their exceptional properties beyond the limitations of naturally available materials has attracted a significant amount of research. These novel materials labelled as meta-materials [12] comprise heavy cores coated with a soft coating layer. It should be noted that the prefix “meta” comes from the Greek preposition and means “beyond”, indicating that the characteristics of these materials are beyond what can be seen in nature. The local resonant phenomenon of these cores absorbs the incident energy through vibration and thus forms its unique characteristics which have not been seen in conventional materials. The origin of this meta-materials concept stemmed from the electrodynamics fields [13], and it has subsequently extended to other branches of physical engineering applications, i.e. acoustics [14, 15], elastodynamics [16, 17], and thermodynamics [18, 19]. At its early stage, researchers have only focused on achieving the favourable negative effective density of materials [20] while the demonstration of the wave manipulation functionalities has rapidly

evolved accordingly. Not until recently, the meta-materials-based concept has been adopted in the context of engineering structures named meta-structures. Instead of relying only on large plastic deformation of materials for energy absorption, the new generation of protective structures would absorb energy by a combination of two mechanisms, i.e. plastic deformation and local resonance. Accordingly, this new generation of protective structures, e.g. meta-structures or meta-panels, is expected to reach a higher loading mitigation efficiency. However, this class of application remains very limited and no experimental study has been conducted yet with respect to their effectiveness in mitigating stress wave propagations subjected to blast/impact loads. It is also a lack of experimental verification regarding their unusual physical properties in bandgap formation. Therefore, this dissertation intends to fill this research gap by analytically, numerically, and experimentally investigating the protective performance of meta-panel against impact and blast loads, which will boost its engineering application in the structural engineering and construction.

1.2 Research objectives

The primary objective of this research is to develop a new form of sandwich structures named “meta-panel” with structural characteristics beyond those of natural materials, which provides potential applications in the field of protective structures. The meta-panel consists of two facesheets and meta-truss bars which comprise solid cores coated with soft layers and embedded inside the hollow tubes. These cores in the meta-truss bar are also known as resonators which will vibrate out-of-phase to absorb incident energy. The meta-panels are expected to yield better dynamic performances and higher energy absorption capacity compared to their conventional counterparts due to its effectiveness in impact and blast mitigation. Three main approaches including analytical analysis, numerical simulation and experimental study are carried out in this dissertation in which the specific research tasks are summarised as follows:

1. Analytical study is firstly conducted to provide an in-depth analysis of the bandgap formation of the meta-materials and a comprehensive analytical approach for bandgap determination. Besides, an improved analytical spring-mass model is proposed to accurately represent the realistic performance of a meta-truss bar which could generate a broader low-frequency bandgap that is under-predicted by the conventional model.
2. A novel concept of meta-panel as protective claddings for enhanced energy absorption and blast/impact loading resistance is developed by adopting the meta-material concept.

Its dynamic performances are numerically compared with the conventional sandwich panels to examine the effectiveness of the proposed panel in suppressing impact/blast loading effects on protected structures. To further achieve the improved performance of the proposed meta-panel, a new design is proposed by utilizing properly tailored arrangements of the inclusions, leading to a significantly improved protection effectiveness against blast/impact loads.

3. Experiments are carried out for further verification and examination of the bandgap formation and dynamic behaviour of the proposed meta-panel. Their transient responses and energy absorption capacity are evaluated and compared with the existing designs, i.e. sandwich panels with hollow-truss bars and solid-truss bars to verify their blast/impact mitigation effectiveness.

1.3 Research outlines

This dissertation consists of eight chapters. The contents of the seven chapters following the introduction in Chapter 1 are summarised below:

Chapter 2 presents a theoretical analysis of meta-materials, validated against numerical and experimental data to clarify the bandgap formation mechanism and inclusively interprets inconsistent bandgap observations which were reported in the literature. The obtained results facilitate meta-material applications in practice by providing a comprehensive approach for bandgap determination. A detailed design guideline of the meta-truss bar for blast/impact resistance is also provided as a representative example.

Chapter 3 proposes a new analytical spring-mass model using the local resonance mechanism and considering the shear stiffness of all multilayers, which has been neglected in previous studies in the literature. In this chapter, the analytical derivations are performed to demonstrate the more accurate bandgap predictions of the proposed model compared to the traditional model which neglects the internal shear stiffness. The results prove that the low-frequency bandgap of the proposed analytical model is broader and more accurate than the traditional model predictions.

Chapter 4 proposes the novel meta-panel as a sacrificial layer against impact loading by leveraging the coupled mechanisms of energy absorption including plastic deformation and local resonance. The superior performance of the proposed panel is exhibited by a significant

increase in energy absorption and a remarkable reduction in the facesheet deflection and the reaction force, i.e., the force transmitted to the protected structure, as compared with its conventional counterparts. Furthermore, a parametric study has been performed to investigate the influences of the truss bar thickness, the material properties, and the impact velocity on the transient responses or the protective effectiveness of the meta-panel.

Chapter 5 further examines the enhanced blast mitigation capacity of the proposed meta-panel with multiple types of resonators. The proposed structure demonstrates its blast-resistant enhancement as compared to its uniform arrangement of resonators owing to the existence of a full bandgap covering the entire range of loading frequencies in the transmission band. A parametric study is conducted to comprehensively examine the influences of the arrangement and shape of resonators on the blast mitigation effect of the proposed panel and identify its recommended designs.

Chapter 6 proposes a new design of the dual-meta panel in which the internal resonator is embedded inside the external resonator to broaden its bandgap ranges, leading to the blast-resistant enhancement. The finite element (FE) models utilizing Ls-Dyna are built to examine the dynamic behaviour of the proposed panel against blast loadings. The proposed dual-meta panel has a better ability for blast-wave mitigation due to the wider bandgap generation compared to the traditional panels. The influences of facesheet thickness, initial boundary conditions, and blast loading profile on the behaviour of the proposed panels are also performed through parametric studies.

Chapter 7 presents the experimental investigations regarding the effectiveness of the meta-panel under impact loading and the effects of impact velocity on its dynamic performance. The experimental results from the impulse hammer excitation test are compared with the analytical solutions to validate the exceptional properties of the meta-truss bar in terms of bandgap regions. Afterwards, the dynamic behaviour of the meta-panel under the pneumatic gas gun test is experimentally observed, which clearly showed that the meta-panel outperformed its traditional counterparts. Furthermore, the influences of impact velocity on the effectiveness of the meta-panel are examined and the determination of the critical factors on the behaviour of the meta-panel is assessed through in-depth discussion.

Chapter 8 summarises the main findings of this dissertation, as well as recommendations for future works.

In general, this dissertation is compiled from the technical articles that have been published or prepared for publication during the PhD program. Each chapter from Chapter 2 to Chapter 7 is constituted by one technical journal article. The published technical articles are formatted according to Curtin University's requirements.

CHAPTER 2. A REINVESTIGATION OF SPRING-MASS MODEL FOR META-MATERIAL BANDGAP PREDICTION

Abstract¹

Meta-concrete and meta-truss bars are a new type of material and structure with favourable characteristics that cannot be found in nature. Meta-materials/meta-structures possess the ability to manipulate wave propagation in certain frequency ranges, termed as bandgaps. Application of meta-materials/meta-structures for structural protection is different from the traditional strategies which resist the external loads by using their strength or energy absorption through plastic deformation, meta-materials and/or meta-structures stop incident stress waves from propagating through them if their frequency contents fall into the bandgaps, thus safeguarding the protected structures. Spring-mass models are commonly utilized to predict the wave propagation characteristics of local resonant meta-materials and meta-structures. It is well understood that the formation of bandgaps is because of the generation of negative effective mass and negative effective stiffness owing to the out-of-phase local vibrations. However, in current literature, some studies derived the bandgaps associated with only the negative effective mass while others derived those from both the negative effective mass and negative effective stiffness. There has not been a systematic study and explanations on these differences, and there is also a lack of understanding of the mechanics of bandgap formation, in particular the low-frequency bandgap. This chapter presents a theoretical study to reinvestigate the formations of bandgaps in meta-concrete and meta-truss bars associated with the effective negative mass and stiffness, provides explanations of the discrepancies in the literature, and identifies the fundamental mechanism for the bandgap formation in meta-concrete and meta-truss structure. A comprehensive analysis is also provided for predicting bandgaps of meta-materials and meta-structures, followed by a design procedure for engineering applications.

¹ The related work in this chapter was published in **International Journal of Mechanical Sciences** with the full bibliographic citation as follows:

N.H. Vo, T.M. Pham, H. Hao, K. Bi, W. Chen. A reinvestigation of the spring-mass model for meta-material bandgap prediction. *International Journal of Mechanical Sciences*. 2022;221:107219.

<https://doi.org/10.1016/j.ijmecsci.2022.107219>

2.1. Introduction

Blast/impact mitigations are of importance in engineering fields to prevent catastrophic consequences from terrorist activities and unexpected accidental explosions. For example, 2,996 people were killed in the 9/11 terrorist attack which caused a loss of US\$135 billion [21], while an accidental explosion at Port of Beirut claimed 218 lives, 7,000 injuries and US\$15 billion in property damage and left 300,000 people homeless [22]. Due to these escalating man-made hazards, the need for more robust protective systems is of vital importance [23-29]. As a topic of particular recent interest, meta-materials have attracted rapidly increasing attention due to their favourable wave mitigation capacity, as well as enormous potential for various practical applications. The concept of meta-materials was first discussed in 1968 [30] and is an interdisciplinary research topic that can be applied to numerous fields, e.g. mechanics, acoustics, optics, electromagnetics, etc. Driven by the promising performance in the manipulation of vibrational energy, the meta-materials considered in this study have been regarded as candidates of enormous potential for many important applications in structural dynamics or vibration mitigation. Meta-materials are artificially engineered materials composed of internal structures that exhibit unusual physical properties in a specific range of excitation frequency [18, 31], which could not be found in nature. These particular characteristics are triggered by the wave interference/out-of-phase motions of the internal components leading to negative effective properties. Accordingly, incident waves are filtered out, or in another word, they cannot propagate through meta-materials if their frequency contents fall into a certain range of frequencies, namely the “bandgap” [32, 33] or “attenuation band” [34, 35]. This characteristic of meta-materials has been widely adopted in many fields, including mechanical and manufacturing engineering as well as civil engineering.

Generally, meta-materials are based on two operating mechanisms to form a bandgap, i.e. Bragg scattering [36-40] and local resonance [41-44]. The characteristics of the bandgap zones generated by these two mechanisms are completely different. While engineered materials with periodic features termed as phononic crystals have been utilized to form a Bragg-scattering type of bandgap due to wave interference (Figure 2-1a), the locally resonant bandgap is attributed to the out-of-phase motions of the resonators (Figure 2-1b). The main limitation of phononic crystals stems from their dependence on the periodic spacing constant, which generates the high-frequency bandgap and thus is not suitable for low-frequency wave mitigations [45, 46]. Conversely, the underlying mechanism of locally resonant meta-material is the out-of-phase

motions of the local resonators, which counteracts the applied excitation on the structures [47-51]. The bandgaps generated by the meta-materials associated with local resonance depend on the resonant frequency of the resonators embedded in the unit cell, thus making them suitable for low-frequency wave attenuation [52-55]. With this advantage, numerous local resonant meta-materials have been proposed and viewed as promising candidates for emerging applications, e.g. stress wave mitigation [42, 56], vibration suppression [57-61], and seismic isolation [62-65].

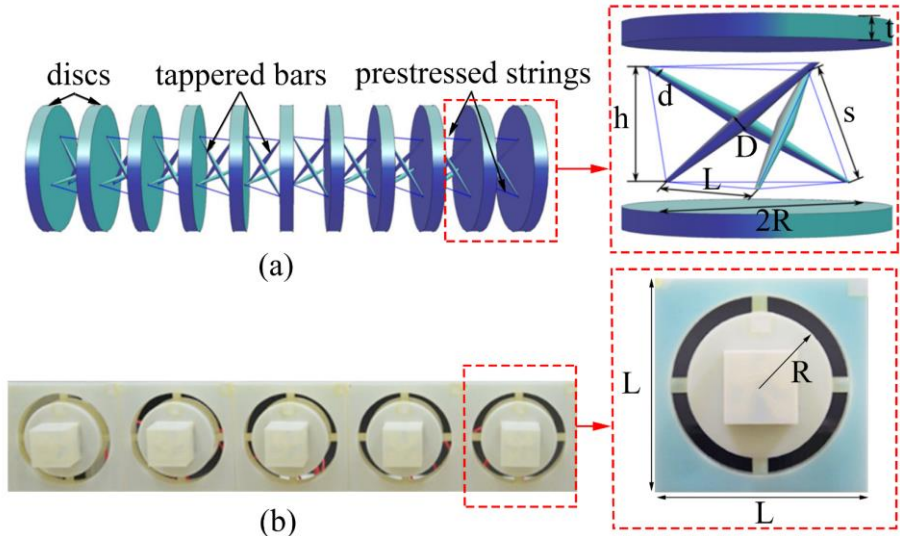


Figure 2-1. Schematic view of meta-materials utilizing (a) Bragg scattering mechanism [66] and (b) local resonant mechanism [67]

Many attempts have been reported using the spring-mass lattice system to examine the dynamic behaviours of meta-materials with local resonators. With their unusual effective characteristics, local resonant meta-materials/meta-structures have demonstrated their effectiveness in many engineering applications. For example, a theoretical investigation on the bandgaps of the meta-beam was firstly proposed by Liu et al. [68] to study its effectiveness in vibration suppression while the negative mass and stiffness in the spring-mass structure were observed in an experimental study [69]. Tremendous efforts have also been made to enhance the wave attenuation of engineered concrete-like materials, i.e., meta-concrete which provides a promising solution for protecting concrete structures. Mitchell et al. [70] analytically and experimentally studied the effect of the design parameters on the performance of the meta-concrete. Subsequently, the influences of the geometries, dimensions, and material properties of resonant engineered aggregates on the prescribed bandgap region were numerically and experimentally investigated by Xu et al. [71-73]. Most of the previous studies on meta-materials or meta-structures for structural protection are based on the spring-mass model for analytical

derivations as shown in Figure 2-2. However, the simplifications in establishing the spring-mass model in previous studies are not necessarily the same, which led to different predictions of bandgaps.

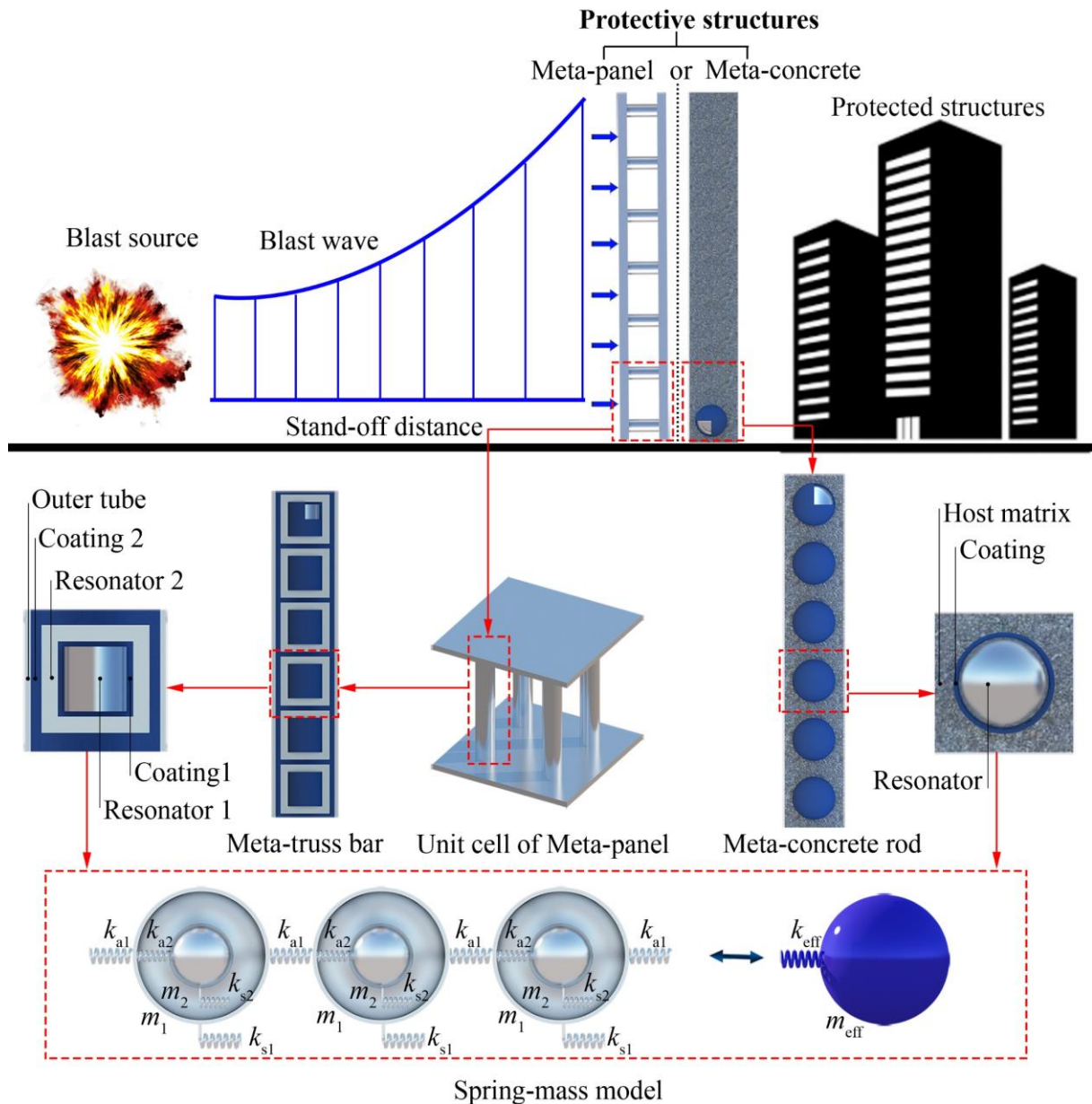


Figure 2-2. Schematic view of the discrete spring-mass model adopted for meta-concrete and meta-truss bar in the meta-panel functioning as sacrificial cladding to protect the main structures from blast loading

The generations of bandgaps in meta-materials and meta-structures for stopping wave propagations depend on the negativity of the effective mass and stiffness. Besides, apart from solely considering the negative effective mass and negative effective stiffness, researchers have also considered the bandgap formation differently by substituting the negative effective

stiffness by the negative effective modulus [74-79]. It should be noted that there is a reciprocal relationship between the negative effective stiffness and the negative effective modulus. In deriving the bandgaps of meta-materials and meta-structures using the simplified spring-mass model, the parameters of the spring-mass model need to be properly determined, otherwise inaccurate bandgaps would be derived. There were a few spring-mass models proposed for meta-materials/meta-structures, i.e. for meta-panels [41, 42], meta-materials in acoustic field [80, 81], and meta-concrete [73, 82]. Theoretically, for a typical single degree of freedom (SDOF) spring-mass model, there should be two bandgaps when the negative effective mass and negative effective stiffness are induced. Some previous studies [68, 83] reported two bandgaps while the other studies [71, 84] only obtained one bandgap even though they all adopted the same type of spring-mass model. A detailed review found that this discrepancy is rooted in the existence of the negative effective stiffness because the former studies obtained both the negative effective mass and the negative effective stiffness while only the negative effective mass was obtained in the latter studies. This variation causes confusion and may lead to incorrect observations and understandings of the generations of bandgaps. Therefore, this chapter conducts theoretical derivations to reinvestigate the frequency bandgaps of meta-materials and meta-structures based on the simplified spring-mass model. The results provide a thorough understanding of the frequency bandgap generations of meta-materials and meta-structures, and also explain the differences in the previous studies. For complete understanding, three methods are utilized to determine the intrinsic bandgaps, including the effective properties (i.e. effective mass and effective stiffness), dispersion curves and transmission coefficient. These three methods are used to confirm the existence of bandgaps in preventing the wave propagations and crosscheck the outputs.

In addition, considering the fact that the frequency content of some popular engineering loading, e.g. earthquake excitation and mechanical vibration, is in low-frequency ranges (e.g. 0.5 – 25 Hz for earthquake loading [85]), tremendous efforts have been devoted to generating the bandgap associated with these low frequencies [85-87]. However, by using a similar spring-mass model, a few studies [68, 83] reported a bandgap in the low-frequency range starting from zero but this low-frequency bandgap is not reported in other studies [73, 84]. Vo et al. [83] found that the shear stiffness of the internal coating layer is responsible for widening the bandwidth of the low-frequency bandgap as observed in [68]. On the other hand, Jin et al. [84] analytically investigated the attenuation mechanism of meta-materials using the spring-mass

model but did not observe the bandgap in the low-frequency range. The reason for this discrepancy is not systematically investigated and discussed.

As can be seen from the above review, two issues need to be clarified, i.e., (1) conditions to form two bandgaps in meta-concrete/meta-truss bar and (2) existence of low-frequency bandgap and the influences of the shear stiffness on the bandgaps. This chapter presents theoretical derivations, supported by experimental and numerical results to examine the mechanisms behind these two issues and provides explanations on why different observations on bandgaps were reported in the previous studies. The results in this chapter foster appropriate design for practical applications of meta-concrete and meta-truss bars. A detailed design procedure of the meta-truss bar for resisting the targeted impulsive loads, especially in the low-frequency range is given as an application example.

2.2. Analytical model

As mentioned previously, the concept of meta-materials or meta-structures has been adopted in numerous engineering applications, e.g. meta-concrete, meta-beam, and meta-panel. The simplified spring-mass models are often utilized for analysis. In this chapter, a spring-mass model for a meta-concrete rod and a meta-truss bar is chosen as an example, as shown in Figure 2-2. It should be noted that the considered meta-concrete rod is a periodic structure consisting of a finite number of meta-concrete unit cells, and in which, normal aggregates of conventional concrete embedded in the host matrix are replaced by spherical resonators comprising a heavy metal core coated with a soft outer layer; and the configuration of the meta-truss bar is a cylindrical hollow tube containing dual resonators suspended by soft coatings in a periodic arrangement.

2.2.1 Spring-mass model for meta-concrete rod

2.2.1.1 Conventional analysis

A discrete spring-mass lattice system containing infinite structural components (called unit cells) that are connected together end-to-end to represent the meta-concrete rod is illustrated in Figure 2-3. In the model, the external mass (i.e. host matrix) is denoted by m_1 while the internal mass (i.e. resonator) and the stiffness of the axial spring connecting the two adjacent outer masses are denoted by m_2 and k_{a1} , respectively. The internal mass is an oscillator whose displacement counteracts that of the external mass when the local resonant phenomenon occurs.

The stiffness of the axial spring connecting the oscillator and the external mass is denoted by k_{a2} . It should be noted that the shear stiffness k_{s1} and k_{s2} in Figure 2-2 are equal to zero in this conceptualized model, as in previous studies [71, 72]. The influence of neglecting the shear stiffness will be discussed later.

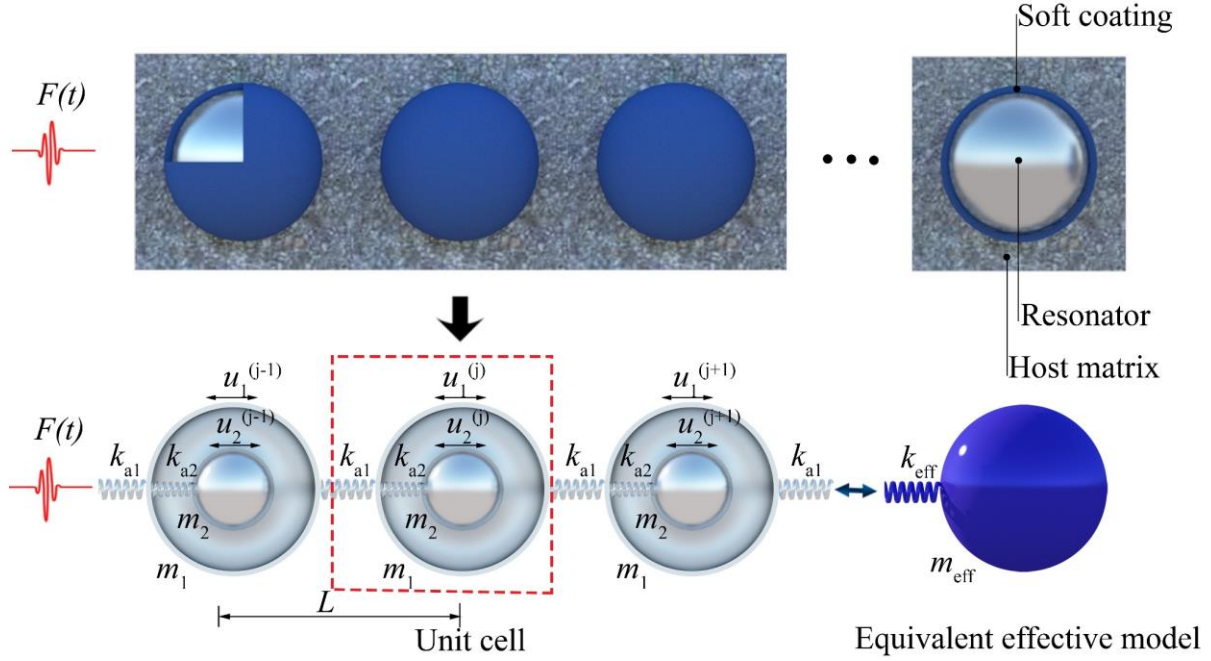


Figure 2-3. Schematic view of the simplified spring-mass model for meta-concrete

To discuss the kinematic modelling of this system, the free vibration equation of motion of the external mass for the j^{th} unit cell can be expressed as Eq. (2-1):

$$m_1 \ddot{u}_1^{(j)} + k_{a1} (2u_1^{(j)} - u_1^{(j+1)} - u_1^{(j-1)}) + k_{a2} (u_1^{(j)} - u_2^{(j)}) = 0 \quad (2-1)$$

where the overdot denotes the derivative with respect to time t while u_1 and u_2 are respectively the displacements of the external and internal masses in the j^{th} unit cell.

The dynamic equilibrium equation for the internal mass of the unit cell j is

$$m_2 \ddot{u}_2^{(j)} + k_{a2} (u_2^{(j)} - u_1^{(j)}) = 0 \quad (2-2)$$

Rewrite Eqs. (2-1) and (2-2) in the matrix form, it has

$$\begin{bmatrix} m_1 & 0 \\ 0 & m_2 \end{bmatrix} \begin{bmatrix} \ddot{u}_1^{(j)} \\ \ddot{u}_2^{(j)} \end{bmatrix} + \begin{bmatrix} 2k_{a1} + k_{a2} & -k_{a2} \\ -k_{a2} & k_{a2} \end{bmatrix} \begin{bmatrix} u_1^{(j)} \\ u_2^{(j)} \end{bmatrix} - \begin{bmatrix} k_{a1} (u_1^{(j+1)} + u_1^{(j-1)}) \\ 0 \end{bmatrix} = \begin{bmatrix} 0 \\ 0 \end{bmatrix} \quad (2-3)$$

The harmonic wave solution for the displacement of the j^{th} unit cell is given as Eq. (2-4) based on Bloch's theorem. This theory was developed to solve differential Schrodinger equations in mathematics and physics.

$$\mathbf{u}^{(j)} = Ue^{i(jqL - \omega t)} \quad (2-4)$$

$$\mathbf{u}^{(j+1)} = Ue^{i(jqL - \omega t)} e^{iqL}$$

$$\mathbf{u}^{(j-1)} = Ue^{i(jqL - \omega t)} e^{-iqL}$$

where L is the length of the unit cell, q is the wavenumber, ω is the angular frequency, i is the imaginary unit, and U is the displacement amplitude.

The lattice system consisting of spring-mass unit cells is considered as an equivalent solid object and substituting Eq. (2-4) into Eq. (2-3) results in an eigenvalue problem of the form $[\mathbf{K}(q) - \mathbf{M}\omega^2]\mathbf{u} = 0$. Solving this eigen function, the vibration frequencies can be obtained and the effective mass (m_{eff}) of the unit cell is derived as [84, 88]:

$$m_{\text{eff}} = m_1 + \frac{m_2 \omega_0^2}{\omega_0^2 - \omega^2}, \quad (2-5)$$

where the natural vibration frequency of the unit cell is $\omega_0^2 = \frac{k_{a2}}{m_2}$.

As shown, the effective mass depends not only on the physical masses m_1 and m_2 , but also on the natural vibration frequency of the unit cell ω_0 and the excitation frequency ω . When the excitation frequency is larger than the natural vibration frequency of the unit cell, the effective mass could become negative. The underlying goal for developing the effective properties of this model is to establish the relationship between the frequency of the incident excitation and the locally resonant frequency of the unit cell. As shown in Eq. (2-5), the effective mass significantly changes when the incident frequency approaches the natural vibration frequency of the resonator and can become negative, leading to the favourable wave attenuation characteristics of the system. When the effective mass (m_{eff}) becomes negative, the motions of m_1 and m_2 are out-of-phase, which implies that the mechanical wave of this frequency range cannot pass through the system. The wave energy is transferred to local vibrations of unit cells and cancelled by one another due to out-of-phase motions instead of propagating through the

system. As a result, the wave energy with frequency coincident with the bandgaps is greatly attenuated.

The physical meaning and mechanism of meta-materials associated with the negative effective mass on attenuating wave propagation have been documented in the previous studies [71, 73]. However, one major limitation of the conventional approach is that it only considers the effective mass negativity which exists in a very narrow bandgap region, specifically near the natural vibration frequency of the internal mass. This approach has been widely adopted by other studies for meta-concrete [73, 82]. Considering only the negative effective mass cannot predict the bandgap in the high-frequency range either as observed in the experimental tests reported by Mitchell et al. [89] as shown in Figure 2-4, in which a meta-concrete rod is similar to the one illustrated in Figure 2-3 was tested. In other words, only considering negative effective mass failed to capture the actual behaviours of meta-concrete since the experimental results exhibited two bandgaps while the analytical prediction gave only one narrow bandgap.

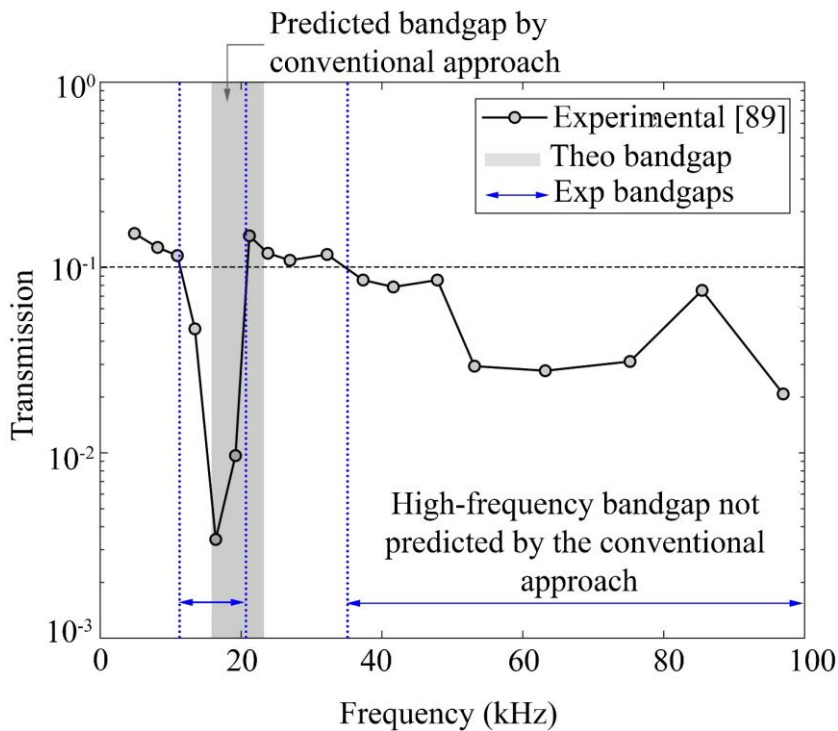


Figure 2-4. Experimental transmission coefficient of the meta-concrete exhibits a high-frequency bandgap not predicted by the conventional approach.

2.2.1.2 Comprehensive analysis

In response to the limitations of the conventional analysis and to gain an insightful understanding of the underlying physics of the negative effective properties based on the

analysis of the spring-mass model, a comprehensive derivation and discussion are presented in this section. This comprehensive derivation includes both the effective mass and the effective stiffness. The system containing an infinite number of periodically-arranged spring-mass units in Figure 2-3 is adopted in this section to study its frequency-dependent wave phenomenon. For double verification of the determined bandgaps from the spring-mass model, three methods including the effective properties, wave dispersive analysis and wave transmission are used in this chapter.

2.2.1.2.1 Identification of the effective parameters

The effective mass and the effective stiffness are the most important parameters of the spring-mass model. In general, bandgaps are formed when these effective parameters become negative. As discussed above, the effective mass is given by Eq. (2-5) while the effective stiffness is neglected in some previous studies [72, 73]. In this subsection, the formula of the negative stiffness is derived to investigate its reciprocal relationship with the bandgaps. To define the effective stiffness from the lumped mass model, the unit cell is assumed as homogeneous and can be calculated as follows [68]:

$$k_{eff} = k_{a1} + \frac{1}{4}k_{a2} - \frac{1}{4}\left(m_1\omega^2 + \frac{k_{a2}\omega_0^2}{\omega_0^2 - \omega^2}\right), \quad \omega_0^2 = \frac{k_{a2}}{m_2} \quad (2-6)$$

From Eq. (2-6), it is obvious that depending on the stiffness, mass and natural vibration frequency, the effective stiffness could also be negative, resulting in favourable bandgaps. The conventional analysis which only considered the effective mass has overlooked this bandgap in its prediction. This chapter provides a comprehensive analysis of bandgap formation considering both the effective mass and the effective stiffness. The bandgaps obtained from the negative effective properties are cross-checked with other methods, which will be derived in the following sections.

2.2.1.2.2 Wave dispersive analysis

In addition to the direct derivation, wave dispersive analysis can be also adopted to determine bandgaps. Dispersion curves provide information on whether or not a wave could propagate through the system at certain frequency ranges. It can be used to determine the frequency stop-bands (bandgaps) wherein the wave vector is imaginary, therefore, the plane waves experience rapid attenuation. To derive the dispersion curves, the solutions of the harmonic wave of the j^{th} ,

$(j+1)^{\text{th}}$, $(j-1)^{\text{th}}$ unit cells in Eq. (2-4) are adopted, and their derivative functions can be obtained as follows:

$$\ddot{u}^{(j)} = -\omega^2 U e^{i(jqL - \omega t)} = -\omega^2 u^{(j)} \quad (2-7)$$

$$\ddot{u}^{(j+1)} = -\omega^2 U e^{i(jqL - \omega t)} e^{iqL} = -\omega^2 u^{(j)} e^{iqL}$$

$$\ddot{u}^{(j-1)} = -\omega^2 U e^{i(jqL - \omega t)} e^{-iqL} = -\omega^2 u^{(j)} e^{-iqL}$$

Substituting Eq. (2-7) into Eq. (2-3), the dynamic equilibrium equation can be rewritten as:

$$\begin{bmatrix} -\omega^2 m_1 & 0 \\ 0 & -\omega^2 m_2 \end{bmatrix} \begin{bmatrix} u_1^{(j)} \\ u_2^{(j)} \end{bmatrix} + \begin{bmatrix} 2k_{a1} + k_{a2} & -k_{a2} \\ -k_{a2} & k_{a2} \end{bmatrix} \begin{bmatrix} u_1^{(j)} \\ u_2^{(j)} \end{bmatrix} - \begin{bmatrix} k_{a1} (e^{iqL} + e^{-iqL}) x_1^{(j)} \\ 0 \end{bmatrix} = \begin{bmatrix} 0 \\ 0 \end{bmatrix} \quad (2-8)$$

By applying the identity $e^{iqL} + e^{-iqL} = 2 \cos(qL)$, Eq. (2-8) becomes:

$$\begin{bmatrix} -\omega^2 m_1 & 0 \\ 0 & -\omega^2 m_2 \end{bmatrix} \begin{bmatrix} u_1^{(j)} \\ u_2^{(j)} \end{bmatrix} + \begin{bmatrix} 2k_{a1} + k_{a2} & -k_{a2} \\ -k_{a2} & k_{a2} \end{bmatrix} \begin{bmatrix} u_1^{(j)} \\ u_2^{(j)} \end{bmatrix} - \begin{bmatrix} 2k_{a1} \cos(qL) x_1^{(j)} \\ 0 \end{bmatrix} = \begin{bmatrix} 0 \\ 0 \end{bmatrix} \quad (2-9)$$

Solving Eq. (2-9), one obtains the relation between the wave number q and the angular frequency ω , which is called the wave dispersion relation.

$$-m_1 \omega^2 u_1^{(j)} + 2k_{a1} (1 - \cos(qL)) u_1^{(j)} + k_{a2} \left(1 - \frac{k_{a2}}{k_{a2} - m_2 \omega^2} \right) u_1^{(j)} = 0 \quad (2-10)$$

The frequency gap between the wave dispersion curves is called the bandgap, which means there is no positive real solution for ω with the change of q in the bandgap frequency range. In these excitation frequency ranges, only exponentially decaying solutions exist.

Eq. (2-10) can be further rearranged as:

$$\cos qL = 1 - \left[m_1 \omega^2 - k_{a2} \left(1 - \frac{\omega_0^2}{\omega_0^2 - \omega^2} \right) \right] \frac{1}{2k_{a1}}, \quad \omega_0^2 = \frac{k_{a2}}{m_2} \quad (2-11)$$

2.2.1.2.3 Wave transmission

Wave transmission analysis can also be used to determine the bandgaps. The wave transmission coefficient of the spring-mass model, defined as the ratio between the displacements of the output signal to the input excitation, can be calculated as:

$$T = \left| \prod_{j=1}^N T^{(j)} \right| = \left| \prod_{j=1}^N \frac{u^{(j)}}{u^{(j-1)}} \right| \quad (2-12)$$

where $u^{(j)}$ is the displacement of the j^{th} unit cell, and N is the total number of the unit cells.

Rearrange Eq. (2-11) as

$$\omega^2 = 2 \frac{k_{a1}}{m_{\text{eff}}} (1 - \cos(qL)) \quad (2-13)$$

and substituting $e^{iqL} + e^{-iqL} = 2 \cos(qL)$, from Eq. (2-9) it has

$$(2k_1 - m_{\text{eff}} \omega^2) u^{(j)} = k_{a1} (u^{(j+1)} + u^{(j-1)}), \quad j = 1, 2, \dots, N-1 \quad (2-14)$$

$$(k_{a1} - m_{\text{eff}} \omega^2) u^{(j)} = k_{a1} u^{(j-1)}, \quad j = N$$

By substituting the above equation into Eq. (2-12), the wave transmission coefficient can be formulated as follows:

$$T^{(j)} = \frac{k_{a1}}{k_{a1} (2 - T^{(j+1)}) - m_{\text{eff}} \omega^2}, \quad j = 1, 2, \dots, N-1 \quad (2-15)$$

$$T^{(N)} = \frac{k_{a1}}{k_{a1} - m_{\text{eff}} \omega^2}, \quad j = N$$

where $T^{(j)}$ is the transmission coefficient of the j^{th} unit cell, and N is the total number of the unit cells.

2.2.2 Spring-mass model for meta-truss bar

It was mentioned previously that the meta-concrete and meta-truss bar adopted a similar concept but their characteristics are slightly different. The cores in the meta-concrete are usually spherical while the core in the meta-truss bar is often cylindrical. Accordingly, the shear stiffness between the core and the mortar matrix in meta-concrete with spherical units is minimum owing to the point contact, but the shear resistance between the matrix and the cylindrical core in the meta-truss bar is considerable owing to the surface contact, therefore

needs to be considered in the spring-mass model. The analytical analysis in this chapter shows this shear stiffness governs the low-frequency bandgap.

To investigate the wave propagation in the meta-truss bar, especially in the low-frequency range, an equivalent spring-mass system with the shear spring stiffness of a continuum unit cell is proposed and illustrated in Figure 2-5. It should be noted that, to straightforwardly compare the bandgap mechanism between this model (i.e. the model considering the shear stiffness) and the model adopted for meta-concrete without considering the shear stiffness, the meta-truss bar in Figure 2-5 is selected as a representative. Besides the axial spring stiffnesses k_{a1} and k_{a2} respectively connecting the external mass with its adjacent unit cell and with the internal mass, this model considers the two shear spring stiffnesses, i.e. k_{s1} and k_{s2} .

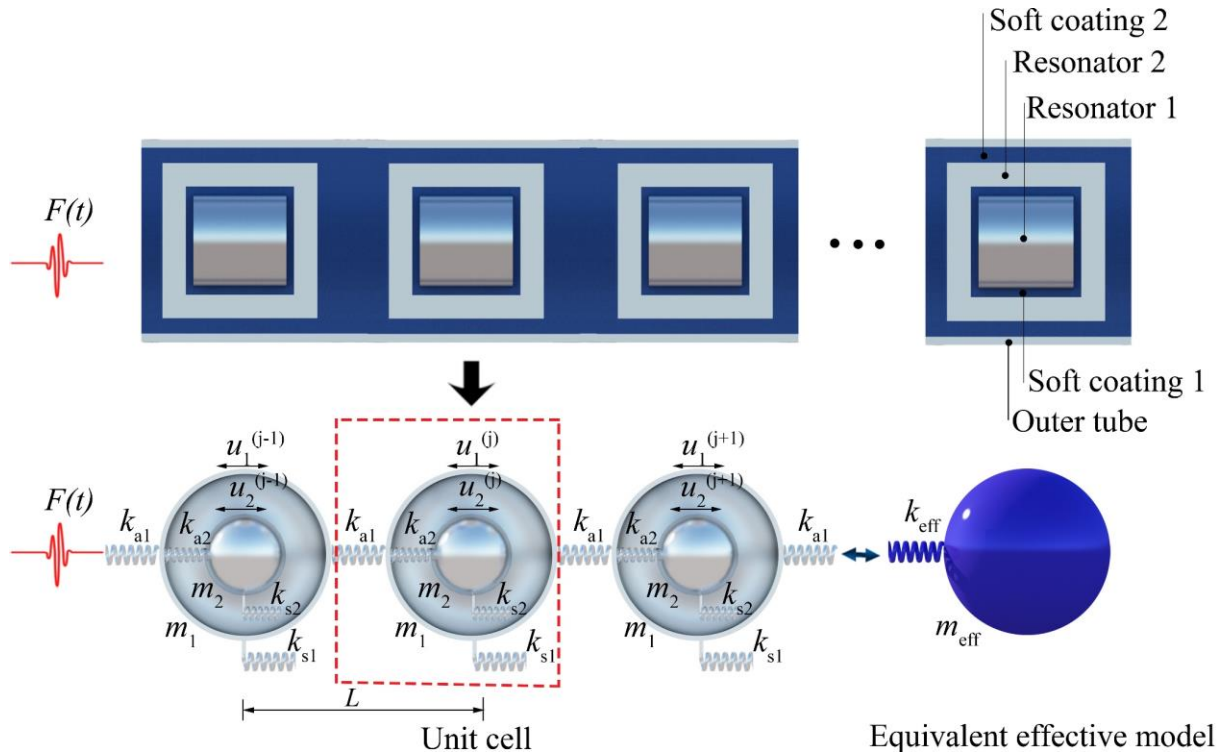


Figure 2-5. Schematic view of the simplified spring-mass model for meta-truss bar

Using the analytical model established in Figure 2-4, one can derive the equations of motion of the unit cell j^{th} as

$$m_1 \ddot{u}_1^{(j)} + k_{a1} (2u_1^{(j)} - u_1^{(j+1)} - u_1^{(j-1)}) + k_{a2} (u_1^{(j)} - u_2^{(j)}) + k_{s1} u_1^{(j)} = 0 \quad (2-16)$$

$$m_2 \ddot{u}_2^{(j)} + k_{a2} (u_2^{(j)} - u_1^{(j)}) + k_{s2} u_2^{(j)} = 0$$

Rewrite Eqs. (2-16) into a matrix

$$\begin{bmatrix} m_1 & 0 \\ 0 & m_2 \end{bmatrix} \begin{bmatrix} \ddot{u}_1^{(j)} \\ \ddot{u}_2^{(j)} \end{bmatrix} + \begin{bmatrix} 2k_{a1} + k_{a2} + k_{s1} & -k_{a2} \\ -k_{a2} & k_{a2} + k_{s2} \end{bmatrix} \begin{bmatrix} u_1^{(j)} \\ u_2^{(j)} \end{bmatrix} - \begin{bmatrix} k_{a1} (u_1^{(j+1)} + u_1^{(j-1)}) \\ 0 \end{bmatrix} = \begin{bmatrix} 0 \\ 0 \end{bmatrix} \quad (2-17)$$

Similar approaches are utilized to determine the effective parameters. The effective mass and the effective stiffness of the system are derived as [83]

$$m_{eff} = m_1 + \left[\frac{k_{a2}^2 / m_2}{\omega_0^2 - \omega^2} - (k_{s1} + k_{a2}) \right] \frac{1}{\omega^2} \quad (2-18)$$

$$k_{eff} = k_1 + \frac{1}{4} (k_{s1} + k_{a2}) - \frac{1}{4} \left(m_1 \omega^2 + \frac{k_{a2}^2 / m_2}{\omega_0^2 - \omega^2} \right)$$

where the natural vibration frequency is defined by $\omega_0^2 = \frac{k_{a2} + k_{s2}}{m_2}$.

Based on the Bloch-Floquet theory, in which the motion must satisfy the Bloch periodicity condition, the dispersion relation can be obtained as

$$\cos qL = 1 - \left[m_1 \omega^2 - (k_{s1} + k_{a2}) + \frac{k_{a2}^2 / m_2}{\omega_0^2 - \omega^2} \right] \frac{1}{2k_{a1}} \quad (2-19)$$

Using the transmission equations of the starting and ending unit cells, the displacement transmission coefficient of the entire system can be expressed as

$$T = \left| \prod_{j=1}^N T^{(j)} \right| = \left| \prod_{j=1}^N \frac{u^{(j)}}{u^{(j-1)}} \right| \quad (2-20)$$

where $T^{(j)} = \frac{k_{a1}}{k_{a1} (2 - T^{(j+1)}) - m_{eff} \omega^2}$ with $j = 1, \dots, N-1$, and $T^{(N)} = \frac{k_{a1}}{k_{a1} - m_{eff} \omega^2}$.

2.3. Verification and discussion of mechanisms for bandgap generation

In this section, the spring-mass models used to predict the bandgaps of meta-concrete and meta-truss bar are verified and discussed. From the above analytical derivations, it is expected that the meta-concrete has two bandgaps while the meta-truss bar has one additional bandgap in the low-frequency range due to the contribution of the shear stiffness. For validation, the

experimental data from the previous study [89] and the numerical results are utilized to verify the analytical models.

2.3.1 Spring-mass model for predicting bandgaps of meta-concrete

A number of experimental tests reported in the literature, e.g., results shown in Figure 2-4 from [89] illustrate that meta-concrete structure has two bandgaps although many studies overlooked the second bandgap and the discussions concentrated mainly on the first bandgap associated with the negative effective mass. This section analytically demonstrates meta-concrete has two bandgaps and presents methodologies on how to determine them. The periodic meta-concrete rod (shown in Figure 2-6) consists of three components, including the matrix (mortar), soft coating (nylon) and spherical inclusion (lead). Each part within the model is assigned with the appropriate properties as given in Table 2-1, where ν denotes Poisson's ratio, while ρ and E respectively represent the density and elastic modulus. Details of the considered structure have been reported in previous studies, which is therefore not repeated herein for brevity. According to the previous explanation, the considered meta-concrete rod is conceptualized as a spring-mass model.

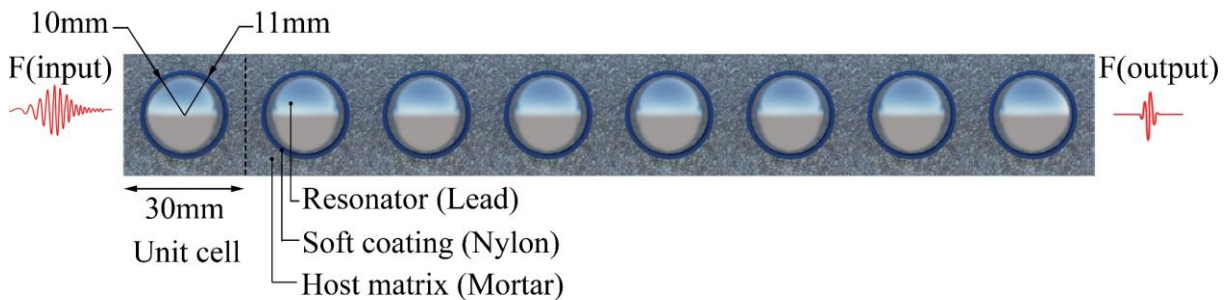


Figure 2-6. Schematic view of a meta-concrete rod used for modal analysis

Table 2-1. Elastic material properties for all components

Materials	Mortar	Lead	Nylon
ρ (kg/m ³)	2,500	11,400	1,150
E (GPa)	30	16	1
ν	0.2	0.44	0.4

To reveal the true relationship between the effective parameters and the bandgaps in the frequency band structure, the formations of the effective mass and effective stiffness are derived in Section 2.2 using the Floquet-Bloch's theory. The effective mass and effective stiffness of the considered model are examined in detail, which will be used as the foundation for the

explanation of the bandgap formation in the system. Figure 2-7 shows the effective mass and effective stiffness of the considered model calculated analytically over the frequencies of interest. As expected, the effective mass of the model becomes negative at a narrow frequency band from 17.5 kHz to 26.4 kHz (blue-shaded area), due to the out-of-phase motions of the resonator and the host matrix. It is worth mentioning that the wave manipulation capacity is significantly influenced by the local resonance of the resonator which is defined in Eq. (2-5) by $\omega_0 = \sqrt{k_{a2} / m_2} = 17.5$ kHz. Figure 2-7 shows that considering the effective mass for determination of the attenuation band can only predict a portion of the first bandgap (blue-shaded area, [17.5 – 26.4]), i.e., under-predicts the first bandgap width. The first bandgap actually consists of the blue-shaded area caused by negative effective mass and the red-shaded area induced by negative effective stiffness, i.e. [13.5 – 17.5] kHz.

Figure 2-7 shows a second bandgap in the red-shaded area, i.e. [> 35.9] kHz, also due to the negative effective stiffness. As illustrated, when the vibration frequency approaches the resonant frequency, the effective stiffness dramatically decreases to negative values in a narrow frequency region, then jumps to high positive values after passing the resonant frequency. Afterwards, the effective stiffness returns rapidly to zero before becoming negative again when the vibration frequency is large. The mechanism for forming a portion of the 1st bandgap of the effective stiffness is attributed to its negative values when approaching the local resonant frequency of the resonator, and its 2nd bandgap is generated when vibration frequency is large, leading to the negative value of the effective stiffness. This result can explain the high-frequency bandgap of the considered model as observed in the tests.

By combining the results in Figure 2-7, two observations can be found. Firstly, there are two bandgaps induced by both the effective mass and effective stiffness, which is different from previous studies on meta-concrete where only one bandgap was reported. Secondly, the first bandgap consists of two portions induced by the negative effective mass and negative effective stiffness. Accordingly, the width of the first bandgap should be wider than the case when only the effective mass is considered as in previous studies [73, 82].

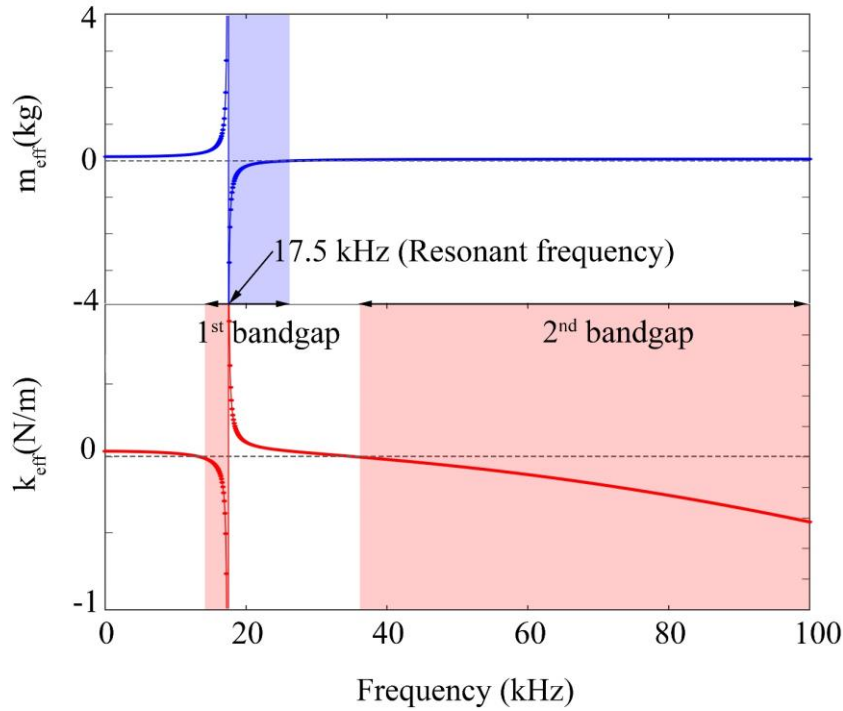


Figure 2-7. Effective parameters of the spring-mass model to show the theoretical bandgap regions of meta-concrete

To further elaborate the mechanism of the considered model and verify the frequency band structure given by the effective properties, the real and imaginary parts of the dispersion curves produced by using the periodic spring-mass model are illustrated in Figure 2-8. The blue line in the figure denotes the real part while the corresponding imaginary part is represented by the red line. As shown, the imaginary part of the wavenumber in the complex frequency band is not equal to zero [$\text{Im}(qL) \neq 0$] at the two regions of frequencies (shaded areas), indicating complete bandgap frequency regions. In other words, the frequency band structure of this model exhibits two bandgaps [$\text{Re}(qL)=0$] and two passbands [$\text{Re}(qL) \neq 0$]. It is clear that the bandgaps in Figure 2-8 match well with the frequency bandgaps derived above based on the negative effective mass and stiffness, i.e., the first bandgap from 13.5 kHz to 26.4 kHz and over 35.9 kHz for the 2nd bandgap. These results indicate that once the effective properties become negative, the corresponding wavenumber would become complex, resulting in wave attenuation and eventually preventing wave transmitting through the system.

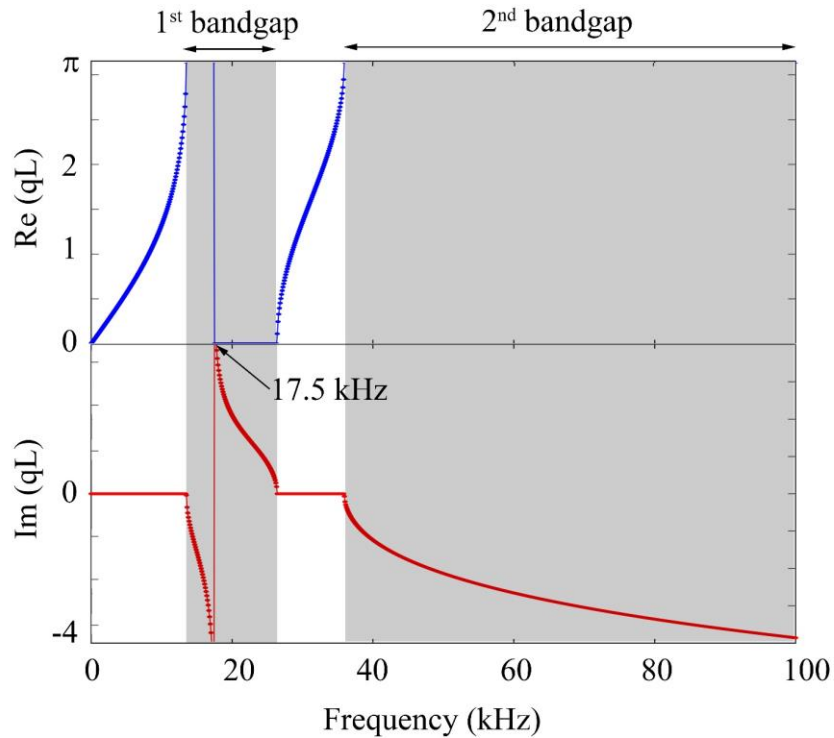


Figure 2-8. Complex frequency band structure of the dispersion curves of the spring-mass model to show the theoretical bandgap regions of meta-concrete

In addition to the wave dispersion curves, the wave transmission can also be utilized to study the mitigation characteristics of wave propagation in meta-concrete. As shown in Figure 2-9, the low transmission of the system is observed in the frequency ranges coincident with the negative effective properties in Figure 2-7. These observations demonstrate that both methods yield the same results. To further validate the bandgaps obtained in the above derivations, the tunable wave transmission coefficients from the experimental results and those obtained above, as well as the bandgaps derived by considering only the negative effective mass are compared in Figure 2-9. As shown, the experimental results also gave two bandgaps as denoted by grey-shaded areas. The bandgap associated with the negative effective mass (i.e. conventional analysis) represented by the red-shaded area only captures a portion of the 1st bandgap of the experimental result (grey-shaded area), demonstrating again that considering the negative effective mass alone is insufficient to obtain the complete bandgaps of meta-concrete. Meanwhile, the combined bandgaps associated with both the negative effective mass and negative effective stiffness match well with the experimental results (Figure 2-9), which confirms the validity of the above analysis and the need for considering the negative effective stiffness in deriving the bandgaps. In particular, a sharp wave transmission dipping at 17.5 kHz is found in both the analytical derivation and experimental test, which is caused by the local

resonance of the resonator. The bandgaps due to the local resonator obtained from the analytical derivation agree well with those observed in the experimental tests. In the experimental tests, the obtained frequency bandgaps are from 12.5 kHz to 23.5 kHz and >34.5 kHz, respectively for the 1st and the 2nd bandgap while the corresponding ranges from the analytical derivation are 13.5 kHz to 26.4 kHz and >35.9 kHz. It should be noted that there are some slight variations between the experimental result and the theoretical results. This is because, as discussed above, in theoretical derivation the model is assumed to be homogeneous with idealized material properties, and an infinite number of unit cells connected by springs, i.e., no boundary reflection, while the tested specimen in the experiment has a finite length with only 8 unit cells and the specimen material properties are inhomogeneous.

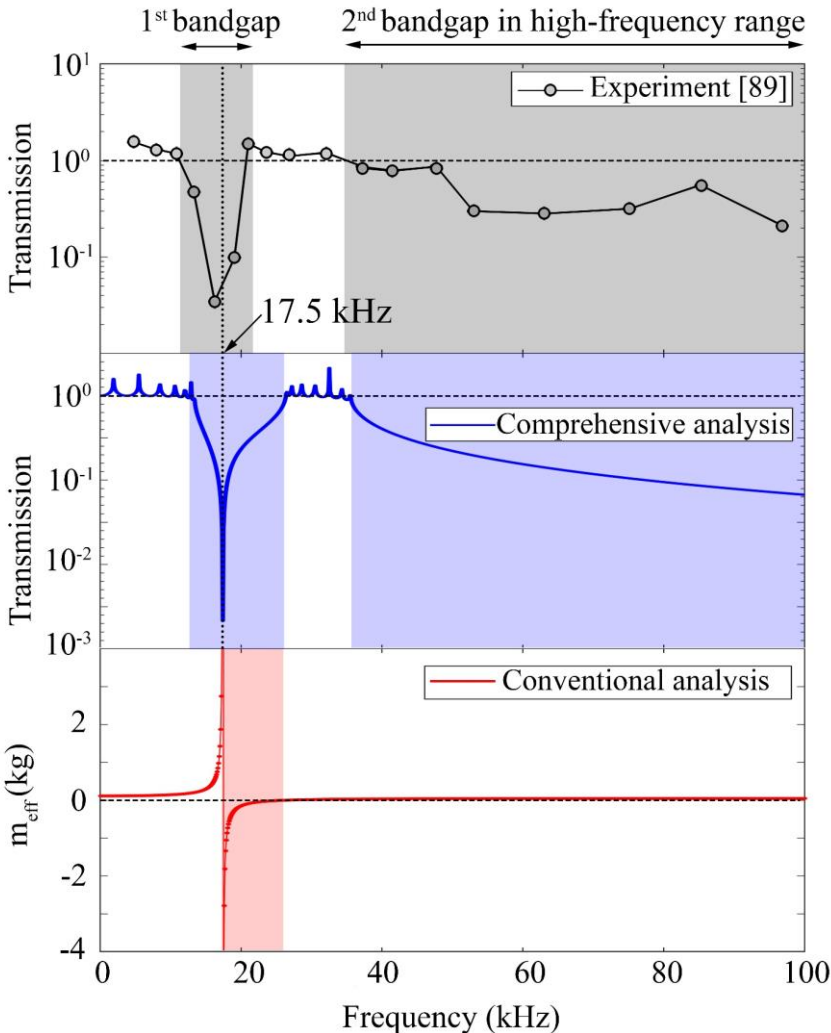


Figure 2-9. Bandgaps obtained from experimental test, prediction considering both the effective mass and effective stiffness, and prediction considering only the effective mass

Besides, as observed from the experiment in Figure 2-9, the transmission coefficients in the low-frequency bandgap are smaller than those in the high-frequency bandgap. It is attributed to the fact that the number of unit cells in the considered structure has a significant effect on the high-frequency bandgap while it has limited influence on the low-frequency bandgap, which is in close proximity of the local resonant frequency (i.e. 17.5 kHz). Specifically, as proven in the previous study [89], when increasing the number of unit cells from 8 units to 36 units, the transmission coefficient in the low-frequency bandgap is unchanged while those of the high-frequency bandgap decrease to a converged value. The above results indicate that both the effective mass and effective stiffness need to be considered in deriving the frequency bandgaps. The analytical results agree well with those observed in the experimental tests.

2.3.2 Spring-mass model for predicting bandgaps of meta-truss bar

Section 2.3.1 discusses a spring-mass model for meta-concrete which ignores the shear behaviour between the resonators and the host matrix. The shear stiffness can be ignored because of the spherical shape of the unit cells in meta-concrete which results in minimum shear resistance between the unit cells and the matrix. For a meta-truss bar, however, the unit cell usually has cylindrical shapes for easy implementation as studied in [41, 42]. When simplifying the meta-truss bar to the spring-mass model, the shear resistance between the resonators and the matrix cannot be ignored because of the large shear area of the cylindrical surface. Without loss of generality, the meta-truss bar (Figure 2-10) consists of eight periodical unit cells, in which each unit cell comprises five components including the outer tube, soft coatings, and resonators. For brevity, details of the meta-truss bar are not presented herein but can refer to a previous study by Vo et al. [41]. The material properties are summarized in Table 2-2.

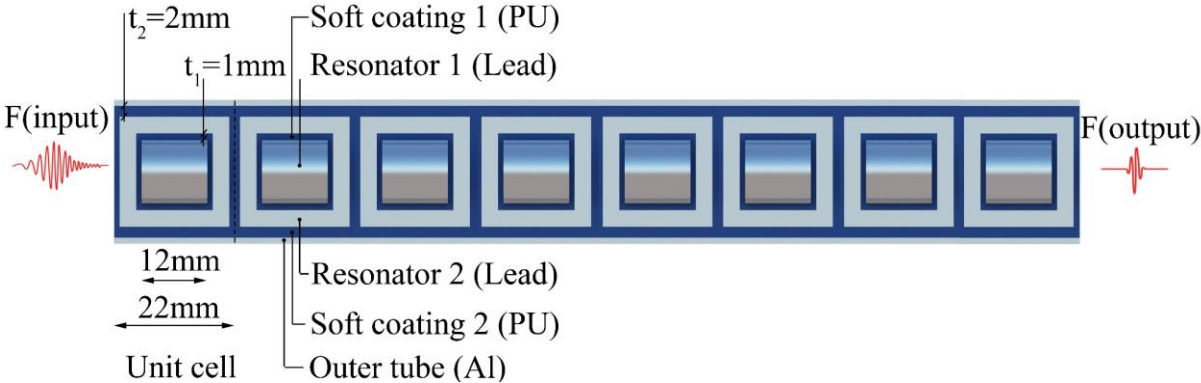


Figure 2-10. Schematic view of the meta-truss bar used for modal analysis

Table 2-2. Elastic material properties for all components of the meta-truss bar [41]

Materials	Aluminium	Polyurethane	Lead
ρ (kg/m ³)	2,770	900	11,400
E (GPa)	70	0.147	16
ν	0.33	0.42	0.44

From the derivations presented in Eq. (2-18), the analytical formulae for the effective mass and effective stiffness with respect to the vibration frequency can be straightforwardly determined. Figure 2-11 shows the effective mass and effective stiffness of the meta-truss bar, in which the bandgaps correspond to their negative values. The blue-shaded regions represent the frequency ranges of the bandgaps related to the negative effective mass while those associated with the negative effective stiffness are marked by red-shaded areas. It is observed again that the bandgap at the local resonant frequency does not start at the natural frequency of the local resonator (i.e. 10.3 kHz), but at a lower frequency because of the contribution of the negative stiffness. The bandgap close to the local resonant frequency is in the range of 9.3 kHz to 11.5 kHz. Combining both the effective parameters, it is found that there are three bandgaps in this considered meta-truss bar. Particularly, two bandgaps in the low and high-frequency regions are independent of each other and are formed because of the negative effective mass and negative effective stiffness, respectively, while the bandgap in the middle is the combination of the negativity of the effective mass and effective stiffness.

Besides, compared to the frequency band structure in Figure 2-7, the second (middle range) and the third (high-frequency range) bandgaps are similar as discussed above in meta-concrete, while the meta-concrete considered above does not have the first (low-frequency range) bandgap associated with the negative effective mass. This is because of the shear stiffness between the matrix and the unit cell in the meta-truss bar that generates this low-frequency bandgap from 0 – 5 kHz. This low-frequency bandgap is of great importance in the field of engineering applications, e.g. vibration control, seismic isolation, and mechanical harness because loading frequencies are mainly in the low-frequency range. This finding is of foremost importance since it reveals how the mechanism can be fully leveraged to achieve a wider range of the bandgap frequencies for which wave propagation is reduced, especially in a low-frequency range.

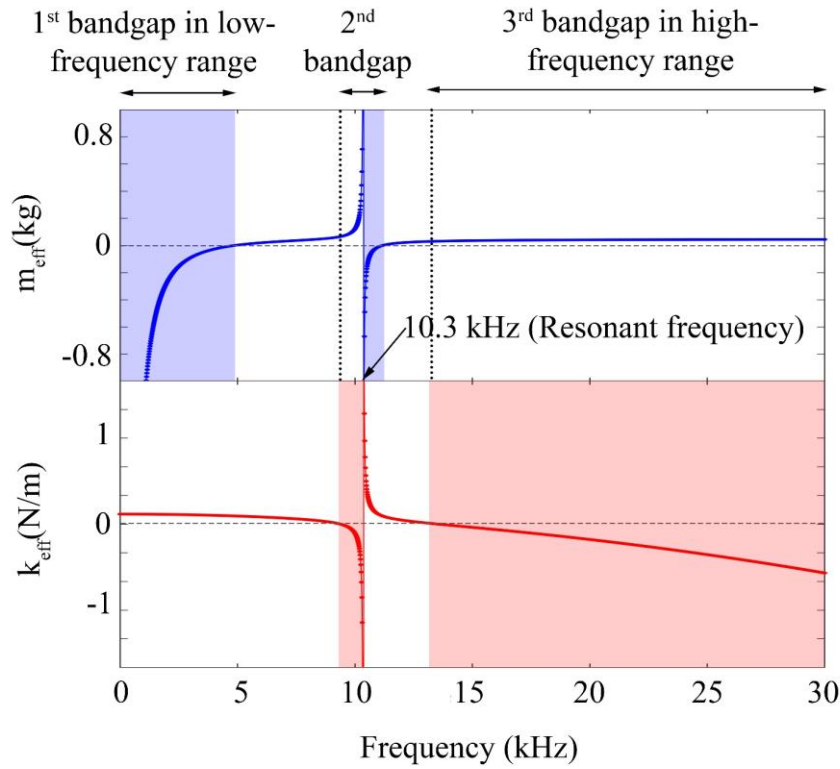


Figure 2-11. Effective parameters of the spring-mass model with shear stiffness to show the theoretical bandgap regions of meta-concrete

To construct the frequency band structure of the meta-truss bar, the theoretical dispersion curves obtained from Eq. (2-19) for wave propagation are illustrated in Figure 2-12. It should be noted that the bandgap corresponds to the frequency range when the imaginary part (the attenuation factor) is not equal to zero. As shown, there are three bandgaps in the frequency band structure of the meta-truss bar, with one additional bandgap in the low-frequency region compared to the model without shear stiffness. Specifically, the three bandgaps are 0 – 5 kHz, 9.3 – 11.5 kHz, and >13.5 kHz, which are denoted as 1st, 2nd, and 3rd bandgaps. In these frequency ranges, no waves can freely propagate through the meta-truss bar. The dividing points of the first and last branches correspond to the locations where the effective mass or effective stiffness becomes zero, respectively. Whereas the dividing points for the middle-frequency band are the combination of both the negative effective mass and negative effective stiffness. It is worth mentioning that the dividing points mean the starting or cutoff frequencies of the bandgaps. Generally, the benefits from the appearance of the 1st bandgap in the low-frequency and the enhancement of the second bandgap demonstrate the significance of the shear stiffness in the spring-mass model.

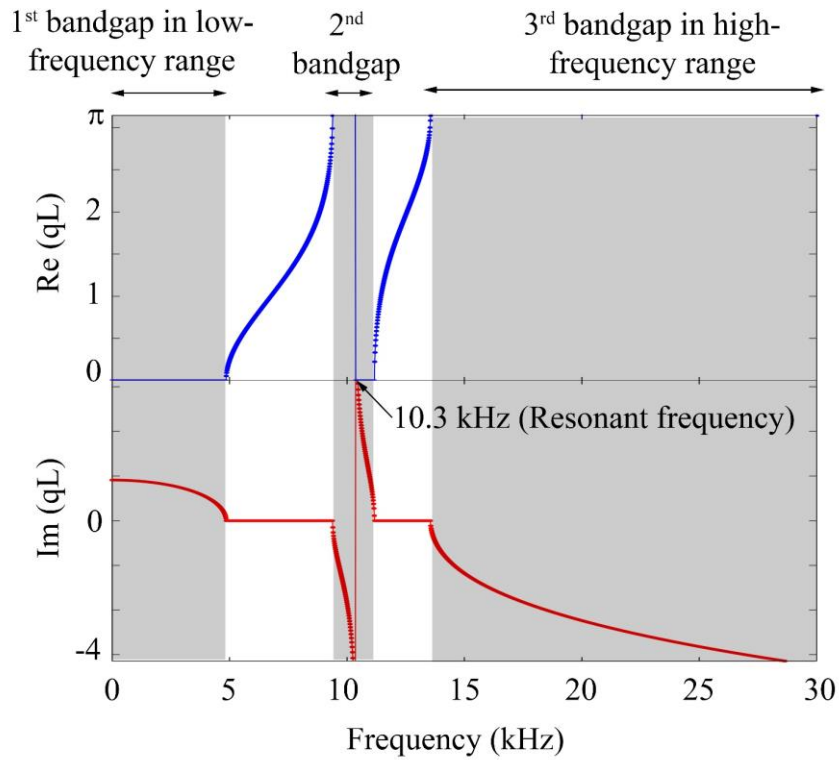


Figure 2-12. Complex frequency band structure of the dispersion curves of the spring-mass model with shear stiffness to show the theoretical bandgap regions of meta-concrete

To further validate the above theoretical predictions, a numerical model of the considered meta-truss bar is developed in the commercial FEA software, LS-Dyna. The transmission coefficient is numerically calculated and compared with the theoretical predictions. The transmission coefficient is the ratio between the output and the input signals of the considered meta-truss bar. For the numerical simulation, the input signal defined by a sweep frequency ranging from 0 – 30 kHz is applied at one end of the meta-truss bar, and the output response at the other end is captured to calculate the transmission coefficient. All elements in the numerical model, i.e. solid hexahedron elements (SOLID 164), are meshed with a minimum meshing size of 1 mm after performing mesh convergence tests. Details of the mesh size sensitivity analysis with the same structure have been reported in the previous study [41], which is therefore not repeated here for brevity. For modelling contact and boundary conditions, the interfaces between the inclusions and coating defined by the keyword `*TIED_SURFACE_TO_SURFACE` are assumed as perfect contact while the keyword `*NON_REFLECTING_BOUNDARY` is applied at one end of the model to minimize stress waves reflection. The material properties used in the numerical model are the same as those in theoretical calculations given in Table 2-2. The transmission coefficient profiles from the analytical analysis and numerical simulation are shown in Figure 2-13. The bandgaps from the analytical transmission coefficient are the same

as those obtained from the dispersive analysis and the effective mass and stiffness. As shown, the bandgap regions corresponding to the wave reduction in the transmission-frequency profiles from the analytical prediction match very well with those from numerical simulation, further confirming the validity of the analytical model for predicting the bandgaps of the meta-truss bar. It should be noted that the locally resonant frequency of the resonator (i.e. 10.3 kHz) corresponds to a big dip displacement in the transmission profile. From the numerical simulation, the first and second bandgaps are respectively at 0 kHz to 4.1 kHz and 8.5 kHz to 12.3 kHz while the high-frequency bandgap is greater than 14.2 kHz. The discrepancies between the numerical and the analytical results can be attributed to the assumption of the infinite number of unit cores in the theoretical derivations while only 8 unit cores are modelled in the numerical simulation, and likely numerical errors because of discretization.

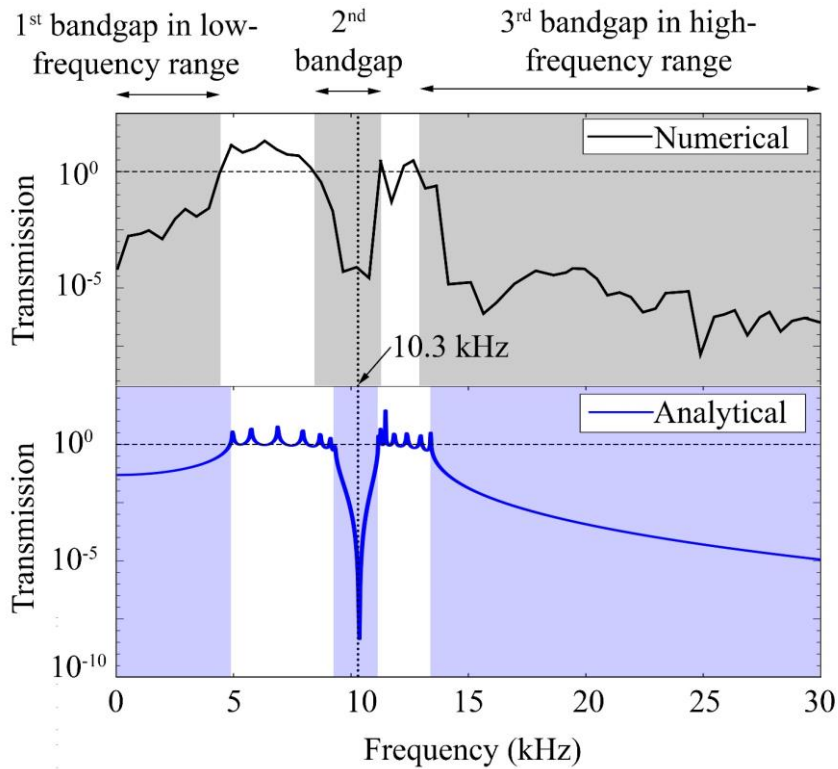


Figure 2-13. Transmission coefficient between numerical and analytical results

The above analyses have proven the considered meta-truss bar can generate three bandgaps and it can mitigate stress wave propagation when the wave frequency falls within these bandgaps. To demonstrate the frequency-filtering performance of the meta-truss bar in the low-frequency range, a harmonic displacement input constituted by three frequencies, i.e.

$$u(t) = \sum_{i=1}^3 \sin(2\pi f_i t), \text{ where } f_1=1 \text{ kHz, } f_2= 3 \text{ kHz, and } f_3= 7 \text{ kHz, is applied to the input end of}$$

the meta-truss bar to examine whether the wave could propagate through the meta-truss bar. The displacement at the other end is recorded as the output signal. It should be noted that f_1 and f_2 are deliberately selected to fall within the first bandgap in the low-frequency range of the meta-truss bar, while f_3 does not fall into any bandgap. Figure 2-14 shows the Fast Fourier Transform (FFT) spectra of displacement-time histories at the two ends of the meta-truss bar (i.e. the input and the output, respectively). As shown, a significant wave reduction in the first bandgap is observed as expected with only the input signal at 7 kHz passing through the meta-truss bar while the other two components at 1 kHz and 3 kHz within the first bandgap are effectively mitigated. Generally, the obtained results indicate that the meta-truss bar has the favourable ability to filter stress waves with frequency contents falling in its bandgap.

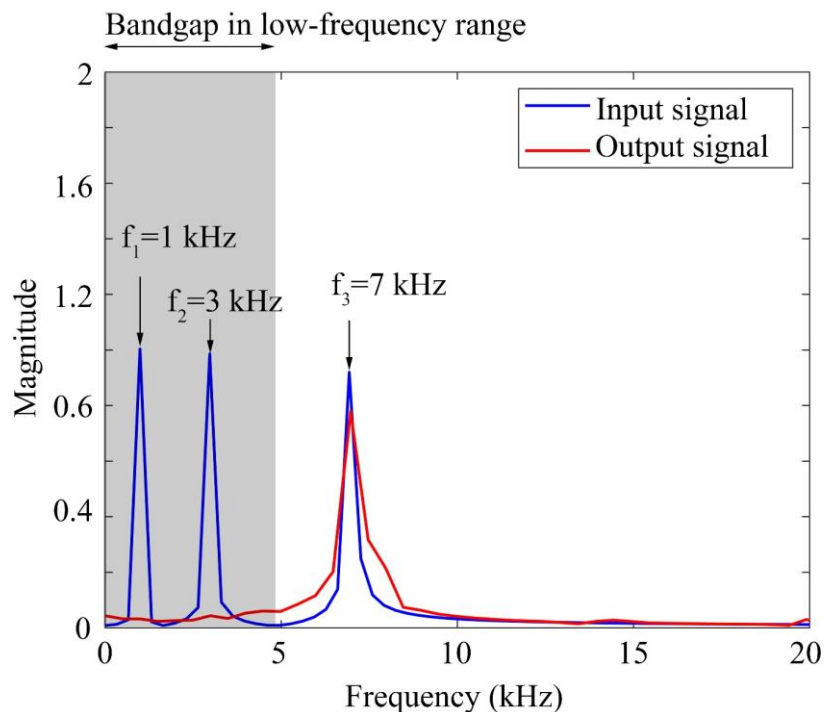


Figure 2-14. FFT spectra of the input and output displacements at center points of two ends of the meta-truss bar

2.3.3 Discussions

Recall the two issues that are defined and discussed in the above sections, namely one or two bandgaps obtained in the meta-concrete in previous analyses by different researchers, and the existence of an additional low-frequency bandgap in the meta-truss bar. Based on the above results, these two issues are discussed here.

For the first issue, it is clear now that the analysis that considers only the negative effective mass in determining the bandgap of the meta-concrete fails to obtain the second high-frequency bandgap associated with the negative effective stiffness. Neglecting the influence of the negative effective stiffness also results in an under-prediction of the width of the first bandgap. Therefore both the negative effective mass and negative effective stiffness need to be considered in determining the bandgaps of meta-concrete. The predicted bandgaps with consideration of both the negative effective mass and stiffness agree well with those obtained in experimental tests, verifying the correctness of the proposed analytical model.

For the second issue, it is clear that if the shear resistance exists between the unit cells and the matrix, a low-frequency bandgap will be generated. In such cases, the meta-structure could have three bandgaps for wave propagation mitigation. The formation of the low-frequency bandgap is of significant importance for practical applications since many loadings on civil, mechanical, and other structures have low-frequency contents. To facilitate engineering applications, a design procedure for meta-panel is presented in the appendix.

In brief, the actual realizations of the predicted bandgaps of resonance-based meta-materials/ meta-structures are presented in this chapter. The results demonstrate that the analytical model can accurately predict the experimental bandgaps of the meta-concrete, including one widened middle bandgap compared to the conventional analysis and another bandgap in the high-frequency range. It is found that at the resonance frequency, a merging bandgap from both the negative effective mass and negative effective stiffness is formed, corresponding to the out-of-phase motions of the resonators. In addition, the meta-truss bar is proven to possess the bandgap in the low-frequency range due to the shear stiffness between the soft coating layers and the truss tube. With such unique capabilities, physically realizable waveguide at different frequencies can be programmably designed for meta-materials/ meta-structures for numerous practical engineering applications.

2.4. Conclusions

This chapter presents an in-depth analysis of the bandgap formation in meta-concrete and meta-truss bars. The effective mass and effective stiffness, the wave dispersion relation, and the transmission coefficient are analytically derived to quantitatively determine the bandgaps of the considered structures, which are validated by experimental study and numerical simulation. The following conclusions can be drawn.

1. Two bandgaps exist in meta-concrete structure, in which the first bandgap is formed by the negative effective mass and the negative effective stiffness while the negative effective stiffness further creates another bandgap in the high-frequency range.
2. The shear stiffness between the cores and the surrounding host matrix governs an additional bandgap in the very low-frequency range in the meta-truss bar. This bandgap only appears when the shear behaviour between the cores and the host matrix is considerable.
3. This work also provides a detailed design in the appendix for programmable waveguides of the meta-panel consisting of meta-truss bars, which can be employed for designing the meta-panel for mitigation of dynamic loading effect.

Appendix

A. Design guide for meta-truss bars with targeted bandgap regions

Based on the above analytical solutions, a design method of meta-truss bars with the desired target bandgaps is proposed in this section.

The proposed design flowchart is illustrated in Figure 2-14. It starts with the parameters of the expected loading $F(t)$ on the considered structure. This loading can be a recorded impact load, blast load or load given in a design code. The next step is to determine the frequency content of $F(t)$ using the Fast Fourier Transform (FFT). From the FFT spectrum of the design load, the desired bandgaps, $BG_i=[f_{i1}-f_{i2}]$, can be determined to ideally cover the entire or primary frequency ranges that the loading energy distributed in the frequency domain for the best loading mitigation effect. It should be noted that the subscript $i=1,2,3$ indicates the first, second, and third bandgaps of the meta-truss bar and ideally BG_i should enclose all frequency ranges $[f_a, \dots, f_b]$ that loading energy distributes to achieve the maximal mitigation effect. The design parameters of the spring-mass model, i.e. m_i and k_i , are analytically calculated based on the theoretical bandgap starting point f_{i1} and cutoff point f_{i2} , which will be discussed later in Appendix B.

Next, the initial design features including geometric parameters, materials are selected as given in Eq. (2-23). After the initial selection of the design parameters, the bandgaps of the meta-truss bar are numerically evaluated using a numerical verification, e.g. using LS-Dyna. If the calculated bandgaps from the initial selection meet the above requirements, it shall move to the final step. If not, the trial and error processes are required to obtain the appropriate design parameters ensuring that the numerical bandgaps cover all or primary frequency contents of the applied loading.

Finally, given a set of design parameters, the meta-structures can be fabricated.

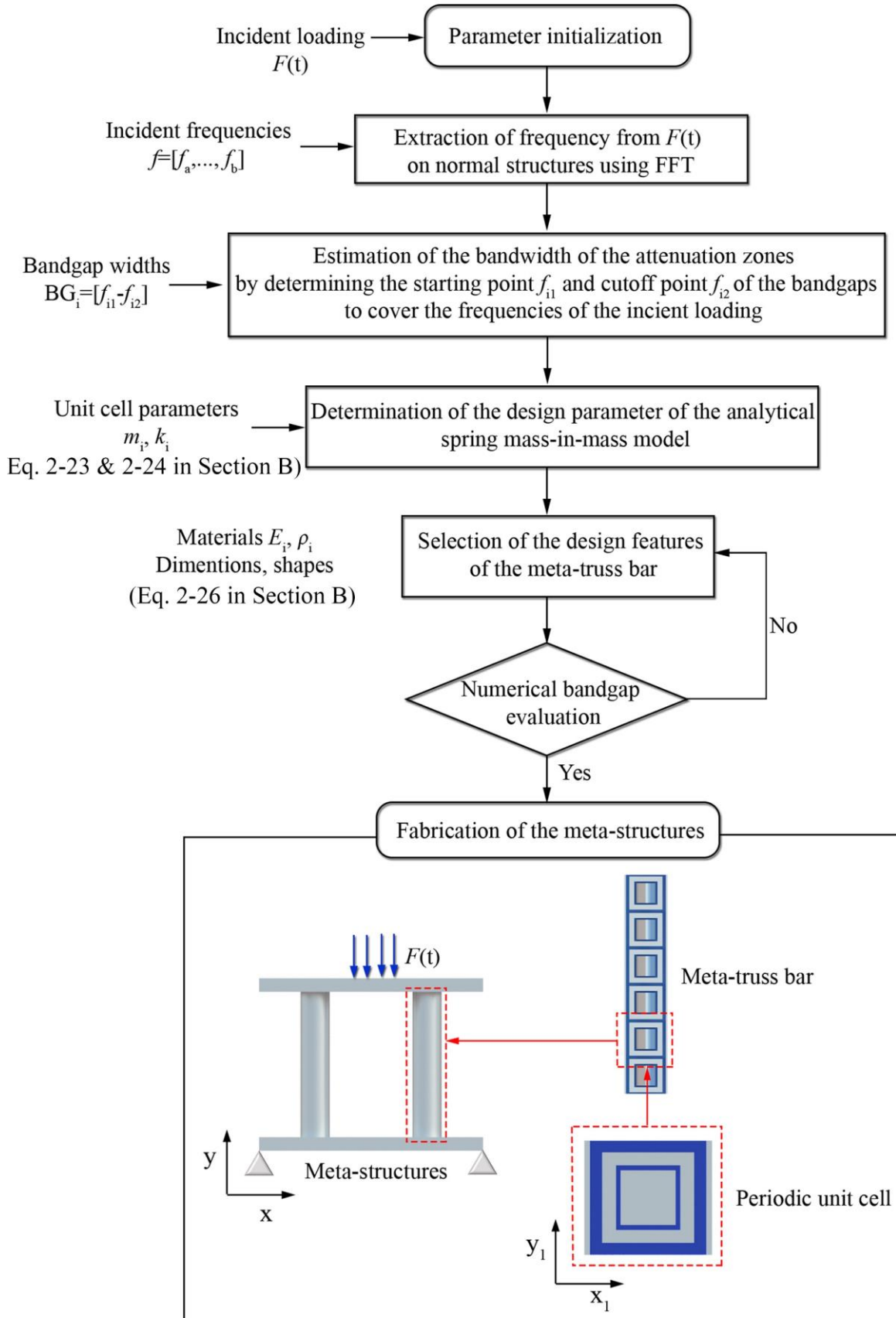


Figure 2-15. Flowchart of the meta-structure design.

B. Determination of the Starting and Cutoff frequencies of a corresponding bandgap

The bandgaps from the comprehensive analysis of the spring-mass model are presented in Figure 2-16. Based on the theoretical results from this chapter, the bandgaps of the meta-truss bar can be divided into three regions including $[0-f_{11}]$ for the 1st bandgap, $[f_{21}-f_{22}]$ for the 2nd bandgap, and $[>f_{31}]$ for the 3rd bandgap. It is worth mentioning that the local resonant frequency of the resonator can be calculated by, $f_0 = \sqrt{\frac{k_{a2} + k_{s2}}{m_2}} / (2\pi)$.

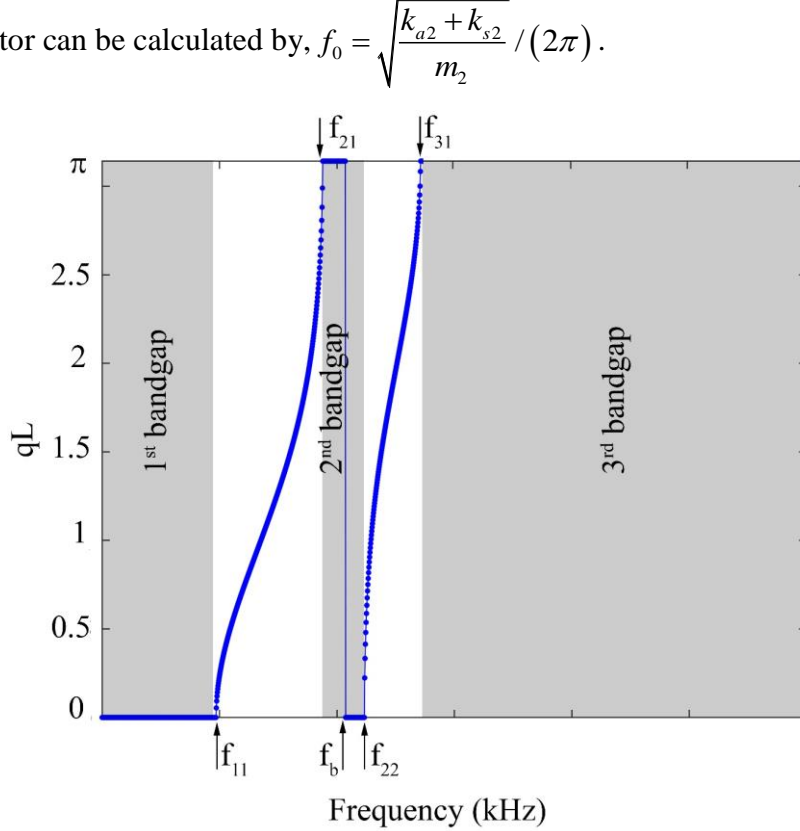


Figure 2-16. Typical bandgap determination based on the dispersion curves is divided into three regions including $[0-f_{11}]$ for the 1st bandgap, $[f_{21}-f_{22}]$ for the 2nd bandgap, and $[>f_{31}]$ for the 3rd bandgap

To define the width of the bandgaps, the dispersion in Eq. (2-19) can be rewritten as

$$m_1 m_2 \omega^4 - [2m_2(1 - \cos qL)k_{a1} + m_2 k_{s1} + (m_1 + m_2)k_{a2} + m_1 k_{s2}] \omega^2 + 2k_{a1}(k_{a2} + k_{s2})(1 - \cos qL) + k_{s1}(k_{a1} + k_{s2}) + k_{a2}k_{s2} = 0 \quad (2-21)$$

The expression of the angular frequency can be obtained by solving Eq. (2-21) as

$$\omega^2 = \frac{2m_2(1 - \cos qL)k_{a1} + m_2 k_{s1} + (m_1 + m_2)k_{a2} + m_1 k_{s2} \pm \sqrt{\Psi - X}}{2m_1 m_2} \quad (2-22)$$

where $\Psi = (2m_2(1 - \cos qL)k_{a1} + m_2k_{s1} + (m_1 + m_2)k_{a2} + m_1k_{s2})^2$ and

$$X = 4m_1m_2[2k_{a1}(k_{a2} + k_{s2})(1 - \cos qL) + k_{s1}(k_{a2} + k_{s2}) + k_{a2}k_{s2}]$$

The starting angular frequencies of the bandgaps can be obtained by substituting $qL = 0$, as

$$\omega_{i1}^2 = \frac{m_2k_{s1} + (m_1 + m_2)k_{a2} + m_1k_{s2} \pm \sqrt{\Gamma}}{2m_1m_2}, \quad i = 1, 2, 3 \quad (2-23)$$

where $\Gamma = (m_2k_{s1} + (m_1 + m_2)k_{a2} + m_1k_{s2})^2 - 4m_1m_2[k_{s1}(k_{a2} + k_{s2}) + k_{a2}k_{s2}]$

The cutoff angular frequencies of the bandgaps can be obtained by substituting $qL = \pi$, as

$$\omega_{i2}^2 = \frac{4m_2k_{a1} + m_2k_{s1} + (m_1 + m_2)k_{a2} + m_1k_{s2} \pm \sqrt{\Lambda - M}}{2m_1m_2}, \quad i = 1, 2, 3 \quad (2-24)$$

where $\Lambda = (4m_2k_{a1} + m_2k_{s1} + (m_1 + m_2)k_{a2} + m_1k_{s2})^2$ and

$$M = 4m_1m_2[4k_{a1}(k_{a2} + k_{s2}) + k_{s1}(k_{a2} + k_{s2}) + k_{a2}k_{s2}]$$

The starting and cutoff frequencies of the bandgaps are

$$f_{ij} = \frac{\omega_{ij}}{2\pi}, \quad i = 1, 2, 3 \text{ and } j = 1, 2, 3 \quad (2-25)$$

The design parameters including internal mass, external mass and stiffnesses can be estimated by Eq. (2-26), where ρ_i and V_i are the material density and volume of the unit cell, and its length and radius are denoted by l_i and r_i , respectively.

$$m_i = \rho_i V_i = \rho_i \pi r_i^2 l_i, \quad i = 1, 2 \quad (2-26)$$

$$k_{ai} = \frac{EA_i}{l_i}, \quad k_{si} = \frac{GA_i}{l_i}$$

where E and A are Young's modulus and the nominal cross-section area of the coating material.

C. Worked-out example

A design example of a meta-panel consisting of four meta-truss bars to resist the impact force induced by a spherical ball with a mass of 1 kg and an impact velocity of 30 m/s is presented here to illustrate the above-proposed design procedure.

- Step 1: Determination of the design load $F(t)$.

The impactor has a spherical shape of 20 mm radius and its weight is 1 kg. The initial velocity of the impactor against the structural panel is 30 m/s. A numerical model is generated in LS-DYNA to predict the impact load on the structure. The predicted impact force-time history $F(t)$ is illustrated in Figure 2-17.

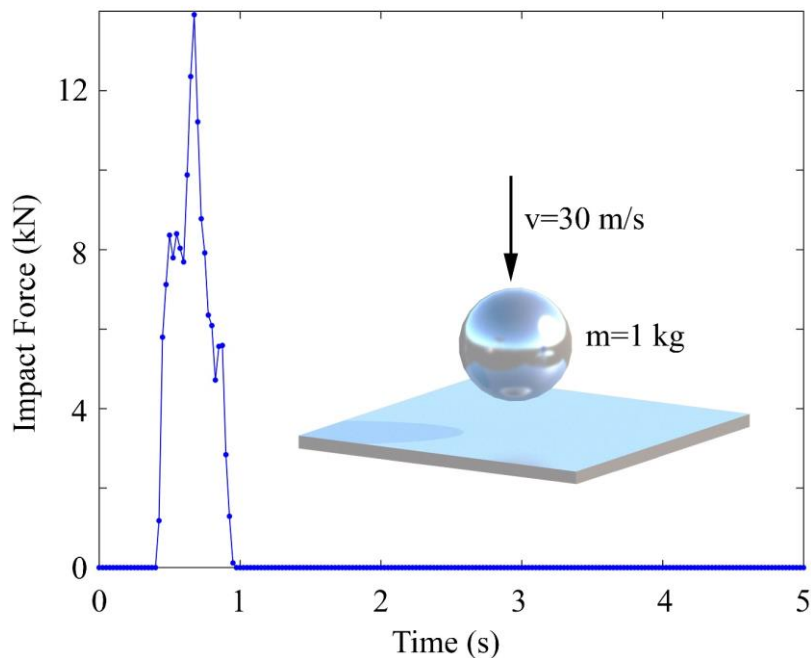


Figure 2-17. Peak impact force time history of the simulated impact loading

- Step 2: Determination of the frequency contents of $F(t)$

The FFT spectrum of the predicted impact force time history $F(t)$ is calculated and shown in Figure 2-18. As shown, the impact loading energy distributes mainly in the frequency regions of [0 – 4.8] kHz, [7.5 – 8.5] kHz, and [9.7 – 12] kHz.

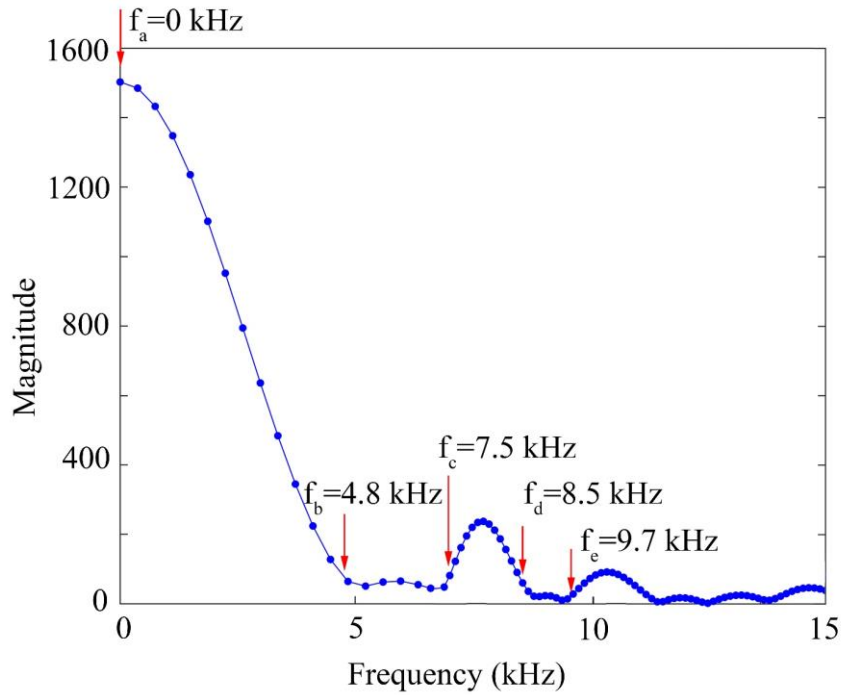


Figure 2-18. FFT spectrum of the impact force time history of the simulated impact loading

- Step 3: Determinations of the bandwidth of the desired bandgaps to cover the frequencies with the most loading energy.

The designed bandgaps are selected according to the FFT spectrum as shown in Figure 2-19

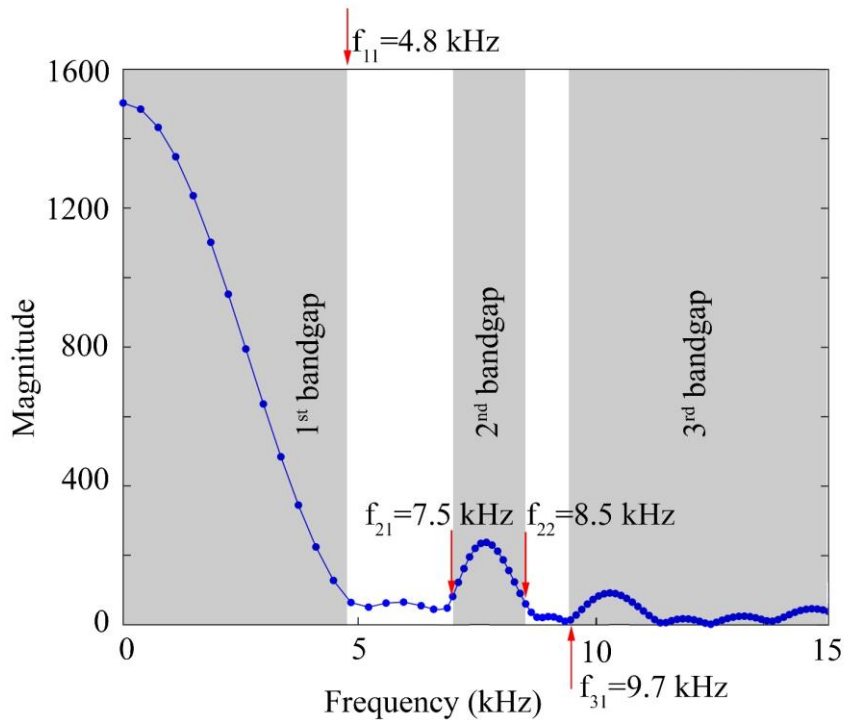


Figure 2-19. Estimated bandgap widths of the designed meta-truss bar

$BG_1 = [0 - f_{11}]$ kHz, $BG_2 = [f_{21} - f_{22}]$ kHz, and $BG_3 = [>f_{31}]$ kHz

where $f_{11} = 4.8$ kHz, $f_{21} = 7.5$ kHz, $f_{22} = 8.5$ kHz, and $f_{31} = 9.7$ kHz.

- Step 4: Calculations of the design parameters

To achieve the above desired bandgaps, the design parameters of the analytical spring-mass model are obtained from Eqs. (2-23), (2-24), (2-25), and they are $m_1 = 4.71 \times 10^{-2}$ (kg), $m_2 = 1.55 \times 10^{-2}$ (kg), $k_{a1} = 2.3 \times 10^8$ (N/m), $k_{a2} = 1.6 \times 10^8$ (N/m), $k_{s1} = 3.2 \times 10^8$ (N/m), and $k_{s2} = 2.3 \times 10^8$ (N/m).

- Step 5: Select the materials and dimensions of the meta-truss bar

Polyurethane is selected for the soft coating while the outer tube and the resonators are made of Aluminium and Lead. The diameters of the internal and external resonators are respectively denoted by r_2 and r_1 , which are calculated by

$$r_2 = \sqrt{\frac{m_2}{\rho_{Lead} \pi l_2}} = \sqrt{\frac{1.55 \times 10^{-2}}{11400 \times \pi \times 12 \times 10^{-9}}} = 6 \text{ (mm)}$$

$$r_1 = \sqrt{\left(\frac{m_1}{\rho_{Lead} \pi} + r^2 l \right) \frac{1}{l_1}} = \sqrt{\left(\frac{4.71 \times 10^{-2}}{11400 \times \pi} + 7^2 \times 14 \times 10^{-9} \right) \frac{1}{20 \times 10^{-3}}} = 10 \text{ (mm)}$$

Thicknesses of the inner and outer coatings, i.e. t_1 and t_2 can be calculated by

$$t_1 = \frac{EA_1}{k_{a1}} = \frac{E \pi \pi r_1^2}{k_{a1}} = \frac{0.147 \times 10^9 \times \pi \times 10^2 \times 10^{-6}}{2.3 \times 10^8} = 2 \text{ (mm)}$$

$$t_2 = \frac{EA_2}{k_{a2}} = \frac{E \pi \pi r_2^2}{k_{a2}} = \frac{0.147 \times 10^9 \times \pi \times 6^2 \times 10^{-6}}{1.6 \times 10^8} = 1 \text{ (mm)}$$

- Step 6: Verification of the bandgaps of the designed meta-truss bar.

To check the bandgaps of the designed meta-truss bar, the above procedures are applied to calculate the bandgap frequencies. Figure 2-20 shows the dispersion curves of the meta-truss bar with the above designed dimensions and material properties. As shown, the bandgaps of the designed meta-truss bar cover the primary frequency contents of the applied loading, implying the meta-truss bar is effective to mitigate the loading effects.

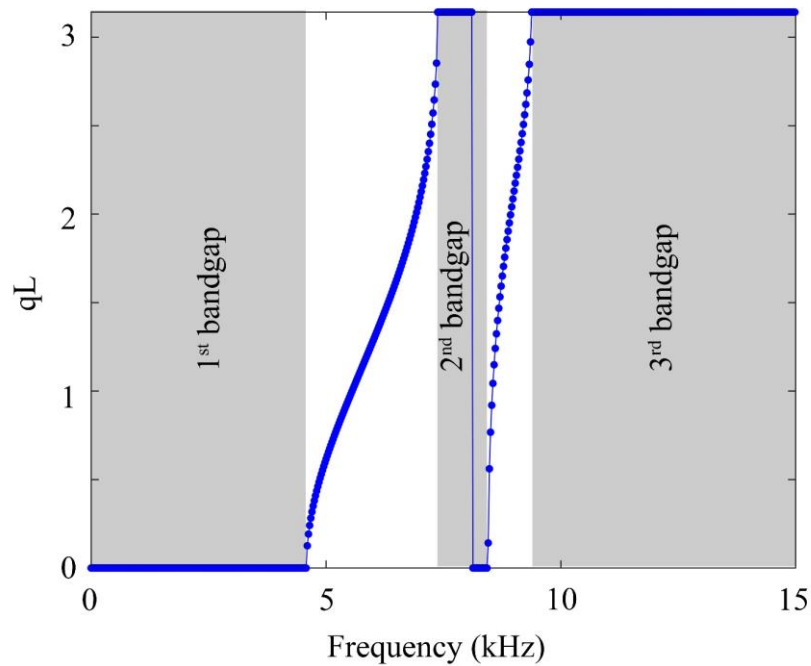


Figure 2-20. Dispersion curve of the designed meta-truss bar

- Step 7: Performance of the meta-panel consisting of 4 designed meta-truss bars.

The meta-panel consisting of four designed meta-truss bars is shown in Figure 2-21. Its performance in mitigating the impact loading effects is evaluated. The numerical model of the meta-panel is built in LS-DYNA and its impact response is shown in Figure 2-22.

As shown, the designed meta-panel functioning as a sacrificial cladding exhibits its superior dynamic performances compared with the traditional designs. In particular, the peak reaction force of the designed meta-panel transmitted to the protected structure is reduced significantly by more than 47% compared to its conventional counterparts including the hollow-truss panel and solid-truss panel. It should be noted that the numerical results from the corresponding panels with solid-truss and hollow-truss bars from [41] was adopted herein for comparison, which is not presented in detail for brevity. More information about these panels can be found in [41]. These results demonstrate that the designed meta-panel yields better protections to structures as compared to the traditional sacrificial panels with solid and hollow truss bars.

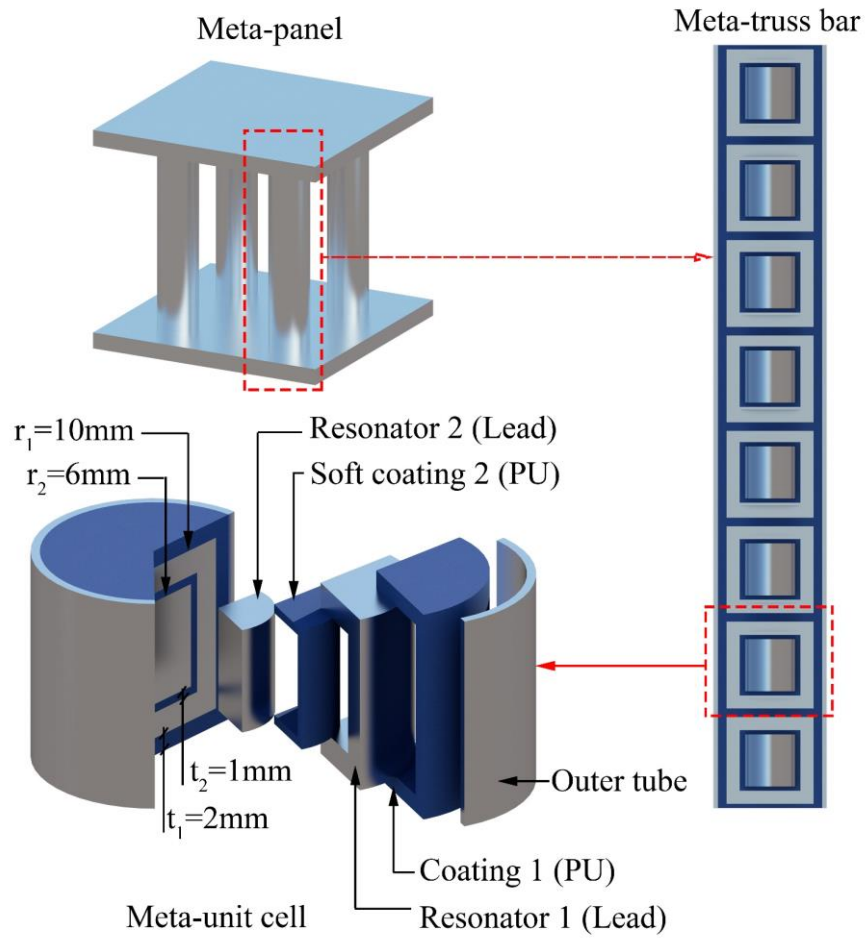


Figure 2-21. Design of meta-panel including the schematic view of the meta-panel

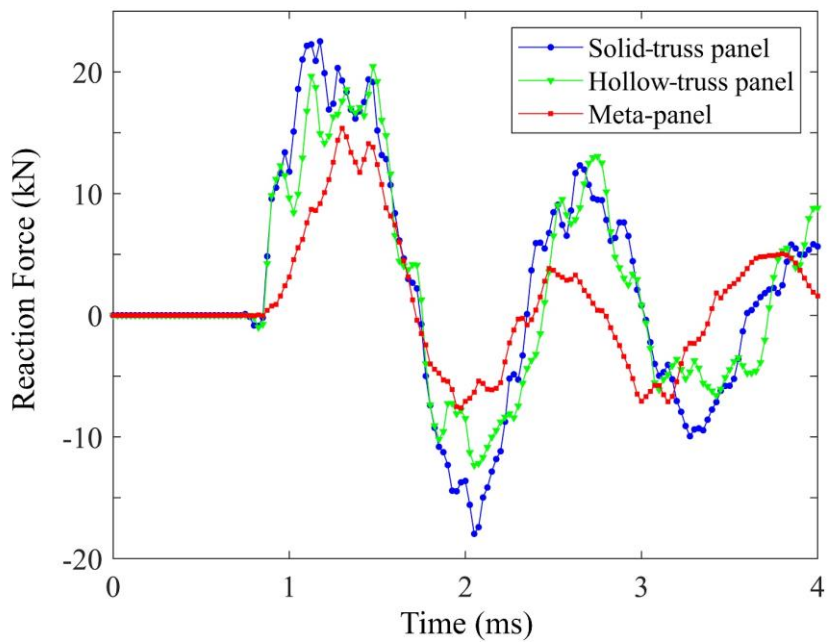


Figure 2-22. Comparison of reaction force of the three panels under impact loading

D. Determination of axial and shear stiffness of the analytical model

With an attempt to accurately estimate the spring stiffness, the commercial software COMSOL MULTIPHYSICS was adopted. A constant force F which is depicted in Figure 2-23a is applied to the model to calculate the value of shear spring stiffness k_{s1} of the internal core while the coupled forces F were put in two directions of the model to estimate the values of k_{a1} as shown in Figure 2-23b. Similarly, the estimation of k_{s2} and k_{a2} is carried out with the same procedure but different dimensions. As seen in Figures 2-23a and 2-23b, the average displacements monitored at the surfaces are denoted as u_i ($i=1,2,3,4$). It is noted that all edges of the outer tube are clamped. The relation between stiffness and displacement of the unit model is expressed as [41].

$$k_{a1}(u_1 + u_2) + k_{s1}u_1 = F, \quad k_{s1}u_3 = F \quad (2-27)$$

$$k_{a2}(u_4 + u_5) + k_{s2}u_4 = F, \quad k_{s2}u_6 = F$$

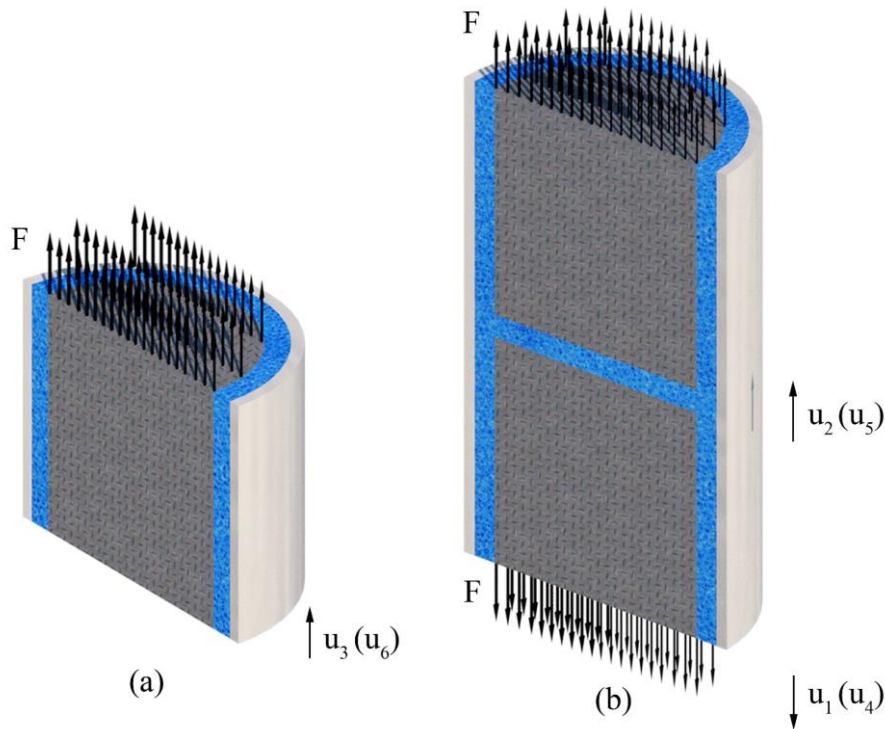


Figure 2-23. Outline model utilized for the calculation of (a) k_{s1} and k_{s2} , and (b) k_{a1} and k_{a2}

CHAPTER 3. MODEL FOR ANALYTICAL INVESTIGATION ON META-TRUSS BAR FOR LOW-FREQUENCY SPATIAL WAVE MANIPULATION

Abstract²

This chapter proposes an analytically unprecedented model of a meta-truss bar with local resonators to generate a broader low-frequency bandgap. By leveraging the mass-spring model, a new equivalent meta-unit cell considering the elastic shear springs is developed to accurately predict the performance of the meta-truss bar in suppressing stress wave propagations. Theoretical analyses and numerical simulations are conducted to examine the effectiveness of the proposed model. Sensitivity analyses are also performed to investigate the influences of masses and spring parameters on the bandgap characteristics of the meta-truss bar. Based on the theoretical prediction, the system transmission coefficient is utilized to examine the transmissibility effect among the resonators. A three-dimensional finite element model of meta-truss bar is also built and its accuracy in predicting the stress wave propagations is verified against the analytical predictions. The structural responses in the time domain and time-frequency domain demonstrate the superiority of the meta-truss bar in the suppression of wave transmission as compared to that predicted by the conventional counterparts.

² The related work in this chapter was published in **Wave Motion** with the full bibliographic citation as follows:

N.H. Vo, T.M. Pham, K. Bi, H. Hao. Model for analytical investigation on meta-lattice truss for low-frequency spatial wave manipulation. *Wave Motion*. 2021;103:102735.

<https://doi.org/10.1016/j.wavemoti.2021.102735>

3.1. Introduction

In the last decade, the field of wave propagation has been revolutionized by the discovery of man-made materials that have the potential for wave manipulation functionalities beyond the limits of naturally available materials [81]. These new concepts of artificial materials are labeled as meta-materials due to their exciting properties [12]. It is often taken into consideration that meta-material is a material that contains artificial microstructures with unique characteristics that are not found in nature. This terminology originated from the field of electrodynamics, now has been extended to other branches of engineering disciplines such as the fields of acoustic and elastic materials [14, 90]. Meta-materials demonstrate some superior dynamic characteristics owing to not only the constituent compositions of materials but also the engineered microstructure of configurations. At its early stage, researchers concentrated on the achievement of unconventional values of effective index [91]. However, it rapidly evolved towards the demonstration of wave manipulation functionalities [92]. Previous studies of meta-materials exert various beneficial applications from its exceptional characteristics, for example, seismic protection [93, 94], sound isolation [95, 96], vibration suppression [97, 98], and blast/impact mitigation [99, 100]. Nonetheless, not until recently, the concept of meta-materials was extended to the context of manipulation of elastic waves in structural elements. Its application, however, still remains limited with even fewer examples of experimental verifications.

Based on their operating mechanisms [101], meta-materials are often classified into two categories, including non-resonant and locally-resonant types. The locally resonant meta-materials are generally made of inclusions in the form of hardcore coated with soft material layers, which are periodically (but not necessarily) distributed in a host matrix of dissimilar material [80, 102]. On the other hand, the non-resonant meta-materials are often made of hardcore only that are buried in a host matrix [103]. There are two mechanisms that can be utilized for meta-materials including Bragg scattering and localized resonance [104]. The bandgap behaviour of non-resonant structures relies on the phenomena of wave diffraction and destructive interference with each other [105], i.e. depends on the Bragg scattering effect to form the bandgap. On the other hand, the bandgap in localized resonances is essentially independent of periodicity and symmetry, but governed by the natural frequency of the resonators.

The bandgap, which is the specific range of frequencies where propagation of an applied wave is stopped, is the most crucial features of meta-materials [31]. Therefore, much research effort primarily contributed to meta-materials' fundamental mechanism with an attempt to seek approaches to broaden the bandgap of meta-materials or make it tunable [106, 107]. To investigate the relation between the effective dynamic mass density and the oscillation frequency, Milton and Willis [108] proposed a rigorous model of meta-materials utilizing the typical motion equations for a rigid bar and Newton's second law to simulate the dynamic effective mass density as a function of the resonant frequency. The single spring-mass model was originally introduced by Huang and Sun [92] offering the negativity of mass property over a specific frequency range and this model was applied to lattice systems to broaden the bandgap by Liu et al. [109]. Motivated by the abovementioned studies, an analytical dual-resonator meta-truss bar which was utilized to investigate the transient response of the meta-truss structure was proposed by Liu et al. [68], hereafter referred as the conventional model, to further broaden the bandgap and improve the suppression of incident waves. Subsequently, the strategy of diatomic mimicking lattice systems [106] was also utilized to broaden the bandwidths of the meta-truss bar. Besides, to investigate the effect of damping on asymmetric elastic-wave transmission, Alamri et al. [110] proposed and designed the dissipative diatomic acoustic meta-truss bar possessing the bandwidth broadening effect. This study investigated the damping effect on the bandgaps of the meta-truss bar while the influences of other parameters such as mass and stiffness, especially shear stiffness have not been investigated.

The conventional analytical model with dual-resonator did not fully consider the importance of the shear stiffness between multilayers within the meta-truss bar, i.e. the shear stiffness between the inner core and the coating. As will be demonstrated in the chapter, this shear stiffness affects the bandgap in the low-frequency range. The accuracy of the model in predicting the transient response is therefore compromised if the shear stiffness is neglected in the analytical model. In particular, as will be proven later in this chapter through numerical simulations, stress wave caused by an excitation with a low range frequency, i.e. 300 Hz, is successfully mitigated in the numerical model, while the corresponding stress wave attenuation is not captured by the conventional analytical model. In other words, the conventional analytical model cannot accurately predict the response of the dual-resonator meta-truss bar, particularly in the low-frequency range because of neglecting the shear stiffness between the inner core and the coating. Therefore, it is necessary to develop an analytical model that can more accurately predict the response of meta-truss bar with dual-resonators. In the chapter, an additional shear

spring is introduced into the conventional analytical model, and the analytical results show the stress wave caused by the excitation with a frequency of 300 Hz is well attenuated as also observed in the numerical investigation, which demonstrates the accuracy of the proposed analytical model.

In brief, this chapter proposes an analytical model for the dual-resonator meta-truss bar by adopting a locally resonant mechanism and taking the shear stiffness of all multilayers into consideration. The widely utilized spring-mass model, with added shear spring to connect the inner resonator and the soft coating, is utilized to derive the analytical solutions. In this article, firstly, the analytical predictions of an infinite meta-truss bar calculated by two models including the proposed model and the conventional one are derived and compared to demonstrate differences regarding the predicted bandgaps from these two models. Analytical results show that the proposed model predicts a wider bandgap in the low-frequency range, the same as the numerical model, which could not be accurately predicted by the conventional model. The comparisons with the numerical predictions based on a finite element analysis demonstrate the accuracy of the developed numerical model in this chapter. Specifically, if the shear stiffness is neglected, the analytical model may not accurately predict the actual response of the meta-truss bar. The numerical model has shown an incident wave that is mitigated but the existing analytical model (without considering the shear stiffness) does not prohibit this incident wave from propagating through the truss. Therefore, this chapter incorporates the shear stiffness in the analytical derivation and the derived model yields good predictions as compared with the numerical results, demonstrating the need to consider the shear stiffness of the inner resonator in the analytical model. To investigate the influence of various parameters of the meta-truss bar on wave propagation, a comprehensive parametric study is carried out and the influences of masses and spring stiffness on the behavior of the bandgap are examined. Finally, the superb stress wave attenuation ability of the meta-truss bar with dual resonators is demonstrated.

3.2. Design of the dual-resonator model

Without loss of generality, the example 3D meta-truss bar model utilized in this investigation consists of 7 unit cells in which each cell comprises of five parts: the outer tube, 2 soft coats, and 2 resonators as shown in Figure 3-1a. The compositions and dimensions of each unit cell are presented in Figures 3-1b and 3-1c, respectively. Aluminium and lead are respectively selected for the outer tube and the resonators, and the two soft coatings are made from rubber.

In the analytical model, the matrix is represented by material 1, i.e., the outer aluminium tube. Meanwhile, material 2 is modelled by two springs including the outside shear spring k_{s1} connecting the resonator with the outer tube and the axial spring k_{a1} connecting the adjacent resonators (refer to Figure 3-3b for more details). Similarly, material 4 is modelled by the axial and shear springs connecting the internal hardcore mass and external hardcore mass, namely k_{a2} and k_{s2} , respectively. The numerical analysis in the following sections indicates that the analytical model without considering k_4 does not reflect the actual response of the meta-truss bar as observed in the numerical simulation presented in this chapter. Acting as resonators, material 3 and material 5 are represented by the external mass m_1 and internal mass m_2 , respectively. It should be noted that this chapter is dedicated to investigate the dynamic performance of the elastic meta-truss bar under the elastic stress wave. The properties of all the materials are summarized in Tables 3-1, 3-2 and 3-4. These material properties are also used in the numerical model in this chapter.

The inner mass and outer mass can be estimated by Eq. (3-1) where ρ_j and V_j are the material density and volume of the j^{th} material, and the length and radius of j^{th} unit are denoted by l_j and r_j , respectively.

$$m_j = \rho_j V_j = \rho_j \pi r_j^2 l_j \quad j = 1, 2 \quad (3-1)$$

Similarly, the spring of each stiffness can be estimated as follows

$$k_{a1} = \frac{E_3 A_1}{l_2}, \quad k_{s1} = \frac{G_3 A_2}{l_1}, \quad G_3 = \frac{E_3}{2(1+\nu_3)} \quad (3-2)$$

$$k_{a2} = \frac{E_3 A_3}{l_3}, \quad k_{s2} = \frac{G_3 A_4}{l_4}$$

in which E and G are the Young's modulus and shear modulus of the soft material, respectively. The values of A_i ($i=1,2,3,4$) which are the nominal cross-sections of the distinct segments of the soft layer presented in the appendix are obtained by FEA due to the shape complexity. The detailed calculation of the spring stiffness is also presented in the appendix. Based on the material properties and dimensions, the relevant estimations of equivalent mass and stiffness are computed as $m_1 = 14.2 \times 10^{-3}$ kg, $m_2 = 17.7 \times 10^{-3}$ kg, $k_{a1} = 424,655$ N/m, $k_{s1} = 102,531$ N/m, $k_{a2} = 280,526$ N/m, and $k_{s2} = 61,425$ N/m.

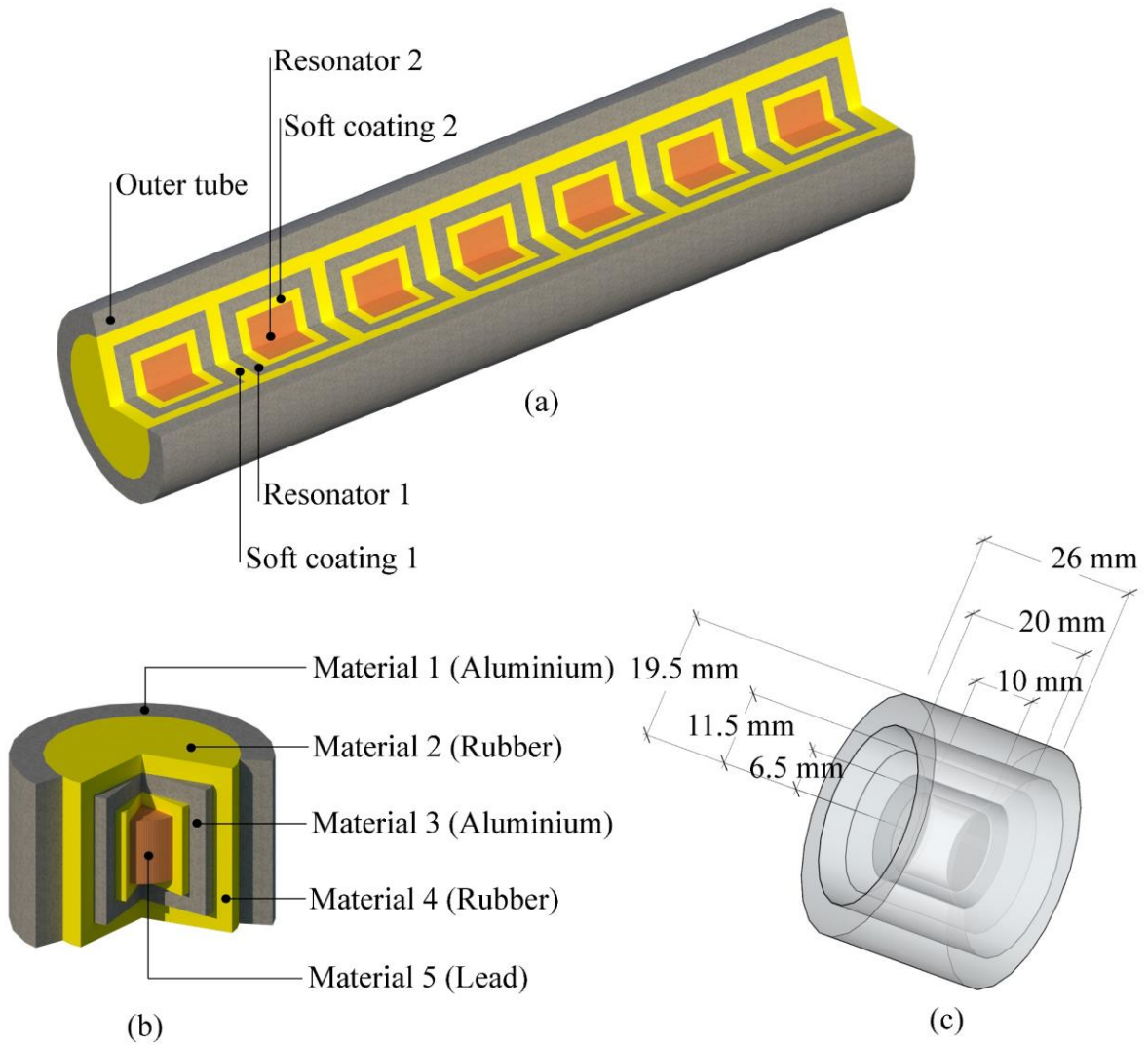


Figure 3-1. (a) Schematic view of 3D meta-truss bar, (b) single unit cell and (c) dimension of the single unit cell

Table 3-1. Elastic material properties used in the numerical simulation [111]

Properties	Materials 1 and 3	Materials 2 and 4	Material 5
	Aluminium	Rubber	Lead
Density ρ (kg/m ³)	2,770	1,200	11,340
Young's modulus E (Pa)	70×10^9	780×10^3	16×10^9
Poisson's ratio ν	0.33	0.47	0.45

3.3. Analytical models

Firstly, the conventional 1D mass-spring chain model with locally resonant microstructures is briefly revisited (Section 3.3.1). Then, a shear spring is introduced into the unit cell, and an

unprecedented model is proposed in Section 3.3.2. The comparisons with the conventional model in terms of transmissibility are also made in this section. Comprehensive parametric studies are further carried out in Section 3.5 to analytically examine the influences of mass and spring stiffness on the bandgaps.

3.3.1 Conventional spring-mass model of meta-truss bar

A meta-truss bar can be represented in the spring-mass formation comprising of masses and springs [68]. An infinite 1D spring-mass system including the resonators is depicted in Figures 3-2a and 3-2b, in which the inner mass m_2 and outer mass m_1 are connected to each other by an axial spring k_{a2} . The shear spring with the stiffness k_{s1} constrains the displacement of the mass m_1 which is periodically linked with each other by the axial spring k_{a1} .

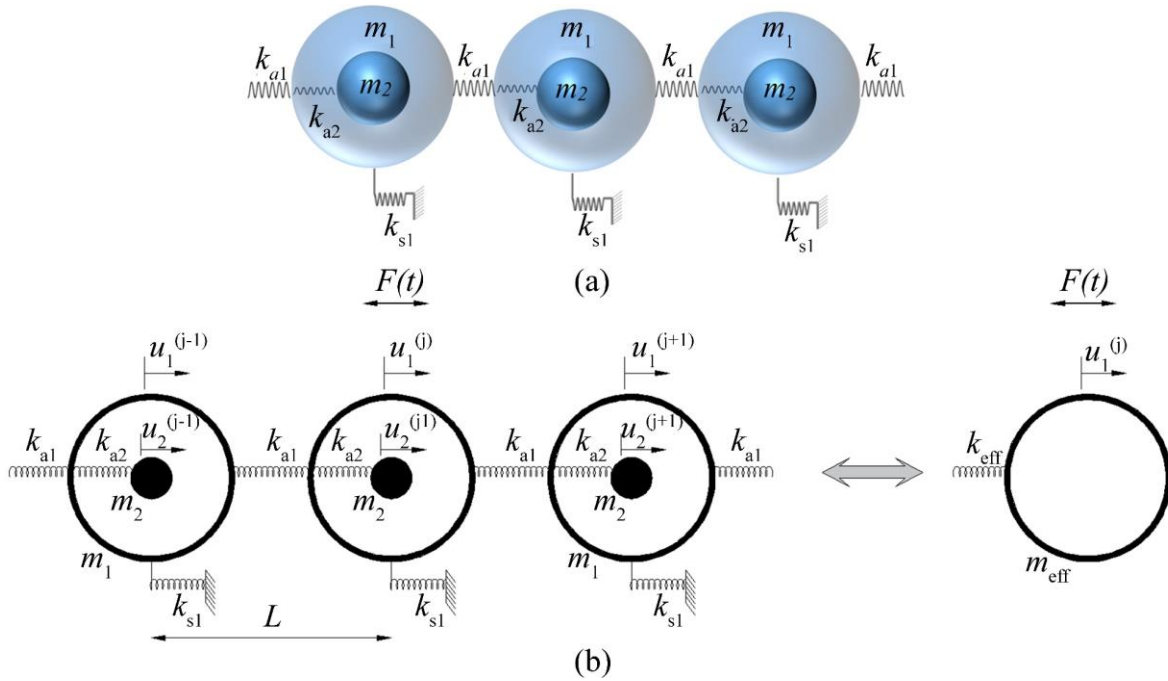


Figure 3-2. (a) Schematic microstructure of the infinite conventional model of meta-truss bar and (b) Equivalent effective spring-mass model

In this one-dimensional meta-truss bar, the internal and external mass displacements are denoted by u_1 and u_2 , respectively, and the motion equations of the j^{th} unit cell can be derived as follows:

$$m_1 \ddot{u}_1^{(j)} + k_{a1} (2u_1^{(j)} - u_1^{(j+1)} - u_1^{(j-1)}) + k_{a2} (u_1^{(j)} - u_2^{(j)}) + k_{s1} u_1^{(j)} = 0 \quad (3-3)$$

$$m_2 \ddot{u}_2^{(j)} + k_{a2} (u_2^{(j)} - u_1^{(j)}) = 0 \quad (3-4)$$

Based on the Floquet-Bloch theorem [112], the solution of harmonic wave of the $(j+n)^{\text{th}}$ and j^{th} unit cells can be expressed in the form of

$$u^{(j+n)} = U e^{i(jqL+nqL-\omega t)} \quad (3-5)$$

$$u^{(j)} = U e^{i(jqL-\omega t)} \quad (3-6)$$

where U is the displacement amplitude, q is the wavenumber, ω is the angular frequency, L is the length of the unit cell.

By substituting Eqs. (3-5) and (3-6) into Eqs. (3-3) and (3-4), the dispersion relation of the lattice system can be derived as follows:

$$\cos qL = 1 - \left[m_1 \omega^2 - (k_{a2} + k_{s1}) + \frac{k_{a2}^2}{k_{a2} - m_2 \omega^2} \right] \frac{1}{2k_{a1}} \quad (3-7)$$

Herein, the lattice system is monatomic, therefore, the following effective mass equation of the microstructure must be satisfied

$$\omega^2 = 2 \frac{k_{a1}}{m_{\text{eff}}} (1 - \cos qL) \quad (3-8)$$

Based on Eqs. (3-7) and (3-8), the effective mass (m_{eff}) of the lattice system can be obtained as:

$$m_{\text{eff}} = m_1 - \frac{k_{s1} + k_{a2}}{\omega^2} + \frac{k_{a2}^2}{k_{a2} \omega^2 - m_2 \omega^4} \quad (3-9)$$

When the unit cell is regarded as homogeneous with the effective mass m_{eff} and effective stiffness k_{eff} (Figure 3-2b), the effective stiffness can be calculated as follows [68]:

$$k_{\text{eff}} = k_{a1} - \frac{1}{4} m_{\text{eff}} \omega^2 = k_{a1} + \frac{1}{4} (k_{s1} + k_{a2}) - \frac{1}{4} \left(m_1 \omega^2 + \frac{k_{a2}^2}{k_{a2} - m_2 \omega^2} \right) \quad (3-10)$$

To define the width of the bandgap, the dispersion in Eq. (3-7) can be solved and the expression of the angular frequency can be obtained as follows:

$$\omega^2 = \frac{m_2 k_{s1} + (m_1 + m_2) k_{a2} + 2k_{a1} m_2 (1 - \cos qL) \pm \sqrt{\beta}}{2m_1 m_2} \quad (3-11)$$

where $\beta = (m_2 k_{s1} + (m_1 + m_2) k_{a2} + 2k_{a1} m_2 (1 - \cos qL))^2 - 4m_1 m_2 [2k_{a1} k_{a2} (1 - \cos qL) + k_{s1} k_{a2}]$

Substituting $qL=0$, the angular frequency at the starting points of two passbands can be obtained as:

$$\omega^2 = \frac{m_2 k_{s1} + (m_1 + m_2) k_{a2} \pm \sqrt{m_2^2 k_{s1}^2 + (m_1 + m_2)^2 k_{a2}^2 + 2k_{s1} k_{a2} (m_2^2 - m_1 m_2)}}{2m_1 m_2} \quad (3-12)$$

and substituting $qL=\pi$, the angular frequency at the two ending points of the passband can be expressed as:

$$\omega^2 = \frac{(m_1 + m_2) k_{a2} + 4m_2 (k_{a1} + k_{s1}) \pm \theta}{2m_1 m_2} \quad (3-13)$$

where $\theta = \sqrt{(m_2 k_{s1} + (m_1 + m_2) k_{a2} + 4k_{a1} m_2)^2 - 4m_1 m_2 [4k_{a1} k_{a2} + k_{s1} k_{a2}]}$

3.3.2 Proposed spring-mass spring model of meta-truss bar

As shown in Figure 3-2 and also discussed in the introduction, the conventional meta-lattice model proposed by Liu et al. [68] only considered the shear spring connected the external mass m_1 and the soft layer (material 2 in Figure 3-1), and it is represented by k_{s1} . The shear spring linking the internal mass m_2 and the corresponding soft layer (material 4 in Figure 3-1) was, however, neglected. It is obvious that the inner mass and the outer mass of a unit cell bear similar characteristics, and the negligence of this stiffness may result in inaccurate bandgap predictions. It is therefore worth considering the shear stiffness of the inner mass to enhance the accuracy of the model. This chapter proposes an improved spring-mass spring model, in which besides the spring with the stiffness k_2 constrains the displacement of the mass m_1 to the matrix, the inner mass m_2 is also restrained by the shear spring stiffness k_{s2} . Figures 3-3a and 3-3b show the corresponding analytical model.

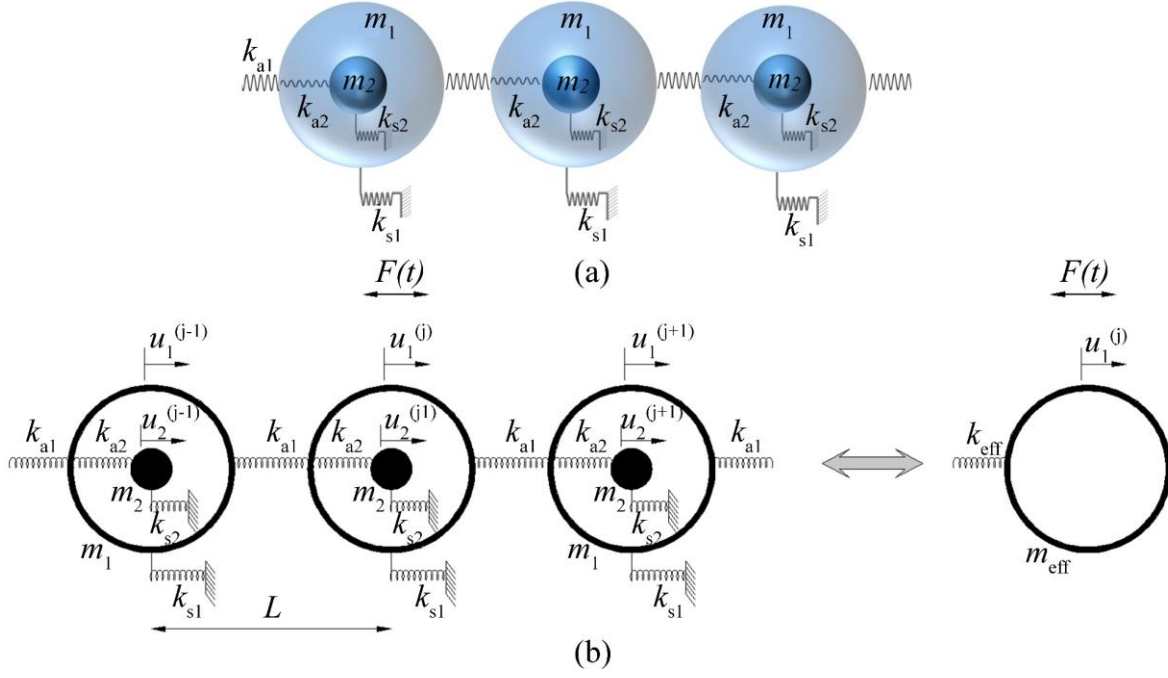


Figure 3-3. (a) Schematic microstructure of the proposed model of meta-truss bar and (b) Equivalent effective mass-spring model

Similar to the conventional spring-mass model as shown in Figure 3-2, the equations of motion of the j^{th} unit cell in Figure 3-3 can be expressed as follows:

$$m_1 \ddot{u}_1^{(j)} + k_{a1} (2u_1^{(j)} - u_1^{(j+1)} - u_1^{(j-1)}) + k_{a2} (u_1^{(j)} - u_2^{(j)}) + k_{s1} u_1^{(j)} = 0 \quad (3-14)$$

$$m_2 \ddot{u}_2^{(j)} + k_{a2} (u_2^{(j)} - u_1^{(j)}) + k_{s2} u_2^{(j)} = 0 \quad (3-15)$$

To derive the dispersion curves, a similar strategy is adopted and the solution of the harmonic wave of the $(j+n)^{\text{th}}$ and j^{th} unit cells can be represented by Eq. (3-5) again, and the derivative function of the solution can be obtained as follows

$$\ddot{u}^{(j)} = -\omega^2 U e^{i(jqL - \omega t)} = -\omega^2 u^{(j)} \quad (3-16)$$

Substituting Eq. (3-16) into Eq. (3-15), the relation between the inner mass and outer mass can be obtained as follows:

$$u_2^{(j)} = \frac{k_3}{k_{a2} + k_{s2} - m_2 \omega^2} u_1^{(j)} \quad (3-17)$$

It is worth noting that the Bloch-Floquet theory consequence is adopted in this chapter, in which the motion must satisfy the Bloch periodicity condition. Hence, by substituting Eqs. (3-16) and (3-17) into Eq. (3-14), one obtains

$$-m_1\omega^2 u_1^{(j)} + k_{a1} \left(2u_1^{(j)} - u_1^{(j)} e^{-iqL} - u_1^{(j)} e^{iqL} \right) + k_{a2} \left(1 - \frac{k_3}{k_{a2} + k_{s2} - m_2\omega^2} \right) u_1^{(j)} + k_{s1} u_1^{(j)} = 0 \quad (3-18)$$

By applying the identity $e^{-iqL} + e^{iqL} = 2\cos(qL)$, Eq. (3-18) can be rewritten to form the dispersion relation as follows:

$$\cos qL = 1 - \left[m_1\omega^2 - (k_{s1} + k_{a2}) + \frac{k_{a2}^2}{(k_{a2} + k_{s2}) - m_2\omega^2} \right] \frac{1}{2k_{a1}} \quad (3-19)$$

Eq. (19) can also be rearranged into the following form

$$\omega^2 = 2 \frac{k_{a1}}{m_{eff}} (1 - \cos qL) \quad (3-20)$$

where

$$m_{eff} = m_1 - \frac{k_{s1} + k_{a2}}{\omega^2} + \frac{k_{a2}^2}{(k_{a2} + k_{s2})\omega^2 - m_2\omega^4} \quad (3-21)$$

and the effective stiffness can also be conveniently formulated due to the homogeneity of the unit cell

$$k_{eff} = k_{a1} + \frac{1}{4}(k_{s1} + k_{a2}) - \frac{1}{4} \left(m_1\omega^2 + \frac{k_{a2}^2}{(k_{a2} + k_{s2}) - m_2\omega^2} \right) \quad (3-22)$$

With an attempt to find the dispersion relation for this system, the angular frequency can be calculated by solving Eq. (3-19) as follows:

$$\omega^2 = \frac{2m_2(1 - \cos qL)k_{a1} + m_2k_{s1} + (m_1 + m_2)k_{a2} + m_1k_{s2} \pm \sqrt{\gamma - \eta}}{2m_1m_2} \quad (3-23)$$

$$\text{where } \gamma = (2m_2(1 - \cos qL)k_{a1} + m_2k_{s1} + (m_1 + m_2)k_{a2} + m_1k_{s2})^2$$

$$\eta = 4m_1m_2 \left[2k_{a1}(k_{a2} + k_{s2})(1 - \cos qL) + k_{s1}(k_{a2} + k_{s2}) + k_{a2}k_{s2} \right].$$

The above derivations are based on the assumption of an infinite unit cell. In practice, the number of unit cells is always finite. In this case, the wave transmission coefficient of the spring-mass chain, which depicts the displacement amplitude ratio of the last unit cell to the input excitation is normally defined, and it can be calculated as follows [69]:

$$T = \left| \prod_{j=1}^N T^{(j)} \right| \quad (3-24)$$

$$\text{where } T^{(j)} = u^{(j)} / u^{(j-1)}$$

From Eq. (3-20), by applying the identities $e^{-iqL} + e^{iqL} = 2 \cos(qL)$ and rearranging the equation the following form can be obtained:

$$(2k_{a1} - \omega^2 m_{eff})u^{(j)} = k_{a1}(u^{(j+1)} + u^{(j-1)}), \quad j = 1, 2, \dots, N-1 \quad (3-25)$$

$$(k_{a1} - \omega^2 m_{eff})u^{(j)} = k_{a1}u^{(j-1)}, \quad j = N \quad (3-26)$$

Substituting $T^{(j)} = u^{(j)} / u^{(j-1)}$ into Eqs. (3-25) and (3-26) gives:

$$2k_{a1} - \omega^2 m_{eff} = k_{a1} \left(T^{(j+1)} + \frac{1}{T^{(j)}} \right) \quad (3-27)$$

Therefore, the wave transmission coefficient can be formulated as follows:

$$T^{(j)} = \frac{k_{a1}}{k_{a1}(2 - T^{(j+1)}) - \omega^2 m_{eff}}, \quad j = 1, 2, \dots, N-1 \quad (3-28)$$

$$T^{(N)} = \frac{k_{a1}}{k_{a1} - \omega^2 m_{eff}}, \quad j = N \quad (3-29)$$

3.4. Numerical simulation

To verify the accuracy of the proposed and conventional analytical models, a 3-D finite element model of the meta-truss bar is built and validated in this section.

3.4.1 Numerical model development

The 3-D numerical model is built to investigate the wave transmission characteristics of the meta-truss bar and verify its accuracy against the analytical predictions by utilizing commercial software LS-DYNA (Figure 3-1). Contact definitions, the prevention of reflected waves, material models, and simulation of prescribed displacement are presented in this section. In this chapter, all elements are modelled by solid elements and the minimum meshing size is 0.2 mm after a convergence test. To define the property of aluminium considering the plastic deformation, *MAT_JOHNSON_COOK is utilized while *MAT_ELASTIC material model is applied to simulate the dynamic behaviour of rubber elements due to their distinguished properties [111].

The Johnson-cook material model requires an equation of state in order to initialize the thermodynamic state of the material [113]. The elastic and plastic material properties are summarized in Tables 3-1 and 3-2, respectively. In this chapter, the equation of state of the Johnson-cook model is defined by the card *EOS_LINEAR_POLYNOMIAL in which the pressure and initial relative volume are denoted by coefficients C_0 - C_6 and V_0 , respectively. The parameters for the equation of state are presented in Table 3-3. Furthermore, for simulation of the lead core, the material properties as implemented in *MAT_PLASTIC_KINEMATIC, are given in Table 3-4 [114]. The contact between the metals and rubber is modelled by the keyword *TIED_SURFACE_TO_SURFACE and the keyword *CONTACT_INTERIOR is utilized for the rubber to eliminate the negative volume issue which often occurs due to large deformation of soft materials.

Additionally, to eliminate the stress wave reflection at the end surface, the keyword *NON_REFLECTING_BOUNDARY is applied at one end. In the numerical model, the far-end of the outer tube is fixed in all directions while the excitation is defined by the *PRESCRIBED_MOTION_SET card, which is applied to the entire near-end surface.

Table 3-2. Johnson-Cook material parameters for aluminium [111]

Density (kg/m ³)	Poisson's ratio	Young's modulus (GPa)	A (GPa)	B (GPa)	C	m	n	T _m	$\dot{\epsilon}$
2,770	0.33	70	0.369	0.675	0.007	1.5	0.7	800	1

Table 3-3. Equation of state for aluminium used in the numerical simulation [113]

C ₀ (Pa)	C ₁ (Pa)	C ₂ (Pa)	C ₃ (Pa)	C ₄	C ₅	C ₆	E ₀ (Pa)	V ₀ (m ³ /m ³)
0	74.2x10 ⁹	60.5x10 ⁹	36.5x10 ⁹	1.96	0	0	0	1

Table 3-4. Plastic kinematic material parameters for lead [114]

Density (kg/m ³)	Poisson's ratio	Young's modulus (GPa)	SIGY (MPa)	ETAN (MPa)	BETA	SRC	SRP	FS	VP (1/s)
11,340	0.45	16	20	50	10 ⁹	10 ⁹	1	0	1

3.4.2 Numerical model verification

Based on the Bloch-Floquet theory and the derivation from Eq. (3-28), a visible manifestation of the theoretical transmittance of the proposed model is shown in Figure 3-4. To verify the model, the meta-truss bar comprising of 7 unit cells described above is built in LS-DYNA. The model is used to simulate wave transmissions of the meta-truss bar. The transmittance is defined by a ratio between the output and the input signals of the structure. Figure 3-4 shows the results from the conventional model, the proposed model, and the numerical simulation. It can be seen that both conventional and the proposed models capture three bandgaps, and the corresponding ranges are [0-289.5], [645-995] and [1,945-5,000] Hz from the conventional model, and [0-375] Hz, [700-1,100] Hz and [1,945-5,000] Hz from the proposed model. The numerical simulation also gives three bandgaps in the range of [0-375] Hz, [895-1,400] Hz and [1,965-5,000] Hz. These results indicate that generally speaking, both the conventional and the proposed model can predict the frequency bandgaps, but compared with the results from the numerical simulations, the proposed model yields more accurate results than the conventional model, especially for the 1st bandgap in the low-frequency range. For example, the proposed

model predicts the same 1st bandgap as compared to the numerical model, whereas the conventional model substantially under-predicts the upper frequency of the first bandgap, i.e., 289.5 Hz and 375 Hz, i.e., a substantially narrower first bandgap by the conventional model. These results demonstrate that neglecting the stiffness k_4 into the conventional analytical model leads to inaccurate predictions of the bandgap width at the low-frequency range. The comparison also shows that a certain discrepancy exists between the analytical and numerical predictions, especially for the second bandgap. This is because the theoretical results are based on the infinite number of unit cells, while the numerical results are obtained from the finite number of cells (7 in this chapter). Moreover, the estimations of the spring stiffness and lumped masses in the analytical derivations may also contribute to this variation.

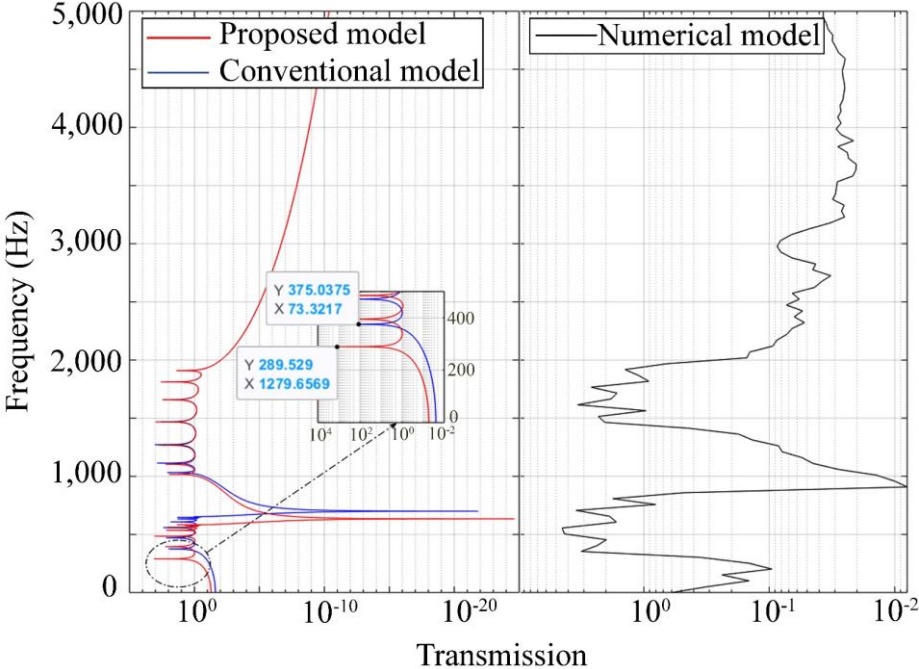


Figure 3-4. Transmittance profiles of meta-truss bar obtained by the proposed model, conventional model, and numerical simulation model

3.4.3 Accuracy of the proposed analytical model

The above results show that the inclusion of k_4 in the proposed model has almost no influence on the third bandgap because the third bandgap is mainly controlled by the external mass and axial stiffness which will be discussed in the following section. For the second bandgap, the lower bound of the proposed model results in a slightly higher value, while its influence on the upper bound is negligible. The most evident effect of the proposed model is on the first bandgap, and the inclusion of k_4 widens the bandgap in the low-frequency range. As shown, the first

bandgap expands from [0-289.5] Hz to [0-375.0] Hz. This result is expected, since the first bandgap is related to the local resonance frequency of the inner mass m_2 which is defined by $\omega = \sqrt{(k_{a2} + k_{s2}) / m_2}$, and the inclusion of k_4 results in an increase in the stiffness in the conventional model. Moreover, the bandwidth of the first bandgap in the low-frequency range is determined by two points including the constant value at zero and a certain value that is linearly dependent on the local resonance frequency. Therefore, introducing the shear stiffness of the internal mass k_4 increases the stiffness of the internal coating layer and resonant frequency ω accordingly, which leads to the increase of the first bandgap range by the reciprocal relationship between the first bandgap and the resonant frequency. This manifestation indicates that the proposed analytical model with considering the shear stiffness of the soft coating leads to a wider bandgap estimation in the low-frequency range than the conventional model, which implies the proposed analytical model would have wider practical applications for stopping the low-frequency wave propagations. It is worth mentioning that, besides varying the stiffness, the low-frequency bandgap can also be changed by altering the resonator's geometry since it is related to the local resonance as discussed above, and will be further discussed in the following investigations.

To further demonstrate the higher accuracy of the proposed analytical model in predicting the bandgap in the low-frequency range compared to the conventional model, the analytically predicted bandgap is compared with the result from the numerical analyses. As discussed above, the inclusion of k_4 most evidently changes the bandgap in the low-frequency range, therefore only the first bandgap is investigated in this section. For the other two bandgaps, more detailed discussions will be given in Section 5. However, it is worth noting that the soft material layer (material 4 in Figure 3-1) is modelled by the solid elements in the numerical simulation, which means the contribution from the shear stiffness of this layer (i.e. k_4) is considered in the numerical model. In the numerical simulation, the meta-truss bar presented in Section 3.2 is subjected to a displacement time history with two frequency components $u(t)=10^{-4}[\sin(2\pi f_1 t) + \sin(2\pi f_2 t)]$, where $f_1=300$ Hz and $f_2=500$ Hz. Figure 3-5a shows the displacement time histories of the excitation at the input and output end of the meta-truss bar. It can be seen that f_1 is deliberately designed to fall within the first bandgap of the proposed model but beyond that of the conventional model, while f_2 is within the passband range of both the models. Figure 3-5b shows the Fourier spectrum of the output data. The numerical results have shown that only one input signal with the frequency of 500 Hz passes through the meta-truss bar while the conventional model predicts both input signals pass through the structure. This observation

shows that the predictions of the conventional model and numerical model are different. Meanwhile, the proposed model predicts only the signal with the frequency of 500 Hz can pass the meta-truss bar while the other one with the frequency of 300 Hz is filtered out, which matches well with the numerical results. This result demonstrates again that neglecting the shear stiffness k_4 in the conventional model leads to inaccurate estimation of the bandgap width in the low-frequency range.

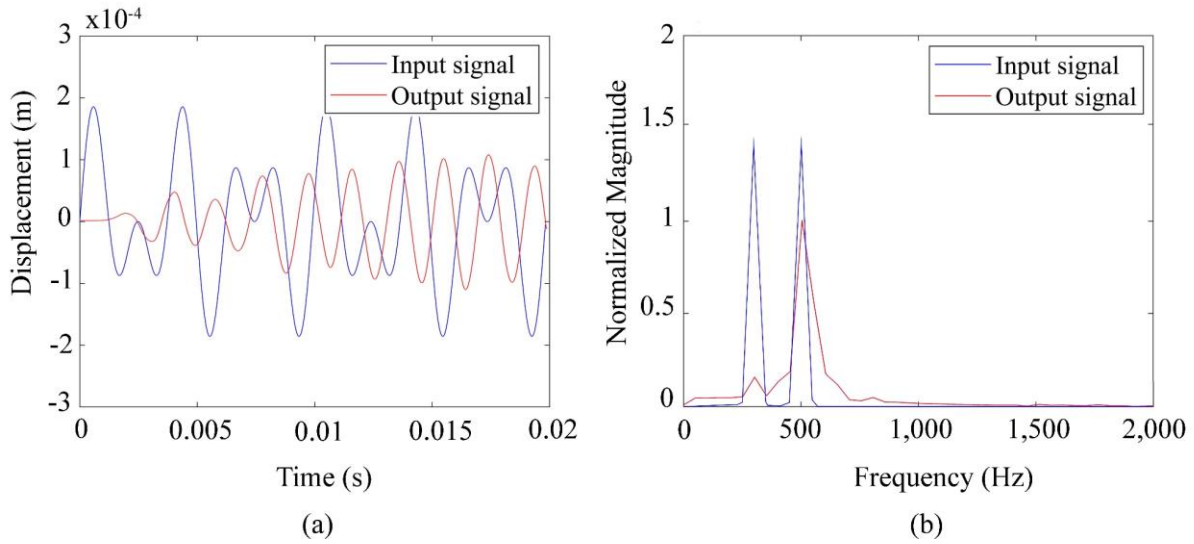


Figure 3-5. (a) Displacement time histories and (b) FFT spectrum of the input and output of the meta-truss bar

3.5. Sensitivity of the bandgap characteristics to mass and stiffness based on the proposed analytical model

The accuracy of the proposed analytical model has been verified against the numerical simulation and thus it is utilized to investigate the mitigation effects of the meta-truss bar. It is worth mentioning that the sensitivity analysis of those parameters has not been presented in the literature yet.

3.5.1 Effect of mass on bandwidth and bandgap position

Herein, the attenuation effect of mass including the inner and outer masses on the overall bandwidth of the meta-truss bar is investigated utilizing the proposed analytical model. Based on the Bloch-Floquet theorem, the analytical dispersion curves for the meta-truss bar are obtained and featured in Figure 3-6 through the theoretical calculation of Eq. (3-19). It should be noted that to calculate the theoretical starting and ending frequencies of the passbands the conditions $qL=0$ and $qL=\pi$ are applied to Eq. (3-23). It can be seen that there is an unequivocal

manifestation from the figure showing that there are two passbands including the first passband at the frequency range of approximately 375–700 Hz and the second passband at a relatively higher frequency range of 1,000–1,945 Hz.

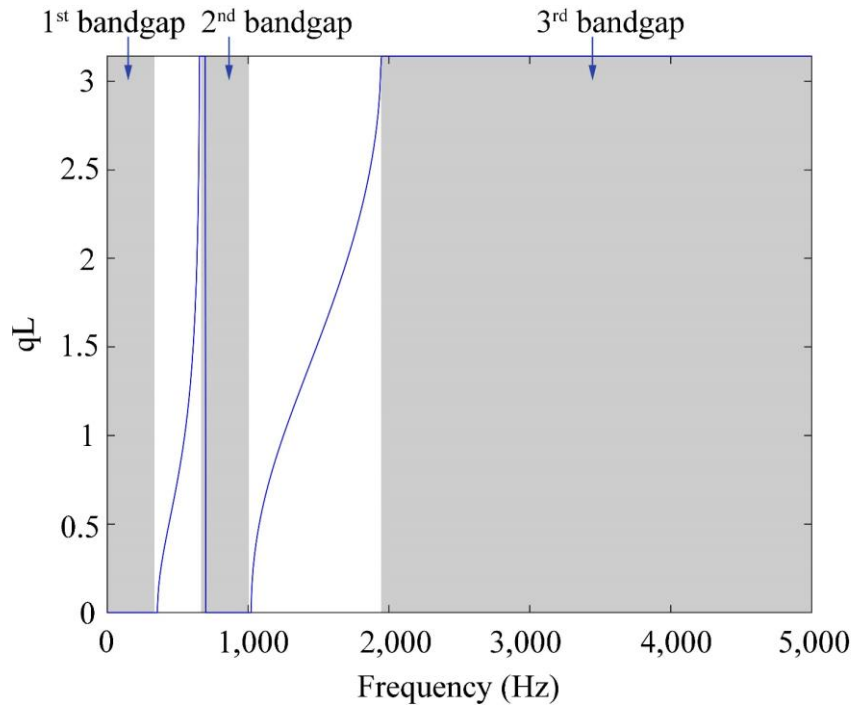
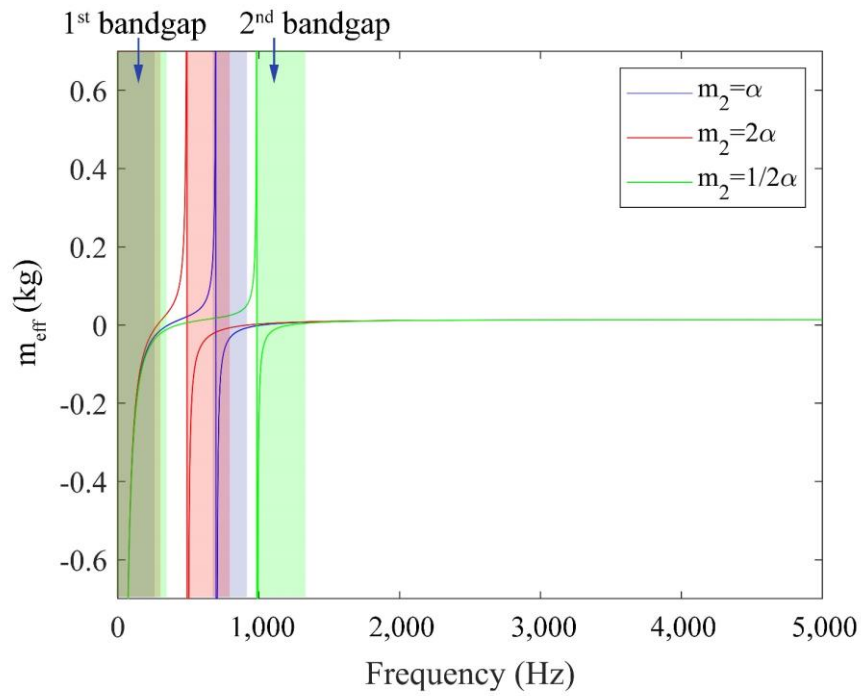
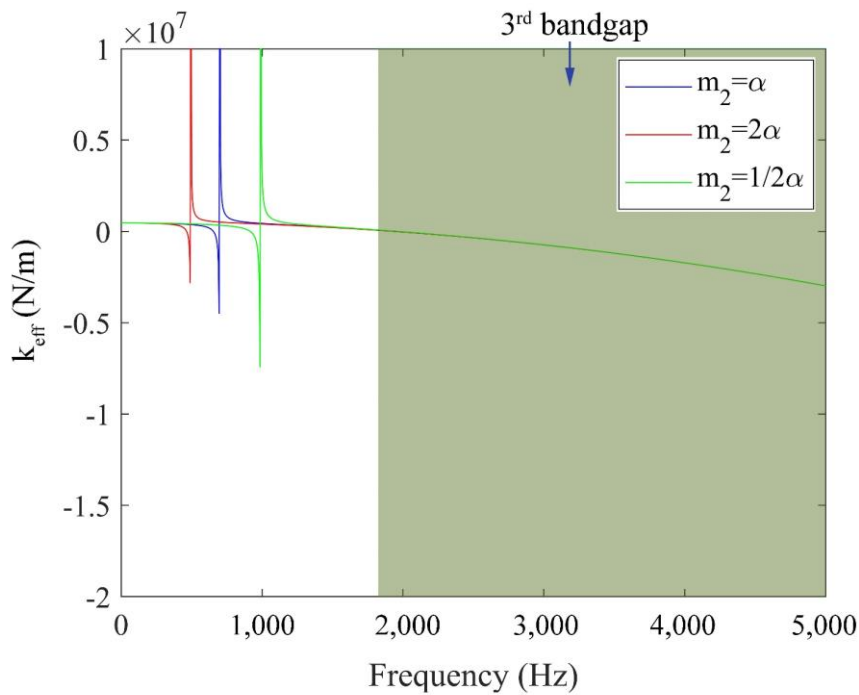


Figure 3-6. Non-dimensionalized dispersion curves obtained by the proposed analytical model

The bandgap behavior of the meta-truss bar is affected remarkably by the peculiar nature of local resonators consisting of the internal mass and external mass. Therefore, it is pivotal to examine the influence of the resonator on the meta-truss bar bandgap with respect to critical masses by utilizing the proposed model. Figures 3-7a and 3-7b show the two integral features of the locally resonant meta-truss bar, i.e. the effective mass and the effective stiffness, by varying the internal mass m_2 (0.5α , α and 2α , where $\alpha = m_2$). It is obvious that the bandwidth and the position of the first two bandgaps (Figure 3-7a) associated with lower frequency are affected by the mass m_2 while the third bandgap (Figure 3-7b) with higher frequency resulting from the stiffness remains unchanged. The analytical results also indicate that the inextricable relationship between the position of the bandgap and the local resonance frequency is a function of m_2 . Figure 3-8a clearly exhibits that the location of the first two bandgaps drastically shifts to the left with an increase of the internal mass. On the contrary, it is clear that the negativity of effective stiffness which forms the third bandwidth shown in Figure 3-7b remains unchanged, irrespective of the changing value of m_2 .



(a)



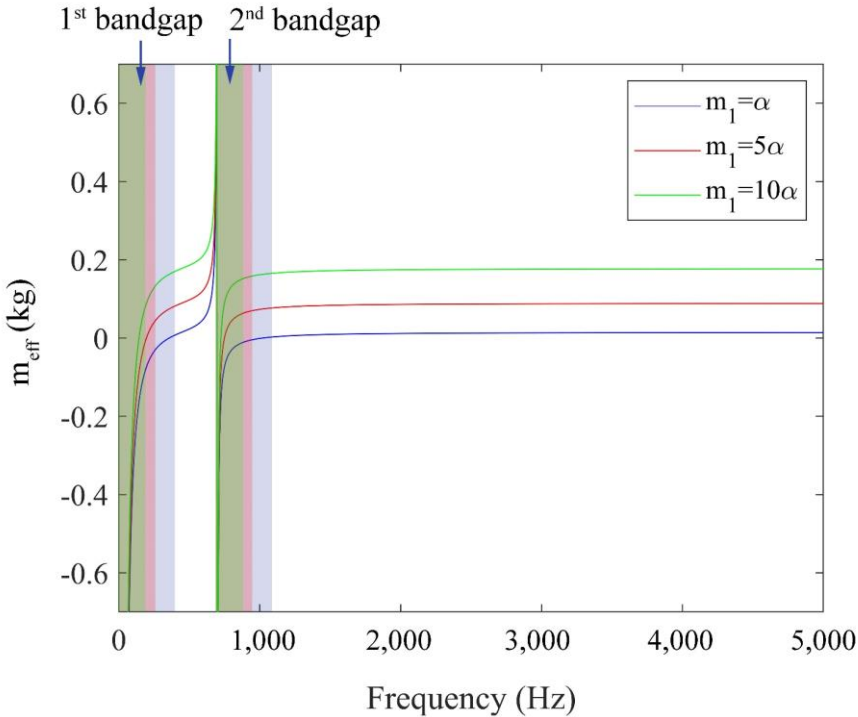
(b)

Figure 3-7. Effect of the internal mass m_2 on the bandgap characteristics (a) effective mass and (b) effective stiffness

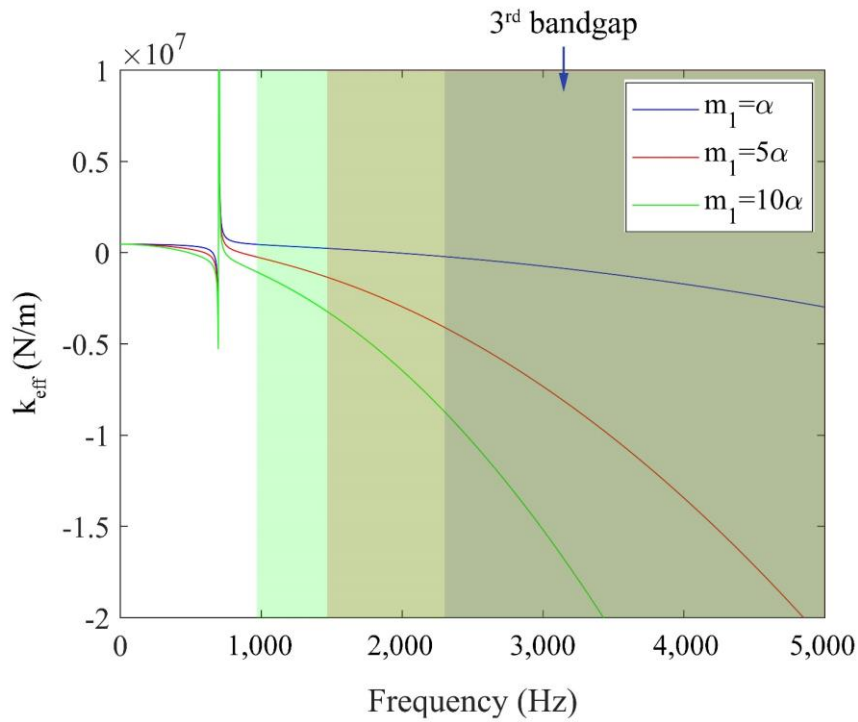
Figures 3-8a and 3-8b show the influence of the outer mass m_1 on the effective mass and stiffness, respectively. The other parameters are exactly the same as those in Table 3-5. Primarily, the bandgap position which is determined by the local resonance frequency has not exerted any effects by varying the value of m_1 . An increase of m_1 results in a reduction in the

first and second bandwidths in which the effective mass becomes negative as shown in Figure 3-8a but increases significantly the third bandwidth which results from the negativity of the effective stiffness (Figure 3-8b). In general, the negativity of the effective mass and effective stiffness relates to the bandgap region of the system in terms of wave propagation.

The above analytical results clearly indicate that the bandgaps could be controlled by varying the values of the internal mass m_2 and external mass m_1 to achieve the desired optimal wave manipulation. Moreover, the outer mass m_1 is more sensitive to the third bandgap associated with higher frequency while the inner mass m_2 shows a more significant influence on the first and second bandgaps which are located in a lower-frequency region. It is noted that the sensitivity can be qualitatively predicted by analyzing the relationship between m_1 and m_2 with m_{eff} and k_{eff} in Eqs. (3-21) and (3-22), considering that m_{eff} is related to the first and second bandgaps while k_{eff} governs the third bandgap. As shown in Figures 3-7 and 3-8, in which the value of m_1 is varied 10 times while that of m_2 is only varied 2 times to show the variation in the bandgap characteristic. This observation indicates that the internal mass which significantly influences the local resonance frequency of the meta-truss bar is more sensitive, compared to the external mass, in terms of the bandgap characteristics in wave propagation.



(a)



(b)

Figure 3-8. Effect of the internal mass m_1 on the bandgap characteristics (a) effective mass and (b) effective stiffness

3.5.2 Effect of stiffness on the bandwidth and bandgap position

The proposed model includes the additional parameter k_{s2} which represents the shear stiffness of the inner core while the other factors that affect the bandgap k_{a2} , k_{a1} , and k_{s1} remain the same. The effect of the stiffness k_{s2} on the bandwidth and the bandgap position is investigated in this section. Figure 3-9 illustrates the typical wave dispersion relations of the meta-truss bar with respect to different values of k_{s2} . From Figure 3-10, the following three primary findings can be summarized: (1) the internal resonance frequency is affected considerably due to the contribution of the stiffness k_{s2} ; (2) dissimilar to the conventional model, the characteristic of the bandgap generated by the proposed model has a wider frequency bandgap at low-frequency range, for instance, the upper bound of the first bandgap increases from 375 Hz to 655 Hz by varying k_{s2} from α to 10α ; and (3) the bandgap in the high-frequency range mostly formed by the negativity of the effective stiffness remains unchanged regardless of the varying k_{s2} .

Analogously, the effects of the parameters k_{a1} , k_{a2} , and k_{s1} on the bandgap behaviour are examined and the results are shown in Table 3-5. It is clear that increasing the shear spring stiffness k_{s1} narrows the frequency region of the third bandgap, but results in a surge of the other two bandgaps. On the other hand, for the axial stiffness k_{a1} and k_{a2} , while increasing the stiffness

exerts no effect on the first bandgap, it narrows the third bandgap and results in an increase and stability on the second bandgap by increasing k_{a1} and k_{a2} , respectively. In summary, the third bandgap associated with high frequencies is more sensitive to the stiffness k_{a1} , k_{a2} and k_{s1} , while the axial stiffness exhibits no influence on the first bandgaps.

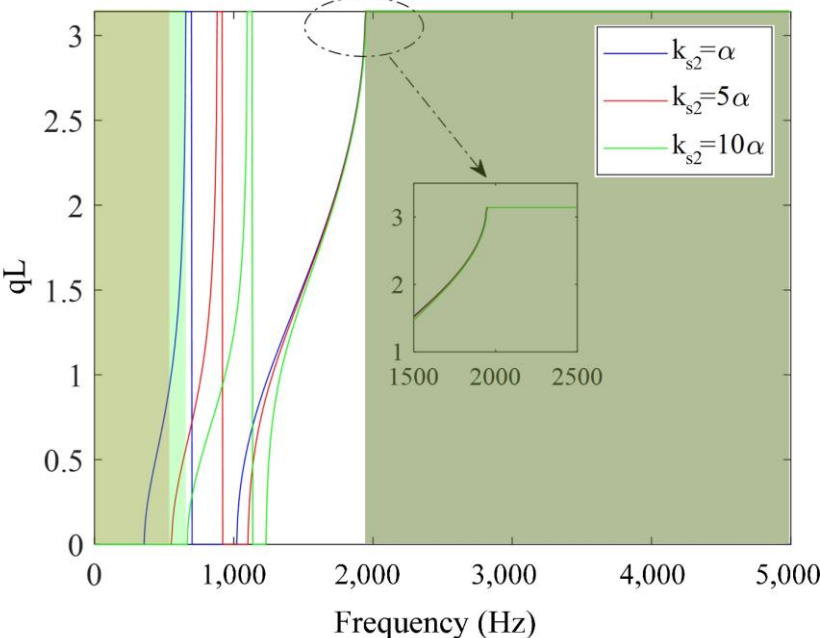


Figure 3-9. Dispersion relations of meta-truss bar embedded with the resonator with varied values of k_{s2}

Table 3-5. Meta-truss bar characteristics with varied stiffness k_{a1} , k_{a2} , and k_{s1}

Stiffness	Value	1 st Bandgap	2 nd Bandgap	3 rd Bandgap
k_{s1}	α	0 – 375 Hz	700 – 1,100 Hz	1,945 – 5,000 Hz
	5α	0 – 550 Hz	700 – 1,250 Hz	2,100 – 5,000 Hz
	10α	0 – 620 Hz	700 – 1,610 Hz	2,305 – 5,000 Hz
k_{a1}	α	0 – 375 Hz	700 – 1,100 Hz	1,945 – 5,000 Hz
	5α	0 – 375 Hz	700 – 1,100 Hz	3,500 – 5,000 Hz
	10α	0 – 375 Hz	700 – 1,100 Hz	3,945 – 5,000 Hz
k_{a2}	α	0 – 375 Hz	700 – 1,100 Hz	1,945 – 5,000 Hz
	5α	0 – 375 Hz	1,400 – 2,100 Hz	2,700 – 5,000 Hz
	10α	0 – 375 Hz	2,000 – 2,900 Hz	3,305 – 5,000 Hz

3.6. Transient response of meta-truss bar based on numerical simulation

The above analytical derivation and solution are valid for the meta-truss bar with some assumptions, i.e., infinite unit cells and harmonic wave solution. In practice, a meta-truss bar is applied with a finite number of unit cells. Deriving an analytical solution for the structural response of such meta-truss bar is not straightforward. To surmount this limitation of the analytical solution, a finite element model of the meta-truss bar is built in LS-DYNA to investigate the stress wave propagation in the structure. In this section, the transient response of the meta-truss bar under harmonic excitation is further examined with two cases including a sweep excitation [1-5,000] Hz in Section 3.6.1 and a dominant frequency at 500 Hz in Section 3.6.2. The stress waves in the time domain at the far end are captured to demonstrate the exceptional characteristics of the meta-truss bar.

3.6.1 Transient response to sweep excitation

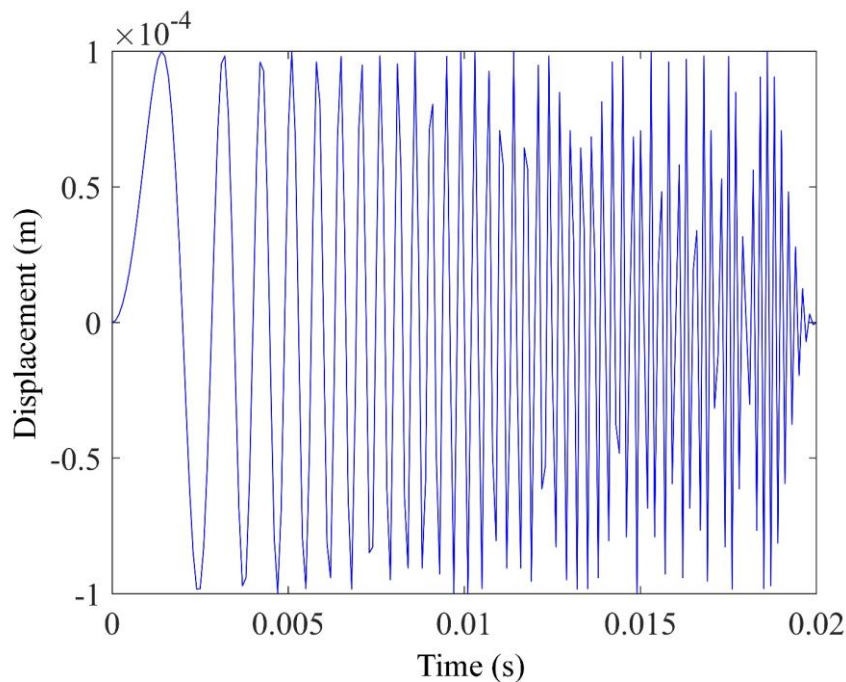


Figure 3-10. Sweep excitation input profiles in time-domain

Figure 3-10 shows the sweep excitation at one end of the meta-truss bar and Figure 3-11 depicts the movement vector of each part of the entire structure at a typical instant. Figure 3-11a shows the displacement contour of each component of the 3D meta-truss bar in which local resonators m_1 and m_2 do not have synchronized motions due to the local resonant mechanism that the hardcore acts as an oscillator. Specifically, the interaction of these two resonators (resonator 1 in white color and resonator 2 in yellow color) includes the in-phase motions (Figure 3-11b)

and the out-of-phase motions (Figure 3-11b) working as energy absorbers can significantly mitigate the stress wave propagating through the structure.

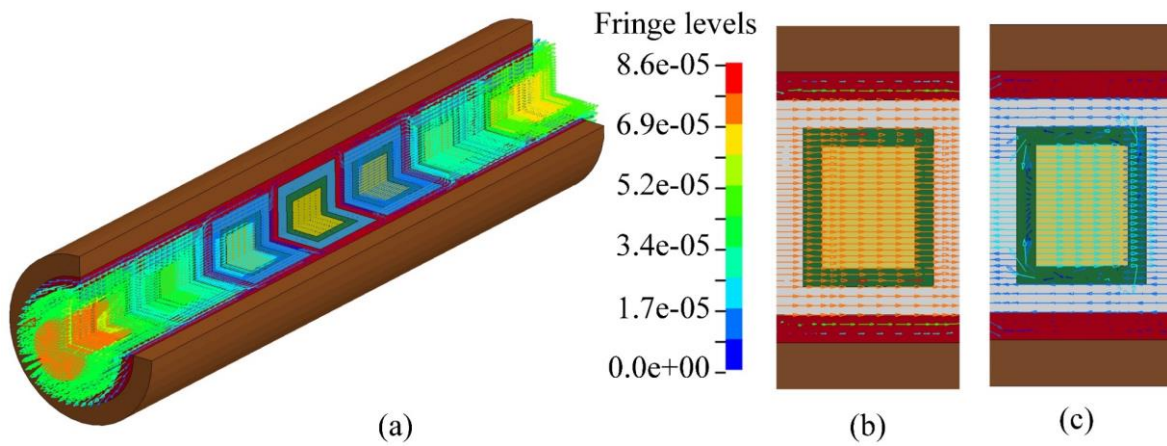


Figure 3-11. Snapshots of the interaction displacement (a) 3D meta-truss bar, (b) cross section of unit 1 at $t = 4.299$ ms, and (c) cross section of unit 1 at $t = 6.449$ ms

To more explicitly show the wave attenuation effect of the meta-truss bar leveraging the locally resonant mechanism, the Z-stress waves at different section of the meta-truss bar including the input section, the middle section and the output section of the aluminium outer tube element (3rd layer in Figure 3-1) and outer rubber element (2nd layer in Figure 3-1) are compared in Figures 3-12a and 3-12b, respectively. It can be seen that the amplitudes of the element close to the input excitation (input section in the figure) are largest, followed by the amplitudes at the middle section while the smallest amplitudes belong to the element at the far-end position (the output section). In particular, the maximum amplitudes of the stress waves at the three sections of the aluminum outer mass are -1.4×10^6 N/m², -0.5×10^6 N/m², -0.3×10^6 N/m², respectively, and the corresponding results in the external layer of rubber are -1.7×10^6 N/m², -0.8×10^6 N/m², -0.4×10^6 N/m². It is evident that both figures exhibit the stress wave attenuation observation from the beginning to the end of the meta-truss bar subjected to the sweep frequency excitation which has the dominant frequencies falling into its bandgap regions.

In general, the transient responses of the meta-truss bar significantly rely on its frequency band structure which are affected by its geometric design. By adopting the local resonance mechanism, the designed meta-truss bar successfully exhibits its stress wave attenuation phenomenon by mitigating the stress waves propagating from the input section to the output section.

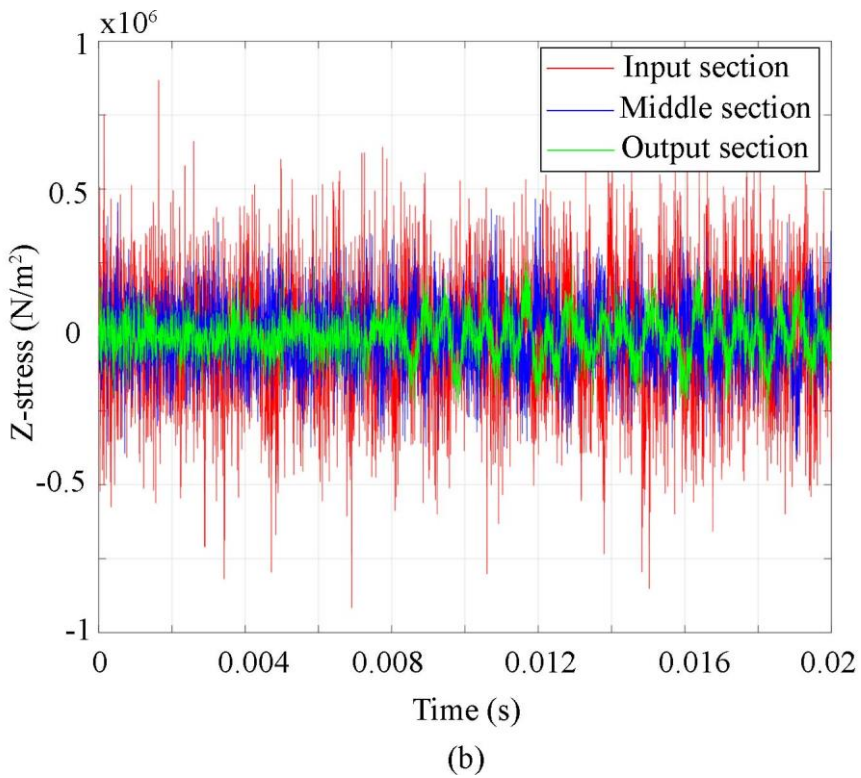
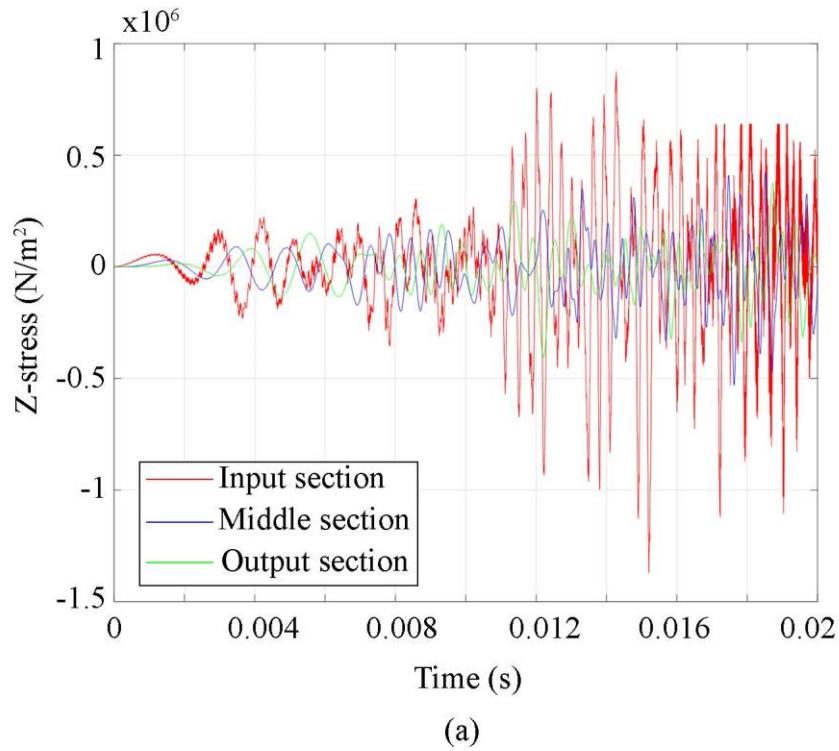


Figure 3-12. Stress waves time histories at different sections of the meta-truss bar at (a) outer mass aluminium and (b) outer coating

To further validate the proposed model, the continuous wavelet transform (CWT) is applied to analyze the output displacements in the time-frequency domain. In this chapter, a Gabor wavelet transform is chosen as the mother wavelet function owing to its multiresolution analysis

capability. Figure 3-13 depicts the multi-frequency CWT profiles of the far-end surface data in the case of sweep excitation. As shown, no energy exists in the output signal within three frequency ranges which are shaded in the figure, which mean the three bandgaps are formed. These bandgaps are well agreed with the analytical results as discussed above.

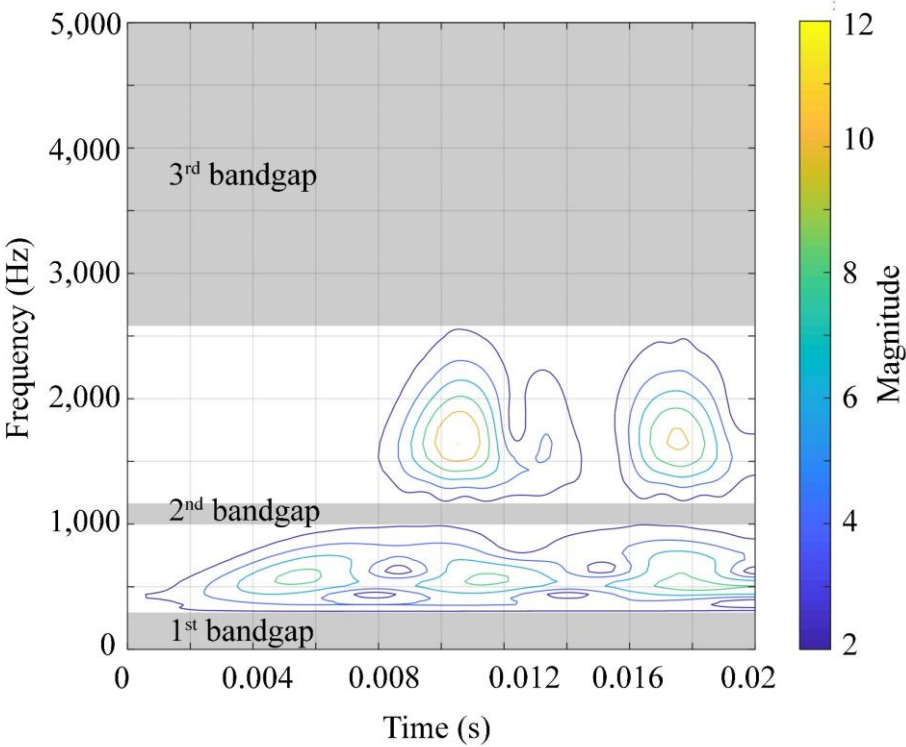


Figure 3-13. Transient response profiles of the output displacement obtained by the CWT method in the time-frequency domain under the sweep excitation

3.6.2 Transient response to a single frequency inside the passband

The dynamic response of the meta-truss bar is further studied by applying a prescribed displacement with a frequency that falls outside the bandgap range. In the numerical simulation, a frequency of 500 Hz is chosen. By applying a similar procedure, the stress waves of an element in the lead core (5th layer in Figure 3-1) and the inner coating (4th layer in Figure 3-1) at the input end, middle part and output end of the model are compared in Figures 3-14a and 3-14b, respectively. It can be seen that no wave attenuation occurs because the wave frequency is outside the bandgap of the meta-truss bar. In other words, the stress wave can propagate through the meta-truss bar without any internal obstructions, there is no prominent change in the stress amplitude.

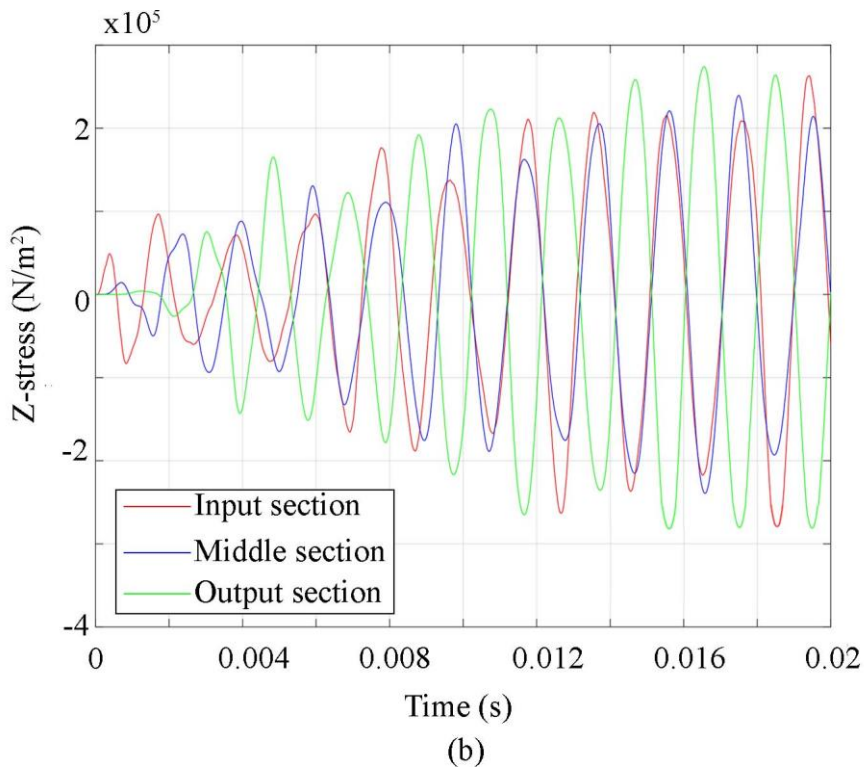
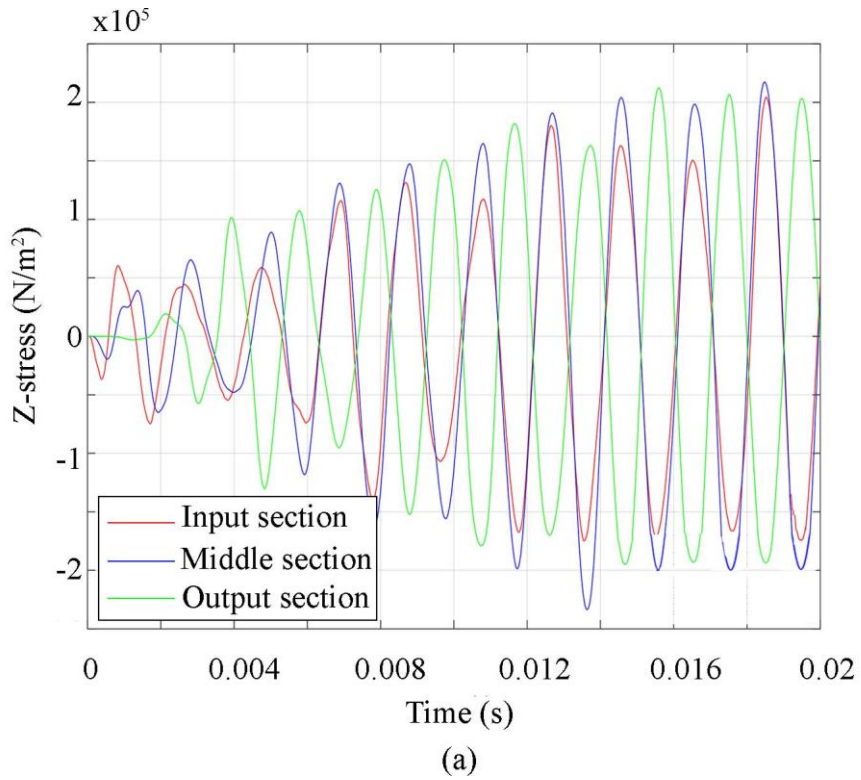


Figure 3-14. Stress waves time histories at different sections of the meta-truss bar subjected to harmonic excitation with frequency in the passband at (a) lead core and (b) inner coating

Figure 3-15 depicts the multi-frequency CWT profiles of the far-end surface subjected to a single frequency excitation (i.e. with the frequency of 500 Hz). As shown in Figure 3-15, the dominant frequency of the transmitted signal remains unchanged at 500 Hz, which means no

wave attenuation phenomena occurs in this area. This is because 500 Hz is within the passband of the meta-truss bar as discussed above.

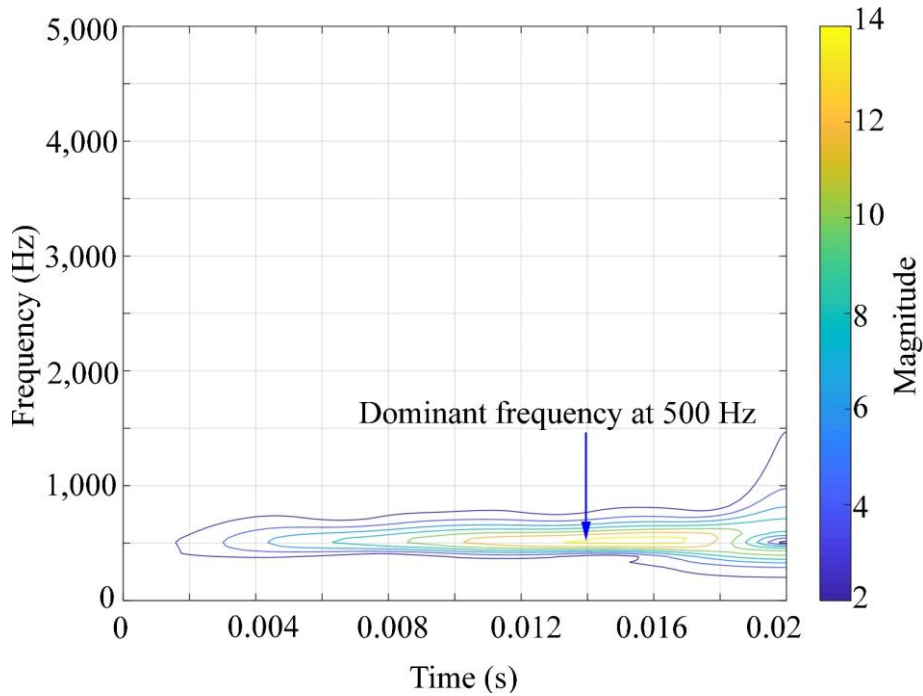


Figure 3-15. Transient response profiles of the output displacement obtained by the CWT method under the excitation with a single frequency of 500 Hz

3.7. Conclusions

In this chapter, an analytical spring-mass model is developed to improve the accuracy of the commonly used analytical model for the dynamic behaviors of the meta-truss bar. In the proposed model, one more spring representing the shear stiffness between the most inner core and the corresponding coating is taken into consideration. From the analytical and numerical investigations, the following conclusions can be drawn:

1. The proposed model results in a broader low-frequency bandgap for the meta-truss bar, while this low-frequency bandgap width is under-predicted by the conventional model owing to neglecting the shear stiffness of the second-layer coating connecting the inner and outer mass.
2. Parametric studies reveal that the first two bandgaps can be broadened by either increasing the internal mass m_1 or decreasing m_2 while the third bandgap remains unchanged irrespective of the value of m_2 but increases with m_1 .
3. Increasing the axial stiffness k_{a1} , and k_{a2} has no effect on the first bandgap but narrows the third bandgap. Increasing shear spring stiffness k_{s1} narrows the third bandgap, but widens the

other two bandgaps. Increasing the shear stiffness k_{s2} , which is neglected in the previous study, has no effect on the bandgap in the high-frequency range but widens the bandgap in the low-frequency range.

In general, the investigated meta-truss bar with dual resonators exhibits excellent performance on stress wave mitigation so that it possesses a great potential to be deployed in protective structures or energy absorbers. The proposed analytical model can predict the performance of the meta-truss bar with a high level of accuracy in the low-frequency range.

CHAPTER 4. IMPACT LOAD MITIGATION OF META-PANELS WITH SINGLE LOCAL RESONATORS

Abstract³

This chapter investigates the influence of design parameters on the impact mitigation capacity of a new meta-panel that leveraged the coupled mechanisms of plastic deformation and local resonance to absorb energy from impact loading. The main objective is to minimize the force to be transmitted to the protected structures through mitigating the stress wave propagation by using local resonators. The meta-panel demonstrates the capability of filtering out the stress wave induced by impact loading with frequencies falling in its bandgaps. A numerical model is built and verified by the analytical solution with a good agreement in terms of the predicted frequency bandgaps. The meta-panel shows a substantial reduction in the mid-span deflection of the facesheets and an increase in the impact energy absorption as compared with the conventional sandwich panels. The peak reaction force of the meta-panel transmitted to the protected structure is also reduced significantly by more than 47% compared to its conventional counterparts. Furthermore, parametric studies are conducted to investigate the effects of the thickness of the hollow-truss bar, core material properties, and impact velocity on the meta-panels impact-resistant behaviour.

³ The related work in this chapter was published in **Engineering Structures** with the full bibliographic citation as follows:

N.H. Vo, T. Pham, K. Bi, W. Chen, H. Hao. Impact Load Mitigation of Meta-panels with Single Local Resonator. *Engineering Structures*. 2022; 265: 114528.

<https://doi.org/10.1016/j.engstruct.2022.114528>

4.1. Introduction

When structural elements, e.g., beams [115], columns, and joints [116] are subjected to impulse loading, their failure/wreckages might cause major loss of human life and economy. It is, therefore, deemed important to develop protective systems to protect critical structures exposed to these threats. Amongst many mitigation strategies, the deployment of sacrificial cladding as a shock attenuator has attracted intensive researches due to its protective functionality and excellent behaviour [117, 118]. Sacrificial claddings often consist of two components, namely the outer facesheets and the inner core [119, 120]. While distributing the load more uniformly is the function of the outer facesheets, the inner core often deforms and absorbs most of the energy from the incident loading via plastic deformation, leading to load mitigation on the main protected structures. Many studies have proven that sandwich panels functioning as sacrificial claddings have a significantly higher dynamic resistance compared to the monolithic plates with the same mass per unit area [121].

Regarding the dynamic mitigation, much effort has been devoted to exploring different forms of protective sandwich panels as sacrificial cladding. Relatively new materials that possess the protective capabilities against dynamic loading have been explored by a few researchers such as aluminium foam panels by Hanssen et al. [7], double-layer foam panels by Ma and Ye [122], and honeycomb core by Hazizan and Cantwell [123], etc. Besides, the superior behaviour of the lattice-truss panels under impact loading has also been explored [124, 125]. These studies proved that the lattice core-based sandwich panels outperform their conventional counterparts such as honeycomb sandwich panels regarding impulsive energy absorption capacity and mitigating effect. Besides, the space provision of the lattice sandwich structures is generally wider compared to honeycomb structures, which can be utilized for other purposes, e.g. heat transfer [126, 127], energy absorbers [128], and sound isolation [129, 130]. Generally, the main mechanism of these types of sandwich panels is based on plastic deformation to absorb energy from the incident loading [23, 29].

More recently, increasing attention has turned to filter incident loading using the local resonances as energy absorbers, e.g. meta-truss bar [41, 83], meta-concrete [73, 82] and meta-materials [33] resulting in the loading mitigation effect. It is worth mentioning that the prefix “meta” originates from the Greek preposition, which meant “beyond”, implying these favourable structural behaviour are superior to other natural counterparts [41]. To filter incident loading, Liu et al. [68] proposed the novel meta-truss bar comprising of single and dual

resonators. Investigations have been carried out to manifest the potential of the meta-truss bar in creating bandgaps to stop wave propagation. For practical applications, the wave propagation mitigation of the meta-structures has been demonstrated in meta-sandwich beam by Chen et al. [131]. The results showed that the local resonance of the embedded resonators in the meta-sandwich beam was activated when the frequencies of the incident loading fall into its bandgaps, thus trapping wave energy to attenuate stress wave propagation. Also, it has been proven that the bandgap is programmable by varying the resonator designs and thus allowing for tailoring the attenuation properties as required by practical applications [132]. A meta-foundation that can both attenuate seismic waves and withstand static loads was proposed by La Salandra et al. [133]. That study investigated the influence of both geometrical and mechanical properties of a foundation inspired by meta-material concept on its dynamic performance as well as its capabilities of bearing gravity loads. Furthermore, the structural configuration of lattice core sandwich panels and the exceptional characteristics of the meta-truss bar to form a meta-panel, resulting in the impact/blast mitigation and higher energy absorption of the panels have been studied [41, 42]. In general, studies on applying meta-truss bar in engineering structures are very limited and no systematic studies have been reported to determine the integral influence that affects the transient response of the meta-panel in literature. In particular, the effects of the design parameters including material properties and truss-bar thickness, as well as the impact velocity on the protective effectiveness of the meta-panel have not been well investigated. Given the above considerations, there is thus a strong need to further study of this promising field towards practical applications.

The impact behaviour of the meta-panel with single resonators functioning as sacrificial cladding (Figure 4-1) are examined in this chapter. It should be noted that the meta-panel adopts the coupled mechanisms of absorbing strain energy through plastic deformation of the outer tube and local resonance of the inclusions. The optimization analyses are carried out to enhance its mitigating effect through comprehensive parametric studies. The impact performances of the meta-panel are simulated using finite element software LS-DYNA to evaluate its impact mitigation capacity compared to those of the conventional panels. The numerical transmission coefficient is verified against the analytical results for validation. In this chapter, the dynamic responses of panels with various designs are evaluated through the criteria including the energy absorption capacity, the central deflections of the facesheet, and the boundary reaction forces. Furthermore, parametric studies have been conducted by varying each parameter to investigate the effects of the truss-bar thickness, the material properties, and the impact velocity on the

transient responses or the protective effect of the meta-panel. This chapter not only numerically and analytically demonstrates the dynamic mitigation mechanism of the meta-panel subjected to impact loads, but presents several favourable findings, which are beneficial for engineering applications. Experimental tests will be carried out in near future to further verify the performance of meta-panels designed according to these findings.

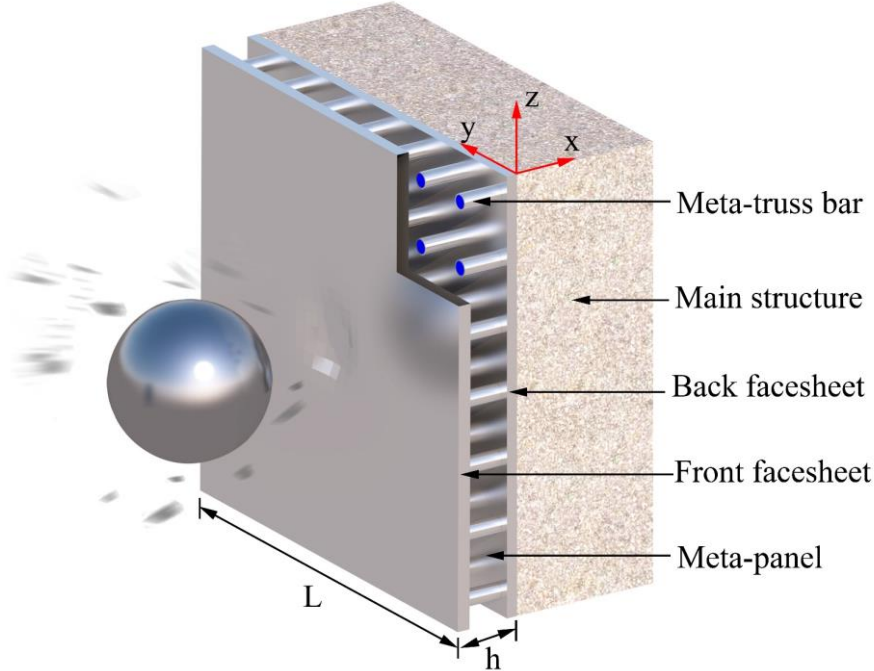


Figure 4-1. Schematic illustration of the protection of meta-panels against impact loading

4.2. Geometric configuration

For the investigated structure, two thin facesheets are bonded to four meta-truss bars to form a symmetric meta-panel as sketched in Figure 4-2a. The distinctive feature of this design lies in the meta-cores made of meta-truss bars that consist of 7 unit cells (Figure 4-2b). With this configuration, the unit model comprises three components, i.e. the outer tube, the soft coat, and the resonator, whose dimensions are depicted in Figure 4-2b while their materials are shown in Figure 4-2c. To endure large deformation, polyurethane (PU) is selected for the soft coating while aluminium 1060 and lead are respectively chosen for the outer tube and the resonator. The two facesheets connected rigidly to the outer tubes to form an integral structure are also made of aluminium 1060. The mechanical properties of all components are tabulated in Table 4-1.

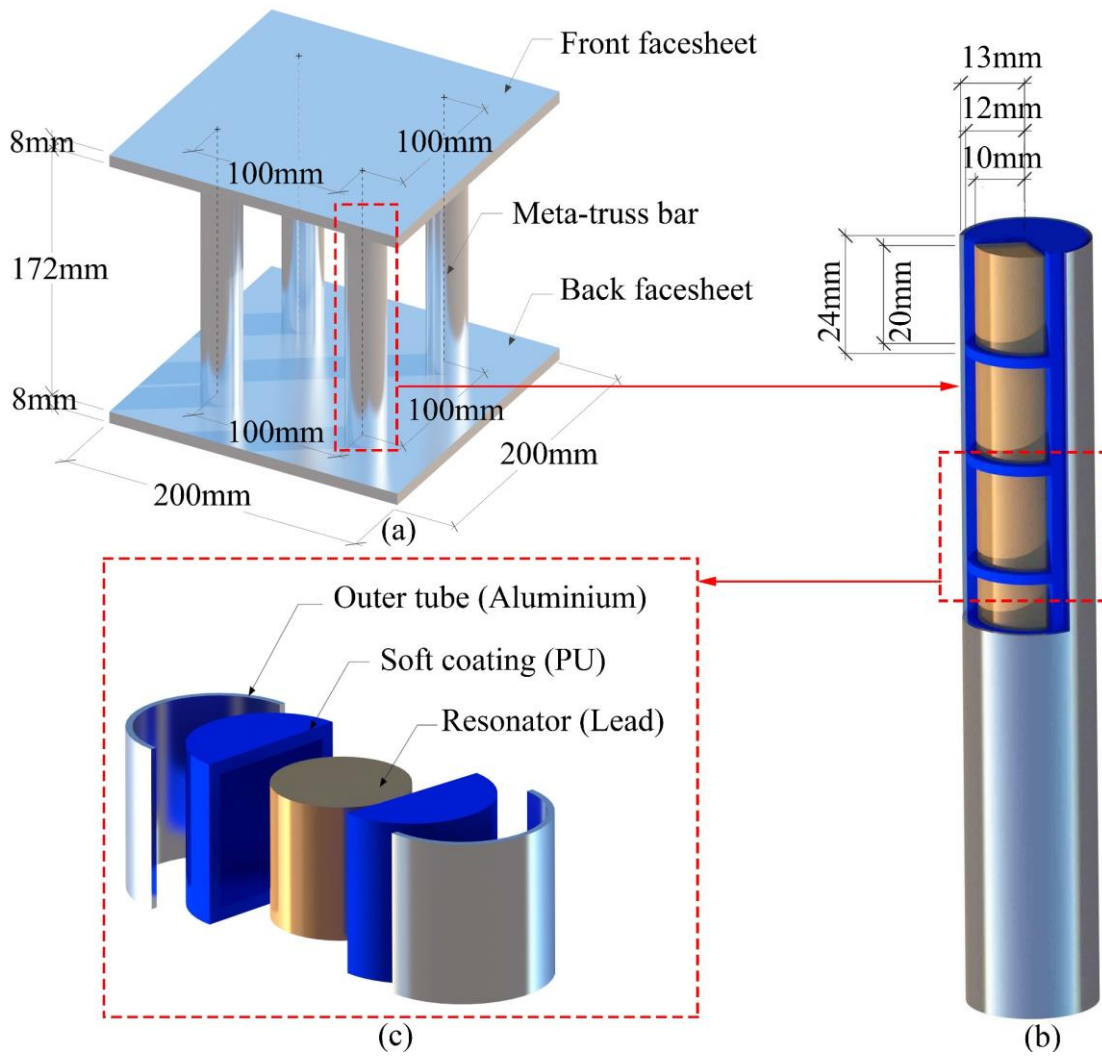


Figure 4-2. Schematic diagrams of (a) the meta-panel under impact loads, (b) meta-truss bar, and (c) unit cell

Table 4-1. Elastic material properties used in the numerical simulation [111]

Materials	Density ρ (kg/m ³)	Young's modulus E (GPa)	Poisson's ratio ν
Aluminium 1060	2,770	70	0.33
PU	900	0.147	0.42
Lead	11,400	16	0.44
Steel	7,850	210	0.29

4.3. Analytical predictions of the bandgaps

The design can be conceptualized as the monotonic unit cells as shown in Figure 4-3, which are analytically described using the spring-mass model. The outer tube represents the matrix in the

model while the resonator is represented by the mass of m_1 . The soft coating is modelled by two springs including the axial spring and the shear spring, i.e., k_{a1}, k_{s1} , respectively for the soft coating. Without loss of generality, the mitigation effects on stress wave propagation of the meta-truss bar are examined by analyzing the performance of elastic stress wave propagation in the idealized meta-truss bar model.

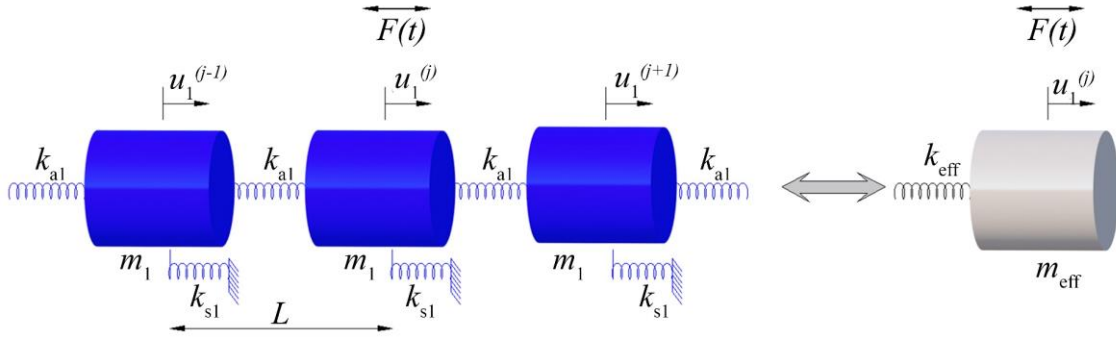


Figure 4-3. Equivalent effective spring-mass model

The mass of the resonator m_1 (with an outer radius, r) can be calculated as

$$m_1 = \rho \pi r^2 l \quad (4-1)$$

where ρ is the material density, r and l are the radius and length of the resonator.

The stiffness of the equivalent springs is estimated using the following equations:

$$k_{a1} = \frac{E_3 A_1}{l_1}, \quad k_{s1} = \frac{G_3 A_2}{l_2}, \quad G_3 = \frac{E_3}{2(1 + \vartheta_3)} \quad (4-2)$$

where G_3 and E_3 respectively denote shear and Young's modulus of the soft coating while ϑ_3 is Poisson's ratio. The determination of the nominal dimension for calculating the equivalent axial and shear spring stiffness, i.e., A_i and l_i ($i=1,2$), k_{a1} and k_{s1} are not straightforward due to the shape complex geometry. Instead of calculating these equivalent geometrical dimensions, in this chapter, the equivalent stiffness k_{a1} and k_{s1} are numerically calculated. It should be noted that the investigation on the relationships between the numerically determined stiffnesses with their theoretical values when varying the thickness l_1 and l_2 demonstrates that both numerical and analytical solutions yield similar estimations of stiffnesses for the considered meta-truss bar, as proven in previous studies [42, 134]. The estimated mass is given by $m_1 = 7.16 \times 10^{-2}$ kg while the axial and shear stiffness are $k_{a1} = 57,375$ kN/m, $k_{s1} = 35,498$ kN/m, respectively.

The characteristics of the meta-truss bar are determined by a process of deduction starting with applying the equation of motion and ending with the negative effective properties, as well as the dispersion relation and transmission coefficients. The equation of motion for the j^{th} unit cell can be derived as:

$$m_1 \frac{\partial^2 u_1^{(j)}}{\partial t^2} + k_{a1} (2u_1^{(j)} - u_1^{(j+1)} - u_1^{(j-1)}) + k_{s1} u_1^{(j)} = 0 \quad (4-3)$$

in which u_1 represents mass displacement.

The displacement for the harmonic wave of the j^{th} unit cell is expressed as:

$$u^{(j)} = U e^{i(jqL - \omega t)} \quad (4-4)$$

where ω and L respectively denote the angular frequency and the distance between two adjacent unit cells. U and q stand for the wave amplitude and wave number, respectively.

Substituting Eq. (4-4) into Eq. (4-3), the dispersion curve is expressed:

$$\cos qL = 1 - \frac{m_1 \omega^2 - k_{s1}}{2k_{a1}} \quad (4-5)$$

To simplify the model, a homogeneous unit cell [68] consisting of an effective mass connected by an effective stiffness as shown in Figure 4-3 can be derived and expressed as:

$$m_{\text{eff}} = m_1 - \frac{k_{s1}}{\omega^2} \quad (4-6)$$

$$k_{\text{eff}} = k_{a1} - \frac{1}{4} m_{\text{eff}} \omega^2 = k_{a1} - \frac{1}{4} \left(m_1 - \frac{k_{s1}}{\omega^2} \right) \omega^2 \quad (4-7)$$

where m_{eff} and k_{eff} are the effective mass and effective stiffness, respectively. It is worth mentioning that the underlying goal for developing the effective properties of the investigated parameters including mass and stiffness in the analytical model is to establish the relationship between the frequency of the incident force and the locally resonant frequency of the system. In the local resonant phase, there is a relative and out-of-phase motion between the resonators and the outer tube. This induces a change in the vibration properties of the system, meaning that the effective parameters for the dynamic response are different from their physical

parameters owing to the local vibrations. The negative effective mass and stiffness are triggered with incident frequencies falling into the bandgaps of the meta-truss bar, leading to the favourable wave attenuation characteristics of the meta-system.

The dispersion relation in Eq. (4-5) is solved to define the width of the passband as:

$$\omega = \sqrt{\frac{2k_{a1}(1 - \cos(qL)) + k_{s1}}{m_1}} \quad (4-8)$$

The starting point of the passband can be obtained by substituting $qL=0$:

$$\omega = \sqrt{\frac{k_{s1}}{m_1}} \quad (4-9)$$

and the ending point of the passband can be expressed by substituting $qL=\pi$, as:

$$\omega = \sqrt{\frac{4k_{a1} + k_{s1}}{m_1}} \quad (4-10)$$

The transmission coefficients of the entire system can be given:

$$T = \left| \prod_{j=1}^N T^{(j)} \right| = \left| \prod_{j=1}^N \frac{u^{(j)}}{u^{(j-1)}} \right| \quad (4-11)$$

Based on the above derivations, Figure 4-4a depicts the analytical dispersion relation of the meta-truss bar whereas the effective parameters are also obtained and shown in Figure 4-4b. It is observed that the theoretical first bandgap of the meta-truss bar is at [0 - 3,500] Hz, which is generated by the negative effective mass (as shown in Figure 4-4b) while the value of effective stiffness becomes negative leading to the second bandgap at [$> 9,500$] Hz. It is shown that the bandgaps can be generated by both negative effective mass and stiffness.

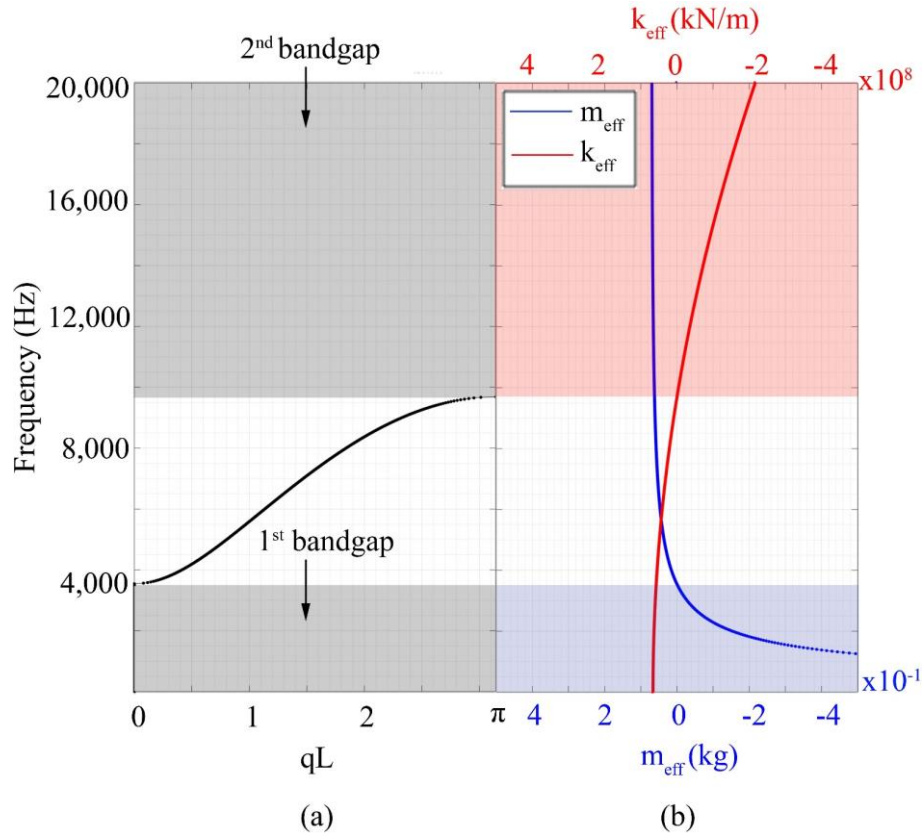


Figure 4-4. (a) Dispersion curve and (b) effective parameters of the meta-truss bar

4.4. Numerical modeling

The bandgap frequencies of the meta-truss bar have been achieved by utilizing the analytical solutions, based on the one-dimensional spring-mass model. However, the above theoretical derivation is based on the assumption of the infinite number of unit cells under harmonic wave input for solving the Eigen frequency and calculating the bandgaps. It is not straightforward to obtain the closed-form theoretical solutions of the case with a finite number of cells, boundary reflections, and subjected to different forms of input. Moreover, it is more difficult to derive the analytical solution of the structural behaviour of the meta-panel under impact load, especially when plastic deformation is considered. To surmount the limitations of the analytical solutions, a numerical investigation is conducted to evaluate the transient responses of the meta-panel subjected to impact loading. The results obtained from the above theoretical solutions based on idealized conditions are utilized to indirectly verify the accuracy of the numerical model of the meta-panel presented in Figure 4-2 in Section 4.2.

4.4.1 Numerical model calibrations

The numerical simulation is conducted by the commercial software LS-DYNA [135] to evaluate the transient responses of the meta-panel subjected to impact loads. This section presents the constitutive material models, initial conditions, element types and sizes, and contact definition of the numerical model.

4.4.1.1 Constitutive material models

Johnson-Cook material model [136] as defined in Eq. (4-12) is adopted in LS-DYNA with the keyword *MAT_JOHNSON_COOK material (Mat_15) to exhibit the rate-dependence of aluminium material. The Johnson-Cook strength model, which is a phenomenological model based on various experimental results, has been widely used to capture the rate-dependent behaviour of aluminium alloy. The model has been successfully validated to describe the mechanical responses of Aluminium experiencing high-rate deformation or melting process [113].

$$\sigma = \left[A + B(\varepsilon^p)^n \right] \left(1 + C \ln \dot{\varepsilon}^* \right) \left(1 - T^{*m} \right) \quad (4-12)$$

where the equivalent von Mises stress is denoted by σ while the equivalent plastic strain is expressed by ε . The plastic strain rate, $\dot{\varepsilon}^*$ is defined by the ratio $\dot{\varepsilon}/\dot{\varepsilon}_0$, in which $\dot{\varepsilon}_0$ is a reference strain rate and is generally set to 1.0 s^{-1} . The ratio $(T - T_r)/(T_m - T_r)$ defines the dimensionless temperature, T^* , in which the material reference temperature is T_r and the melting temperature is T_m . Besides, Table 4-3 gives the equation of state for the Johnson-cook model, which is adopted by card *EOS_LINEAR_POLYNOMIAL.

The card *MAT_MOONEY_RIVLIN_RUBBER in Eq. (4-13) is simulated the performance of the PU material model while for the lead cores, the keyword *MAT_PLASTIC_KINEMATIC in Eq. (4-14) is chosen. It is because this material model is commonly used for modelling metal with bi-linear elastic-plastic constitutive relationship and isotropic or kinematic hardening plasticity which is defined by a hardening parameter β . In this chapter, β is set to 1 which represents isotropic hardening. The steel impact ball is assumed as rigid and modelled by the card *MAT_RIGID. The material properties used in the numerical simulation are listed in Table 4-2. Soft materials have nonlinear stress-strain behaviour for relatively large deformations. Under such conditions, they are generally assumed as nearly incompressible. To model these hyperelastic materials through FE analysis, the Mooney-Rivlin model is adopted

on the polynomial development of total strain energy. Two Mooney-Rivlin parameters (C_{10} and C_{01}) given in Table 4-2 are often used to describe the hyper-elastic rubber deformation.

Table 4-2. Material properties in the numerical model

Category	Material models	Parameters	Value
Al 1060 [41]	MAT_JOHNSON_COOK	Density	2,770 kg/m ³
		Poisson's ratio	0.33
		Young's modulus	70 GPa
		Yield stress A	0.369 GPa
		Hardening constant B	0.675 GPa
		Strain rate constant C	0.007
		Softening exponent m	1.5
		Hardening exponent n	0.7
		Melting temperature T_m	800 K
Lead [114]	MAT_PLASTIC_KINEMATIC	Density	11,400 kg/m ³
		Poisson's ratio	0.44
		Young's modulus	16 GPa
		Yield stress	20 MPa
		Tangent modulus	50 MPa
		Hardening parameter	10 ⁹
		Strain rate parameter C	10 ⁹
		Strain rate parameter P	1
		Failure strain	0
PU [137]	MAT_MOONEY_RIVLIN_RUBBER	Density	900 kg/m ³
		Poisson's ratio	0.42
		Constant C_{10}	21.5 MPa
		Constant C_{01}	4.3 MPa

The Mooney-Rivlin material model has previously been used to successfully predict the behaviour of PE. The Mooney-Rivlin strain energy potential is adopted as follows [138].

$$\sigma_{ij} = \frac{\partial W}{\partial \varepsilon_{ij}} \quad (4-13)$$

$$W = \sum_{k+m=1}^n C_{km} (I_1 - 3)^k + (I_2 - 3)^m + \frac{1}{2} k (I_3 - 1)^2$$

where W is the strain energy per unit of reference volume while I_1, I_2, I_3 are the strain variants. k is the bulk modulus and $I_3 = 1$ for incompressible material behaviour; C_{km} is the constant of the Mooney-Rivlin material.

The input parameters defined in the *MAT_PLASTIC-KINEMATIC model are based on quasi-static material testing. The strain rate effect is taken into consideration by using the Cowper-Symonds model whose equation is given as:

$$\frac{\sigma_d}{\sigma_s} = 1 + \left(\frac{\dot{\varepsilon}}{C} \right)^{1/p} \quad (4-14)$$

where σ_d and σ_s are the dynamic yield stress and static yield stress at the plastic strain rate $\dot{\varepsilon}$, respectively. The constant strain rate parameters are expressed by Cowper C and Symonds P .

Table 4-3. Equation of state for aluminium [113]

C_0 (Pa)	C_1 (GPa)	C_2 (GPa)	C_3 (GPa)	C_4	C_5	C_6	E_0 (GPa)	V_0 (m ³ /m ³)
0	74.2	60.5	36.5	1.96	0	0	0	1

4.4.1.2 Modelling contacts and boundary conditions

The model utilized to simulate the contact between the impactor and front facesheet of the panel is applied by the card *AUTOMATIC_SURFACE_TO_SURFACE while the contact definition between the metals and polyurethane is *TIED_SURFACE_TO_SURFACE to assume their perfect bond. Since it is assumed that the interfaces between PU and the metals of the meta-panel are perfectly bonded, hence no debonding analysis is carried out. Besides, the card *TIED_NODE_TO_SURFACE is adopted to simulate the joint between the facesheets and the meta-truss bars. All nodes along the perimeter of the back facesheet are fixed in all directions using the *BOUNDARY_SPC_SET. In this chapter, solid hexahedron elements (SOLID 164) are utilized to model all the elements. LS-DYNA provides two types of bulk viscosity coefficients namely Q_1 and Q_2 to treat shocks. While Q_1 helps to smear the shocks

and also prevents the element from collapsing under high velocities, Q_2 , called as a linear term, helps to rapidly damp out the oscillations. By default, these coefficients are fixed at $Q_1=1.5$ and $Q_2=0.06$ and both are active for solid elements in this chapter [139].

4.4.1.3 Impactor

The steel impactor is modelled as a rigid body. The impactor has a spherical shape of 20 mm radius and its weight is 1 kg. The initial velocity of the impactor against the panel is 3 m/s and is defined by the *INITIAL_VELOCITY_GENERATION card, which is applied to all nodes of the impactor. The predicted impact force-time history is shown in Figure 4-5a while Figure 4-5b depicts the corresponding FFT spectrum. As shown, the peak impact force is nearly 10 kN with the dominant frequencies of impact loading up to approximately 3,000 Hz.

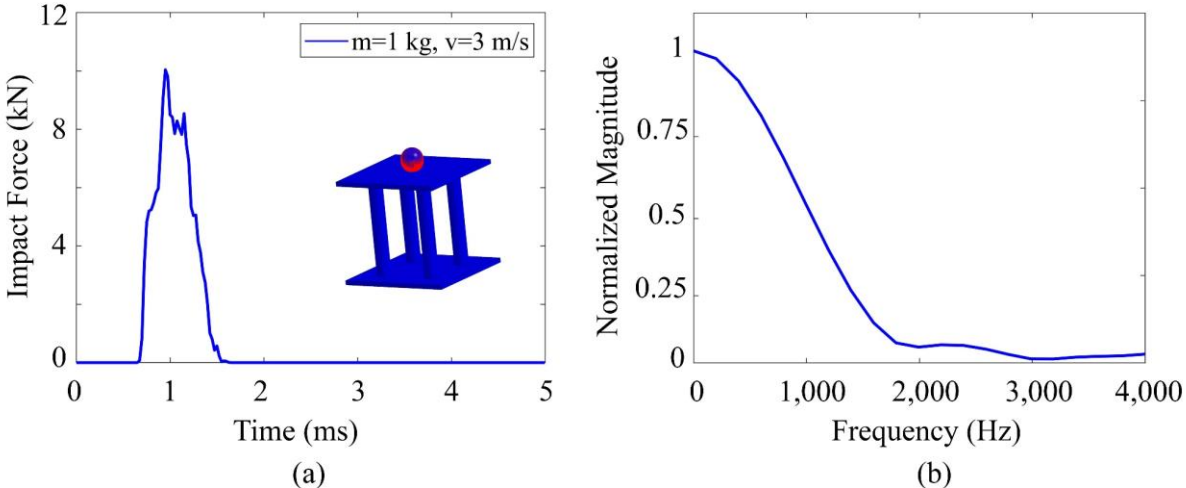


Figure 4-5. (a) Time history of impact force and (b) frequency domain

4.4.2 Mesh convergence study

Typically, to secure the accuracy of the numerical simulations, a mesh convergent study is conducted by varying mesh sizes, i.e. 3 mm, 2 mm, 1 mm, 0.5 mm, and gradient mesh which represents coarse, medium, and fine meshes. Figure 4-6a shows the schematic diagram of gradient mesh sizes for the meta-panel, in which a uniform mesh size of 1 mm is adopted for the meta-truss bar while for the facesheets, the mesh sizes of 0.5 mm and 1 mm are set for the impact area (60 x 60 mm² in the centre area) and the remaining area, respectively. The central point displacement of the front facesheet of the meta-panel and the computational cost corresponding to various mesh sizes are shown in Figure 4-6b. As observed, the mesh size of 0.5 mm and gradient mesh result in similar outcomes. The mesh size is considered to converge at about 0.5 mm while its computational cost is greatly higher than that of the gradient mesh

sizes. Therefore, the gradient mesh size is utilized in the subsequent numerical simulations when considering both the accuracy and efficiency.

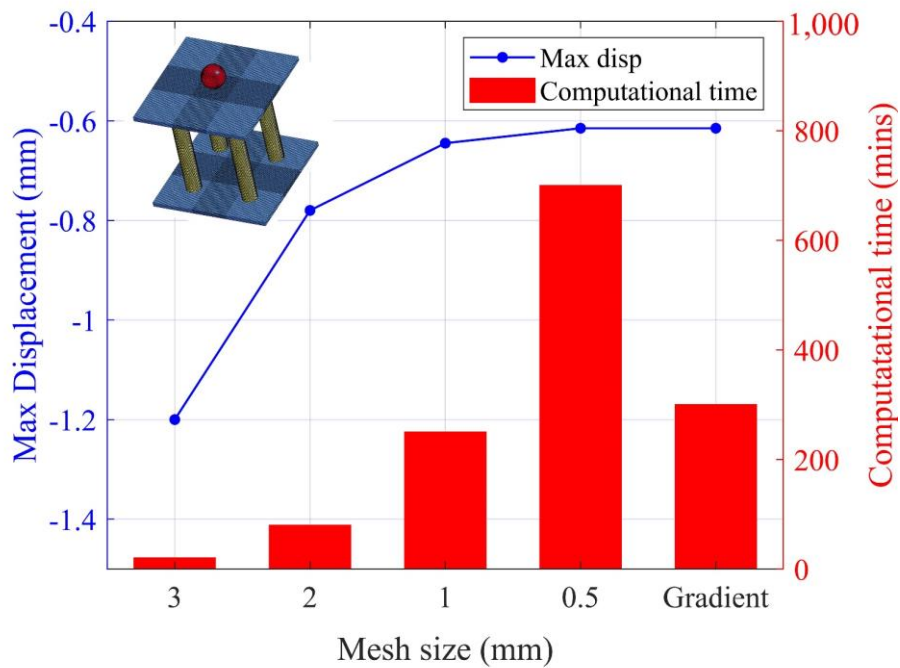


Figure 4-6. Mesh convergence analysis

4.4.3 Model validation

The transmission coefficient from both numerical and analytical derivation is utilized for model validation. One end of the meta-truss bar is excited by the input signal in a form of prescribed displacement with a sweep frequency of $[0 - 20,000]$ Hz while the output response is captured at the other end to calculate the transmission coefficient. It is worth mentioning that the prescribed displacement is generated by the sweep-frequency cosine function named “Chirp” in Matlab. Then, it is applied to the meta-truss bar model in Ls-Dyna using the keyword *PRESCRIBED_MOTION_SET. As shown in Figure 4-7, the numerical and the theoretical transmission coefficients are in good agreement, implying the validity of the model. For the numerical simulation, the frequency ranges of $[0 - 3,600]$ Hz and $[>9,000]$ Hz are respectively the 1st and the 2nd bandgap while the corresponding regions of the bandgap from the theoretical results are $[0 - 3,500]$ Hz and $[>9,500]$ Hz as presented above. It is observed that there are some slight discrepancies between the two approaches. This is because, as discussed above, the assumption of the infinite number of cells in the theoretical derivation of the meta-truss bar, while in the numerical model only a finite length of the meta-truss bar is modelled. Furthermore,

boundary reflections of the wave propagating in the finite length truss bar also affect the numerical results.

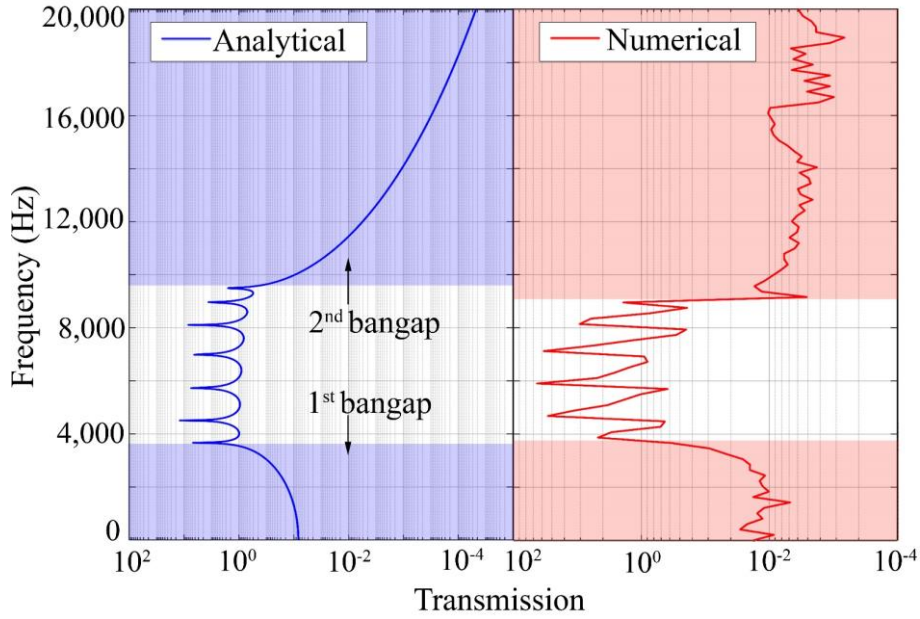


Figure 4-7. Analytical and numerical transmission coefficients of the meta-truss bar

To further validate the numerical simulation, a prescribed displacement with multi-frequency components [92] is excited at one end of the meta-truss bar (as shown in Figure 4-2b) to verify its frequency suppression capacity as follows:

$$u(t) = 10^{-4} \sum_{n=1}^3 \sin[2\pi f_n t] H(t) \quad (4-15)$$

where $H(t)$ is the unit step function and given as

$$H(t) = \begin{cases} 1, & t \geq 0 \\ 0, & t < 0 \end{cases} \quad (4-16)$$

and $f_n = [200; 1,000; 6,000]$ Hz, $n = 1, 2, 3$, respectively. The frequencies f_1 and f_2 are purposely chosen at low frequencies which are often in the frequency range of impact loading and also fall into the bandgap of the meta-truss bar while f_3 is within its passband as shown in Figure 4-7. The input and output signals are compared by the displacement-time histories and the FFT spectra, which are shown in Figures 4-8a and 4-8b, respectively. It is found that only the frequency of 6,000 Hz can travel through the meta-truss bar whereas the frequencies of 200 Hz and 1,000 Hz, which fall into its bandgap as shown in Figure 4-7 are completely suppressed. These results indicate the filtering capacity of the meta-truss bar with frequencies falling in its

bandgaps. In summary, by introducing meta-cores inside the hollow truss bar, frequency bandgaps can be generated to effectively filter out stress waves propagating through the meta-truss bar.

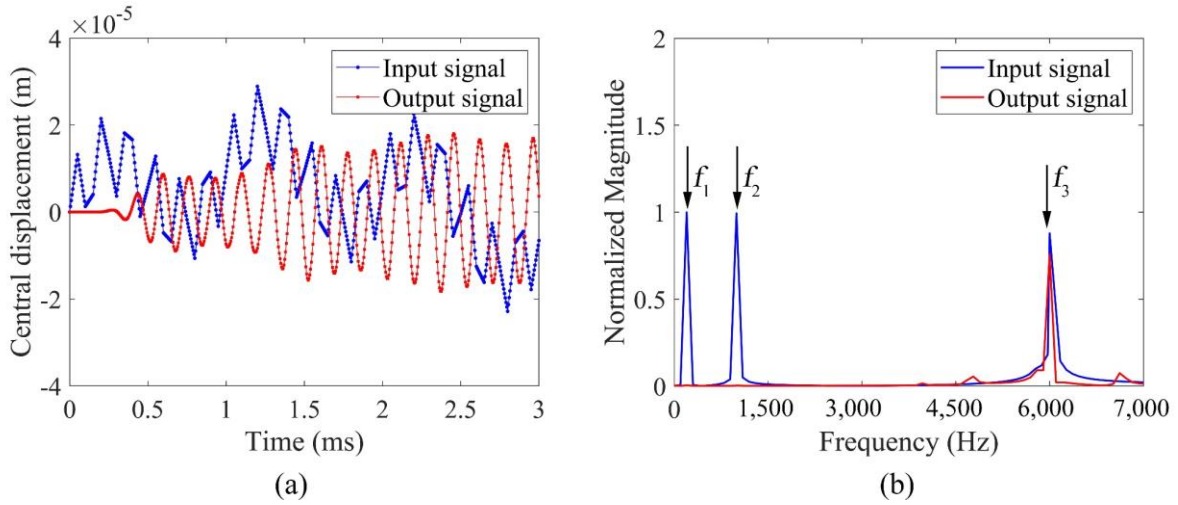


Figure 4-8. (a) Displacement-time histories and (b) FFT spectra at the center points of the meta-truss bar

4.4.4 Results and discussions

The numerical model of the meta-panel (shown in Figure 4-2) is developed by using the explicit finite element code LS-DYNA in this subsection to demonstrate its structural performance in withstanding impact loading. Two conventional panels comprising solid bars and hollow bars as respectively shown in Figures 4-9a and 4-9b are built for comparison. These panels are intentionally designed with the same geometric parameters as the meta-panel, and the only different component among them is the truss-cores connecting two facesheets. Specifically, the solid-truss bar, hollow-truss bar, and meta-truss bar have the same diameter. In this chapter, the main aim is to examine the dynamic behaviour of the meta-truss bar in attenuating the impact load, therefore, the truss bar size remains the same instead of making the same weight due to two reasons. Firstly, if the hollow truss bar thickness and/or diameter is tailored to have a similar mass as the solid bar, its size could be very large which also influences its deformation and hence energy absorption. Secondly, to maintain the same weight, the diameters of the solid truss and hollow truss bar have to be greater than the meta-truss bar due to the higher density of lead core than the aluminium core. This results in decreasing energy absorption of these panels. Therefore the same size of the three sacrificial panels is considered in the analysis in this chapter. The structural responses including the central displacement of the facesheets, the reaction force-time history, and energy absorption are evaluated among these three panels to

validate the effectiveness of the meta-panel in mitigating the impact loading effects, which is described in Section 4.4.1.3.

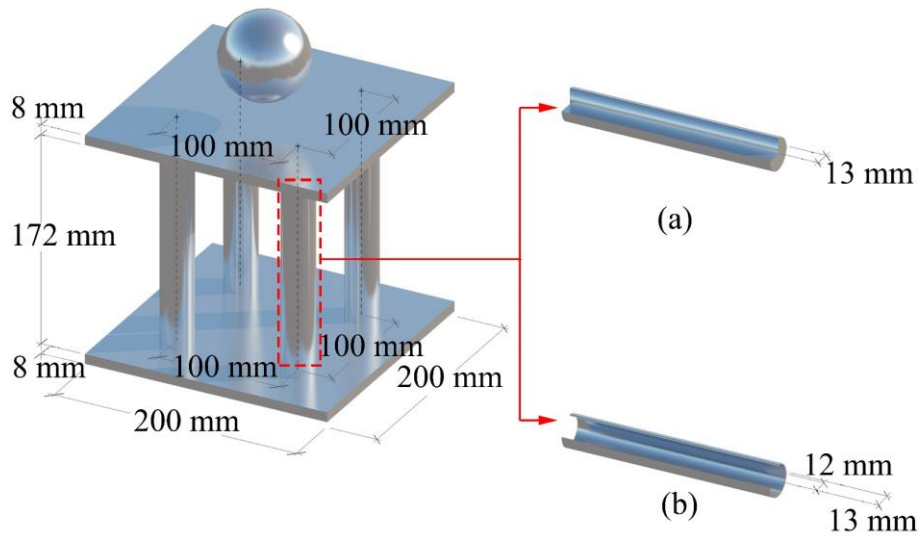
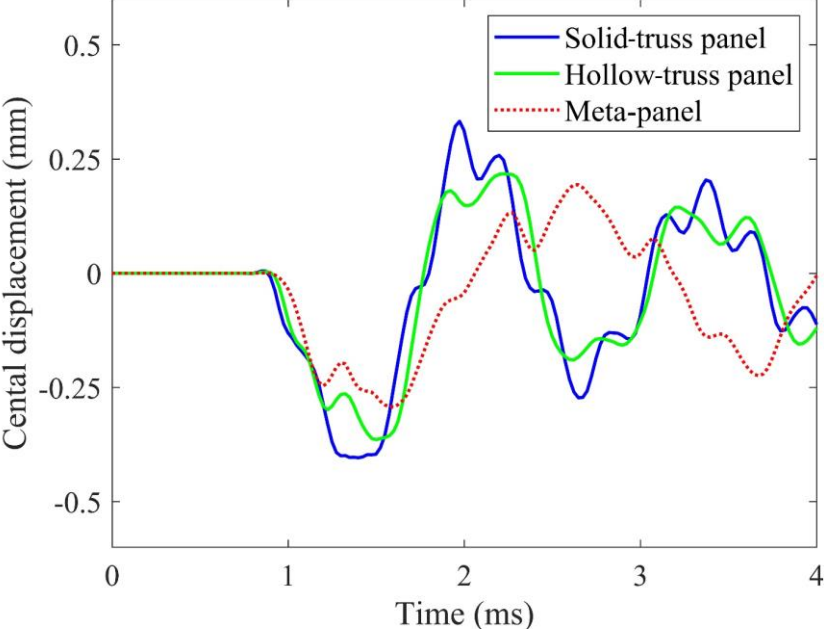


Figure 4-9. Schematic diagram of panels comprising of (a) solid-truss bar and (b) hollow-truss bar

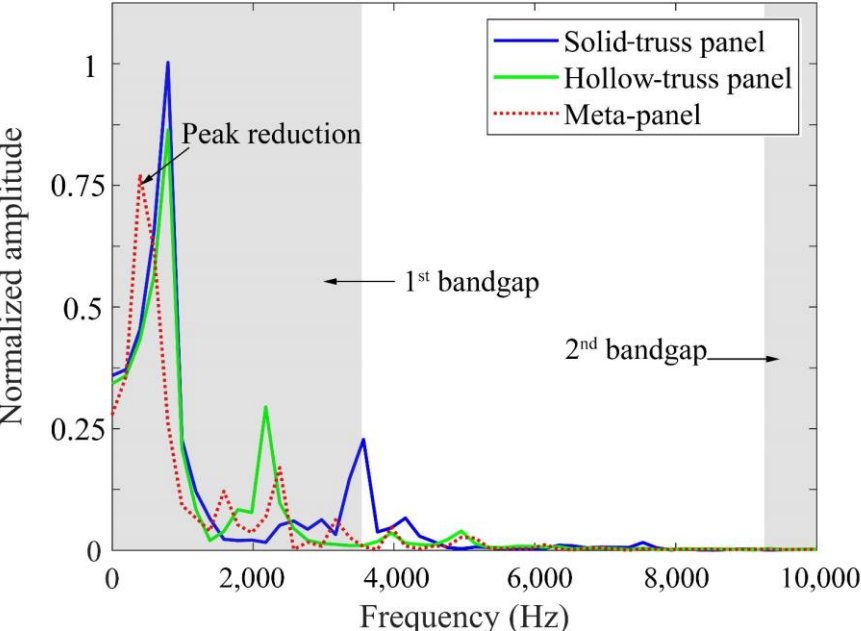
4.4.4.1 Deformation analysis

Figure 4-10a shows the displacement of the back facesheet of the panels with solid-truss bars, hollow-truss bars, and meta-truss bars, respectively while their displacement contours are illustrated in Figure 4-44. As shown, the maximum displacement of the meta-panel is 0.31 mm, which is 20% and 33% lower than those of the panel with hollow-truss bars and solid-truss bars, respectively. This is because the vibration of meta-cores, which generates bandgaps and filters the incident waves within its bandgaps, results in lower impulse transferring to the back facesheet of the panel. The FFT spectrum of displacement response of the three panels is illustrated in Figure 4-10b. For the meta-panel, a reduction of the peak amplitude of the central displacement occurs in the 1st bandgap around 0 – 3,500 Hz, which well agrees with the prediction in Section 3. However, as can be noted, unlike those shown in Figure 4-8, only partial incident wave is mitigated within the bandgap, i.e., wave energy is still transmitted in the bandgap of the meta-panel although some reductions are observed as compared to the other two reference panels. This is because only a portion of the incident wave propagates through the meta-core and thus is mitigated while other portions of wave energy travel through the outer tube of the truss bars. In the above section 4.4.3, the incident displacement is only applied to the core so that it is completely filtered within the bandgap while in the meta-panel, it is a combination of three components, i.e, the facesheets, the outer tubes, and the meta-cores and

only the meta-core has bandgaps to filter out wave energy. In general, the meta-panel has a smaller deformation compared to its conventional counterparts, indicating its effectiveness in mitigating the impact loading effect for structure protection.



(a)



(b)

Figure 4-10. Displacements of the back facesheet (a) time histories, (b) frequency spectra

Displacement (mm)

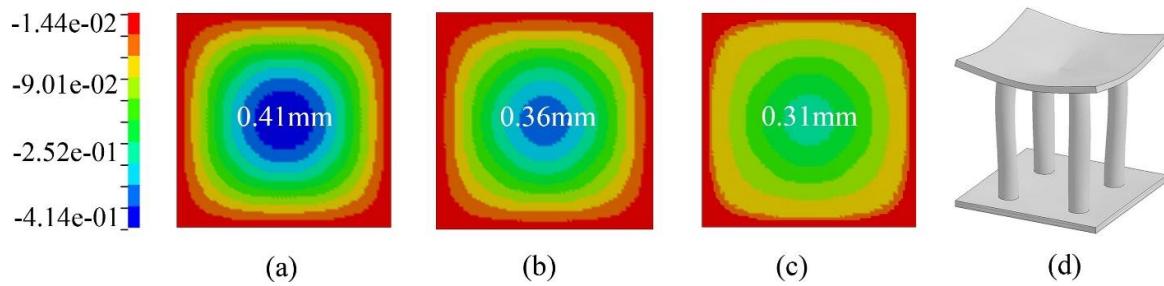


Figure 4-11. Displacement contour of the back facesheets (a) solid-truss panel, (b) hollow-truss panel, (c) meta-panel, and (d) deformation pattern of the meta-panel

4.4.4.2 Energy absorption characteristics

To obtain an inclusive comprehension of its impact mitigation, analysis on the energy absorption capacity of the meta-panel subjected to impact loads is conducted. Figure 4-12a shows the total energy while Figures 4-12b and 4-12c exhibit the kinetic energy, and the internal energy absorbed by each constituent of the meta-panel under impact loads, respectively. As shown, due to the existence of the soft coating, there is a relative movement between the lead cores and the aluminium tube which absorbs a significant amount of energy. This movement is observed because when the energy absorption by the coating and the core increases to a peak value, the energy in the outer tubes is at its minimum. This effect is very obvious at a late stage when t is larger than about 1.5 ms as shown in the figure. At the beginning of the impact, the energy absorbed by the core is relatively small since it takes time for the cores to be activated. The obtained findings reveal the damage mitigation effect to the outer tube by the impact load due to the local vibrations of the meta-cores which absorb energy. As shown, the hollow tube deformation contributes significantly to the internal energy of the meta-panel, while the motions of the meta-cores result in a significant amount of kinetic energy and partially to the small internal energy through the elastic deformation of the coatings. It is worth mentioning that the initial energy of the impactor is 4.5 J and entirely in the kinetic form before the impact with the velocity of 3 m/s. At 1.2 ms when the velocity of the impactor equals 0, it changes direction, implying the deformation of the meta-panel at the maximum value and the impactor starts to rebound. After the impact at around 1.5 ms, the velocity of the impactor slightly reduces but the change is very small due to the extremely short duration of the impact event so that the residual velocity looks constant. In general, these findings indicate that the meta-panel utilizes a coupled mechanism of energy absorption by combining the local resonance of the meta-cores and deformation of the outer hollow tubes, leading to a high energy absorption capacity.

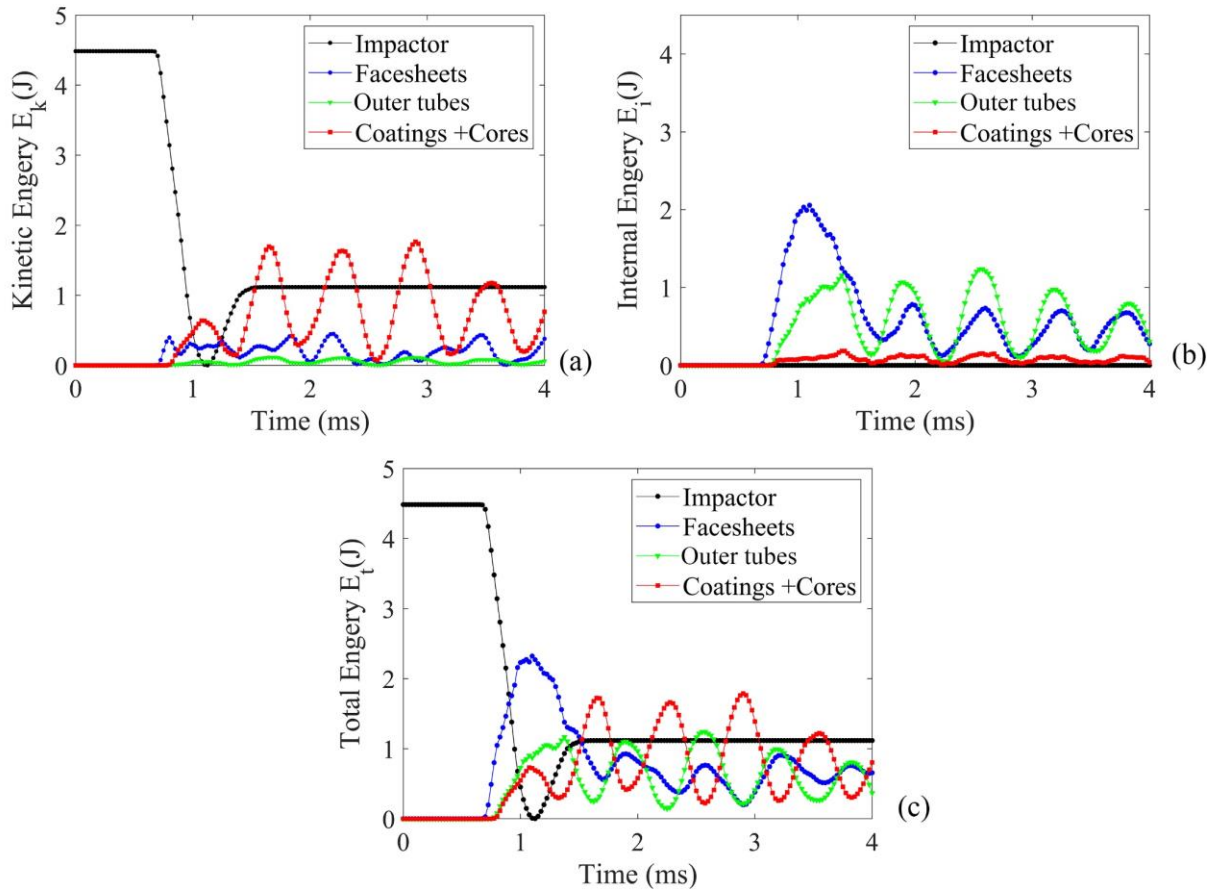


Figure 4-12. (a) kinetic energy, and (b) internal energy, and (c) total energy of meta-panels

Figure 4-13 depicts the total energy absorption of the three panels and each constituent in these panels to evaluate the effectiveness of the meta-panel. As shown, the total energy absorption of the meta-panel is the highest among these considered panels, indicating that the meta-panel has more advantages in terms of energy absorption capacity. This is because the meta-panel absorbs energy through the outer tubes and the facesheets deformation, combined with the local resonant of the lead cores while both the reference panels absorb energy only through plastic deformation of the truss bars and the facesheets. Conversely, the energy absorbed by the hollow truss bars is the largest compared to other panels, implying its largest plastic deformation. It is worth mentioning that although the total energy absorption of the meta-panel is higher than the reference panels, the energy absorbed by the facesheets is the smallest, indicating less damage to facesheets and outer tubes. Therefore, the thickness of the facesheets and the outer tubes of the meta-panel could be reduced to absorb the same amount of energy compared to the referenced panels, meaning less material consumption on the facesheets and the outer tubes of the meta-panel. The above findings further exhibit the superiority of the meta-panel in impact resistance.

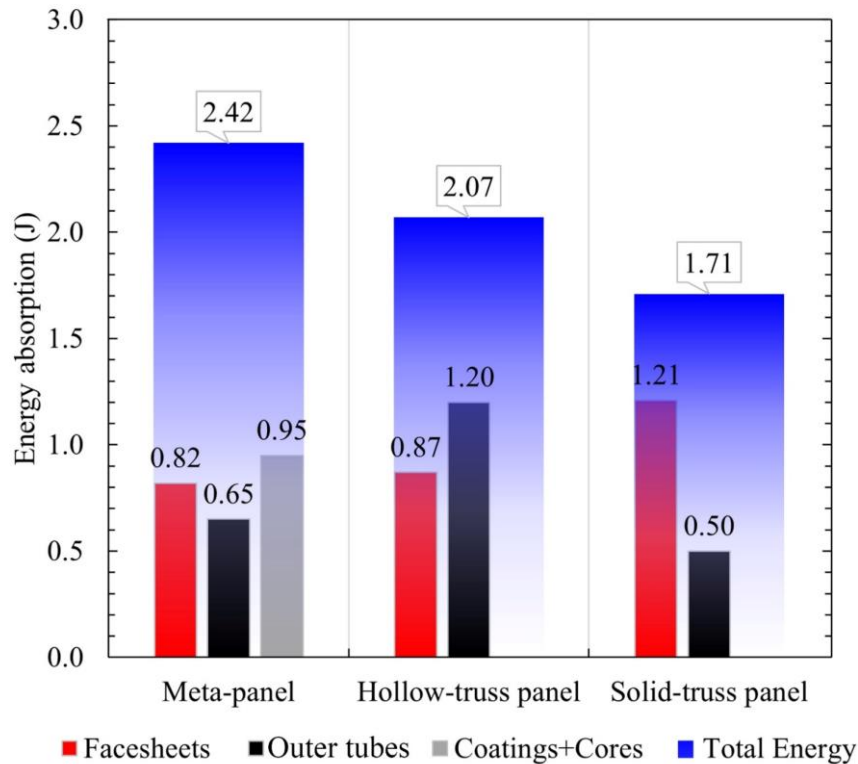


Figure 4-13. Energy absorption of the three panels

4.4.4.3 Reaction force and Von Mises stress response

The objective of utilizing sacrificial cladding is to mitigate the impact load and reduce the transmitted force to the protected structures. The transmitted force-time history is obtained from the numerical simulation by plotting the reaction force exerted on the base of the structure. The cumulative reaction force around the boundary of the back facesheet is set as a main criterion for the evaluation and is taken as the sum of nodal forces distributed around the boundary. As shown in Figure 4-14a, the peak value of reaction force to the base structure from the meta-panel is respectively 46.7% and 33.4% less than the corresponding of other panels with hollow truss and solid truss, indicating its effectiveness in reducing the transmitted force to the base structure under impact loads. It can be attributed to the fact that the movements of the resonator and the soft coating generate the bandgap which can filter out the stress from the impact load, resulting in a reduction in stress transmission from the impact load to the back facesheet and then the supports. Furthermore, spectrum analysis of reaction forces in the frequency domain of the three panels is illustrated in Figure 4-14b. As shown, a clear reduction of the peak amplitude of the reaction force of the meta-panel is observed in the 1st bandgap of 0 – 3,500 Hz, but the reaction force in this frequency band is not completely suppressed because the outer tube of the truss bars can transmit a certain amount of impact load as discussed above. Overall,

the meta-panel outperforms the other two reference cladding panels by yielding a smaller reaction force which demonstrates its superiority over the two reference panels.

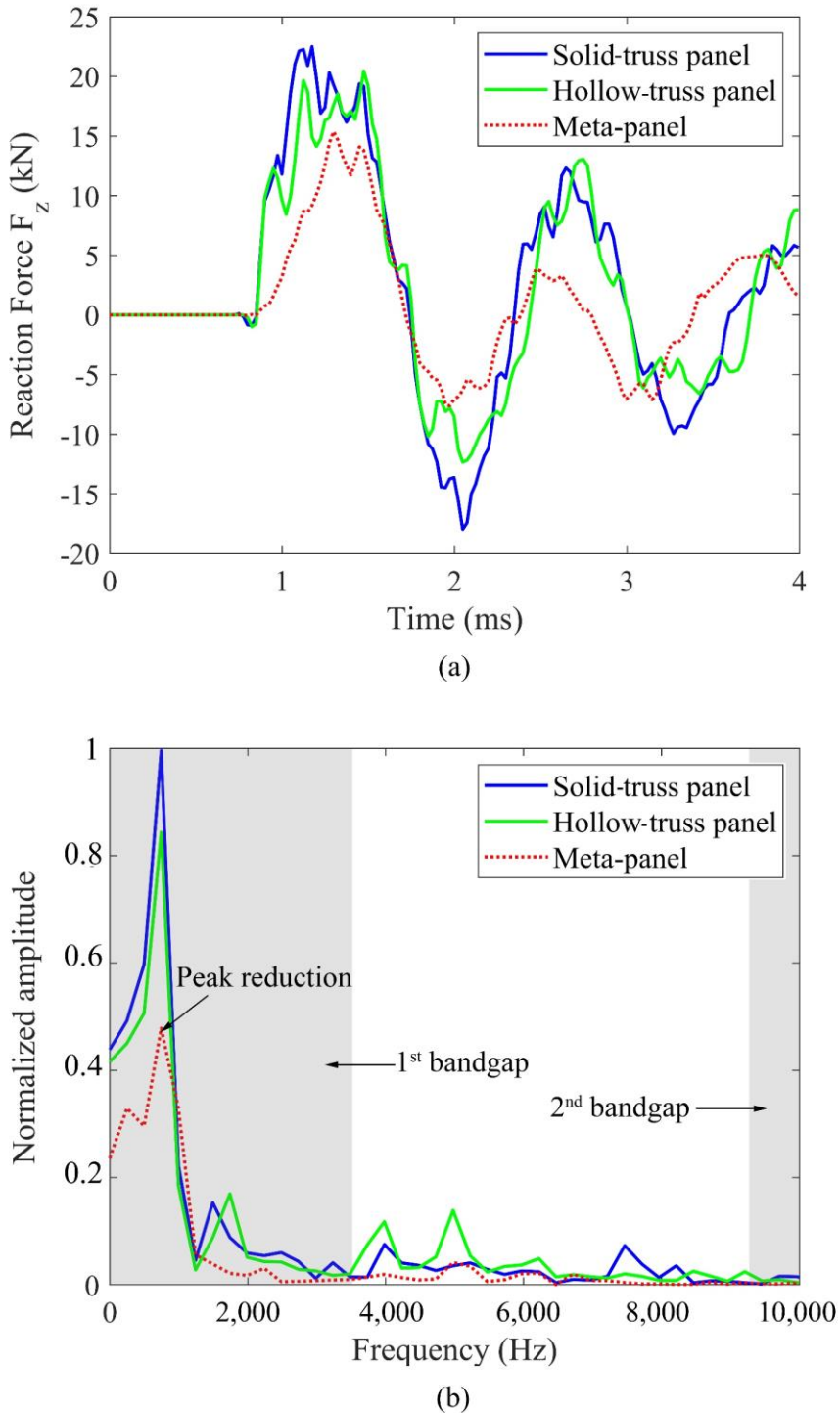


Figure 4-14. Reaction force of the three panels (a) time histories, (b) frequency spectra

To obtain a better realization of the working mechanism, the von Mises stress distribution occurring at the back facesheet is also used. The stress contours at back facesheets of all considered panels are shown in Figure 4-15. It is clear from the figure, the stress distribution is

similar for all the panels, and stress is concentrated at the connections between the cores and the facesheets. The results also show that the back facesheet of the meta-panel experiences the smallest von Mises stresses among the considered panels, followed by the hollow truss panel solid-truss panels, respectively. This means that the stresses transferred to the back facesheets are effectively mitigated by the meta-cores, implying the superior performance of the meta-panel in terms of the stress wave mitigation capability.

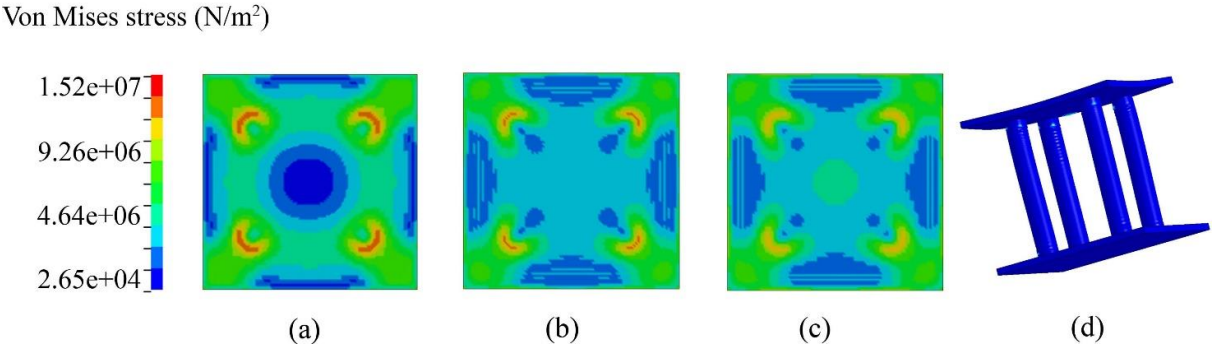


Figure 4-15. Von Mises stress contours at the back facesheets of (a) solid-truss panel, (b) hollow-truss panel, (c) meta-panel, and (d) plastic deformation of the meta-panel

4.4.5 Parametric studies

In this section, the effects of the crucial factors, e.g., the outer tube thickness, meta-core properties, and impact velocity on its transient responses under impact loading are studied. The meta-panels with various investigated parameters are modelled. Under impact loading, the optimal design is expected to enhance as compared to other designs, because of the broader bandgap created that covers larger regions of the targeted frequency band with most impact energy. For comparison, the dynamic responses of different designs of meta-panel are numerically evaluated.

4.4.5.1 Effect of the outer tube thickness

To examine the influence of the thickness of the outer tube in the meta-panel, four different outer tube thicknesses, i.e. 4 mm, 3 mm, 2 mm, and 1 mm, with the same inner diameter of 24 mm (Figure 4-16) are considered. While the truss thickness is varied, other dimensions of the meta-panel and the impactor (Section 4.4.1.3) are kept the same in this investigation.

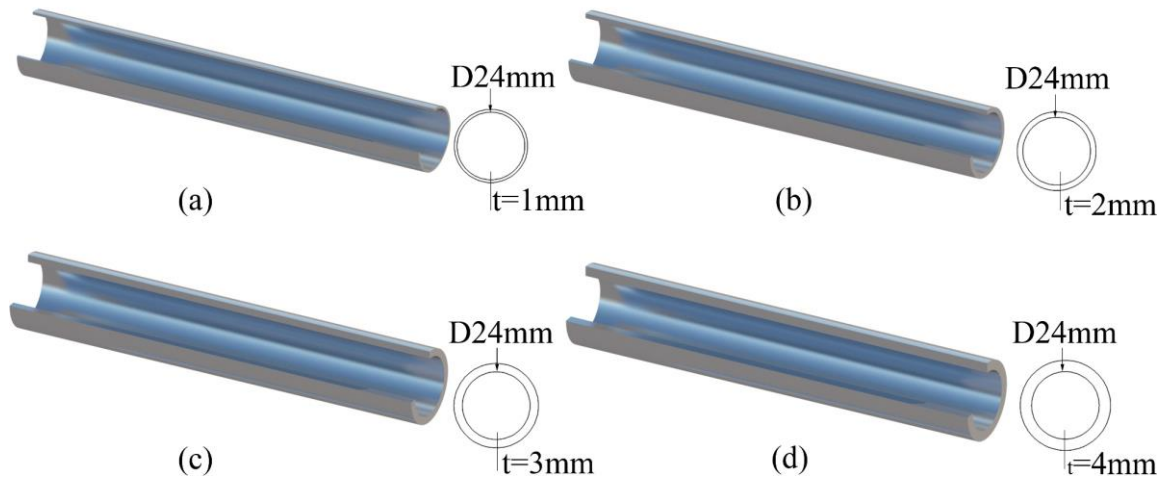


Figure 4-16. Schematic diagram of various thickness configurations of the outer tube of meta-truss bar

Figures 4-17a and 4-17e show the comparison of the back and front facesheet deflection of meta-panel with varying truss thicknesses, respectively. As expected, there is a slight decrease in the central deflection of the front facesheet while that of the back facesheet increases with the increased thickness of the outer tube. This is because the ratio of stress propagating through the outer tube and the meta-core in the meta-truss bar critically relies on the ratios of the cross-sectional area and stiffness. Increasing the thickness of the outer tube leads to less stress waves from the impact load propagating through the meta-core, implying less efficiency of the meta-panel. A significant reduction in the displacement of the back facesheet by decreasing the truss tube thickness proves its impact mitigating effect. As observed in Figures 4-17c and 4-17f the reaction force increases with the thickness of the outer tube increasing from 1 mm to 4 mm while there is a substantial reduction of the total energy absorption, accordingly. This is attributed to the fact that the less deflection of the facesheets and deformation of the outer tube, indicating less energy absorption through their plastic deformations as well as fewer stress waves passing through the meta-core, meaning less conversion of impact energy to the kinetic energy of the meta-core. The FFT spectrum of displacement and reaction force of the three panels are illustrated in Figures 4-17b and 4-17d. For the meta-panel, a reduction of the peak amplitude of the central displacement and reaction force occurs in the 1st bandgap at approximately 0 – 3,500 Hz, which well agrees with the prediction in Section 4.3. In summary, the reaction force, which is a critical criterion in designing sacrificial claddings, is significantly affected by the truss thickness and it is suggested to utilize a thin outer tube in practice. Therefore, the recommended configuration of the meta-panel should possess a relatively thin outer tube to fully leverage its protective performance as a sacrificial cladding.

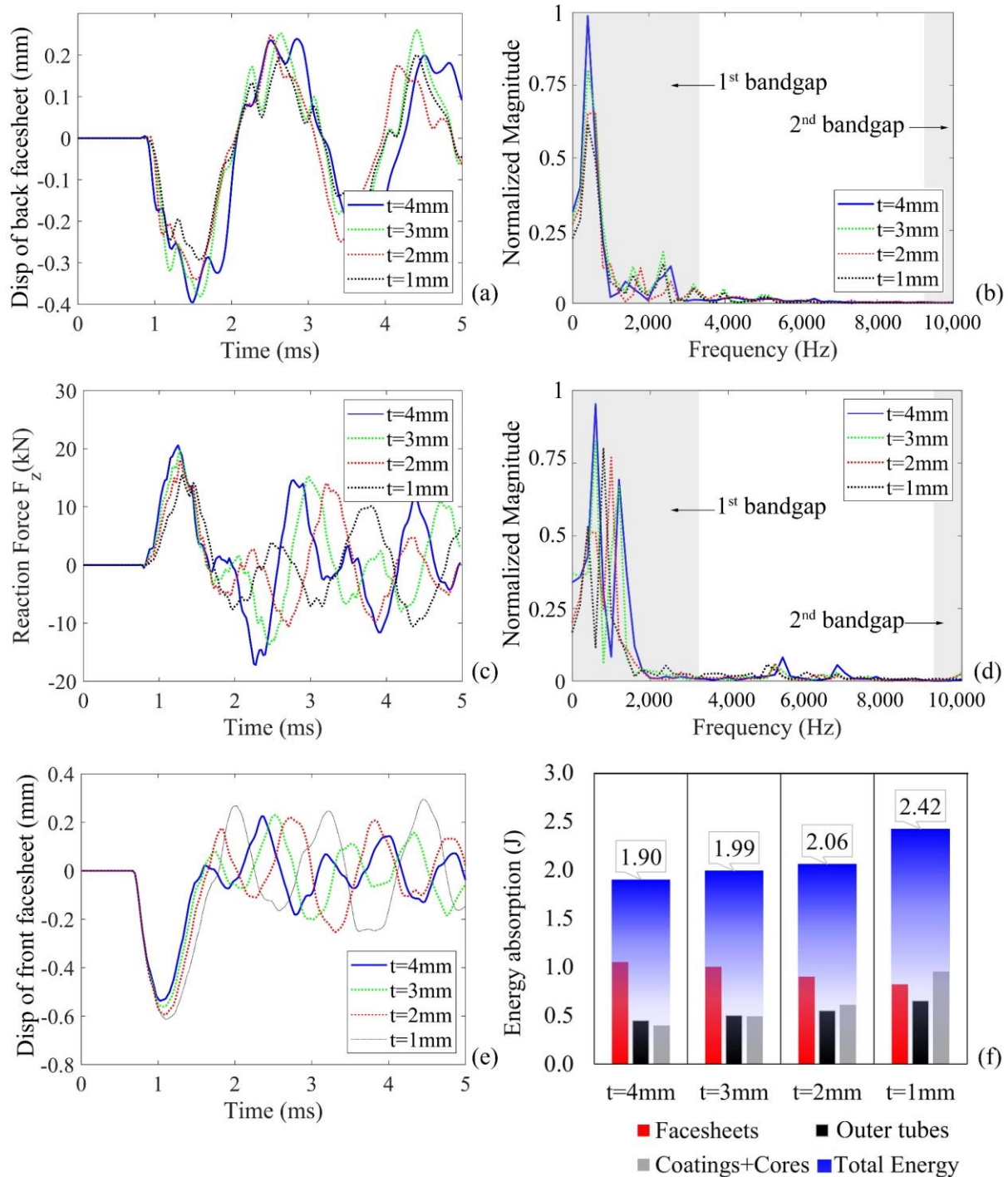


Figure 4-17. Effects of the outer tube thickness (a-b) displacement of back facesheet in time histories and FFT spectra, (c-d) reaction force in time histories and FFT spectra, and (e-f) displacement of front facesheet and energy absorption

4.4.5.2 Effects of meta-core properties

The influence of the meta-core properties including coating modulus (E_c) and core density (ρ_c) on the dynamic responses of the meta-panel under impact loads are examined in this section.

The geometry of the panel and the impactor used in this section is the same as in Section 4.2 and Section 4.4.1.3.

4.4.5.2.1 Effect of coating modulus (E_c)

To investigate the effect of the stiffness of the soft coating on the impact mitigating behaviour of the meta-panel, the coating modulus of $E_{c1} = 1.47 \times 10^1$ MPa, $E_{c2} = 1.47 \times 10^2$ MPa, $E_{c3} = 1.47 \times 10^3$ MPa are considered, which represent very soft, medium, and hard polyurethane materials [84]. In this section, only the soft coating modulus of the meta-core is changed while all other parameters are kept the same as defined in Section 4.2.

The displacement and velocity-time histories of core 1 with different Young's modulus of the coating are respectively shown in Figures 4-18a and 4-18c while their corresponding dominant frequencies are depicted in Figures 4-18b and 4-18d. It is observed that the smaller the coating modulus, the larger displacement of the lead core would be. It is because the role of the soft coating in the meta-core is to allow relative movement of the lead core, accordingly, it would be easier to vibrate in the softer coating. Figure 4-20f depicts the energy absorption of each constituent in the meta-panel corresponding to the three elastic moduli of the soft coating. It is seen that the lead core has the highest energy absorption when $E_{c2} = 1.47 \times 10^2$ MPa although the displacement of core 1 with $E_{c1} = 1.47 \times 10^1$ MPa is the largest among all considered cases. This is attributed to the fact that with the very soft coating, the energy transmitted to the core is small even though the movements of the cores are ample but their vibrations are more slowly compared to the case with medium elastic modulus. On the other hand, with the very hard coating, i.e., $E_{c3} = 1.47 \times 10^3$ MPa, the core is difficult to vibrate and the displacement of core 1 is relatively small, leading to small energy absorption by the meta-core.

Hence, to obtain the optimal performance of the meta-core of the meta-panel in mitigating impact loading, it is necessary to carry out a proper analysis to determine the optimal elastic modulus of the soft coating. The best performing soft coating in this chapter is a polyurethane (PU) with an elastic modulus of 1.47×10^2 MPa. This result is consistent with other meta-related structures such as meta-concrete [84].

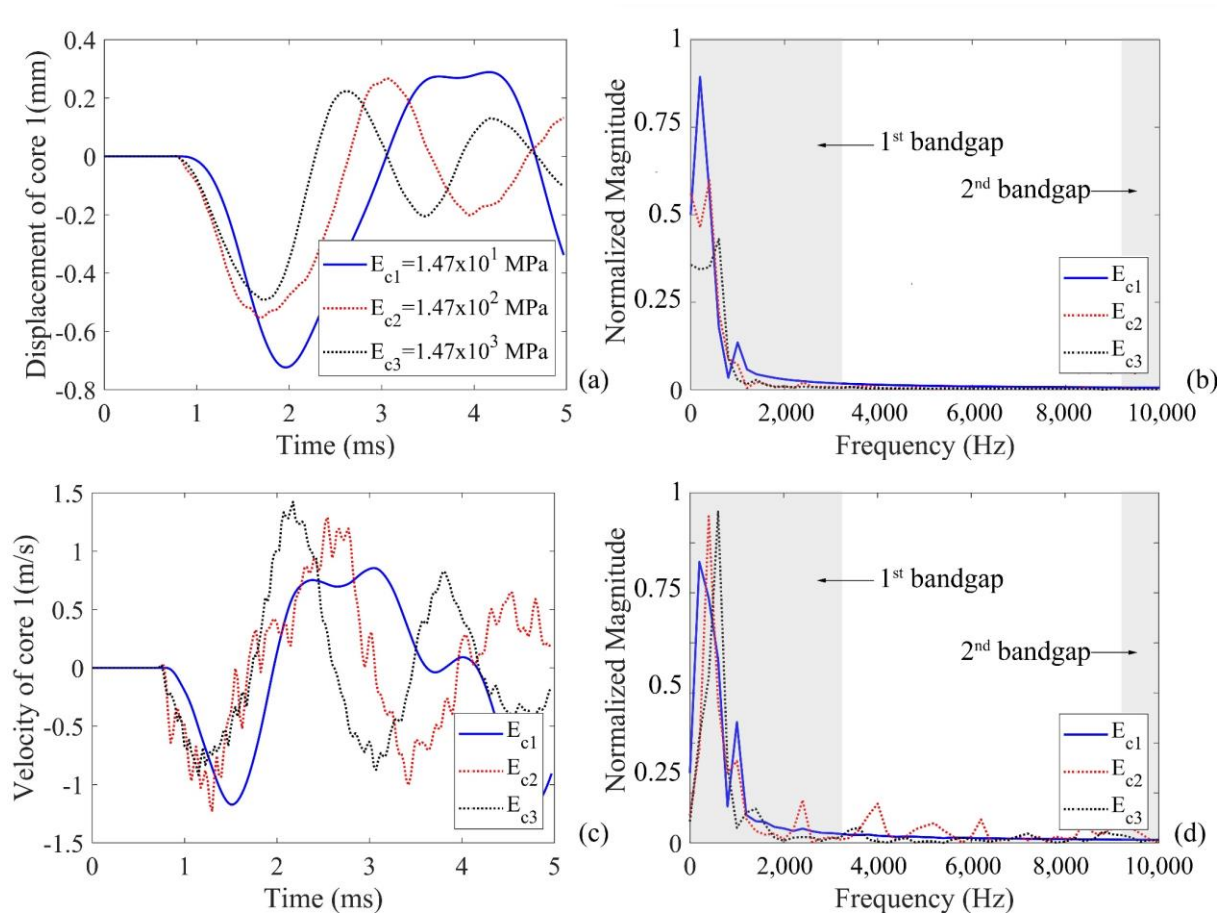


Figure 4-18. Dynamic responses of core 1 (a-b) displacement of core 1 in time histories and FFT spectra, and (c-d) velocity of core 1 in time histories and FFT spectra

When changing the coating elastic modulus, the displacement of the front facesheet of the meta-panel is the same initially but becomes different subsequently as shown in Figure 4-19e. This is because the stress waves induced by the impact loading propagate orderly from the front facesheet to the back facesheet. Irrespective of the coating modulus, the front facesheet always resists the impact loading firstly, therefore, its displacement is not affected by the coating modulus of the meta-truss bars. Nonetheless, the front facesheet displacement becomes different after the first peak response because changing the coating stiffness is equivalent to changing the supporting stiffness of the front facesheet, and the supporting stiffness influence vibration responses of the facesheet. As shown in Figures 4-19a and 4-19c, the smallest displacement at the back facesheet and the reaction force is observed when the coating elastic modulus is medium while the very soft and very hard coating is less effective in mitigating the stress wave propagation from the impact loading. The FFT analysis of displacement and reaction force response shown in Figures 4-20b and 4-20d indicates a reduction of the peak amplitude of the central displacement and reaction force that occurs in the predicted bandgap.

These results, again, indicate that a properly selected elastic modulus of the meta-panel is necessary to achieve its optimal performance in mitigating the impact loading effect.

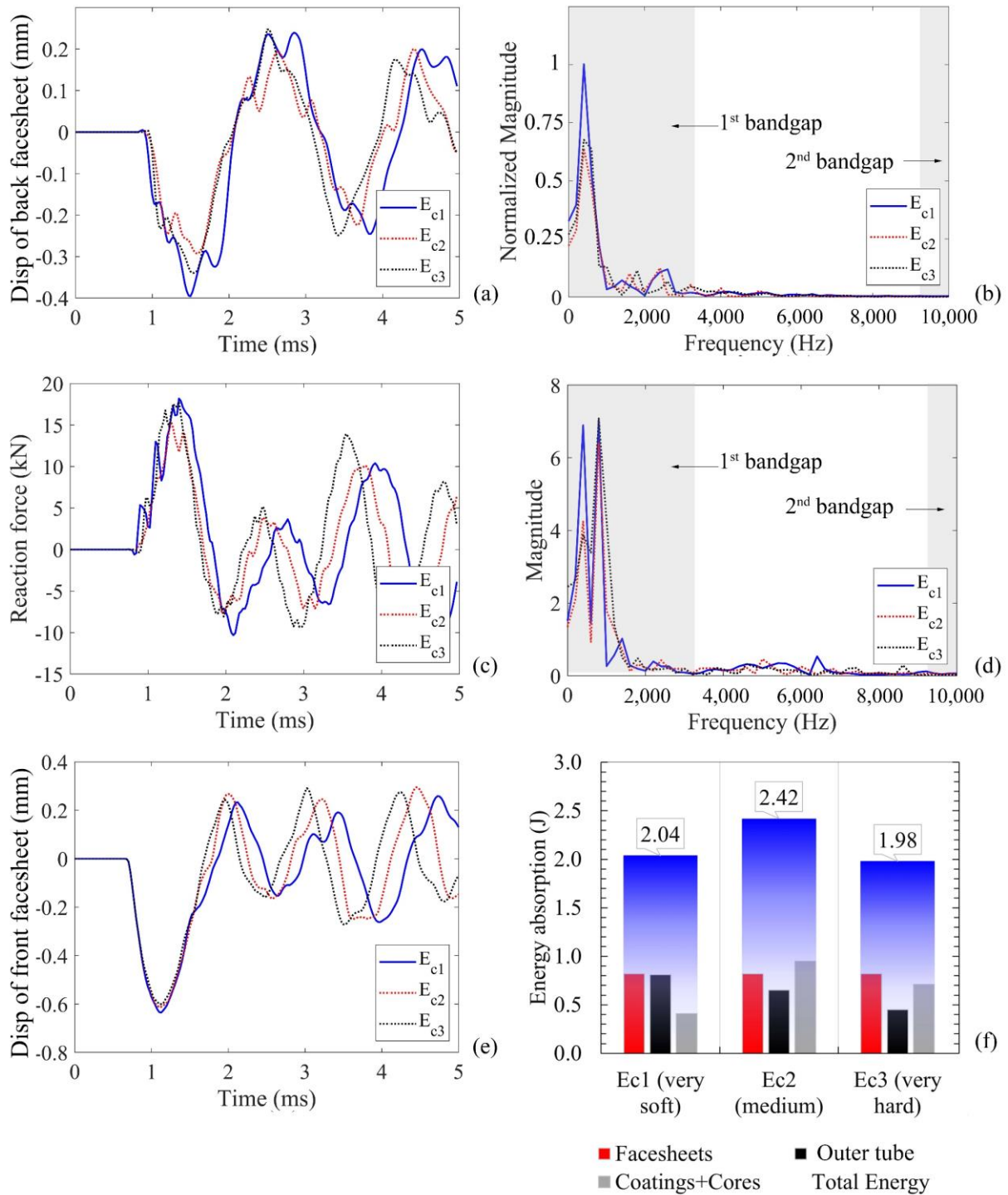


Figure 4-19. Effects of the coating modulus (a-b) displacement of back facesheet in time histories and FFT spectra, (c-d) reaction force in time histories and FFT spectra, and (e-f) displacement of front facesheet and energy absorption

4.4.5.2.2 Effect of core density (ρ_c)

To investigate the influence of the core density on the performance of the meta-panel, three core material densities, i.e., $\rho_{c1}=11,400 \text{ kg/m}^3$, $\rho_{c2}=7,850 \text{ kg/m}^3$, and $\rho_{c3}=2,770 \text{ kg/m}^3$, which correspond to lead, steel, and aluminium, respectively, are considered herein. Other parameters such as the geometries of the panel and the impactor used in the model are the same as those defined above.

Figure 4-20 depicts the transmission coefficient of the meta-truss bar when the core densities are different. As shown, the region of the passband which is the range of frequency where the stress wave can propagate through becomes wider with the decreasing core density. In other words, the heavier the density of the core is, the narrower passband the meta-truss bar would have, implying the more effective of the meta-panel. For instance, the passband width changes from [3,500 - 9,500] Hz to [7,500 - 19,000] Hz by changing ρ_{c1} to ρ_{c3} , while the frequency passband of the case ρ_{c2} is [4,600 - 12,000] Hz. The reason causing changes in the passband range is that increasing the core density increases the mass of the core, resulting in a decrease in the upper bound frequency of the 1st bandgap and an increase in the lower bound frequency of the 2nd bandgap, which leads to a narrower passband width. Therefore, it can be concluded that the passband of the meta-truss bar is sensitive to the variation of the core density and it decreases with the rising core density when the core size and the coating are unchanged.

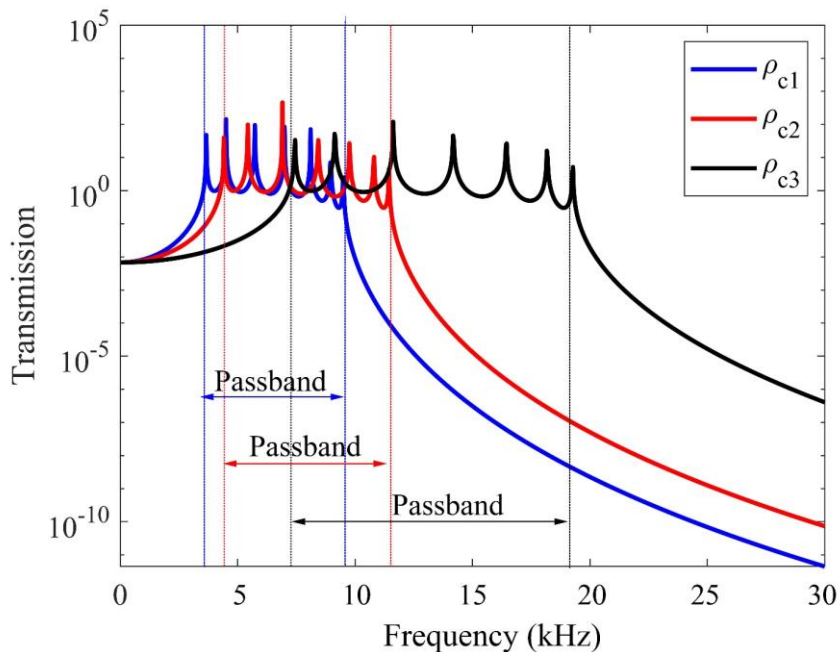


Figure 4-20. Transmission coefficients of the meta-truss bar with different core densities

However, it is observed from Table 4-4 that the transient responses of the meta-panel are not prominently affected by the considered core densities. It is because although there is an increase in the bandgaps of the meta-core when increasing the core density, the dominant frequency of the impact loading as described in Figure 4-5 ranging from [0 - 3,000] Hz falls in the 1st bandgap of all the considered cases. In general, increasing the core density results in a narrower 1st bandgap but a broader total region of the bandgap range of the meta-core while it has a limited effect on the transient performances of the meta-panel within the studied range of impact loading.

Table 4-4. Effect of core density on displacements, reaction force, and energy absorptions

Core density	Displacement (mm)		Reaction force (kN)		Energy absorption (J)		
	Front	Back	F_z	Facesheets	Outer tubes	Coating + Core	Total
	facesheet	facesheet					
ρ_{c1}	0.61	0.32	15.0	0.82	0.65	0.95	2.42
ρ_{c2}	0.61	0.33	15.3	0.82	0.65	0.91	2.38
ρ_{c3}	0.61	0.34	15.4	0.82	0.65	0.87	2.34

4.4.5.3 Effect of impact velocity

As reported in previous studies [140, 141], the impact velocity has a significant influence on the performance of the sandwich panels. In this chapter, the impact is performed by an impactor having the same mass but different velocities resulting in different impact energies. Four impact scenarios with various velocities but the same mass are considered. The range of impact energy levels is attained by utilizing four different impact velocities, i.e. $v_1=1$ m/s, $v_2=5$ m/s, $v_3=20$ m/s, and $v_4=30$ m/s with a constant impactor mass of 0.5 kg. As shown in Figure 4-21a, increasing impact velocity results in a higher impact force peak, but has limited influence on the duration of the impact loadings [142]. It should be noted that although the dominant frequencies of the impact forces of the considered examples are still in the 1st bandgap of [0 - 3,000] Hz, increasing impact velocity results in more impact force energies in the higher frequency range that fall into the passband of the meta-panel. The impact energy in the bandgaps of the investigated meta-truss bar is determined by the shaded area (A_{bandgap}) as shown in Figure 4-21b. Besides, Table 4-6 gives the impact energy percentage corresponding to each bandgap which is estimated by the ratio between the energy in each bandgap and the total impact energy (A_{total}). Lower velocities lead to more percentage of energy in the bandgaps, i.e.,

100.0%, 80.9%, 75.5%, and 70.2% respectively for the loadings v_1 to v_4 , indicating the meta-panel is less effective in alleviating the impact load-induced from the high velocity.

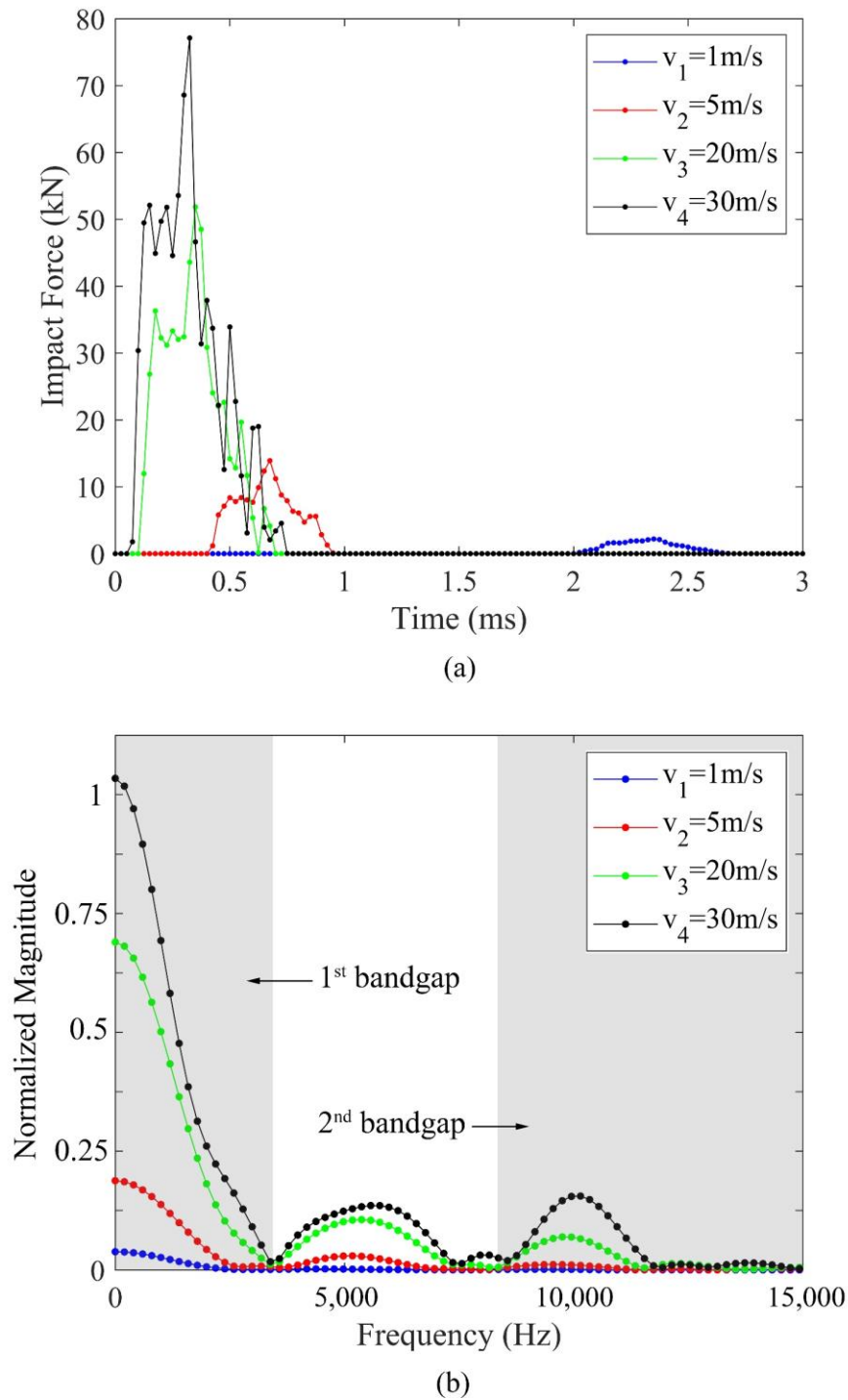


Figure 4-21. Impact loading with various velocities, (a) time-histories, and (b) FFT

The structural responses of the meta-panel under impact loads with various velocities are given in Table 4-6 while Figure 4-22 depicts the deformation contour of the meta-panel with various velocities. As shown, transient behaviour of the meta-panel depend on the impact loading

impulse and the frequency band structure. Specifically, rising the loading impulse leads to the increase of the facesheet displacements, the energy absorption, and the reaction forces of the meta-panel. The case with velocity v_1 corresponds to the highest proportion of impact energy being absorbed by the coating and the core at 37.1% of the total energy as shown in Table 4-5, followed by 34.6%, 30.9%, and 28.7% respectively for the impact case with velocity v_2 , v_3 , and v_4 even though there is an increase in the total energy absorbed owing to the increased impact energy from v_1 to v_4 . This is attributed to the decrease in the proportion of the impact energy from case v_1 to case v_4 falling in the bandgap, indicating the more percentage of the impact loading falling in the bandgaps, the more effective of the meta-panels in impact mitigation.

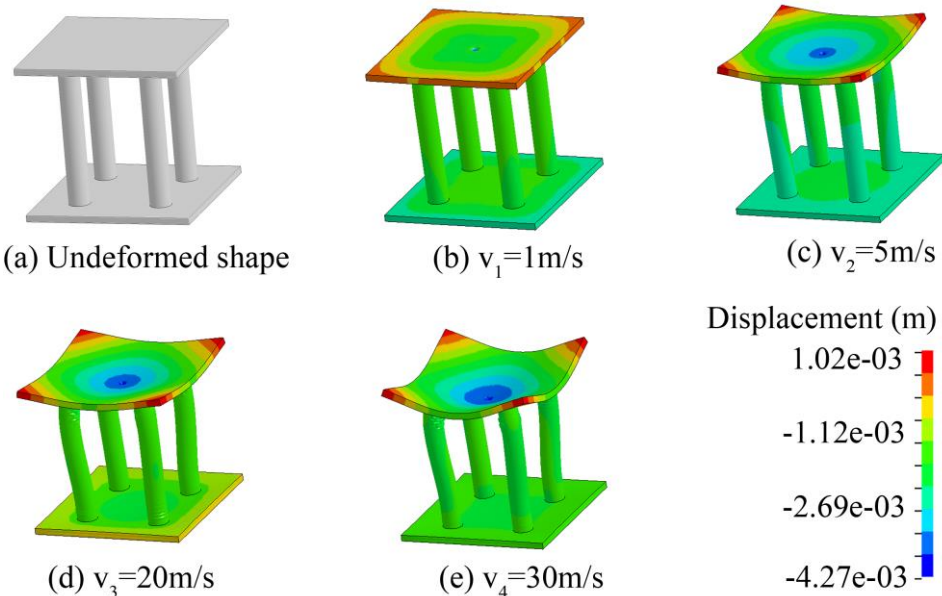


Figure 4-22. Undeformed and deformed contour of the meta-panel under various impact velocities

Table 4-5. Proportion of impact energy with various velocities in the bandgaps

Impact velocity	1 st bandgap		2 nd bandgap		Total %
	$\frac{A_{\text{bandgap}}}{A_{\text{total}}}$	%	$\frac{A_{\text{bandgap}}}{A_{\text{total}}}$	%	
v_1	$\frac{502,861}{502,861}$	100.0%	$\frac{0}{502,861}$	0.0%	100.0%
v_2	$\frac{2,232,767}{3,109,261}$	71.8%	$\frac{283,731}{3,109,261}$	9.1%	80.9%
v_3	$\frac{8,004,936}{12,410,755}$	64.5%	$\frac{1,373,717}{12,410,755}$	11.0%	75.5%
v_4	$\frac{10,410,843}{19,118,717}$	54.4%	$\frac{3,026,258}{19,118,717}$	15.8%	70.2%

Table 4-6. Effect of impact velocities on the transient response of the meta-panels

Impact velocity	Displacement (mm)		Reaction force (kN)	Energy absorption (J)			
	Front facesheet	Back facesheet	F_z	Face-sheets	Outer tubes	Coating + Core	Total
v_1	0.14	0.11	3.0	0.046	0.030	0.045	0.121
v_2	0.67	0.34	17.5	1.210	0.830	1.080	3.120
v_3	2.61	1.33	64.4	18.38	10.90	13.15	42.43
v_4	4.01	1.86	84.8	30.48	23.69	21.81	75.98

4.5. Concluding remarks

In this chapter, the transient responses of the sandwich panel with the meta-truss core leveraging the coupled mechanisms of plastic deformation and local resonance are investigated and compared with the conventional panels with solid truss and hollow truss core. The influence of key parameters on its mitigating effectiveness under impact loads is investigated using validated numerical models. Through these investigations, the following conclusions can be drawn:

1. Compared with the solid-truss and hollow-truss panels, the meta-panel exhibits excellent impact-resistant performances. Specifically, there are considerable decreases in the peak displacement of the back facesheet (33%) and the reaction force (up to 47%) of the meta-panel compared to the traditional panels subjected to the same impact load.
2. Utilizing a fairly thin outer tube can lead to enhanced dynamic responses of the meta-panel. The effectiveness of the meta-panel is highly sensitive to the modulus of the soft coating. The properly selected coating can lead to better energy absorption capability of the meta-panel. Also, increasing the core density can lead to a broader bandgap region of the meta-core.
3. The impact velocity significantly affects the performance of the meta-panel because it changes the primary frequency band of impact energy distribution. Increasing impact velocity results in a higher impact force peak and more impact energy distribution in the higher frequency range. The meta-panel is the most effective in mitigating the impact loading effect when the primary frequencies of impact energy fall into the bandgap of the meta-panel.

In general, the results from this chapter demonstrate that the meta-panel can be more effective for structure protections than the conventional claddings with hollow and solid truss cores. It

has a great potential to be deployed in protective structures or energy absorbers. However, further investigations need to be carried out to study the effects of possible debonding between the soft coating and the metals, core materials, different core materials, core shapes, and coating materials on the performances of the meta-panel subjected to impact loading of different characteristics, and also to carry out laboratory and/or field tests to experimentally verify the performances of the meta-panels.

CHAPTER 5. BLAST RESISTANT ENHANCEMENT OF META-PANELS USING MULTIPLE TYPES OF RESONATORS

Abstract⁴

A new design is proposed for the meta-panel that consists of three components including two thin facesheets bonded to meta-truss cores to enhance its blast resistance and energy absorption capacity. The meta-truss core comprising solid inclusions with coated soft layers exhibits exceptional wave-filtering properties by activating the local vibration of the inclusions, leading to the negative effective mass and stiffness of the meta-truss core in the corresponding frequency bandgaps, hence reducing the wave propagations. When frequencies of the applied loading fall within the bandgaps, the loading effects are not able to be transferred or significantly mitigated by the meta-truss core. In this chapter, the result from a previous theoretical derivation of wave propagation in an idealized meta-truss bar is used to validate the numerical model. Then, analyses of the meta-truss core configurations, e.g. the inclusion arrangement and inclusion shape on its bandgap regions and the transient responses of the meta-panel are carried out with the verified numerical model. It is revealed that a complete wave attenuation design can be achieved by utilizing properly tailored arrangements of inclusions, leading to a significantly improved protective effectiveness of the panel against blast loading. The results present a base for the optimal design of the meta-panel for structural protections against blast loading.

⁴ The related work in this chapter was published in **International Journal of Mechanical Sciences** with the full bibliographic citation as follows:

N.H. Vo, T.M. Pham, H. Hao, K. Bi, W. Chen, N.S. Ha. Blast resistant enhancement of meta-panels using multiple types of resonators. *International Journal of Mechanical Sciences*. 2022;215:106965.

<https://doi.org/10.1016/j.ijmecsci.2021.106965>

5.1. Introduction

Increased terrorist activities and unexpected accidental explosions in recent years have caused catastrophic consequences and imposed great threats to public security and the economy worldwide. Ever-increasing demands to protect engineering structures used for both civil and military applications have led to the development of sandwich panels functioning as sacrificial claddings [118, 141]. Sandwich panels consisting of two thin facesheets and low-density cores are widely utilized as energy absorbers due to their superiority in stiffness-to-weight ratio and crashworthiness [26, 143]. By installing on the surface of the protected structures, the role of the traditional panels is to absorb energy through plastic deformation and reduce the load transmission to the structure behind the cladding, thus protecting the main structures [48, 144].

The wide variety of sandwich structures stems largely from the diversity of sandwich core topologies and the variation of the component materials. While many different topologies of the cladding core including honeycomb [145, 146], auxetic structures [147, 148], corrugated [149, 150], and bio-inspired [28, 29] have been intensively studied, sandwich core materials also range widely from stochastic cellular materials (i.e. metallic [151-154] and polymeric foams [155, 156]) to periodic lattice materials [157, 158]. Specifically, metallic lattice structures have been proposed with various topologies such as pyramidal [159, 160], tetrahedral [161, 162], and hollow truss [161, 163]. The dynamic performance of sandwich structures having metallic cores has been investigated extensively, both experimentally and theoretically. For instance, Liu et al. [164] performed experimental and numerical investigations of the responses of hollow cylinders with metallic foam core panels subjected to air blast. The simulation results well captured the deformation patterns of the sandwich panels observed in the tests. For applications under impact and blast loads, investigations on the transient responses of sandwich panels have shown great energy absorption capacity compared to the monolithic panel as sacrificial claddings [165, 166].

Recent attention has been directed to the field of locally resonant meta-structures [41, 83], which are the hybrid of meta-material-based concepts with optimal lattice topology. It is worth mentioning that the prefix “meta” originates from the Greek preposition, which meant “beyond”, implying these favourable structural behaviours are superior to other natural counterparts. These novel engineering structures are expected to possess the ability to generate exceptional wave propagation mitigations in frequency ranges called “bandgap” [167, 168], leading to unique wave attenuation properties not found in nature [169, 170]. Such properties

are activated due to the presence of specially designed man-made structures [111]. A bandgap is a frequency band in which incoming waves cannot propagate due to the activation of local resonance within the inclusions [83, 171]. Potential practical applications in engineering fields by generating favourable bandgaps of these structures including dynamic load mitigation [100, 172], vibration control [60, 173], sound isolation [95], and seismic isolation [54, 94], etc. Multiple techniques have been employed to explore the unique characteristics of these structures. For instance, a local resonant structure that utilizes steel balls coated with silicone and covered in an epoxy cube was proposed by Liu et al. [174], which demonstrated that when the frequency of the excitation force is close to the local resonance frequency, the effective mass becomes negative. This unusual property originates from the interaction between the propagating waves and the resonance of the steel balls. For instance, Li et al. [111] proposed meta-lattice sandwich panels with single-resonators, which show the blast attenuation and high energy absorption owing to the local resonance of the internal resonator with soft coatings. They also carried out experimental investigations on the wave-filtering characteristics of the meta-truss bar for validation [110]. It was demonstrated that the performance of the meta-panels is superior to that of the solid counterparts with the same mass due to the coupled mechanism of absorbing strain energy through both plastic deformation and local resonance. Subsequently, to enhance the dynamic performance of the meta-panel against blast loads by broadening its bandgap regions, the dual-meta panel was proposed [41]. The theoretical results showed that a dual-meta panel has wider bandgaps than those with single-resonators, indicating it can filter wave energy in wider frequency ranges and thus has higher protection efficiency. However, despite all these recent works on mitigation wave propagation, the relevant research on the effectiveness of the meta-panel on structural protection against impact and blast loading, especially blast loading, is still very limited. Therefore, further study of the meta-truss core to achieve the most effective dynamic loading mitigation performance of meta-panels for structural protection is needed.

This chapter systematically performs numerical investigations on the behaviours of meta-panel subjected to blast loading and proposes a new design of the meta-panel with multiple types of meta-cores as a sacrificial cladding against blast loading (see Figure 5-1). To validate the accuracy of the numerical model, the meta-truss bar used to form the meta-panel is firstly modelled numerically. The theoretically derived results of an idealized meta-truss bar in a previous study are used to verify the numerical model in terms of the bandgap regions and transmission coefficient. The verified model is utilized to build the numerical model of the

meta-panel and perform a series of parametric studies to investigate the influences of the inclusion arrangement and inclusion shape on the effectiveness of the meta-panel on wave propagation mitigation. The best performing designs are identified to maximize the blast-resistant performance of the meta-panels. In-depth discussions on the influences of critical parameters on the bandgap regions and the dynamic behaviours of the meta-panel are also given. This chapter numerically and analytically demonstrates the dynamic mitigation mechanism of the proposed meta-panel under blast loads. The obtained results provide interesting findings which can be used for various engineering applications.

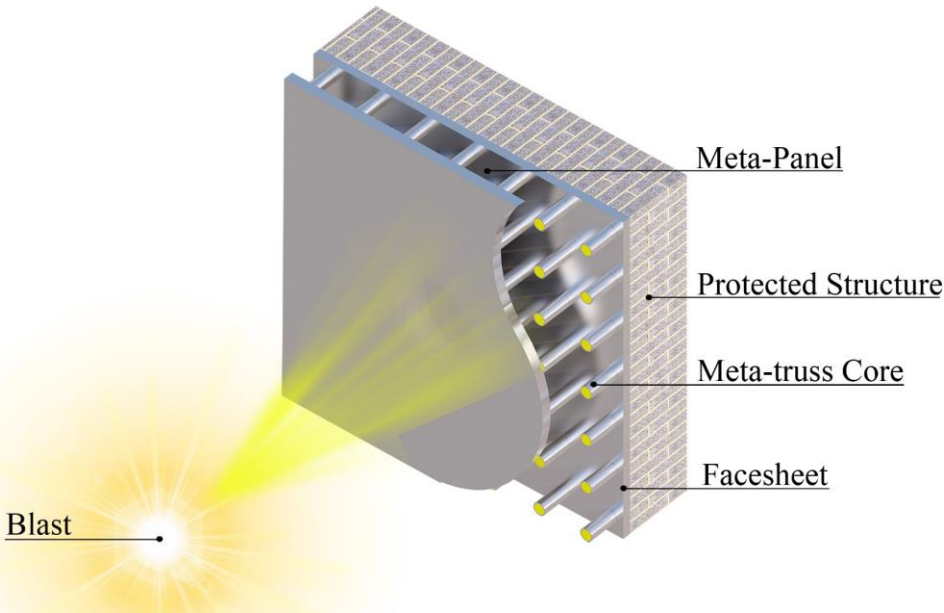


Figure 5-1. Schematic diagram of the meta-panel functions as a sacrificial cladding

5.2. Meta-panel configurations

The configuration of the meta-panel shown in Figure 5-2a consists of two identical aluminium facesheets with the dimension of 120 mm × 120 mm and the meta-truss cores. The meta-truss bar with resonators (see Figure 5-2b) considered in this chapter comprises 6 modules in which each module (shown in Figure 5-2c) has three components including the outer tube, soft coating, and resonators. While the tube and resonators are made of aluminium, polyurethane (PU) which can experience large plastic deformation is selected for the soft coating. It should be noted that tungsten is also used to make resonators in the parametric analysis in this chapter to investigate

the influences of resonator core materials on meta-panel properties. The dimensions and materials are chosen to preserve the bandgap-generating behaviours at large strain for the meta-panel, which is important for structures under extreme loading threats. Also, its structural design could be tailored to adapt to different loadings by adjusting geometrical parameters. The influences of different parameters will be compared in Section 5.5.2. All material properties used in the numerical model in this chapter are listed in Table 5-1.

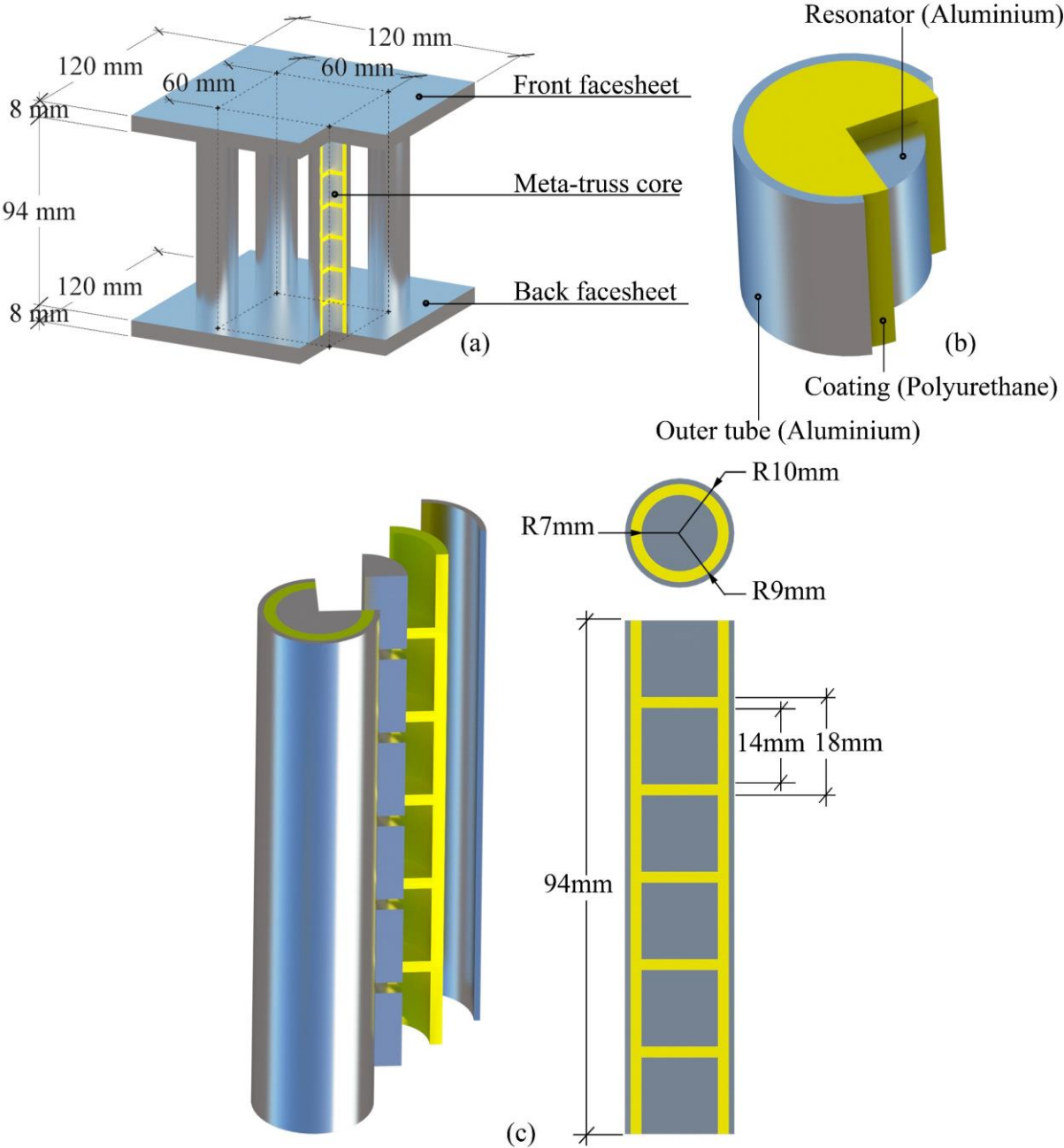


Figure 5-2. (a) Schematic view of the meta-panel, (b) a unit cell, and (c) meta-truss bar

Table 5-1. Material properties of the meta-panel [111]

Materials	Material properties		
	Density ρ (kg/m ³)	Young's modulus E (GPa)	Poisson's ratio ν
Aluminium	2,770	70	0.33
Polyurethane	900	0.147	0.42
Tungsten	19,300	411	0.28

5.3. Programmable negative properties

To quantify the bandgap regions of the meta-truss bar induced by the resonant feature of the meta-core, the dynamic effective mass m_{eff} and effective stiffness k_{eff} using a one-dimensional spring-mass model (Figure 5-3) with internal resonators can be expressed as follows

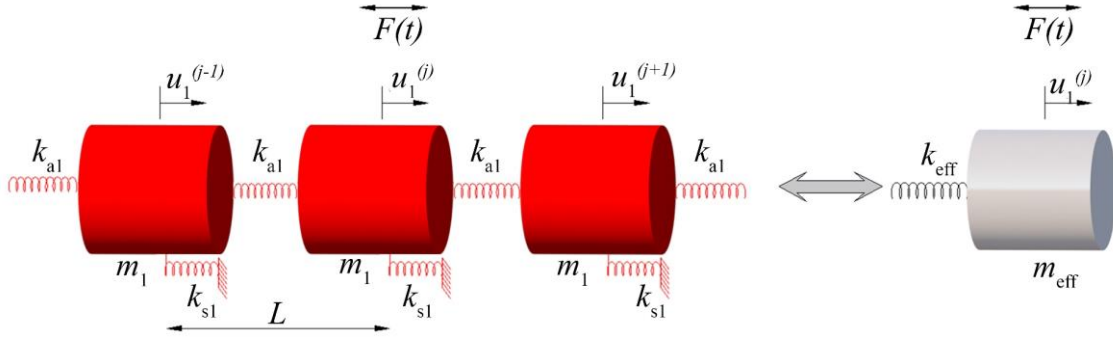


Figure 5-3. The simplified spring-mass model

$$m_{eff} = m_1 - \frac{k_{s1}}{\omega^2} \quad (5-1)$$

$$k_{eff} = k_{a1} - \frac{1}{4} \left(m_1 - \frac{k_{s1}}{\omega^2} \right) \omega^2 \quad (5-2)$$

in which m_1 is the mass of the resonator in the spring-mass model, k_{a1} and k_{s1} respectively represent the axial spring and the shear spring of the soft coating while the angular frequency is denoted by ω . As seen in Figure 5-4, the dynamic effective mass becomes negative in the frequency range of 0 kHz to 9.1 kHz and then gradually increases to positive values. Whereas in the frequency range of 23.2 kHz to 50 kHz, the effective stiffness is negative. It is worth mentioning that the interested frequency range in this chapter is only up to 50 kHz, covering the frequency band of common blast loads acting on structures [175]. The associated frequency regions where m_{eff} and k_{eff} become negative are termed as the 1st bandgap and the 2nd bandgap,

respectively. The resonators move out-of-phase against each other, leading to wave propagation mitigation in the bandgap. The incident wave within these frequency ranges can be significantly mitigated due to the energy being transferred and stored in the relative motions of the resonators.

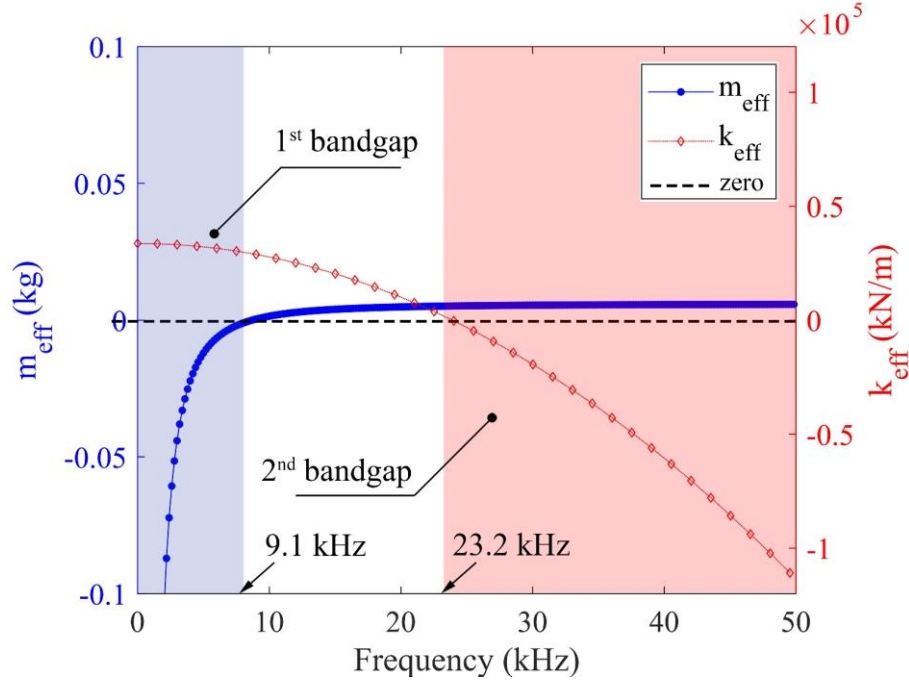


Figure 5-4. Effective parameters of the spring-mass model to show the theoretical bandgap regions of the meta-truss bar

The transmission of energy of the entire system can be quantified by using the transmission coefficients, T , which can be computed as follows:

$$T = \left| \prod_{j=1}^N T^{(j)} \right| = \left| \prod_{j=1}^N \frac{u^{(j)}}{u^{(j-1)}} \right| \quad (5-3)$$

where $u^{(j)}$ is the displacement of the j^{th} unit cell, and N is the total number of the unit cells.

5.4. Blasting wave characteristics

Determining the dominant frequencies of the applied loading is the vital step for the engineering design of the meta-panel. It is because the negativity of the effective parameters is only triggered when the applied loading frequency falls into the bandgap region of the meta-panel, leading to its favourable mitigation performance. In this chapter, the blast load is applied on the front facesheet of the meta-panel. The keyword *LOAD_BLAST_ENHANCED is widely utilized in LS-DYNA to generate blast load via the Conventional Weapon Effects (CONWEP)

program, which predicts the air blast load based on empirical data from blasting tests. This model was also adopted in the Unified Facilities Criteria (UFC 3-340-02) in graphical form for designing structures to resist the effects of the explosion. The loading area definition is determined by the keyword *LOAD_BLAST_SEGMENT whereas the function *DATABASE_BINARY_BLSFOR is utilized to compute the blast pressure. The blast pressure is calculated by the equivalent amount of Trinitrotoluene (TNT), the stand-off distance, and the angle of incidence. The blast pressure is predicted as follows [176]:

$$P(t) = P_r \cos^2 \theta + P_i (1 + \cos^2 \theta - 2 \cos \theta) \tag{5-4}$$

where P_i and P_r are respectively the incident pressure and reflected pressure while θ denotes the angle of incidence. Computation of P_i and P_r is based on the scaled distance, $Z = R / \sqrt[3]{W}$, in which R and W are the stand-off distance and the equivalent amount of TNT, respectively [177]. In this chapter, the blast charge TNT is placed perpendicularly to the centre of the front facesheet at a distance of 0.35 m, in which the angle of incidence θ is defined as 0. The size of the charge is 0.4 kg which corresponds to the scaled distance of 0.41 m/kg^{1/3}. Figure 5-5a shows the reflected pressure time-history of the blast loading. To obtain the corresponding frequency spectrum, the blast time history is converted to the frequency domain by utilizing the Fast Fourier Transform (FFT) method, the FFT spectrum of the blast load is shown in Figure 5-5b. As shown, the peak reflected pressure is approximately 36 MPa and the dominant blast loading energy distributes in the frequency band up to 50 kHz.

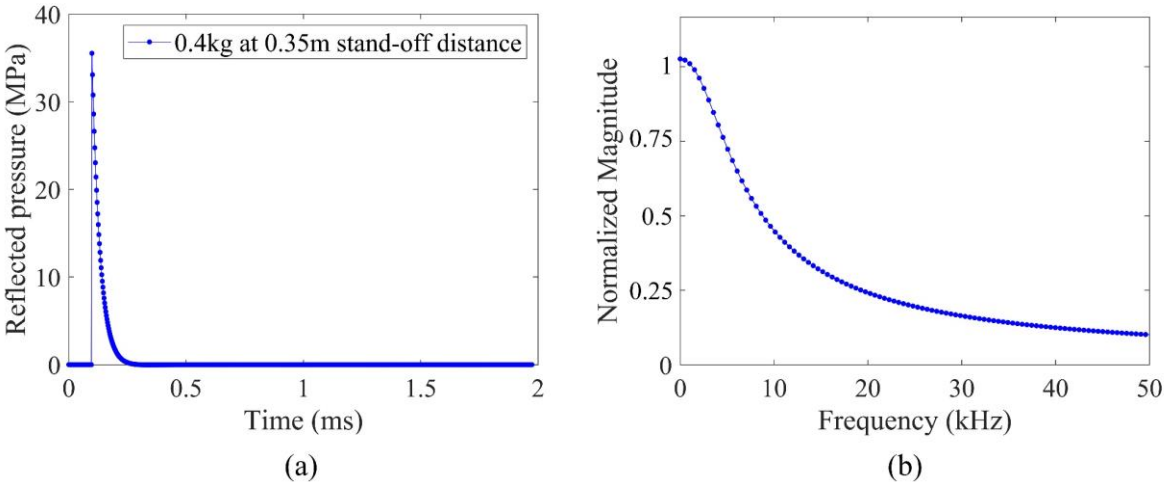


Figure 5-5. Peak reflected pressure profile of the simulated blast loading generated by 0.4 kg TNT at 0.35m stand-off distance (a-b) in time history and its FFT spectrum

5.5. Comprehensive numerical investigations

The complete bandgap of the meta-truss bar generated by the arrangement of multiple resonators is proposed in the present model and its effect on the dynamic performance of the meta-panel is analysed in this section. The influence of the inclusion geometry on the transient response of the meta-panel is also numerically investigated for various shapes. In addition, the model validation is carried out to check the accuracy of the simulations in this section.

5.5.1 Model development and verification

The theoretical solution has been used to calculate the bandgap regions of the meta-truss bar based on the one-dimensional spring-mass model. Due to the complexity, the infinite number of modules and single harmonic wave input have been assumed to analytically solve the Eigen frequencies and calculate the bandgap regions. It is not straightforward to derive the closed-form theoretical solutions of the complex case considering the finite number of modules, boundary reflections, and various input loading conditions. In addition, the structural responses of the meta-panel subjected to blast loading are more challenging to obtain analytically when considering plastic deformation. To overcome the limitations mentioned above, numerical simulations are performed to investigate the bandgap regions and the transient responses of the meta-panel subjected to blast loadings. The results obtained from the above theoretical solutions based on idealized conditions are utilized to verify the accuracy of the numerical simulations.

In this chapter, commercial software LS-DYNA is utilized to evaluate the bandgap regions of the meta-truss bar (Figure 5-2c) and the dynamic behaviours of the meta-panel (Figure 5-2a). As illustrated in Figure 5-6, the entire meta-panel is modelled. In the simulation, all elements are meshed by the solid hexahedron elements with a minimum mesh size of 1 mm after performing a mesh convergence analysis. The interfaces between the inclusions and polyurethane are modelled by the kinematic constraint method in which the selected segments are tied to each other and assumed to be perfectly bonded. This contact is chosen to prevent the slide or detachment between the meta-cores and the soft coating which is of significance to activating the local resonance of the resonators. To obtain rigid connections, the contact between the outer truss bar and the two facesheets is also defined by the kinematic constraint method while the interior contact between layers of interior surfaces of polyurethane is adopted to eliminate the negative volume issue which often occurs due to large deformation of soft materials. In addition, all nodes along the facesheet edges are assumed to be constrained in all

three directions, which account for the peripherally clamped boundary of the back facesheet. The material properties used in LS-DYNA are listed in Tables 5-1 and 5-2.

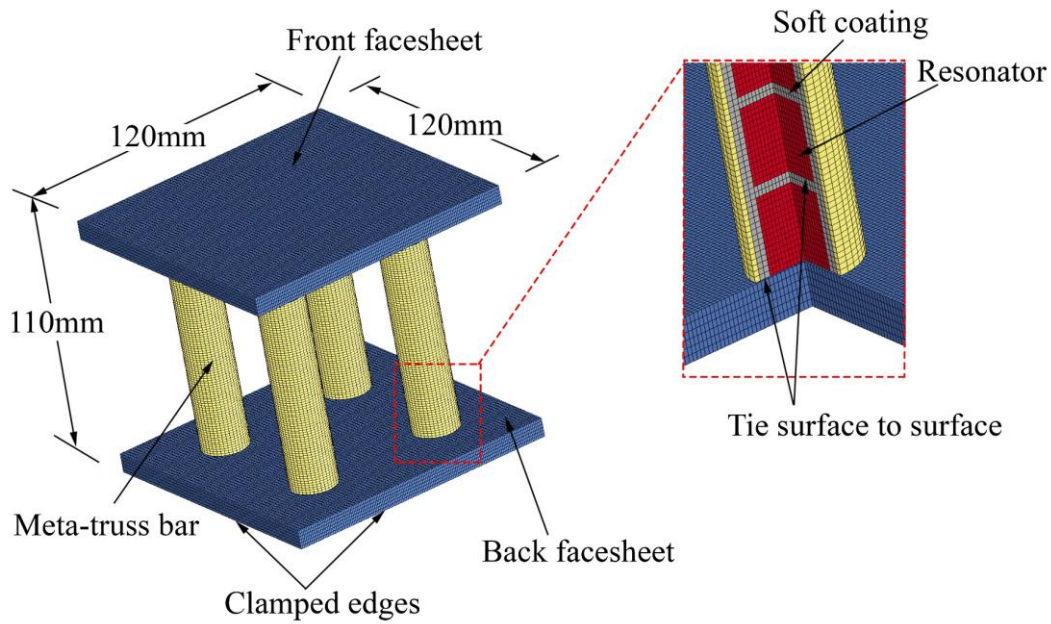


Figure 5-6. Schematic of the finite element model

Table 5-2. Johnson-Cook material parameters for aluminium [111]

Density (kg/m ³)	Poisson's ratio	Young's modulus (GPa)	A (GPa)	B (GPa)	C	m	n	T _m (K)	T _r (K)	ε̇
2,770	0.33	70	0.369	0.675	0.007	1.5	0.7	800	293	1

To verify the developed numerical model, the derived theoretical analysis of the transmission coefficient of a single truss bar obtained by Eq. (5-3) is calculated to compare with the corresponding numerical results. A meta-truss bar consisting of 6 unit cells as shown in Figure 5-2 (c) is numerically built. The input signal is applied at one end of the meta-truss bar by a sweep frequency ranging from 0 – 50 kHz while the output signal is captured at the other opposite end. It should be noted that the clamped boundary condition is adopted on the peripheral edges of the truss bar to represent the practical boundary condition in reality. The numerical transmission coefficient of the meta-truss bar displayed in Figure 5-7 agrees closely with the analytical result, indicating the validity of the model. In particular, it is depicted in Figure 5-6 that the meta-truss bar possesses two bandgaps in the frequency ranges of [0 – 9.1] kHz for the 1st bandgap and [23.2 – 50] kHz for the 2nd bandgap while the corresponding ranges from the numerical result are [0 – 9.3] kHz and [22.5 – 50] kHz. There is a slight bandgap

disagreement between the two approaches and oscillations of the numerical results. This is because the infinite number of unit cores is assumed in the analytical derivation, while the numerical meta-truss bar has a finite length with 6 unit cores. In addition, each unit core is numerically modelled with its respective elastic material property and density instead of the lumped mass connected with idealized lumped springs in the analytical solution.

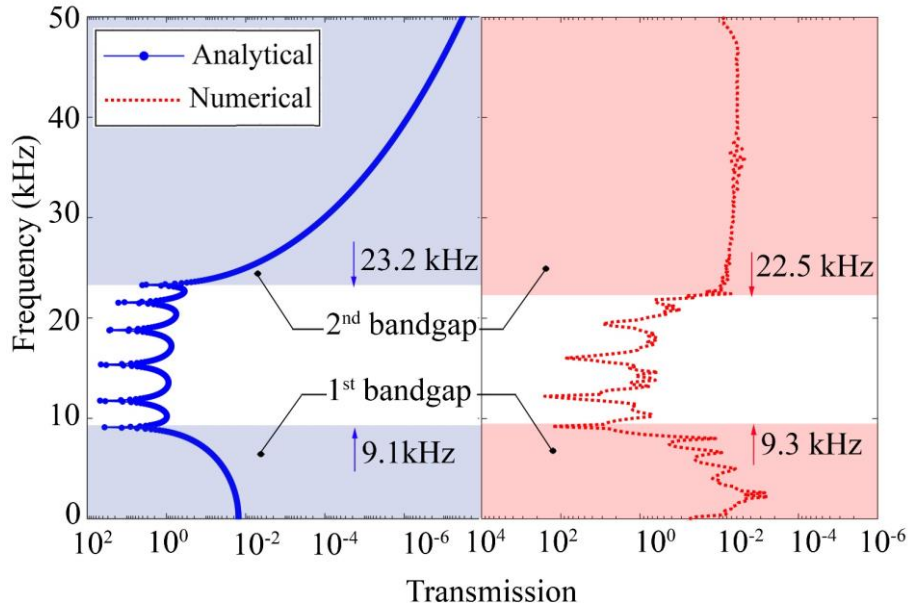


Figure 5-7. Comparison of the transmission coefficients of the meta-truss bar including the analytical solution and the numerical result

For further validation, a prescribed displacement $u(t)$ with the amplitude of 10^{-4} (m) and multi-frequency components including $f_1 = 5$ kHz, $f_2 = 16$ kHz, and $f_3 = 30$ kHz, [i.e., $u(t) = 10^{-4} (\sin[2\pi \times 5t] + \sin[2\pi \times 16t] + \sin[2\pi \times 30t])$], is applied to the input end of the meta-truss bar and the output end is set free. Figure 5-8 shows the displacement-time histories at the two ends of the meta-truss bar (i.e. the input and the output, respectively) and the corresponding FFT spectra. As observed, waves attenuation is observed as expected with only one input signal of 16 kHz passing through the meta-truss bar while other signals of 5 kHz and 30 kHz, which fall in its bandgap are eliminated. This demonstrates that the meta-truss bar possesses the wave filtering capacity at the frequencies falling in its two bandgaps. Generally, the numerical models and analytical predictions are well matched. The numerical model in predicting the bandgaps and wave attenuations of the meta-truss bar is verified, which is extended to model the meta-truss panel for the investigation of its blast mitigating performance.

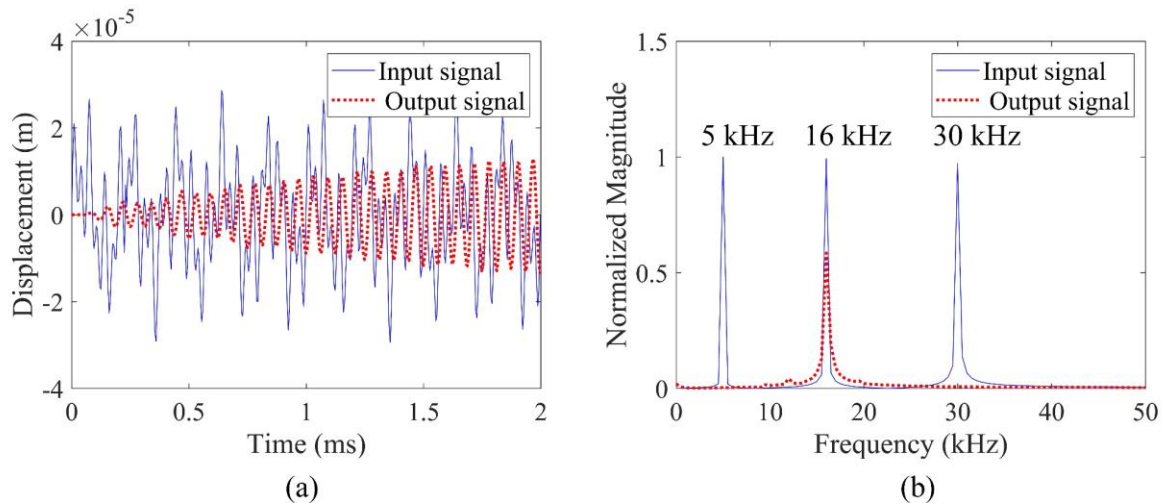


Figure 5-8. Input prescribed displacement is excited at one end of the meta-truss bar while the output displacement is captured at the other end

5.5.2 Parametric studies

The meta-panel was found to possess superior blast mitigation capacity and outperforms other conventional counterparts, e.g. sandwich panels with hollow trusses and solid trusses under blast loading [41]. To obtain the favourable design of the meta-panel, systematic parametric studies with the aims of maximizing the bandgaps of the meta-truss cores and thus its blast-resistant performance are conducted in this section. Inclusion arrangements and inclusion shapes are selected as parameters for investigation because with their appropriate design, the better wave attenuation of the meta-truss bar and the enhanced performance of the meta-panel can be achieved. The blast loading described in Section 5.4 is applied to all considered panels while the description of the meta-panel in Section 5.2 is referred as the reference. To evaluate the blast mitigation capacities, the critical criteria such as peak force transmitted to the protected structure, energy absorption, and the central displacement of the back facesheet are compared among the panels with different core configurations. These particular criteria are chosen due to the main functionality of the meta-panel as a sacrificial cladding is to absorb energies from the incident loadings, therefore, minimizing force transmissions to the protected structures. Besides, the central displacement is measured to determine the response amplitude and damage of the meta-panels subjected to blast loading.

5.5.2.1 Influence of inclusion arrangement

In this section, the meta-panel with multiple types of resonators is modelled. Under blast loading, its blast-resistant performances are expected to enhance as compared to the meta-panel

with uniform resonators, because of the complete bandgap created by its arrangement that covers the entire targeted frequency band with most blast loading energy. For comparison, the dynamic responses of the meta-panels with traditionally uniform resonators are also evaluated.

5.5.2.1.1 Influence of multiple types of meta-core material

While travelling through a meta-truss bar, stress waves can either propagate in the passband or be attenuated in the bandgaps depending on the frequency of the applied loading. A uniform arrangement of identical resonators, i.e., meta-cores, limits the width of the bandgaps to a narrow frequency range. To overcome this limitation and intensify the performance of the meta-core, instead of utilizing the same repetitive units, the meta-truss bar with multiple types of meta-cores is proposed to maximize the width of the bandgap and minimize the corresponding passband. It should be noted that the materials and dimensions of the facesheets and outer tube of the meta-truss bar remain unchanged. This proposed meta-truss bar (Figure 5-9a) composes of two zones, denoted by Zone 1 and Zone 2. Each zone has uniform unit cells with the same geometry, but different resonators made of tungsten (W) and aluminium (Al), with their properties given in Table 5-1.

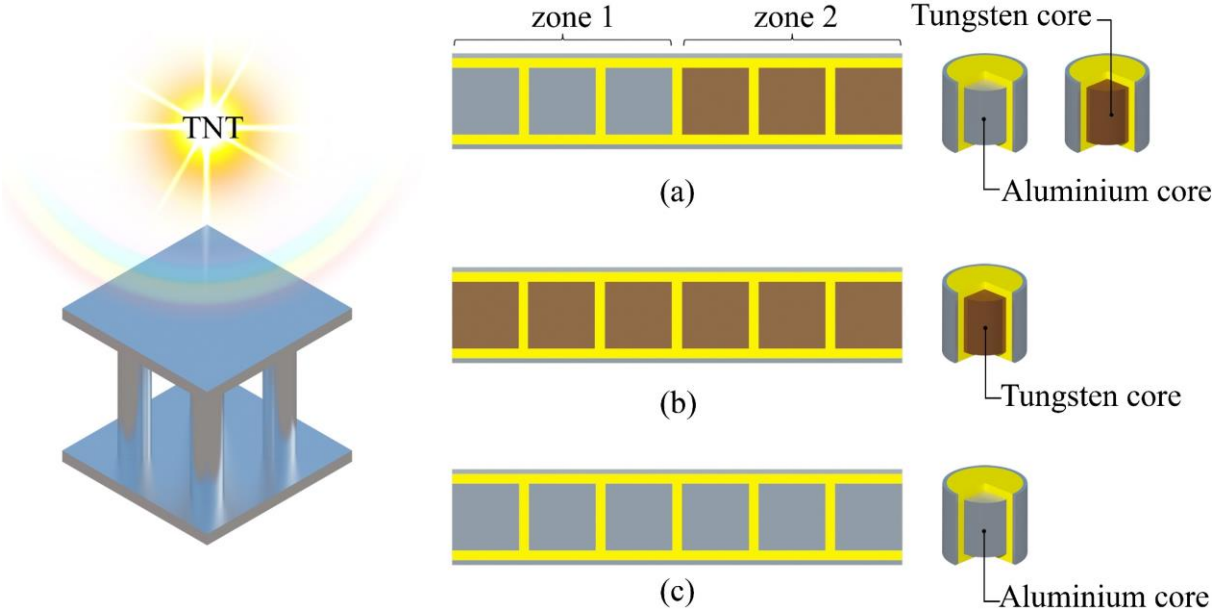


Figure 5-9. Schematic diagrams of the meta-panel with different arrangements of resonators (a) combination of Aluminium and Tungsten, (b) Tungsten, and (c) Aluminium

Figure 5-10 illustrates the analytical transmission coefficient of two zones of the meta-truss bar. The bandgap of Zone 1 corresponding to the aluminium meta-truss core is divided into a low (LB_1) and a high (HB_1) sub-band while its passband is denoted by PB_1 . In the frequency band

structure [178], which is an interval in the frequency domain comprising the bandgap and the passband [179], HB_1 exhibits negative effective stiffness whilst the negativity of effective mass is reflected by LB_1 . Similarly, the passband of Zone 2 (PB_2) corresponding to the meta-truss bar with tungsten core lies between the first and second attenuation bands which are denoted by LB_2 and HB_2 , respectively. In theory, it is practically impossible to eliminate the passband utilizing a uniform arrangement of the resonator due to the existence of the passband. Given these properties, the combination of two or more zones with different materials in each zone makes it possible to minimize or even eliminate the passband if the passband of one zone falls into the bandgap of another zone, and vice versa. In other words, the passbands PB_1 and PB_2 can be eliminated by combining two different zones in their structural arrangements. Specifically, PB_2 falls into the low bandgap of Zone 1 (LB_1), while the high attenuation band of Zone 2 (HB_2) covers all the passbands of zone 1 (PB_1). This finding agrees with those reported in the literature on locally resonant acoustic meta-material [31]. From the theoretical point of view, a properly programmable arrangement of resonators can maximize the bandgap width of the meta-truss bar to cover all the loading frequency bands. It means that all the incident waves can be completely stopped by the proposed meta-truss bar. Therefore, the meta-truss bar can be properly designed with multiple types of resonators to have their combined bandgaps cover the entire frequency band of the input dynamic loadings for best mitigation of loading effects, hence the most effective structural protections.

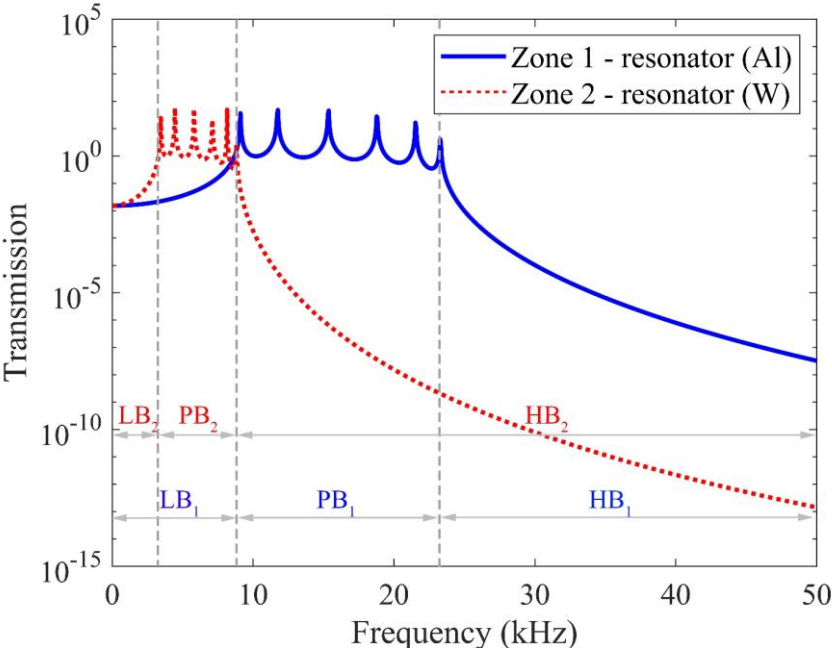


Figure 5-10. Analytical transmission coefficient profile of two zones of the meta-truss bar

The physical meaning and mechanism of wave attenuation can be well understood by observing wave propagation through the meta-truss bar with two types of resonators. To demonstrate this, a prescribed displacement consisting of three sinusoidal waves with the same amplitude but different frequencies, *i.e.* $u(t) = 10^{-4}(\sin[2\pi t] + \sin[2\pi \times 4t] + \sin[2\pi \times 12t])$ is used as input to the truss bar. It is worth noting that the frequencies are chosen in such a way that each zone attenuates different frequencies. Figure 5-11 shows the longitudinal displacement profile at different points in the central axis of the meta-truss bar denoted by A, B, and C. These displacements represent the input signal, response at the end of Zone 1, and response at the end of Zone 2, respectively. As shown, the peak value of the displacement is sequentially reduced by each zone of the meta-truss bar, and two zones with different resonators can attenuate the three harmonics, therefore only very low values of displacement are present at the end of the meta-truss bar. This result agrees with the previous findings on locally resonant acoustic meta-material from Comi and Driemeier [31]. In general, the newly proposed configuration with multiple types of resonators proves to be more efficient for wave filtering.

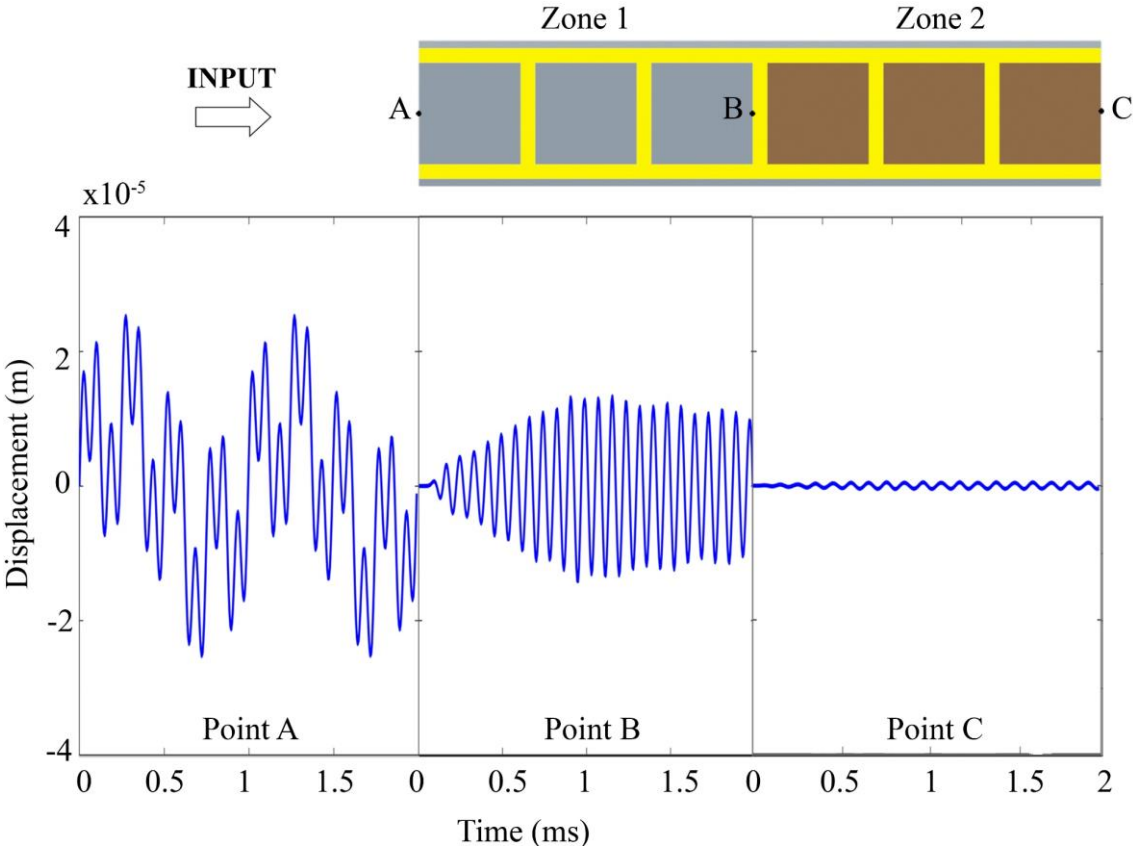


Figure 5-11. Displacement-time history at three points, *i.e.* the input point (A), the middle point (B), and the output point (C) in the meta-truss bar with two types of resonators

To further clarify this effect, the responses at three different locations (one for each lattice zone), are shown in the frequency domain in Figure 5-12. After propagating through Zone 1 (point B), only the frequencies of 1 kHz and 4 kHz are attenuated, therefore, the response has one peak at 12 kHz which falls into the passband of Zone 1. The second region of the considered meta-truss bar (Zone 2) continues attenuating the wave energy at the frequency of 12 kHz because it falls into the bandgap of Zone 2, leading to the complete attenuation of the input wave by the meta-truss bar at point C. It is noted that a small amount of energy is still transmitted as indicated by a small peak at 12 kHz in the signal after propagating through the meta-truss bar. This is because when the core starts vibrating inside the unit cell, the initial out-of-phase vibration greatly attenuates the wave energy transmission through the unit. The reverse vibration of the core, however, still results in a small amount of wave energy transmission.

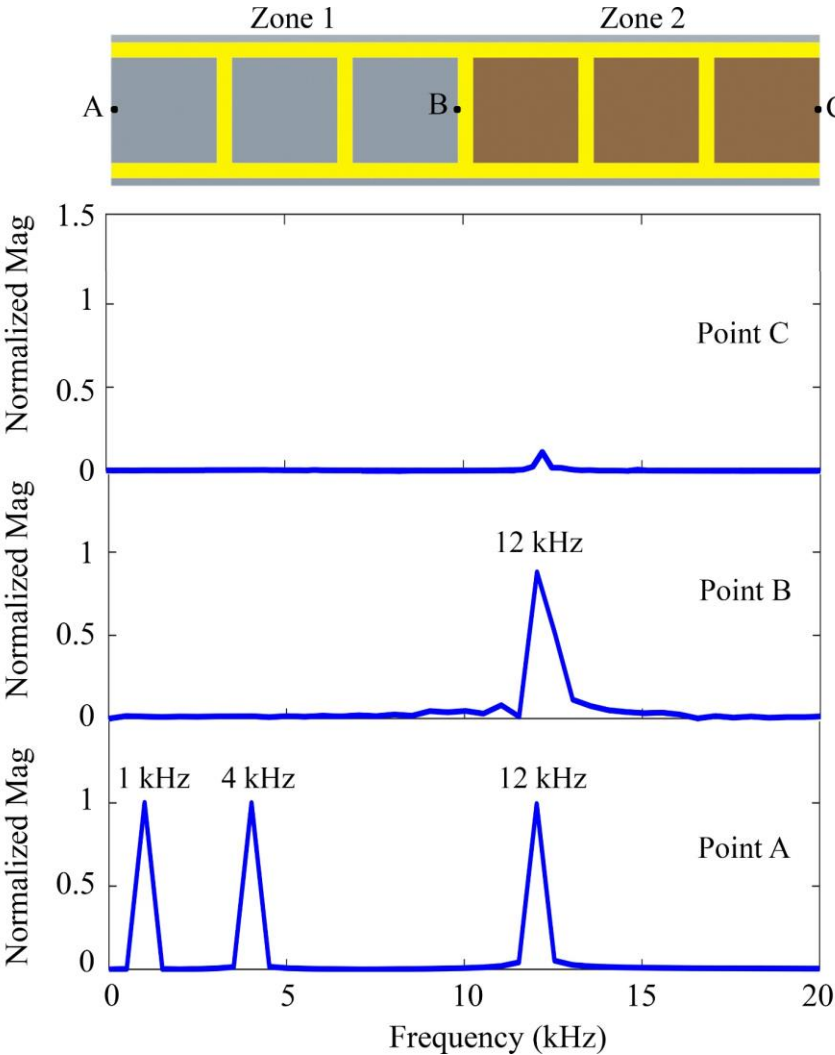


Figure 5-12. FFT spectrum of displacement at the three considered points

For further demonstration, the continuous wavelet transform (CWT) [111] is adopted to analyse the wave propagation in the meta-truss bar at three considered points in the time-frequency domain. In this chapter, a Gabor wavelet transform is chosen as the mother wavelet function owing to its multiresolution analysis capability. Figure 5-13 depicts the multi-frequency CWT profiles at three locations along the meta-truss bar in the case of prescribed displacement excitation with multi-frequency components. As shown, the signal energy of point A is focused at the frequencies of 1 kHz, 4 kHz, and 12 kHz (Figure 5-13a) while there is very little energy exists in the output signal (point C), implying a complete wave attenuation phenomenon in these frequency bands (Figure 5-13c). Besides, Figure 5-13b shows the energy reduction occurs particularly at the frequencies of 1 kHz and 4 kHz, which fall into the bandgap of Zone 1. These bandgaps well agree with the analytical results as discussed above.

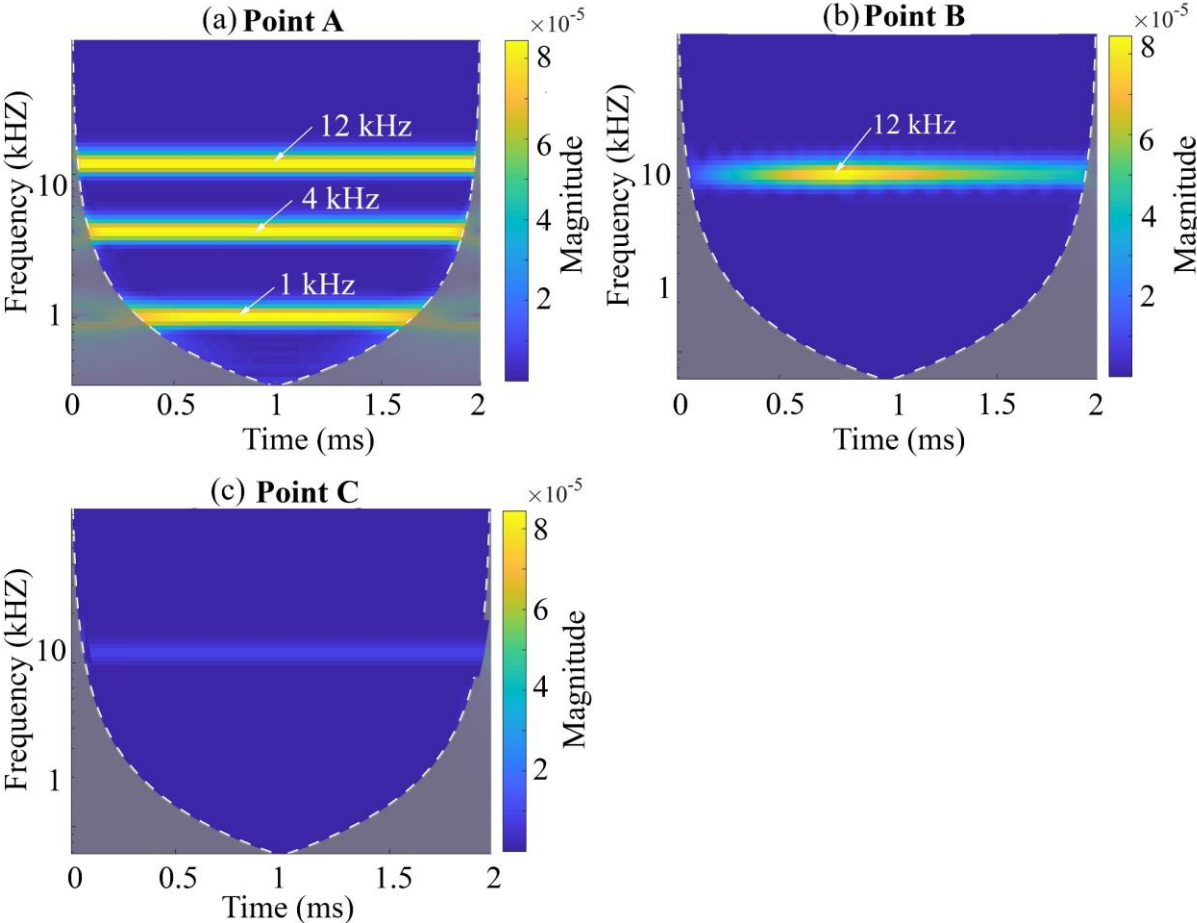


Figure 5-13. Scalograms of displacement in the time-frequency domain at different points (a) point A, (b) point B, and (c) point C

The design optimization analysis for the meta-panels considered in this chapter under blast loadings is evaluated by using combinations of multiple types of meta-cores. Structural

responses (i.e. displacement of the back facesheet and reaction force) and energy absorption capacity of the meta-panels with uniform resonators (i.e. aluminium and tungsten) and two types of resonators subjected to blast loading are compared. It is noted that the displacement is recorded at the centre of the back facesheet in all cases, and the absolute peak values are presented wherever applicable. The blast load time history generated above as shown in Figure 5-5 is used in all the analyses. Figure 5-14 shows the simulated deformation of the meta-panel and displacements on the central symmetric plane of the back facesheet of the three meta-panels. In particular, Figure 5-14(a) shows the deformation contour when the meta-panel is composed of the meta-truss bar with two types of cores, and those with the meta-truss bar having only tungsten or aluminium cores are shown in Figure 5-14b and Figure 5-14c, respectively. As shown, the meta-panel consisting of the meta-truss bar with two types of resonators results in the lowest value of the peak central point displacements of the back facesheet, i.e. 2.6 mm, followed by 3.4 mm and 3.7 mm, respectively for uniform resonators of W and Al. These results indicate that using two types of meta-core together in the truss bar leads to a significant reduction of the peak response of the meta-panel as compared to the case with the uniform meta-core. This is because the combination of these two cores results in wider bandgaps of the meta-truss bar, therefore, leading to more effective stress wave propagation mitigation.

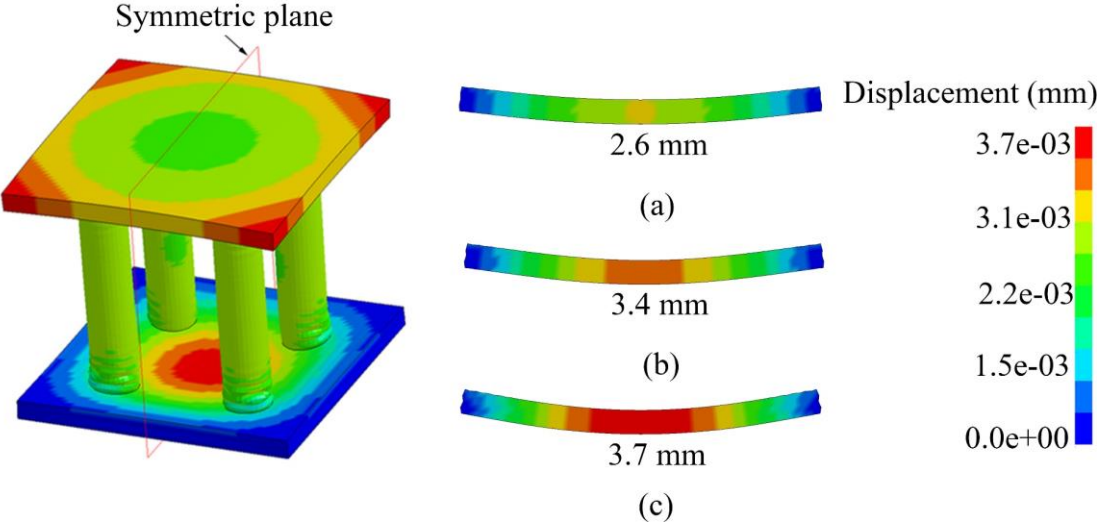


Figure 5-14. Diagrams showing deformed meta-panel and the deformation of the back facesheet of three meta-panels with different meta-truss bar (a) aluminium and tungsten resonators and (b-c) uniform tungsten and aluminium, respectively

To further compare the dynamic response of meta-panels with different resonator arrangements, the time histories of the reaction force around the edges are shown in Figure 5-15. It is observed

that the peak reaction force is significantly affected by the resonator arrangements. When the two types of resonators are used in the meta-panel, it results in more reduction of the reaction force in comparison with the two meta-panels with the single type of resonators considered in the present investigation. The lowest reaction force is observed to be 140 kN in the meta-panel with the meta-truss bar consisting of two types of meta-cores, which is around 21% and 10% less than that of the panel with uniform Al and W meta-cores, respectively. This is because the meta-truss bar with two types of meta-cores has a wider frequency bandgap as demonstrated above, therefore leading to more effective stress wave mitigation, thus less stress from the blast load is transferred to the back facesheet and then the supports.

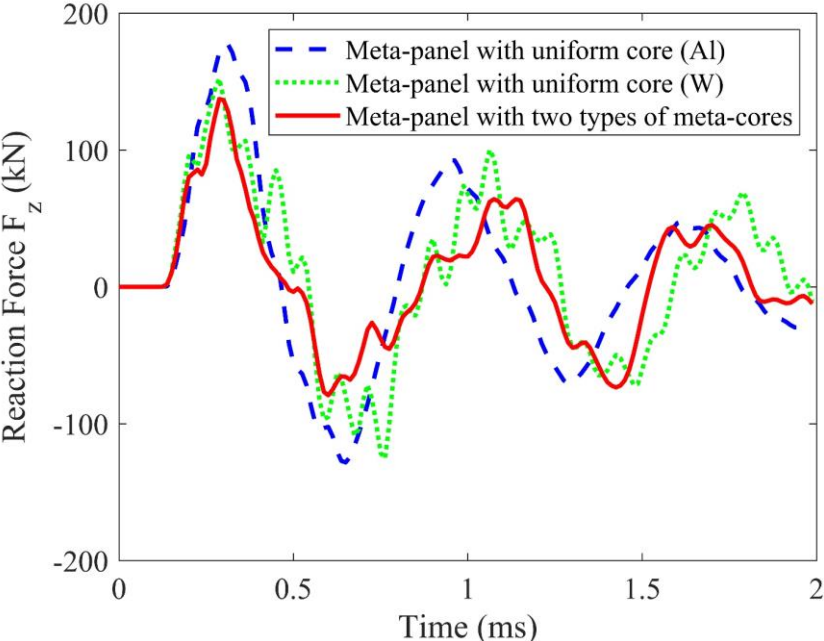


Figure 5-15. Comparison of reaction force-time history curves between the three meta-panels

Furthermore, to gain insight into blast response mitigation, energies absorbed by individual components, i.e. front facesheet, back facesheet, outer tube, and coating+core for all panels are presented in Figure 5-16. It is noted that the total energy imparted from the applied blast load to the meta-panels is converted to kinetic and internal energies. While the internal energy is dissipated by inelastic deformation of the facesheet and the outer tube, the kinetic energy is stored elastically by coating+core by their relative movements. As shown, the meta-panel with two types of meta-cores has the highest total energy absorption (i.e. 310 J), indicating its best protective effectiveness. This substantial increase in total energy absorption is mainly contributed by the rising in energy absorption by the coating+core (i.e. 33%) because by introducing two zones of resonators, the meta-core possesses a wider bandgap and filters more

stress waves from the blast loading, leading to more energy absorption. As a result, the back facesheet of the meta-panel with two types of meta-cores absorbs less energy (i.e. 14%) compared to the other two meta-panels with the single type of meta-core due to its less deformation, while the energy absorption of the front facesheet and the outer tube remains unchanged among the three considered panels. This effectiveness is due to the energy absorption associated with the motion of the resonator masses. No such energy absorption mechanism is available for the meta-panel with uniform resonators. Among the three panels investigated, the meta-panel with two types of resonators yields the best blast effect attenuation performance due to the merging bandgap of two different zones of resonators.

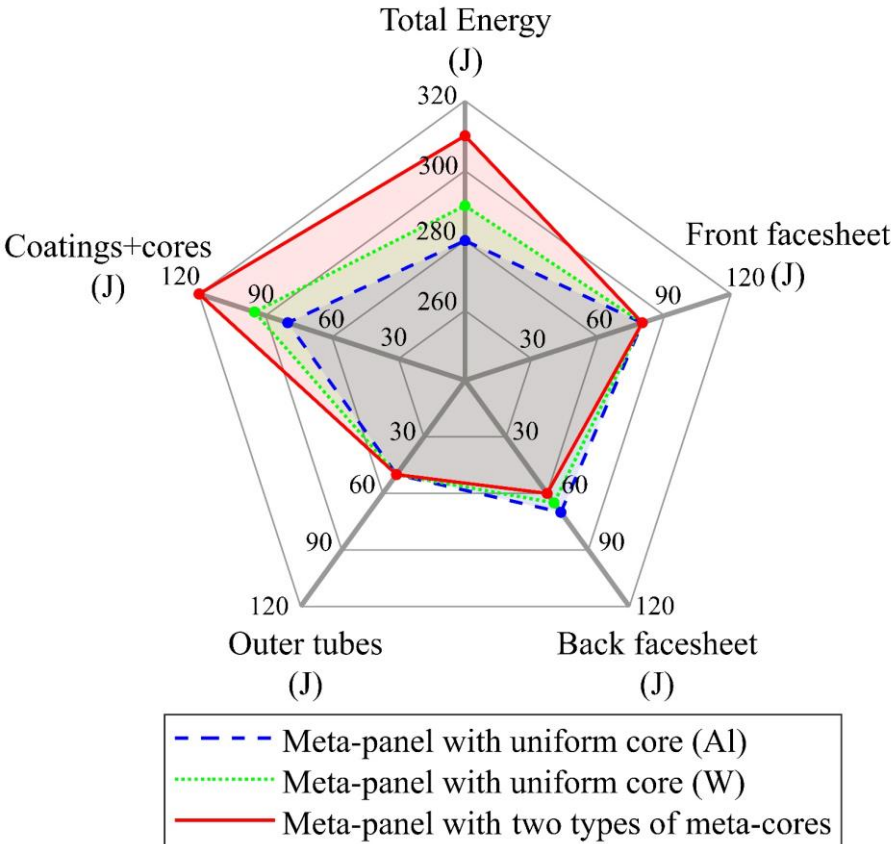


Figure 5-16. Comparison of energy absorptions of different parts of the three meta-panels

Overall, the panel with the meta-truss bar composing two types of resonators possesses better blast mitigation and higher energy absorption capability compared to the uniform-resonator panel, even the panel with the meta-truss bar made of tungsten cores, which is heavier because of the higher density of tungsten than aluminium. Therefore, it is crucial to choose a proper combination of the meta-cores for the meta-panel in such a way that it results in wider bandgaps for better blast protection of structures.

5.5.2.1.2 Influence of multiple types of meta-core size

Besides material properties, the bandgap of the meta-core is also affected by its dimension and geometry [171]. Therefore the desired bandgap of the meta-core can also be achieved by adjusting the dimension and geometry of the core. In this section, the influences of the meta-core size on the frequency bandgaps are investigated. Figure 5-17a depicts the proposed meta-truss bar which consists of two types of resonators with different radii while the meta-truss bars with uniform aluminium resonators of 7 mm and 4 mm radius are illustrated in Figures 5-17b and 5-17c, respectively. Other parameters, namely the material properties, the diameter and the thickness of the outer tube remain unchanged in the three meta-truss bars.

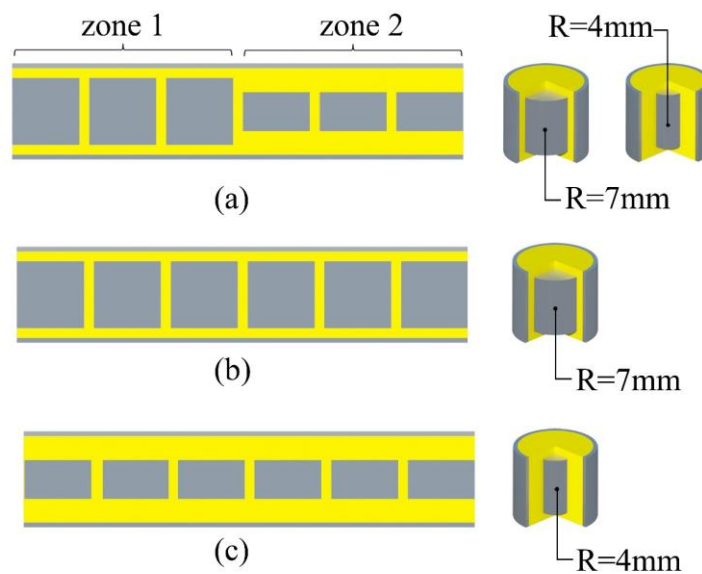


Figure 5-17. Schematic diagram of meta-truss bars with different sizes of resonators (a) non-uniform resonator meta-truss bar with two sizes of resonators and (b-c) are uniform resonators meta-truss bar with the core radius of 7 mm and 4 mm, respectively

Figure 5-18 illustrates the bandgaps of two meta-cores of two sizes. Same as the results presented above, the frequency band structure of the individual zone consists of two bandgaps and one passband as highlighted in blue and red, respectively. It can be seen that in the bandgaps denoted by LB_i and HB_i ($i=1,2$), combining the bandgaps of these two meta-cores generates a wider bandgap covering the entire frequency band from 0 to 50 kHz. In other words, by introducing two zones of resonators with different sizes, the passband PB_i in the range of 0 to 50 kHz can be eliminated, leading to complete wave attenuation. This is because reducing the core size by introducing Zone 2 decreases the mass of the inclusion while increasing the thickness of the coating mass. As the result, the value of the mass and shear stiffness

significantly decreases, resulting in a higher lower bound frequency and a broader range of the 1st bandgap that completely covers the passband of Zone 1. As a consequence, wave energy in the frequency band of 0 to 50 kHz would be greatly mitigated by the truss bar with these two types of meta-cores.

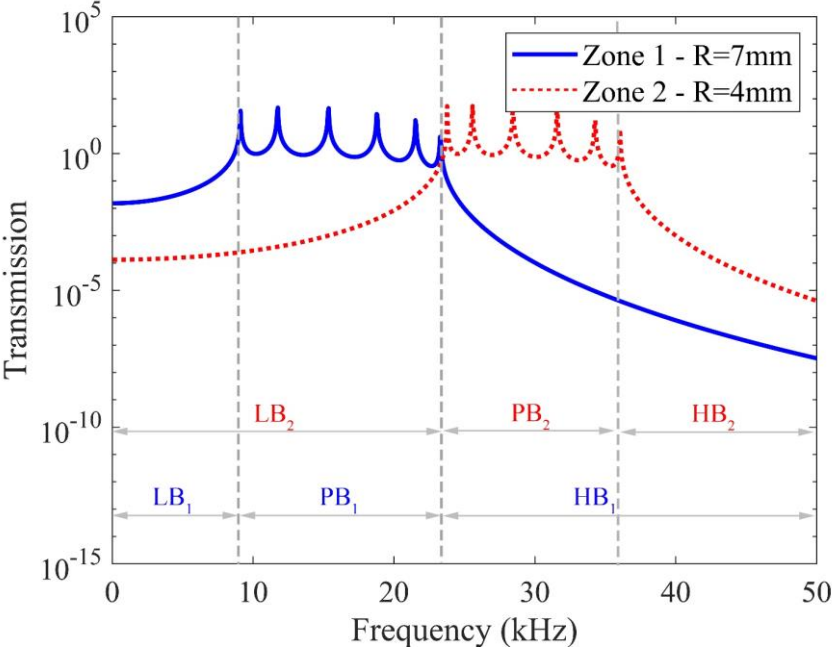


Figure 5-18. Analytical transmission coefficient profile of two zones of the meta-truss bar with two types of resonators with the radii of 7 mm and 4 mm

For clarification, a sweep excitation in the frequency range [0 – 50] kHz is applied to one end of the meta-truss bar while at the central and far ends, the vibration displacements are compared (Figure 5-19). It is noted that the input displacement amplitude of the excitation is high, which decreases at the end of Zone 1 because the bandgap of Zone 1 mitigates the transmission of wave energy with the frequencies falling in its bandgap. The displacement amplitude reduces almost to zero at the end of the truss bar because the remaining wave energy has frequencies mainly inside the bandgap of Zone 2. The effectiveness of the bandgap, resulting in the mitigation of the input excitation, is demonstrated in Figure 5-18, showing the response time histories at different locations of the truss bar.

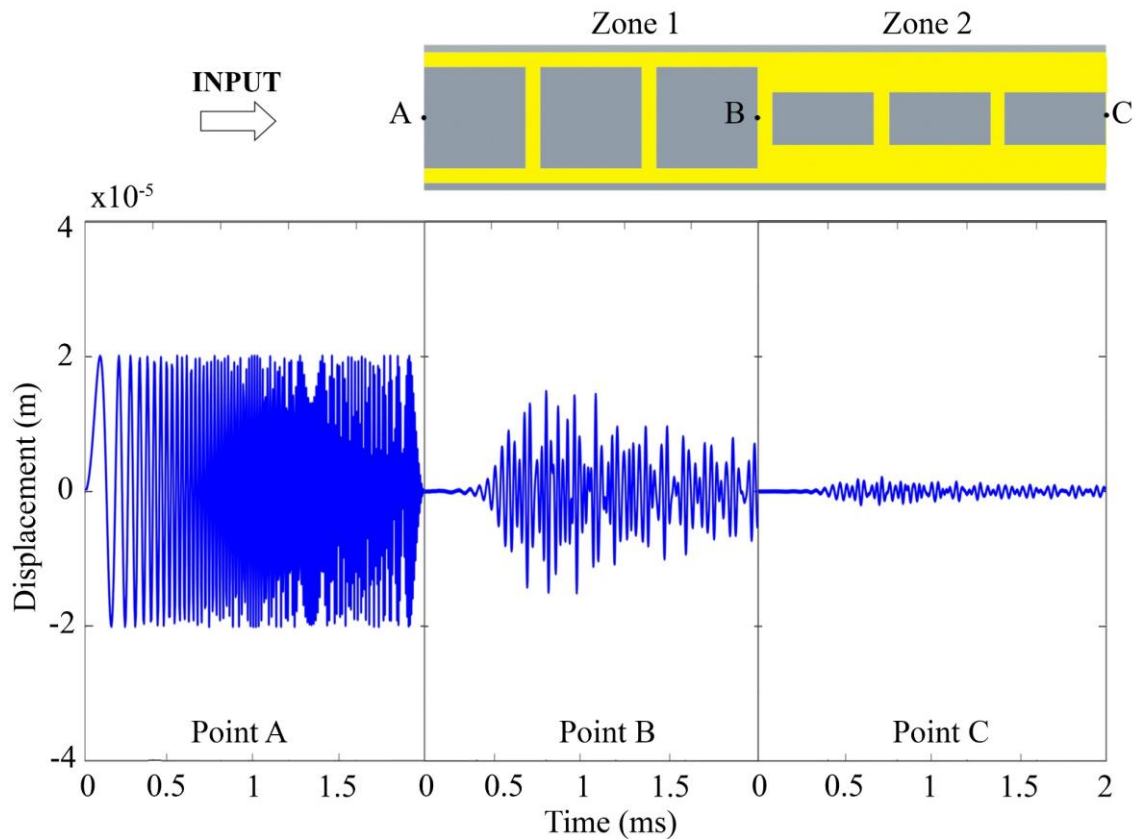


Figure 5-19. Displacement-time history at the three points, i.e. the input point (A), the middle point (B), and the output point (C) in the meta-truss bar with two resonator sizes

Figure 5-20 shows the FFT spectrum of the displacement time histories shown in Figure 5-19. The effect of the bandgap in filtering the wave energy is obvious. As shown, at point B after wave propagating through the meta-cores in Zone 1, wave energy in the frequencies in the bandgap of 0 – 9.1 kHz and 23.2 – 50 kHz is attenuated. After further propagating through meta-cores in Zone 2, most wave energy is attenuated. Figure 5-21 shows the multi-frequency CWT profiles of the time histories at three locations along the meta-truss bar shown in Figure 5-19. Similar observations can be drawn again. These findings indicate that the predicted bandgaps of the meta-cores from the analytical results exist in the meta-truss bars, which effectively mitigate wave propagations.

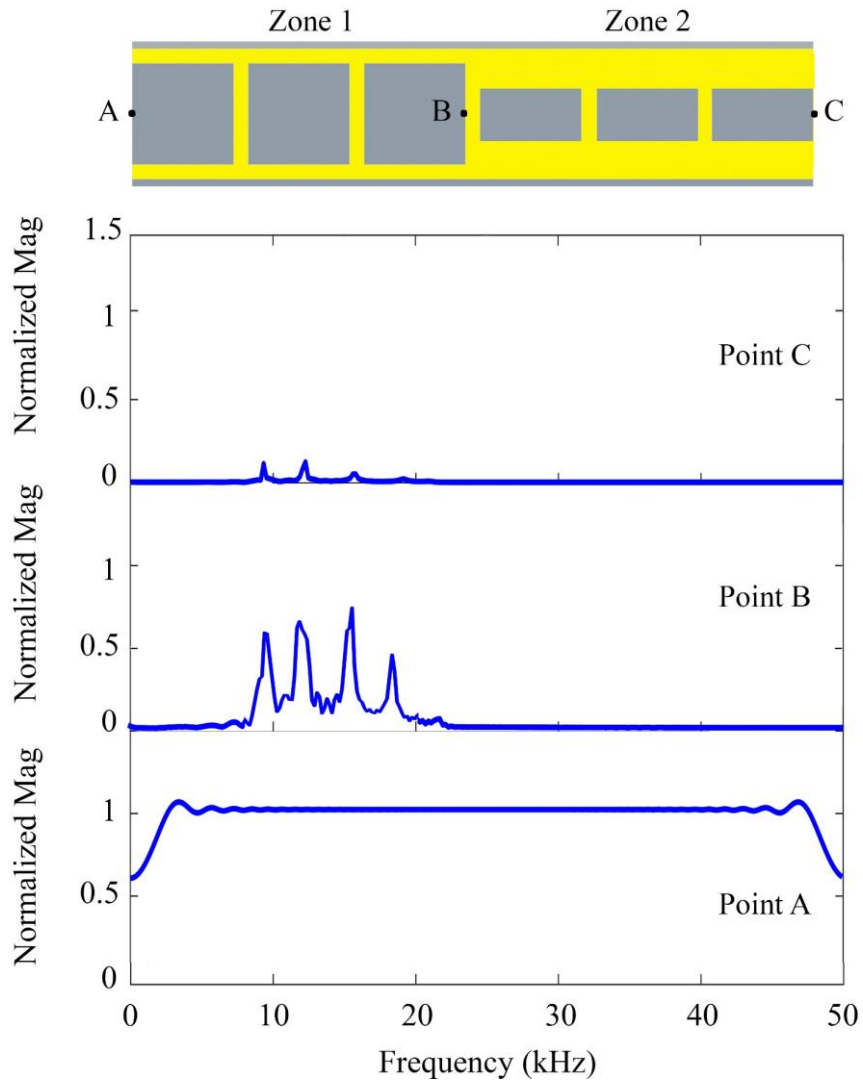
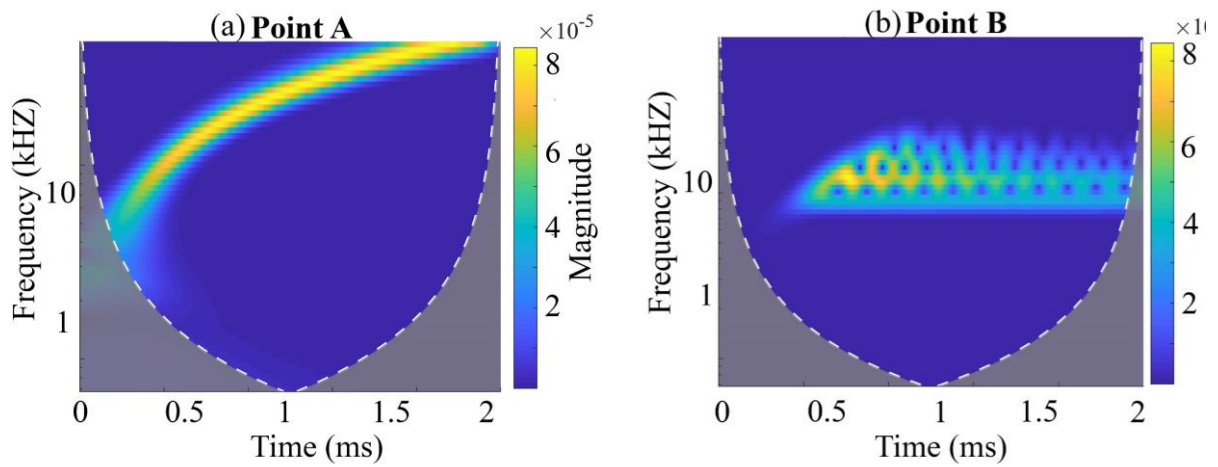


Figure 5-20. FFT spectrum of displacement at the three points, i.e. the input point (A), the middle point (B), and the output point (C) in the meta-truss bar with two resonator sizes



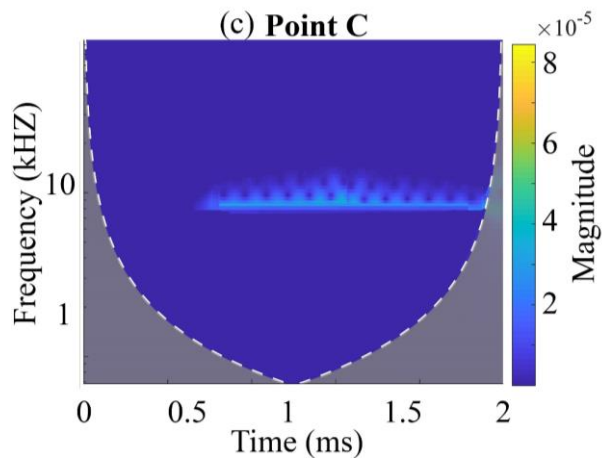


Figure 5-21. Scalograms for displacement in the time-frequency domain at different points (a) point A, (b) point B, and (c) point C

Three meta-panels with the above meta-truss bars, i.e., uniform meta-cores with the radius of 7 mm and 4 mm (R7 and R4) and combined cores with both radii of 7 mm and 4 mm subjected to blast loading are considered. For illustration, the peak displacement of the back facesheet of the meta-panels is shown in Figure 5-22 while the reaction force of the panel around the edges is given in Table 5-3. As shown, the meta-panel consisting of two resonator zones demonstrates better performance in all criteria, with the smallest displacement of the back facesheet, the lowest reaction force, and the highest energy absorption among the three considered meta-panels. In particular, the results show that the peak displacements at the centre point of the back facesheet of the panel with uniform resonator (i.e. R7 and R4) are 3.7 mm and 3.9 mm respectively, compared to 2.7 mm of the panel with meta-truss bar consisting of two sizes of cores.

As expected, the meta-panel with two types of meta-cores shows a significant reduction in reaction force. The peak reaction force of 137 kN is around 22% and 28% less than that of the panel with meta-truss consisting of the uniform resonator of R7 and R4, respectively because of the wider frequency bandgap of the truss bar with combined cores than the meta-truss bar with uniform cores as discussed above. The energy absorption by “coating + core” of the meta-truss bar with non-uniform cores is also higher, which leads to smaller energy absorption by the back facesheet of the non-uniform resonator panel, indicating smaller plastic deformation of the back facesheet and better protection of the panel. In addition, the meta-panel with uniform resonators (R7) outperforms its peer with R4 against blast loading. This is because the bandgap becomes wider with the increased mass of the resonator [71]. Overall, the panel with the meta-

truss bar composing two types of cores with wider frequency bandgaps possesses better blast mitigation and higher energy absorption capability.

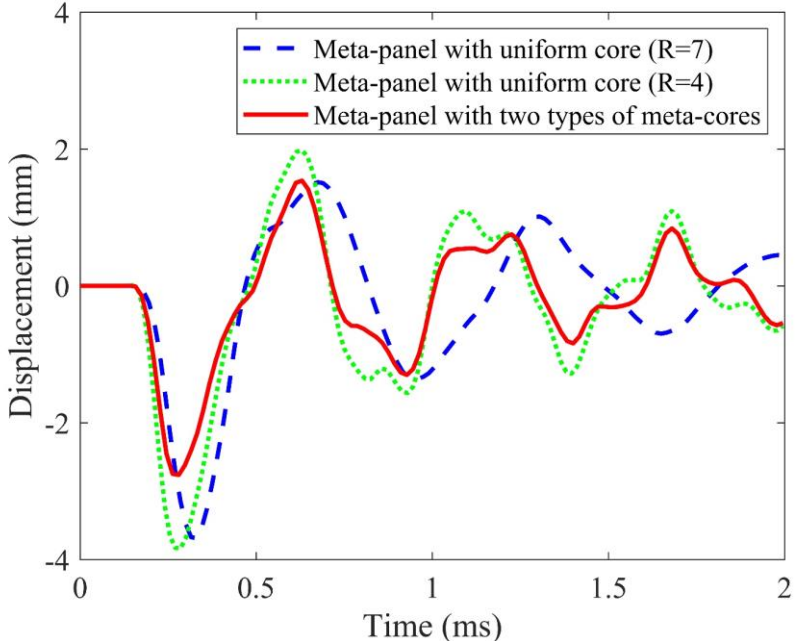


Figure 5-22. Comparison of displacement-time history curves of the back facesheet between the three meta-panels

Table 5-2. Influence of non-uniform inclusion on reaction force and energy absorption

Inclusion arrangement	Reaction force (kN)	Energy absorption (J)				
	F_z	Front facesheet	Back facesheet	Truss	Coating + Core	Total
Uniform (R=7 mm)	177.5	80	70	50	80	280
Uniform (R=4 mm)	190.4	81	74	50	60	265
Non-uniform	137.0	79	61	50	120	310

5.5.2.2 Influence of inclusion shape

Previous studies have investigated the inclusion configurations and their effects on the bandgap locations and the bandwidth of locally resonant acoustic meta-materials [71, 80, 180-182]. There is only limited research of this effect on the meta-truss bar and dynamic behaviours of meta-panels [80]. In this subsection, four regular shapes including cylinder, cuboid, pentagonal prism, and hexagonal prism are considered to evaluate the influence of the core geometry on the bandgap characteristics and the transient responses of the meta-panel made of truss bars with those meta-cores. The schematic diagrams of the unit cell with various inclusion shapes

of meta-truss bars embedded in the soft coating are illustrated in Figure 5-23. While the inclusion shape is different, other parameters of the meta-panel (Section 5.2) and the blast loading (Section 5.4) are kept the same in this investigation. It is worth mentioning that the mass and the length of the inclusion are respectively kept constant at 5.97×10^{-3} kg and 14 mm for all considered cases.

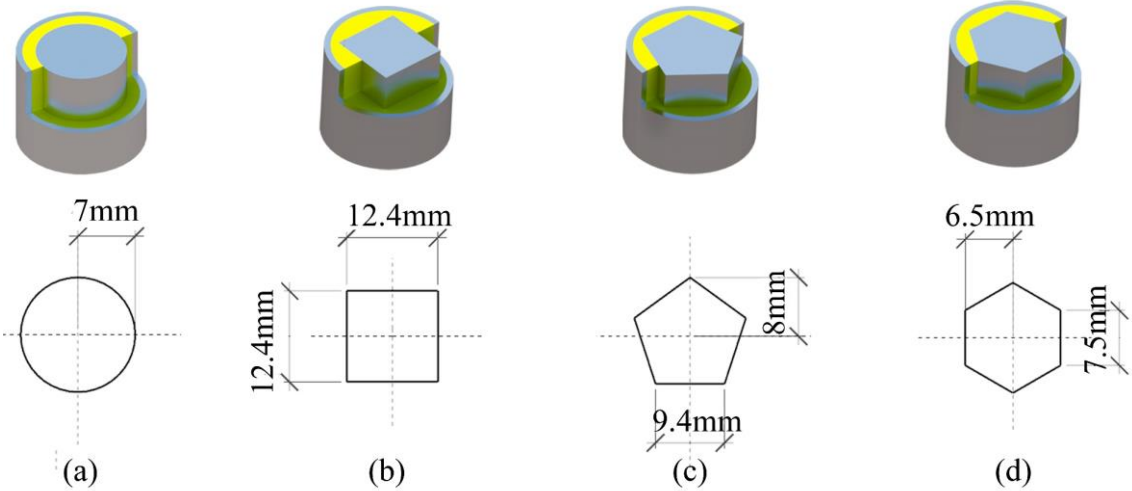


Figure 5-23. Representation and dimensions of meta-unit cells with various inclusion shapes including (a) cylinder, (b) cuboid, (c) pentagonal prism, and (d) hexagonal prism

Figure 5-24 shows the frequency band structures and the percentage of blast energy in the bandgaps of the meta-truss bar with different inclusion shapes, in which the bandgap regions are shown by solid bars while dashed line and solid line denote the complete passbands and the blast loading energy in the bandgap region, respectively. It is worth mentioning that the percentage of the blast loading energy falling in the bandgap is calculated by dividing the energy falling in the bandgaps by the total blast loading energy. It can be observed that the frequency band structures change pronouncedly for different cases, indicating the effect of the shape inclusion on the bandgap regions. In Figure 5-24, the lower bound and upper bound of the band structures are evaluated by solving Eqs. (1) and (2). As shown, the cuboid core generates the widest first bandgap from 0 to 10.9 kHz, while the cylinder core has a narrowest first bandgap from 0 to 9.1 kHz among the four considered core geometries. This can be attributed to the relationship between the shear stiffness (k_2) which is related to the lateral surface area and the width of the 1st bandgap. It was reported that the 1st bandgap width increases with the shear stiffness [83]. Of all the considered shapes, the cuboid has the largest surface area in the transverse direction which corresponds to the largest shear stiffness.

On the other hand, there are no substantial variations regarding the 2nd bandgap width and the lower bound frequency of the 2nd bandgap by varying the inclusion shape. Therefore, the meta-truss with the cuboid core has the narrowest passband and hence the best wave mitigation capacity, as shown in Figure 5-24. These results are consistent with those reported in the previous findings on locally resonant acoustic meta-material [80] and meta-concrete [71]. Specifically, cuboid inclusion could decrease the passband width from 14.1 kHz to 13 kHz as compared to the cylindrical shape. It shows that the pentagonal and hexagonal prism inclusions generate a narrower passband width by 0.7 kHz and 0.2 kHz, respectively as compared to the cylinder inclusion. Although there is no significant difference regarding the bandgap width in the 2nd bandgap, the shape of the inclusion could influence the 1st region of the bandgap which is the dominant frequency region of the blast loading, therefore is more critical to blast loading mitigation of the meta-panel.

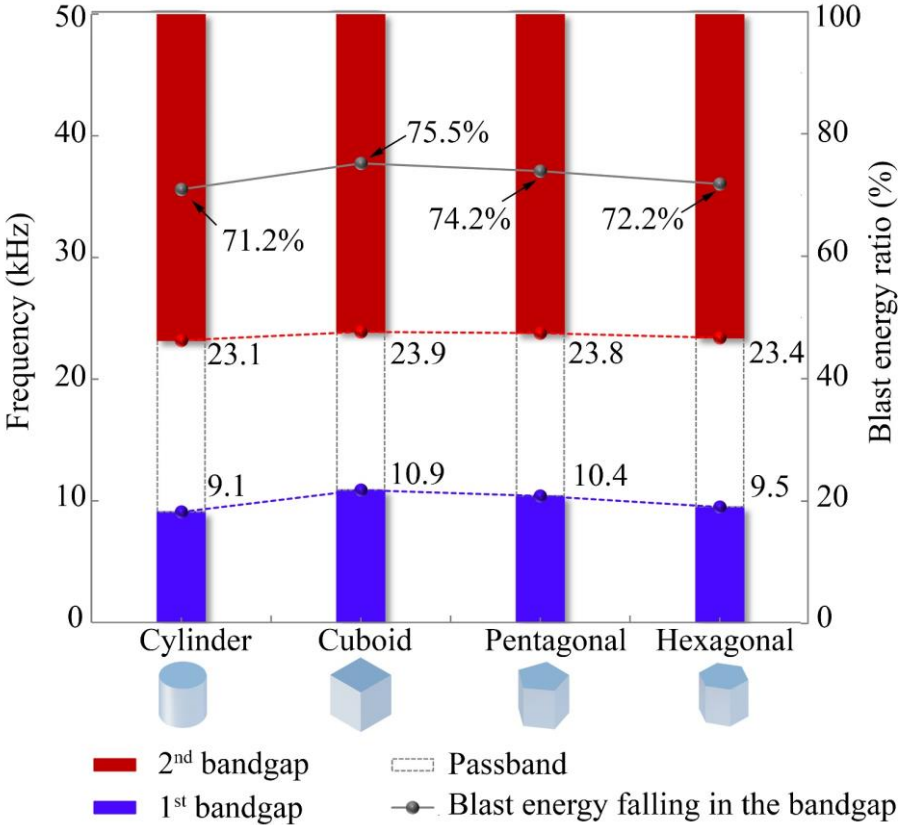


Figure 5-24. Frequency band structures of the meta-truss bar with different inclusion shapes

Figure 5-25 presents the blast energy percentage in the passband of the meta-truss bar with the considered inclusion shapes. The blast loading energy in the passband of the meta-truss bar can be calculated by the area enclosed by the FFT spectrum of the blast loading in the passband as illustrated in Figure 5-25. As shown in Figure 5-24, the highest percentage of blast energy

falling into the bandgap of the meta-truss bar with a cuboid shape core is 75.5%, because the meta-truss bar with cuboid shape cores has the widest 1st bandgap. The maximum passband corresponds to the inclusion with cylindrical shape and the blast loading energy fall in this passband is 28.8%, followed by 27.9% and 25.5% for the pentagonal and hexagonal shapes, respectively. The truss bar with the cuboid cores has the least percentage of blast energy transmission of 24.5%.

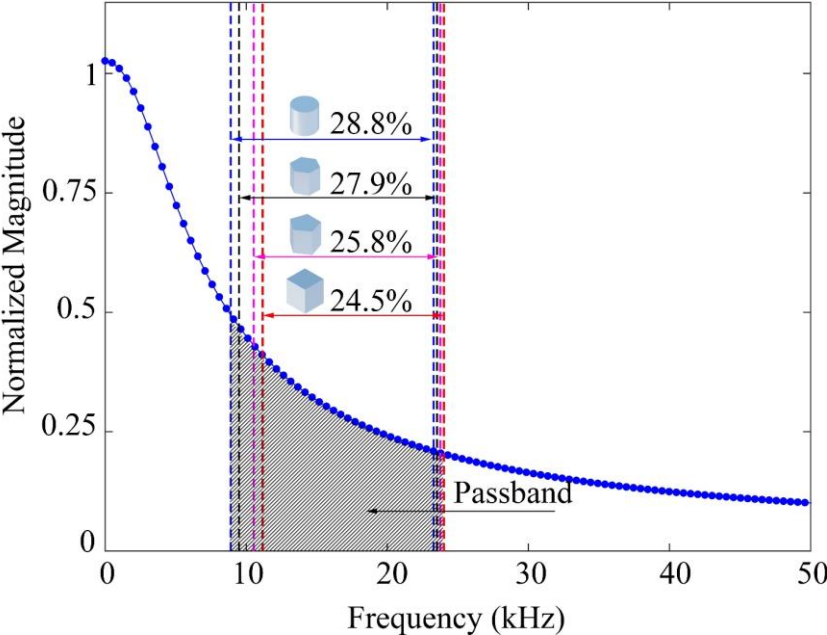


Figure 5-25. Effect of inclusion shape on blast energy percentage in the passband of the meta-truss bar

As expected, it can be observed from Figure 5-26 that the meta-panel with cuboid inclusion shows a reduction in the central displacement of the back facesheet and reaction force compared to the panels with other meta-truss bars. The varying inclusion geometries effectively affect the bandgaps, especially the 1st bandgap which covers the dominant frequency band of the blast loading, leading to the enhanced performance of the meta-panel. Consequently, the total energy absorption of the meta-panel with cuboid inclusion is the highest (i.e. 296 J) while the smallest energy absorption is associated with the meta-truss bar with cylindrical cores as shown in Figure 5-27. It is worth noting that the energy absorption of other components including the front facesheet and the outer tube is similar among all the considered panels due to the same stiffness. The back facesheet of the panel with cylindrical inclusion experiences the largest deformation, implying higher energy absorption of the back facesheet compared to other considered cases. As expected, the meta-core with the cuboid inclusion absorbs the most amount of energy, in

which the most energy is the combination of the kinetic energy of the core and the internal energy of the coating. The least amount of energy absorption by the coatings and the cores corresponds to the cylindrical case, which is 80 J, followed by 85 J, and 90 J respectively for the hexagonal, and pentagonal cases. The best mitigation effectiveness of the meta-panels with cuboid resonators over the other resonator shapes is expected due to the smallest percentage of blast energy falling in its passband, as shown in Figure 5-25. For a typical blasting wave, as shown in the FFT spectrum, the energy associated with the low-frequency range is significantly greater than that in the high-frequency range. Thus, though the resonator shape does not significantly affect the bandgap in the high-frequency range, it enhances the dynamic performance of the meta-panel by attenuating more energy falling in the low-frequency range. Particularly, the meta-truss bar with the cuboid resonator has the widest first bandgap among all the considered resonator shapes, indicating its best performance in resisting blast loading. In general, the transient responses of the meta-panel significantly rely on the band structures of the meta-truss bar which are affected by the geometry of the inclusion. Although the cuboid shape exhibits better performance, due to the complex fabrication process and aligning with the cylindrical shape of the truss bar, the inclusion of the cylindrical shape is recommended for practical application.

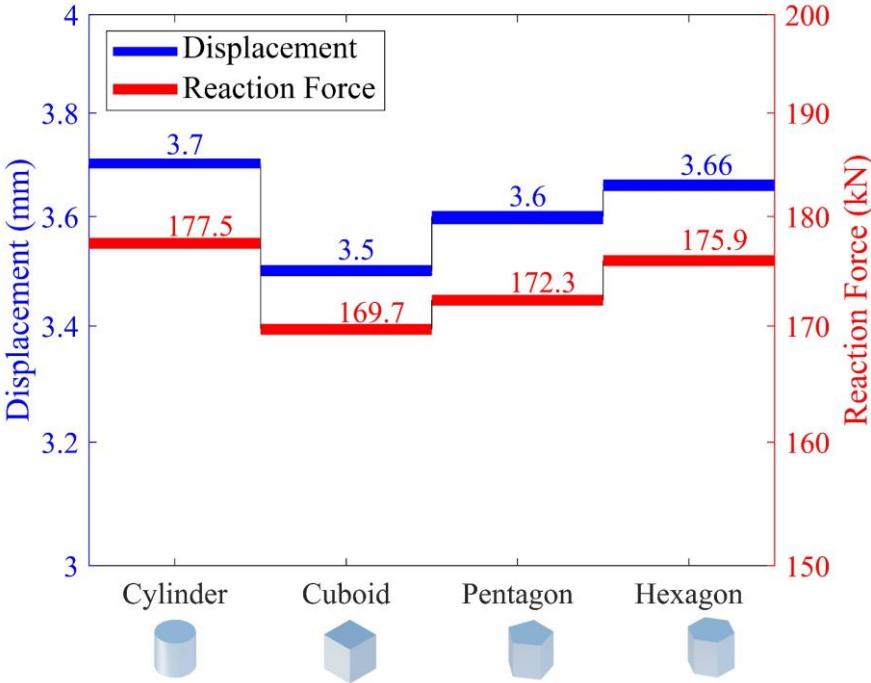


Figure 5-26. Comparison of displacements and reaction forces between four meta-panels

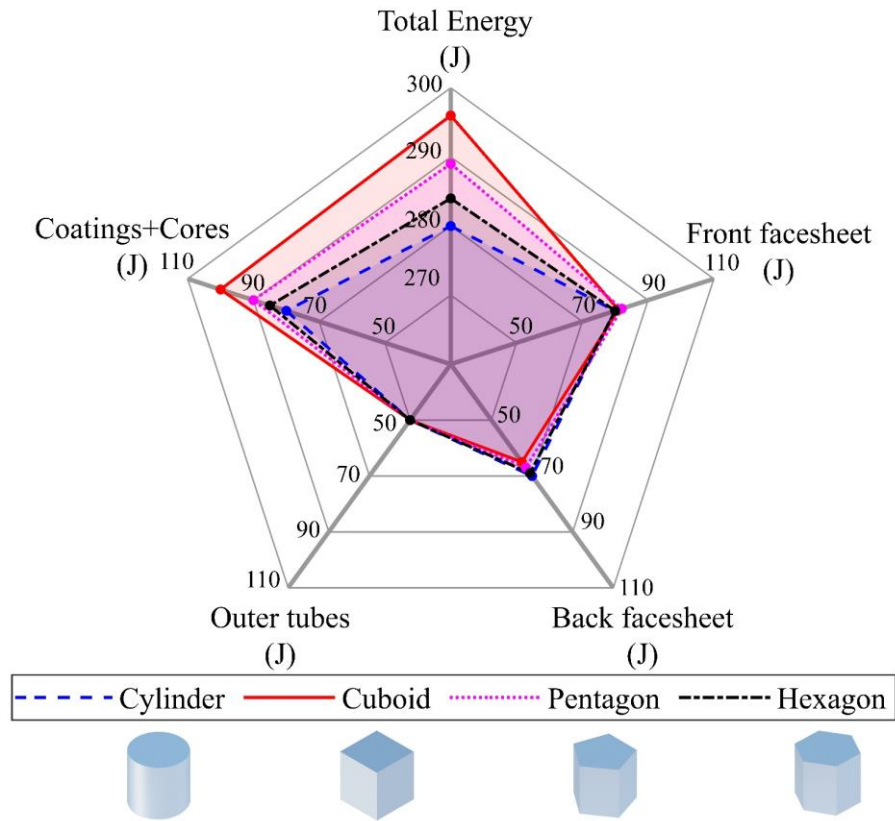


Figure 5-27. Comparison of energy absorption of the meta-panel embedded with various inclusion shapes under blast loading

5.6. Conclusions

In this chapter, the dynamic responses of meta-panels subjected to blast loads are parametrically examined. The main findings are summarized as follows:

1. Using non-uniform inclusions in the meta-truss bar composing of multiple types of resonators by changing core materials, sizes, and/or geometries may significantly change the transient performance of the meta-panel, therefore appropriately design the core arrangements of the meta-truss bar would lead to better wave propagation mitigation and hence structural protection.
2. The frequency band structure of the meta-truss core depends on the shape of inclusion and the cuboid inclusion is found to have the widest bandgaps among the four shapes considered in this chapter, therefore the meta-panel with cuboid resonator performs the best in blast loading effect mitigation. However, the inclusion of a cylindrical shape is recommended for practical application due to its easy fabrication.

The results obtained in this chapter demonstrate the possibility of properly adjusting the materials, sizes, and geometries of resonator cores in the meta-truss bar to achieve the desired bandgaps for effective wave propagation mitigation, hence better structural protection performance of the meta-panel.

CHAPTER 6. STRESS WAVE MITIGATION PROPERTIES OF DUAL-META PANELS AGAINST BLAST LOADS

Abstract⁵

A dual-meta panel functioning as a sacrificial cladding is proposed and its blast mitigation capacity is investigated in this chapter. The proposed panel possesses the potential to generate bandgaps that target at a specific range of frequencies to stop stress waves propagating through the panel, leading to the favourable stress wave mitigation for structural protection. Aside from the unique stress wave manipulation capability, more energy can be absorbed by a combination of plastic deformation and local resonance. The effectiveness of the proposed panel is validated through numerical simulations. An analytical solution of wave propagation in an ideal meta truss bar is derived to validate the numerical model with good agreement. It is found that the proposed dual-meta panel exhibits an increase in energy absorption, a reduction in transmitted reaction force (up to 30%), and the back facesheet central displacements (up to 20%) compared to other conventional sandwich panels, e.g. sandwich panel with hollow trusses and solid trusses, in resisting blast loadings. In pursuit of optimizing the performance of the proposed panel, parametric investigations are also conducted to examine the influences of the facesheet thickness, boundary condition, and the blast load profiles including duration and intensity on the transient response of the proposed dual-meta panel.

⁵ The related work in this chapter was published in **International Journal of Impact Engineering** with the full bibliographic citation as follows:

N.H. Vo, T.M. Pham, K. Bi, W. Chen, H. Hao. Stress Wave Mitigation Properties of Dual-meta Panels against Blast Loads. *International Journal of Impact Engineering*. 2021;154:103877.

<https://doi.org/10.1016/j.ijimpeng.2021.103877>

6.1. Introduction

With the increasing risk of extreme incidents (e.g. explosive and ballistic attacks) worldwide, there are escalating demands for more robust protective structures. Whereas solid monolithic structures [5] and porous materials [6] are currently popular candidates for protective structures, the underlying drivers to refrain from using these types of structures are that they are likely to be cumbersome and bulky. It is, therefore, essential to promote and apply sandwich panels for blast-resistants [177, 183]. The use of sandwich panels attached to main structures as sacrificial cladding was investigated by many researchers, e.g., Hanssen et al. [7]. The role of the panel is to deform in such a way that it absorbs energies from the incident loadings, therefore, minimizing transmitted energy to the protected structure.

Sandwich panels consist of two facesheets referred as front and back facesheets separated by a core, have provided promising solutions for energy absorptions from blast loadings. The core comprises materials categorized as cellular foam or lattice type while the facesheets are often made of thin metals or composite laminates. Generally, sandwich panels can be classified into two categories by the core topology including cellular material cores, e.g. foams [155], kirigami folded [143], honeycombs [145]; and periodic lattice cores, e.g. tetrahedral hollow trusses [161], pyramidal solid trusses [184]. Their means of energy absorption to mitigate dynamic damage rely significantly on plastic deformation mechanisms [156, 185]. For instance, substantial energy can be absorbed by aluminium foams through plastic dissipation [155], thus demonstrating promising potential against blast loadings. Recently, indebted to the proliferation of the fabrication technology, the core topology developments of sacrificial cladding in blast-resistant structures have attracted many researchers. The experimental investigation was carried out to examine the response of the sandwich panel with layered pyramidal truss cores subjected to blast loadings by Wadley et al. [186]. The blast and impact resistance of the sandwich panels was comprehensively presented in a review by Yuen et al. [8]. It was found that the sandwich panels outperform solid facesheets of the same material and the same mass [9], indicating the significant advantages of the sandwich panels over monolithic facesheets in blast-resistant functions.

Apart from solely applying the deformation mechanism for blast loading effect mitigation, researchers have approached the problem differently by filtering blast-induced stress waves using the localized resonance mechanism, thus resulting in the loading mitigation. These structures are called meta-structures [187], in which the prefix “meta” comes from the Greek

preposition and means “beyond”, indicating that the characteristics of these structures are beyond what can be seen in nature [188]. The primary concept of these structures is to utilize artificially designed and fabricated structural units to achieve the designed properties and functionalities. In 2016, Li and Tan [170] proposed a meta-truss bar which is a proportional elastic wave filter based on the unique local resonance of elastic meta-material to achieve an asymmetric low-frequency bandgap. Subsequently, Li et al. [111] proposed meta-lattice sandwich panels with single-resonators, which show the impact/blast attenuation and higher energy absorption owing to the local resonance of the internal resonator with soft coating. Regarding the dynamic resistance, sandwich structures with lattice cores show better performance compared to the conventional honeycomb sandwich structures [189, 190]. Besides, the application of the meta-material concept for blast protection has also been found in developing meta-concrete by Jin et al. [84], and Xu et al. [71]. However, despite all these recent works, the relevant research to the application of meta-materials for wave manipulation is still very limited, especially on the comprehensive investigations of the performance of meta-structures under blast loadings. Therefore, further studies on this topic are deemed necessary.

This chapter proposes a new meta-sandwich panel with dual-cores as a sacrificial cladding (Figure 6-1) by adopting the coupled mechanisms of absorbing strain energy through plastic deformation and local resonance. In this chapter, the transient responses of the proposed panel against blast loadings are investigated by numerical simulation utilizing LS-DYNA. The bandgap frequency ranges obtained from the numerical simulation are compared with the analytical solution for model validation. For comparison, the responses of the conventional panels – namely solid and hollow-truss panels are also simulated to evaluate their blast mitigation capacity compared to the proposed panel. The central displacements of the facesheets, peak reaction forces, and energy absorption are utilized to assess the performance of panels with different configurations. Parametric studies on the proposed panel are also performed to examine the effects of facesheet thickness, boundary condition, and blast loading profiles on its transient responses. The results prove that the proposed dual-meta panel possesses superior characteristics that enhance its protective effectiveness against blast loadings compared to its conventional counterparts. Although the physical phenomenon for mitigating effect of the dual-meta panel under blast loading was demonstrated in this chapter through numerical and analytical analysis, the results also lead to several interesting observations, some of which may pave the way for future work through experimental study to comprehensively understand and demonstrate the performance of the dual-meta panel.

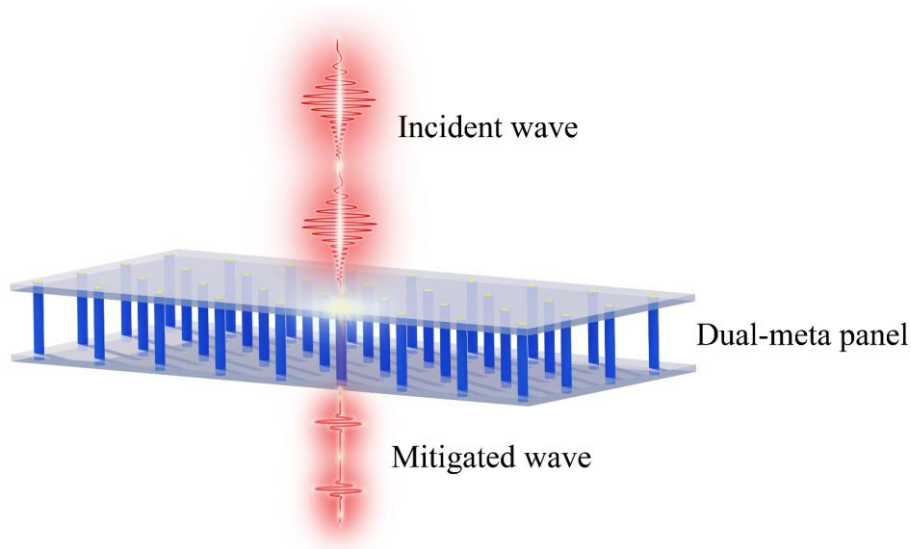


Figure 6-1. Schematic diagram of the Dual-meta panel

6.2. Design of the Dual-meta panel

Without loss of generality, the proposed dual-meta panel consisting of two thin facesheets is connected to the meta-truss bar as shown in Figure 6-2a. The meta-truss bar element considered in this chapter comprises 7 unit cells (Figure 6-2c). Each unit cell has five parts including the outer tube, two soft coats, and two resonators as shown in Figure 6-2b. The compositions and dimensions of each unit cell are presented in Figures 6-2b and 6-2c, respectively. Aluminium and lead are respectively selected for facesheets, the tube and the resonators, while the two soft coatings are made from Polyurethane (PU) which can deform elastically to large strain. As a sacrificial cladding, the perimeter of the back facesheet is clamped whereas there is no boundary condition imposed on the front facesheet. All material properties are summarized in Table 6-1 and also used in the numerical model in this chapter.

Table 6-1. Elastic material properties used in the numerical simulation [111], [84]

Properties	Material 1	Materials 2 & 4	Materials 3&5
	Aluminium (Al)	Polyurethane (PU)	Lead (Pb)
Density ρ (kg/m ³)	2,770	900	11,400
Young's modulus E (Pa)	70×10^9	1.47×10^8	16×10^9
Poisson's ratio ν	0.33	0.42	0.44

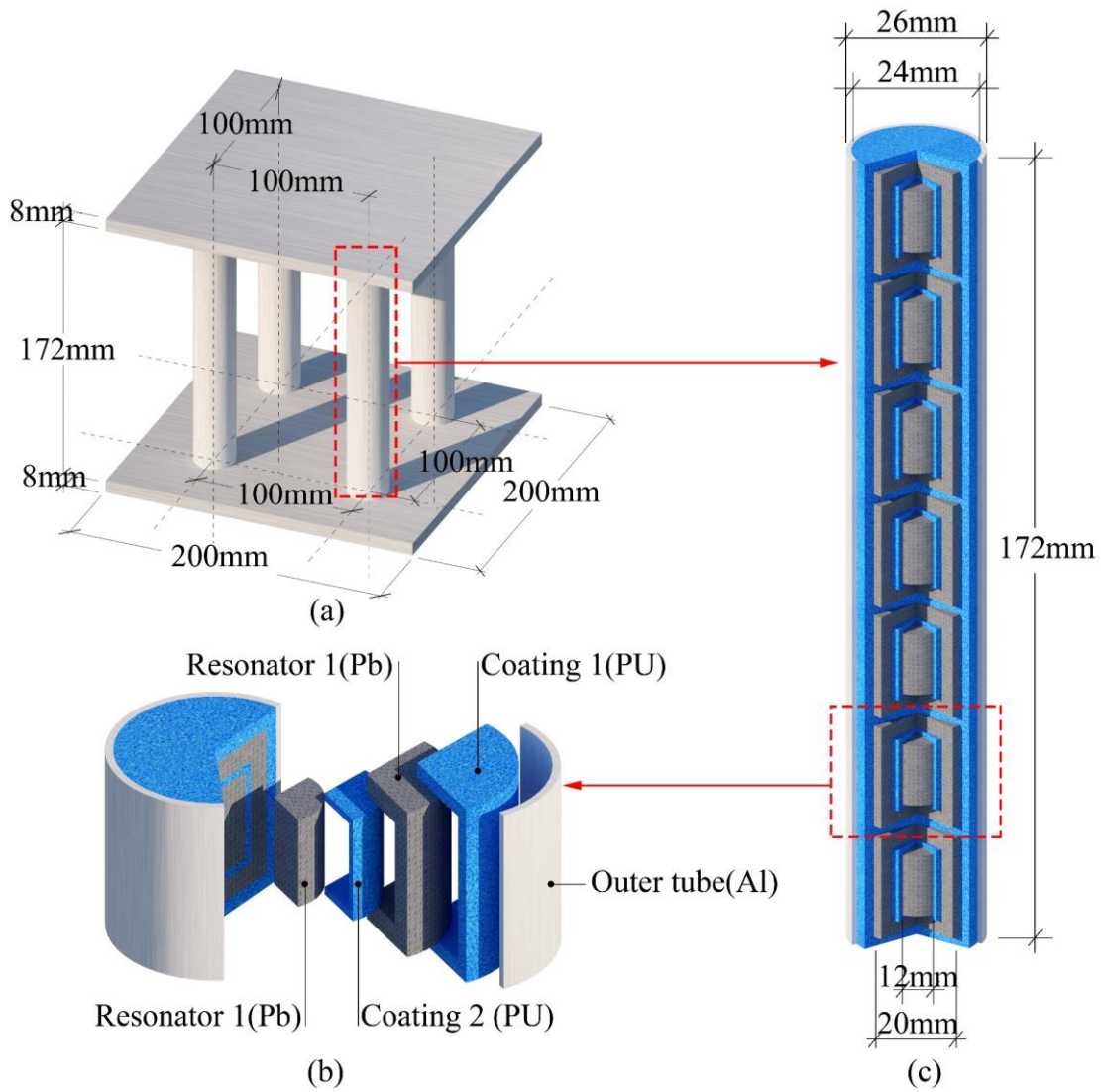


Figure 6-2. (a) Schematic view of the dual-meta panel, (b) unit cell, and c) meta-truss bar

6.3. Analytical method

A spring-mass model can be utilized to analytically describe the diatomic unit cell as depicted in Figure 6-3a. In the model, the matrix is represented by material 1, i.e., the aluminium truss bar while the two masses of m_1 and m_2 represent the external and internal masses made of material 3 and material 5, respectively. The outer soft coating made of material 2 is modelled by two springs including the outside shear spring k_{s1} connecting the resonator with the outer truss bar and the axial spring k_{a1} connecting the adjacent resonators. Similarly, two springs k_{a2} and k_{s2} are respectively introduced to describe the axial and shear springs of material 4 connecting the internal mass and external mass.

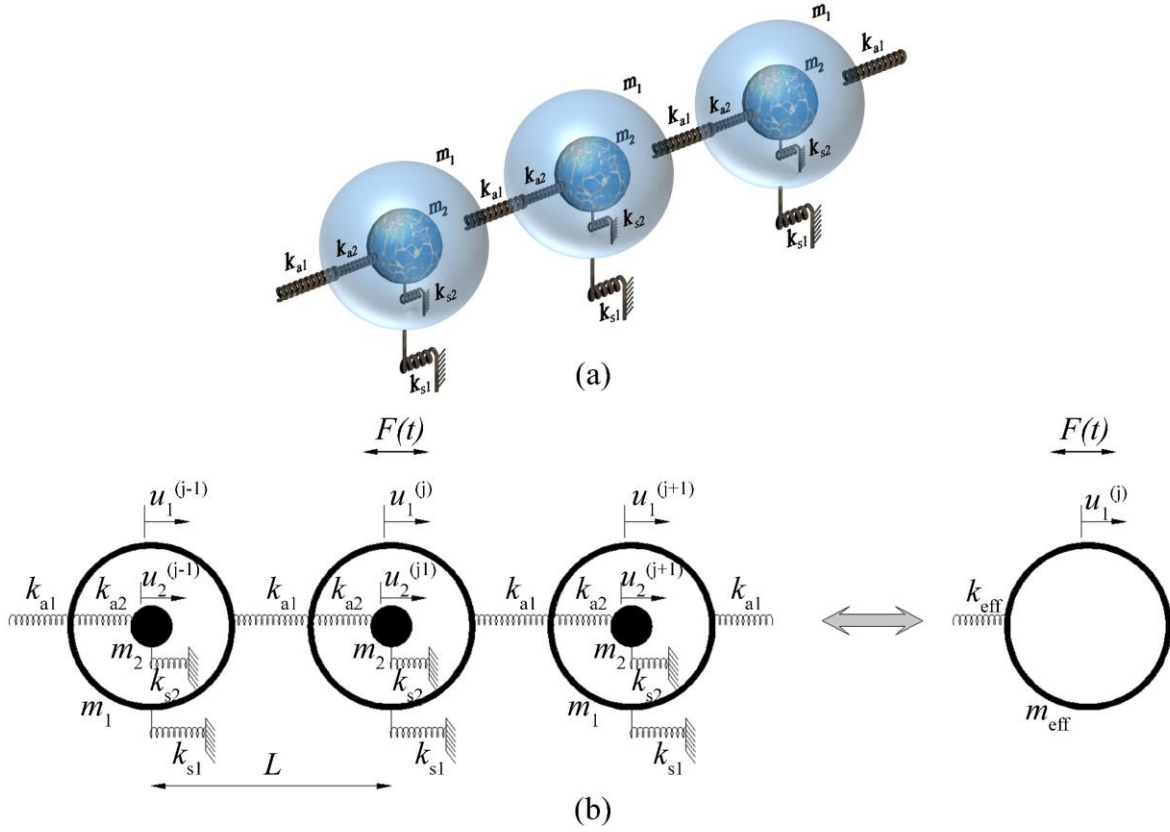


Figure 6-3. (a) Schematic microstructure of infinite dual-core meta-materials, (b) Equivalent effective mass-spring model

The approximate values of the inner mass and outer mass can be calculated as

$$m_\alpha = \rho_\alpha V_\alpha = \rho_\alpha \pi r_\alpha^2 l_\alpha \quad \alpha = 1, 2 \quad (6-1)$$

where ρ_α and V_α are the material density and volume of the α^{th} material while the length and radius of the α^{th} unit are denoted by l_α and r_α , respectively.

Besides, the stiffness of equivalent spring can be calculated as follows:

$$k_{a1,2} = \frac{E_3 A_{1,3}}{l_{2,3}}, \quad k_{s1,2} = \frac{G_3 A_{2,4}}{l_{1,4}}, \quad G_3 = \frac{E_3}{2(1+\nu_3)} \quad (6-2)$$

where Young's modulus and shear modulus of the soft material are denoted as E and G , respectively. Due to the shape complexity, the nominal cross-sections of the distinct segments of the soft layer A_i ($i=1,2,3,4$) presented in the appendix are obtained by FEA. The relevant estimations of the equivalent mass and stiffness are computed as $m_1 = 4.71 \times 10^{-2}$ kg, $m_2 = 1.55 \times 10^{-2}$ kg, $k_{a1} = 57,375$ kN/m, $k_{s1} = 35,498$ kN/m, $k_{a2} = 40,760$ kN/m, and $k_{s2} = 24,802$ kN/m.

For an infinite lattice system in which u_1 and u_2 represent the internal and external mass displacements (as shown in Figure 6-3b). The equations of motion for the j^{th} unit cell can be expressed as:

$$m_1 \ddot{u}_1^{(j)} + k_{a1} \left(2u_1^{(j)} - u_1^{(j+1)} - u_1^{(j-1)} \right) + k_{a2} \left(u_1^{(j)} - u_2^{(j)} \right) + k_{s1} u_1^{(j)} = 0 \quad (6-3)$$

$$m_2 \ddot{u}_2^{(j)} + k_{a2} \left(u_2^{(j)} - u_1^{(j)} \right) + k_{s2} u_2^{(j)} = 0 \quad (6-4)$$

For harmonic wave solution based on the theory of Floquet-Bloch [112], the displacement of the j^{th} unit cells are given as follows:

$$u^{(j)} = U e^{i(jqL - \omega t)} \quad (6-5)$$

where the displacement amplitude and the wavenumber are denoted by U and q , respectively while ω is the angular frequency and L is the length of the unit cell.

The dispersion relation can be obtained by applying the identity $e^{-iqL} + e^{iqL} = 2 \cos(qL)$ and substitute Eq. (6-5) into Eqs. (6-3) and (6-4) as

$$\cos qL = 1 - \left[m_1 \omega^2 - (k_{s1} + k_{a2}) + \frac{k_{a2}^2}{(k_{a2} + k_{s2}) - m_2 \omega^2} \right] \frac{1}{2k_{a1}} \quad (6-6)$$

Based on dispersion relation derivation from Eq. (6-6), the effective mass (m_{eff}) and effective stiffness (k_{eff}) of the equivalent system can be derived as [68]

$$m_{\text{eff}} = m_1 - \frac{k_{s1} + k_{a2}}{\omega^2} + \frac{k_{a2}^2}{(k_{a2} + k_{s2}) \omega^2 - m_2 \omega^4} \quad (6-7)$$

$$k_{\text{eff}} = k_{a1} + \frac{1}{4} (k_{s1} + k_{a2}) - \frac{1}{4} \left(m_1 \omega^2 + \frac{k_{a2}^2}{(k_{a2} + k_{s2}) - m_2 \omega^2} \right) \quad (6-8)$$

The transmission coefficients of the system, T , can be calculated as follows:

$$T = \left| \prod_{j=1}^N \frac{u^{(j)}}{u^{(j-1)}} \right| = \left| \prod_{j=1}^N T^{(j)} \right| \quad (6-9)$$

where the wave transmission of the j^{th} and N^{th} unit cells can be expressed as

$$T^{(j)} = \frac{k_1}{k_1(2 - T^{(j+1)}) - \omega^2 m_{eff}}, \quad j \in [1, N-1] \quad (6-10)$$

$$T^{(N)} = \frac{k_1}{k_1 - \omega^2 m_{eff}}, \quad j=N \quad (6-11)$$

Based on Eqs. (6-7), (6-8), and (6-9), the analytical dispersion curve of the meta-truss bar can be calculated and it is depicted in Figure 6-4a, while Figures 6-4b and 6-4c show the corresponding effective mass and effective stiffness with respect to frequencies, respectively. It is evident that the first and the third bandgaps which are at [0-5] kHz and [13.5-50] kHz are independently formed when the effective mass and the effective stiffness become negative, respectively (see Figures 6-4b and 6-4c). Whereas the negativity of both of them collaboratively constitutes the second bandgap which is at [9.3-11.5] kHz (Figures 6-4b and 6-4c). It is worth mentioning that the interested frequency range in this chapter is only up to 50 kHz, covering the frequency band of common blast loads acting on structures [175].

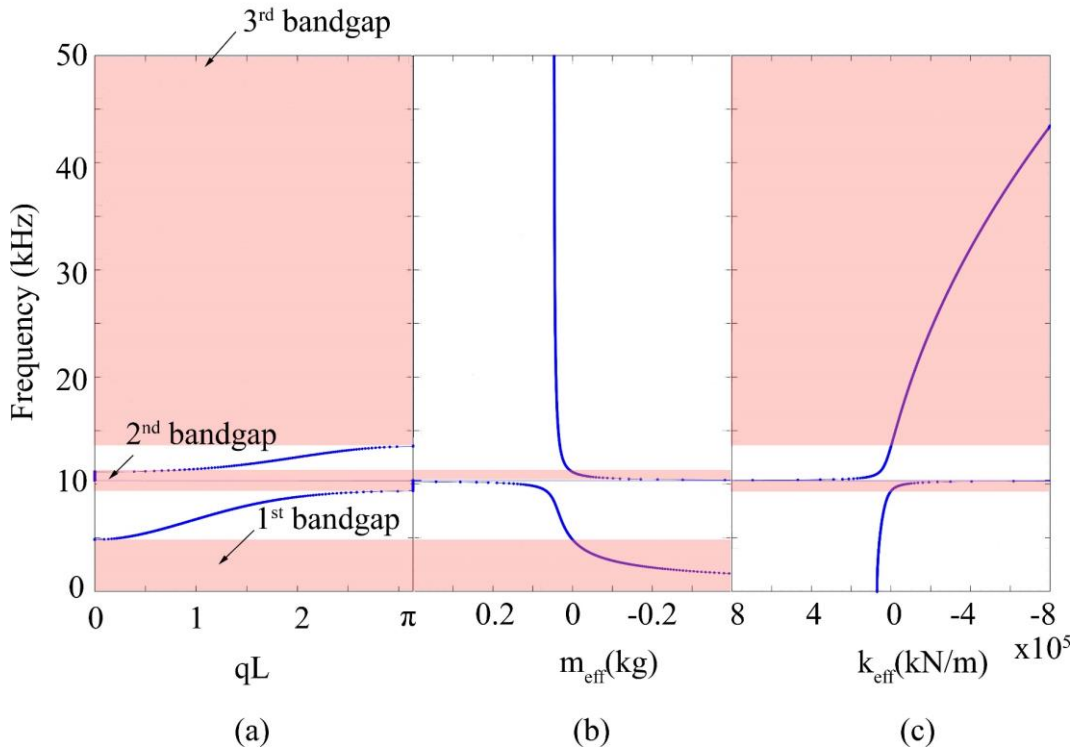


Figure 6-4. Analytical solution of the bandgaps range for meta-truss bar (a) dispersion curve, (b) effective mass, and (c) effective stiffness

6.4. Numerical approach

Owing to the complexity, the infinite unit cells and single harmonic wave assumptions have been applied to analytically solve the Eigen frequency and calculate the bandgaps. Since no study of structural responses and stress wave propagations in the dual-meta panel against the blast loadings has been reported yet, and it is not straightforward to derive such responses analytically, especially when the combined effect of material plastic deformation and meta-truss bar bandgaps on wave energy dissipation and absorption is considered. The above derivations based on idealized conditions are used in the numerical model to implicitly verify the accuracy of the model. The design of the proposed dual-meta panel and its dimension were presented in Section 6.2 and shown in Figure 6-2.

6.4.1 Model development

In this chapter, commercial software LS-DYNA is employed to investigate the characteristics of the dual-meta panel. Constitutive material models, contact definition, initial conditions, element sizes, and blast load modeling are also presented in this section.

6.4.1.1 Constitutive material models

The *MAT_JOHNSON_COOK material (Mat_15) is adopted to capture the behaviour of aluminium while the dynamic behaviour of polyurethane elements is simulated by *MAT_ELASTIC material model due to their distinguished properties [111]. The elastic and plastic material properties are summarized in Tables 6-1 and 6-2, respectively. To initialize the thermodynamic state of the material, the Johnson-Cook material model requires an equation of state [113] which is defined by the card *EOS_LINEAR_POLYNOMIAL in which the pressure and initial relative volume are denoted by coefficients C0-C6 and V0, respectively and is presented in Table 6-3. Furthermore, for simulation of the lead cores, the model *MAT_PLASTIC_KINEMATIC is used and the material properties are given in Table 6-4 [114].

The Johnson-Cook material model can be expressed as [191]

$$\sigma = \left[A + B(\varepsilon^p)^n \right] (1 + C \ln \dot{\varepsilon}^*) (1 - T^{*m}) \quad (6-12)$$

where the dynamic yield stress and the equivalent plastic strain are represented by σ and ε^p , respectively while $\dot{\varepsilon}^* = \dot{\varepsilon} / \dot{\varepsilon}_0$ is the dimensionless plastic strain rate, where $\dot{\varepsilon}_0$ is a reference

strain rate which is generally set to 1.0 s^{-1} . The temperature $T^* = (T - T_r) / (T_m - T_r)$ is defined as the homologous temperature, in which T_r and T_m are the material reference and the melting temperature, respectively. In this chapter, the room temperature ($T_r = 20 \text{ }^\circ\text{C}$) is applied as the reference temperature [113]. In Eq. (6-22), there are five material constants including the yield stress determined by the quasi-static compressive strain-stress data represented by A , the influences of strain hardening B and n , the effect of thermal softening m , and the strain rate effect which is represented by C .

Table 6-2. Johnson-cook material parameters for aluminium [111]

Density (kg/m^3)	Poisson's ratio	Young's modulus (GPa)	A (GPa)	B (GPa)	C	m	n	T_m	$\dot{\epsilon}$
2,770	0.33	70	0.369	0.675	0.007	1.5	0.7	800	1.0

Table 6-3. Equation of state for aluminium used in the numerical simulation [113]

C_0 (Pa)	C_1 (Pa)	C_2 (Pa)	C_3 (Pa)	C_4	C_5	C_6	E_0 (Pa)	V_0 (m^3/m^3)
0	74.2×10^9	60.5×10^9	36.5×10^9	1.96	0	0	0	1

Table 6-4. Plastic kinematic material parameters for lead [114]

Density (kg/m^3)	Poisson's ratio	Young's modulus (GPa)	SIGY (MPa)	ETAN (MPa)	BETA	SRC	SRP	FS	VP (1/s)
11,400	0.44	16	20	50	10^9	10^9	1	0	1

6.4.1.2 Constraint and initial conditions

The *BOUNDARY_SPC_SET option in LS-DYNA was adopted to account for the fully clamped boundary along the perimeter of the back facesheet. The contact between the metals and polyurethane is defined by the keyword *TIED_SURFACE_TO_SURFACE and the keyword *CONTACT_INTERIOR option was utilized for polyurethane to model the slippage and contact failure between materials. Besides, the contact between the outer truss bar and the two facesheets is defined by the keyword *TIED_NODE_TO_SURFACE to make rigid connections. In this chapter, all the elements are modeled by the solid hexahedron element

(SOLID 164), and the minimum meshing size of 1 mm for all elements is chosen after performing a mesh convergence test, as will be detailed later.

6.4.1.3 Blast load modeling

The keyword *LOAD_BLAST_ENHANCED is widely utilized in LS-DYNA to generate blast load [177, 183] via the CONWEP feature. The definition of the loading area on the front facesheet is determined by the keyword *LOAD_BLAST_SEGMENT whereas the function *DATABASE_BINARY_BLSFOR is utilized to compute the blast pressure data. The transient blast pressure on the dual-meta panel is determined by the amount of Trinitrotoluene (TNT), the stand-off distance, and the angle of incidence. The blast pressure is computed by the following equation [135].

$$P(t) = P_r \cos^2 \theta + P_i (1 + \cos^2 \theta - 2 \cos \theta) \quad (6-13)$$

where θ is the angle of incidence. The incident pressure and the reflected one are denoted by P_i and P_r , respectively. These peak pressures are calculated by the scaled distance, $Z = R/W^{1/3}$, in which R and W are the stand-off distance and the amount of TNT, respectively. In this chapter, 0.15 kg TNT is detonated at a distance of 0.35 m above the front facesheet of the dual-meta panel, which corresponds to the scaled distance of 0.65 m/kg^{1/3}. The reflected pressure time history at the center point of the front facesheet and the corresponding FFT spectrum is illustrated in Figure 6-5. As shown, the peak reflected pressure is approximately 13.5 MPa and the dominant blast loading energy distributes in the frequency band up to 50 kHz.

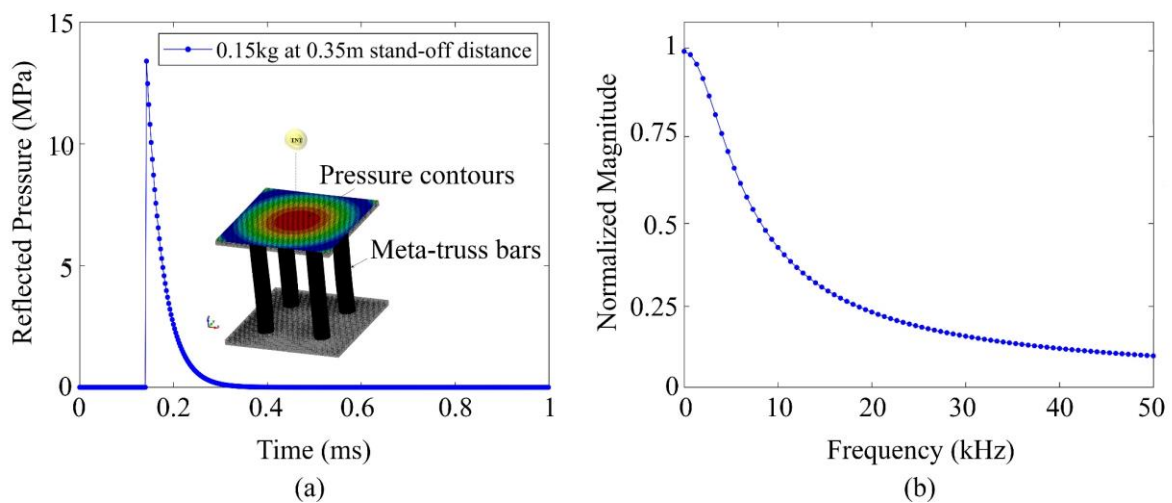


Figure 6-5. Peak reflected pressure profile (a) Time history, and (b) FFT spectrum

6.4.2 Mesh convergence test

A convergence test is necessary to be carried out to determine the size of elements in finite element modeling for computational accuracy and efficiency. To obtain the optimal solution, different mesh sizes comprise 3 mm, 2 mm, 1 mm, 0.5 mm, and 0.25 mm representing coarse, medium, and fine meshes are considered in the convergence test. The calculated displacements at the central point of the back facesheet of the dual-meta panel corresponding to the various mesh sizes are shown in Figure 6-6. It can be seen from the figure that the displacement becomes converged when the mesh size is 1 mm. Further reducing the mesh size does not considerably affect the predicted displacement but increases significantly the computational cost. The mesh size of 1 mm is, therefore, utilized in the subsequent investigations.

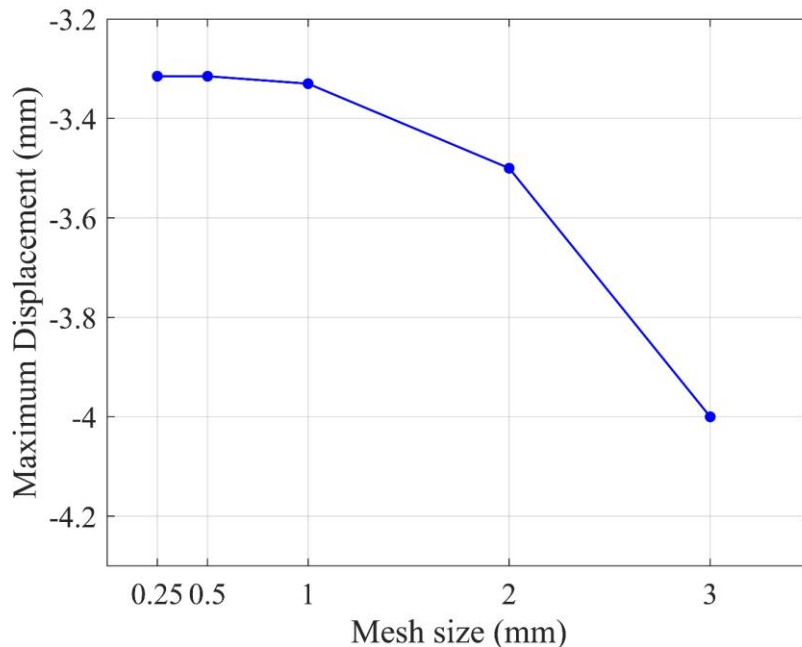


Figure 6-6. Effect of mesh sensitivity on the maximum displacement of the back facesheet

6.4.3 Model validation

To validate the numerical simulation, the transmission coefficient of a single meta-truss bar calculated by the numerical simulation is compared with that obtained by the above analytical derivation. The transmission coefficient is the ratio between the output and the input signals of the structure. For the numerical simulation, the input signal defined by a sweep frequency ranging from 0 – 50 kHz is applied at one end of the meta-truss bar, and the displacement response at the other end is calculated to derive the transmission coefficient. The numerical transmission coefficient of the meta-truss bar is shown in Figure 6-7 along with the analytical

result. The numerical simulation shows that the meta-truss bar possesses three bandgaps at the frequency ranges of [0-5] kHz for the 1st bandgap, [8.1-11.8] kHz for the 2nd bandgap, and [13.3-50] kHz for the 3rd bandgap, while the corresponding ranges from the analytical solution are [0-5] kHz, [9.3-11.5] kHz, and [13.5-50] kHz as presented above. These results indicate that the numerical results agree closely with the theoretical transmission coefficient, implying the validity of the model. The slight variations in the bandgaps between the analytical and the oscillations of the numerical results are because the meta-truss bar is assumed continuous with an infinite number of unit cells connected by springs in the analytical derivation, while the numerical meta-truss bar has a finite length with 7 unit cells only, and each component is modelled with its respective elastic material property and density instead of the lumped mass connected with idealized springs.

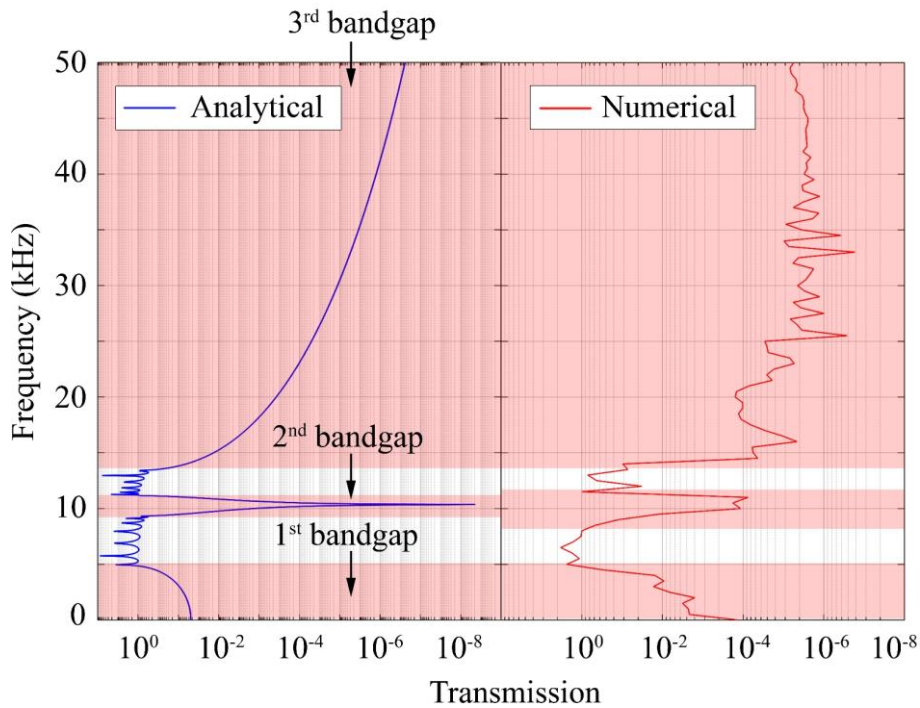


Figure 6-7. Transmission profiles of meta-truss bar under sweep frequency input: analytical analysis vs numerical simulation

To further testify the frequency suppression capacity of the meta-truss bar, an excitation is generated by a prescribed displacement time history with multi-frequency components [92] as

$$u(t) = 10^{-4} \left[\sin(2\pi f_1 t) + \sin(2\pi f_2 t) + \sin(2\pi f_3 t) \right] H(t) \quad (6-14)$$

where the unit-step function $H(t)$ is defined as

$$H(t) = \begin{cases} 1, & t \geq 0 \\ 0, & t < 0 \end{cases} \quad (6-15)$$

and $f_1=2$ kHz, $f_2=7$ kHz, and $f_3=10$ kHz. This excitation is applied at one end of the meta-truss bar to calculate the response at its other end. Figure 6-8a shows the displacement time history at the two ends of the meta-truss bar (i.e. the input and the output, respectively). It is worth mentioning that f_1 and f_3 are intentionally designed to fall within the first and the second bandgap, respectively, while f_2 is within its passband range. Theoretically, only the signal with f_2 can pass while other signals will be stopped by the meta-cores. The FFT spectrum of the input and output signal are shown in Figure 6-8b. As shown, only one input signal with the frequency of 7 kHz can pass through the meta-truss bar while the other two signals at frequencies of 2 kHz and 10 kHz are suppressed by the meta-truss bar.

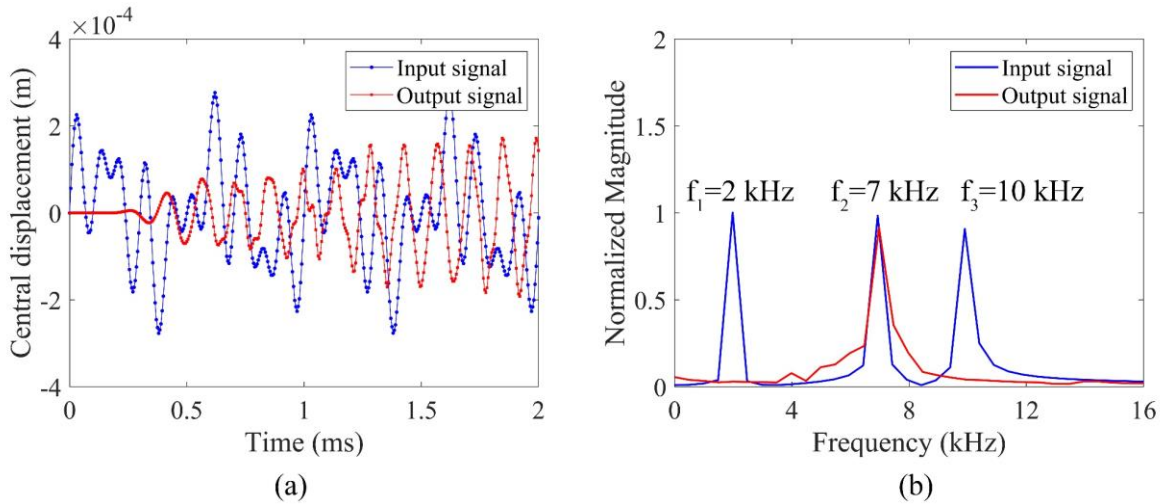


Figure 6-8. Input and Output displacement at the center points of two ends of the meta-truss bar (a) time histories and (b) FFT spectra

6.4.4 Results and discussions

To further demonstrate the favourable characteristics of the dual-meta panel in resisting blast load, responses of the proposed dual-meta panel consisting of four meta-truss bars (shown in Figure 6-2) subjected to the blast loads defined in Figure 6-5 are calculated. For comparison, two conventional sandwich panels with solid trusses and hollow trusses as shown in Figure 6-9a and 6-9b, respectively, are also modelled.

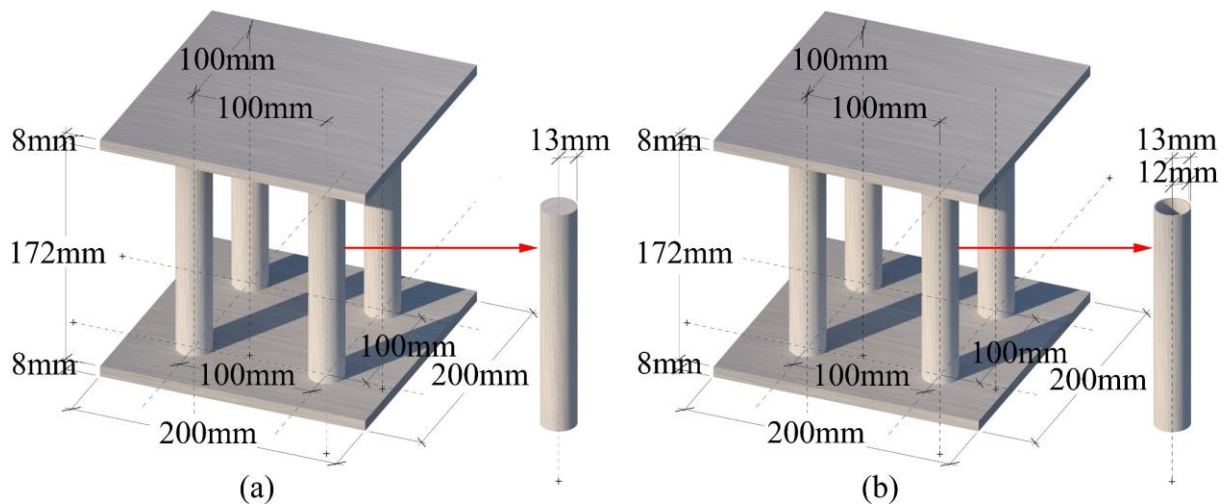


Figure 6-9. Schematic view of the panels with (a) Solid-truss bars and (b) Hollow-truss bars

As shown in Figure 6-10, the two conventional sandwich panels have the same geometries and dimensions as the proposed dual-meta panel. The only difference between the three panels is the truss bars connecting the two facesheets. The diameter of the solid truss bar is the same as the meta-truss bar, and the hollow truss bar is the same as the outer hollow tube of the meta-truss bar. It should be noted that the total weight of these three structures is not the same. To make the total weight of the three structures the same, the size of the solid and hollow truss bars need to be adjusted. Since the primary objective of this chapter is to investigate the performance of the meta-truss bar in mitigating the blast loading effect, the size of the truss bars is kept the same instead of making the weight the same in the analysis. It is because to keep the mass constant in the chapter, the thickness and/or diameter of the hollow truss and the solid truss need to be adjusted, which affects the stiffness of the core and hence the deformation and energy absorption of the structure. Specifically, the wall of the hollow truss will be thicker or its diameter larger compared to the current referenced hollow truss because the mass has to be increased to match the mass of the soft coats and the lead cores. Similarly, the diameter of the solid truss has to be increased because the density of the lead core is higher than the aluminium tube. This would increase the stiffness of the core and decrease the deformation and the energy absorption of these panels.

This phenomenon can be seen from the results that the hollow truss panel outperforms the solid truss panel as a sacrificial cladding for blast resistance due to its higher energy absorption capacity. However, it should be noted that increasing the mass enhances the inertial resistance of the structure, hence the structural capacity to resist the blast load. Although the primary design targets of a sacrificial panel are energy absorption and load transferred to the protected

structure, instead of the loading resistance capacity of the sacrificial structure itself, it would be interesting to also compare the performance of the proposed dual-meta panel with reference panels having the same mass. Nonetheless, the scenario of the three panels having the same mass is not considered in this investigation, but it is believed that increasing the mass of the traditional panels with hollow truss and solid truss bars would reduce their energy absorption capacity and increase the loading amplitude acting on the protected structures because of the increased stiffness of the core.

Figure 6-10 compares the displacement time histories at the center point of the back facesheet of the three panels. It is seen that the panel with solid trusses has a higher maximum displacement (i.e. 4 mm), followed by the panel with the hollow trusses (i.e. 3.81 mm). The corresponding maximum displacement of the dual-meta panel is 3.36 mm, i.e., 13.5%, and 20.0% lower than that of the hollow truss panel and solid truss panel, respectively. It is also noted that there is a substantial reduction in the second negative peak displacement in comparison between the dual-meta panel with the panels with solid truss (i.e. 40.9%) and hollow truss (i.e. 52.0%). These can be attributed to the fact that the effect of meta-cores results in lower impulse transfer to the back facesheet of the panel. Placing the meta-cores inside the truss bars of the panel results in a considerable reduction of the maximum peak central displacement of the back facesheet compared to the conventional panel, indicating the dual-meta panel has better protective performance.

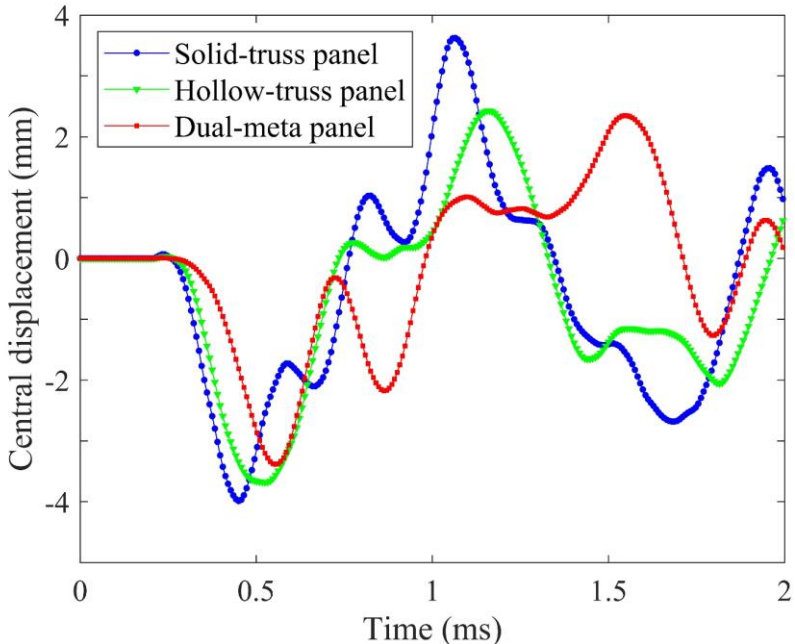


Figure 6-10. Time histories of central displacement of the back facesheet of the three panels

To gain a comprehensive insight into blast response mitigation, investigations on the energy absorption of the dual-meta panel are carried out. The total energy (E_t), the kinetic energy (E_k), and the internal energy (E_i) absorbed by each component of the dual-meta panel subjected to blast loading are shown in Figures 6-11a, 6-11b, and 6-11c, respectively. It should be noted that, since the energy fluctuates in the time histories, the estimated energy in this chapter is its mean value. It is observed that the amount of energy absorbed by the meta-cores and the soft coating is generally higher than that of the outer hollow truss bars. The energy absorption by the hollow truss bars is mainly associated with its plastic deformation, while the energy absorption by the meta-cores and soft coatings is primarily caused by local vibrations of the cores.

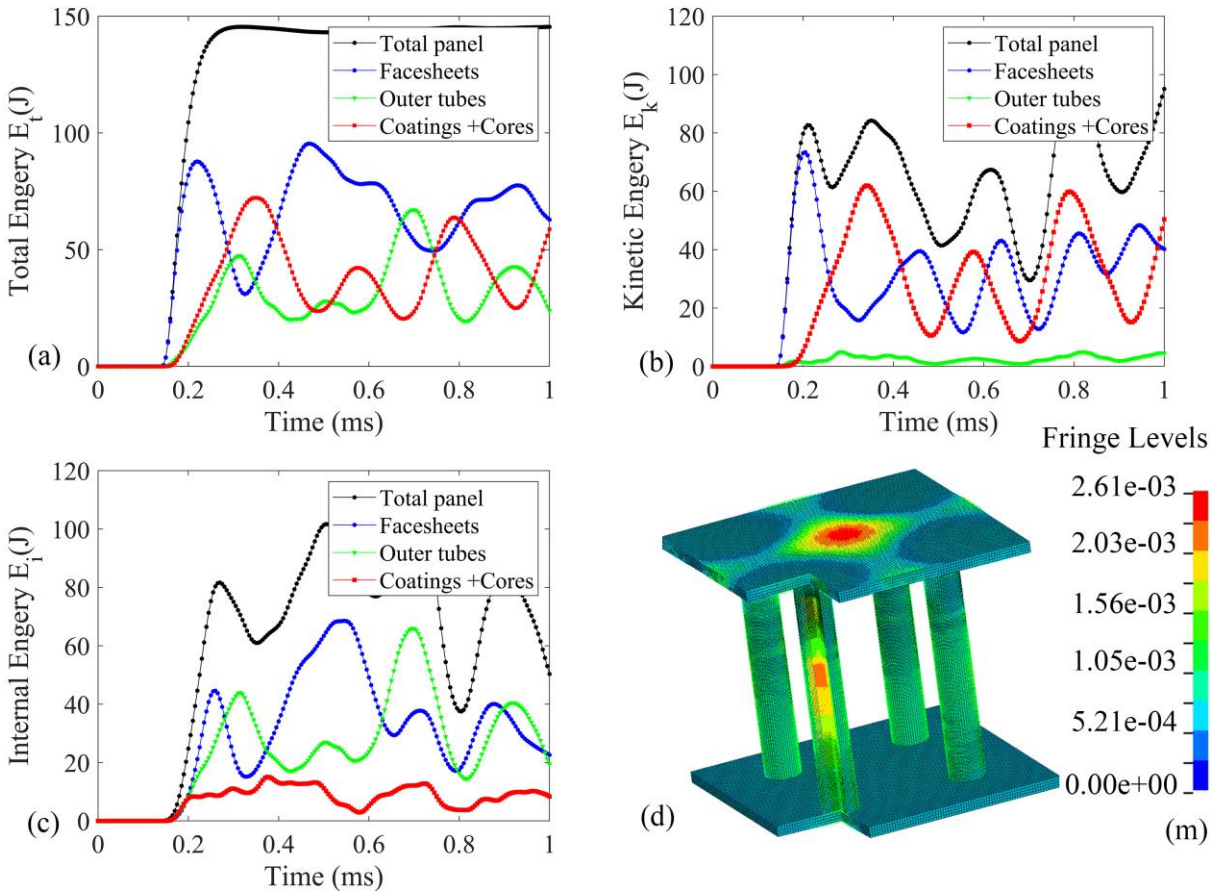


Figure 6-11. Energy time histories of each component of the dual-meta panel (a) total energy, (b) kinetic energy, (c) internal energy, and (d) displacement contour

These results indicate the damage to the truss bars by the blast load is reduced because of the local vibrations of the meta-cores. As shown, the outer hollow tubes of the meta-truss bars experience plastic deformation which also consumes energy imparted to the panel (Figure 6-11 c), whereas the relative movement of the meta-cores contributes mainly to kinetic energy

(Figure 6-11b) and partly to the internal energy due to the deformation of the coatings. These results indicate the dual-meta panel possesses the high energy absorption capability through the local vibration of the meta-cores, which not only protects the back facesheet of the sandwich structure but also reduces the damage to the outer hollow tube of the meta-truss bars. Figure 6-11d shows the movements of each component in the panel including the two facesheets, the outer tube, the soft coatings, and the cores. It is worth noting that there are out-of-phase motions between the meta-cores and the outer tube due to the existence of the soft coatings, which effectively mitigate the blast loading effect on the back facesheet. For comparison, the energy absorptions of the two reference panels are also calculated. The total energy absorption of the whole panel and each component of the three panels are shown in Figure 6-12. The dual-meta panel shows the highest total energy absorption. Among the three panels, the panel with solid truss bars absorbs the least amount of energy, and in which the most energy absorption is due to the plastic deformation of the facesheets, indicating the least protective effectiveness. The panel with hollow truss bars absorbs energy through plastic deformation of the facesheets and the truss bars. The energies absorbed by the facesheets and the truss bars of the dual-meta panel are the smallest among the three panels although the dual-meta panel absorbs more energy than the two reference panels, indicating the smallest plastic deformation and hence the mitigation of damages to facesheets and outer tubes. These results further demonstrate the good performance of the proposed dual-meta panel.

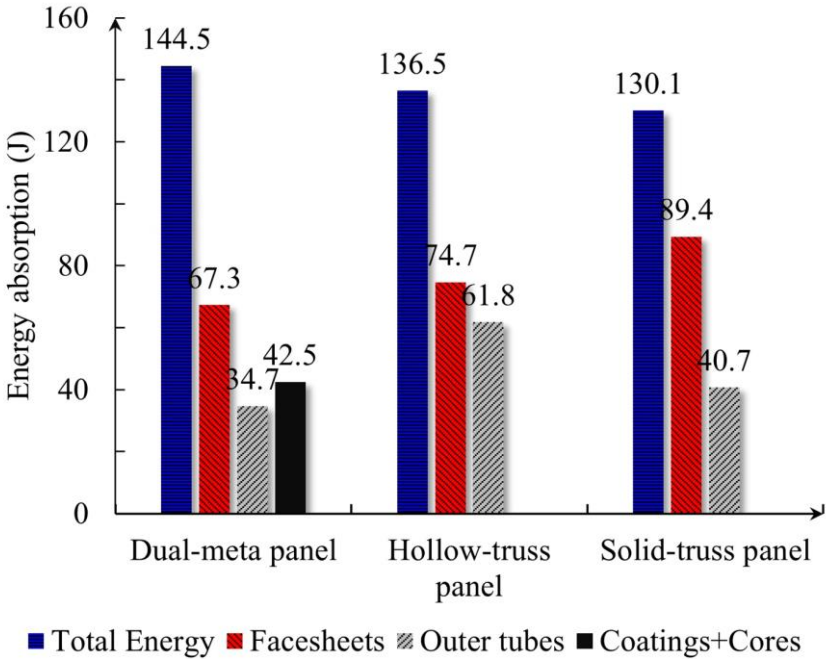


Figure 6-12. Energy absorption of the three panels

The reaction force in Z-direction (F_z) along the boundary of the back panel is also a key factor for the assessment of the protective effectiveness of the sacrificial panels. To evaluate this factor, the reaction force time histories of the three panels are shown in Figure 6-13. It is worth mentioning that the investigated reaction force is the sum of the reaction forces distributed around the boundary. As observed, the dual-meta panel is effective in reducing the reaction force of the sandwich panel. The maximum reaction force of the dual-meta panel is 18.2% and 30.1% less compared to that of the hollow truss and solid truss panels, respectively. The reaction force of the dual-meta panel almost stabilizes (25 kN) after the first positive peak at 2 ms while the second positive peaks of the reaction force of the other two panels are still large (90~115 kN which is comparable to the first peak). The second positive peak of the reaction force of the dual-meta panel reduces by 72% and 78% as compared to that of the panel with the hollow truss and solid truss core, respectively. This is because the meta-cores filter out the stress from the blast loading due to the relative movement of the meta-core and the soft coating, thus less stress from the blast load is transferred to the back facesheet and then the supports. The reaction force at the supports, therefore, reduces which in turn relieves the demand on support designs of the sandwich panel and loading on the protected structure.

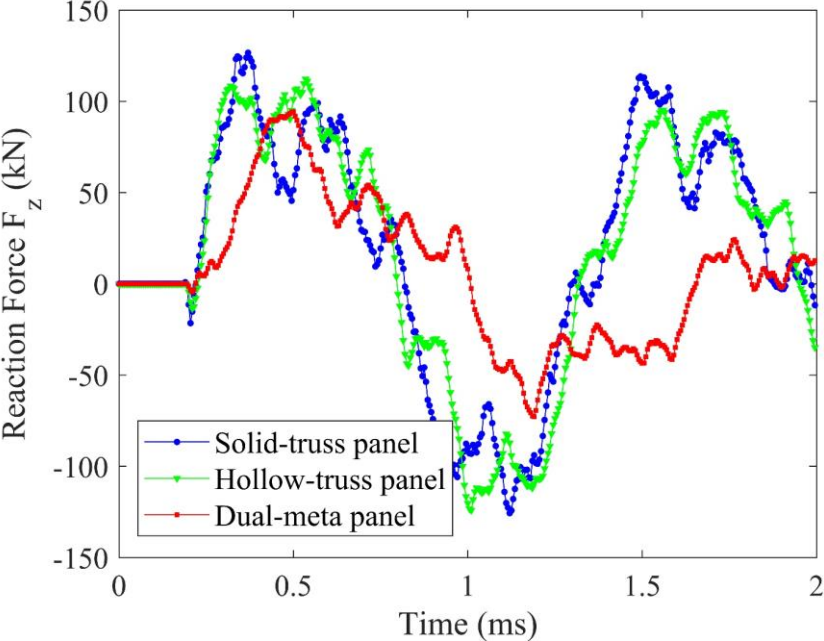


Figure 6-13. Comparison of the reaction force time histories of the three panels under blast loading

The effective performance of the dual-meta panel is further evaluated by analyzing the von Mises stress distribution of the back facesheet. Figure 6-14 shows the stress contours at the

back facesheet of the dual-meta panel, solid truss panel, and hollow truss panel, respectively. As shown in the figure, the back facesheet exhibits the stress concentration at the connections between the truss bars and the back facesheet since the blast loading generates the stress wave propagating through the truss bars. The results clearly show that the von Mises stress in the back facesheet of the dual-meta panel is the smallest among the three panels, while that of the solid truss panel is the largest, indicating again the effectiveness of the stress wave mitigation capability of the dual-meta panel.

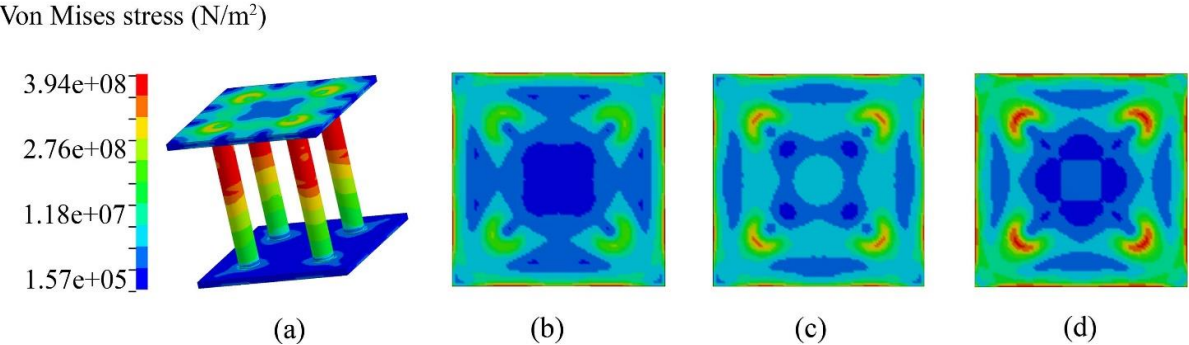


Figure 6-14. (a) Stress contours of 3D dual-meta panel and stress contours at the back facesheet of (b) Dual-meta panel, (c) Hollow truss panel, and (d) Solid truss panel

To further compare the blast resistance of the panels with the same mass, two other conventional panels with hollow truss bars and solid truss bars are also considered. The masses of these panels are kept the same as that of the dual-meta panel and thus the diameter of the truss bars of these three panels are different. Geometries of these panels and the blast loading are kept the same as described in Section 6.4.4 except for the diameter of the solid truss bar and the thickness of the hollow truss bar, which are adjusted to have the same mass as the meta-truss bar. The solid truss bar has a radius of 25.5 mm and the hollow truss bar has the outer and inner radii of 28 mm and 12 mm, respectively. The results show that the energy absorption of these panels (i.e. 74.1 J and 69.5 J for panels with hollow trusses and solid trusses, respectively) are significantly smaller than that of the dual-meta panel (144.5 J). Therefore, it demonstrates again that the dual-meta panel outperforms the same mass conventional panels. In summary, the proposed dual-meta panel reduces the maximum displacement of the back facesheet (up to 20.0% for the first peak and 52.0% for the second peak) and the reaction forces (up to 30.0% for the first peak and 78.0% for the second peak) and absorbs more energy compared to the conventional panel with solid and hollow truss bars. The local vibration of the meta-cores also reduces the stress and plastic deformation of the truss bars and the back facesheets of the sandwich panel, therefore mitigating the damage to these components of the panel. These

results demonstrate the better performance of the dual-meta panel as a sacrificial cladding to resist blast loading than the conventional sandwich panels with solid and hollow truss bars.

6.4.5 Parametric investigations

In this section, the influences of critical parameters such as the thickness of the facesheet, boundary condition, blast load duration and intensity on the performance of the dual-meta panel are numerically investigated. This section is carried out to gain further insights into the performance of the dual-meta panel subjected to confined blast loading as a sacrificial cladding.

6.4.5.1 Effect of the thicknesses of the facesheets

Herein, the transient response of the dual-meta panel is examined with varying front facesheet thickness while keeping the back facesheet thickness unchanged and vice versa. Three thicknesses, i.e. 4 mm, 6 mm, and 12 mm, are taken into consideration. Therefore, six panels with different combinations of thicknesses of front facesheet and back facesheet are considered in this section including 4 mm (F) + 8 mm (B), 6 mm (F) + 8 mm (B), 12 mm (F) + 8 mm (B), 8 mm (F) + 4 mm (B), 8 mm (F) + 6 mm (B), and 8 mm (F) + 12 mm (B). Figures 6-15a and 6-15b depict the central deflection of the back and front facesheets with varying facesheet thicknesses. It should be noted that the above facesheet configurations are determined to obtain a more comprehensive and valid comparison of protective effectiveness, i.e., the panels experience different levels of deformation without failure. This predetermined condition also assumes these panels after deformation would not touch the main structure and only transfer the load to the main structure through their supports.

As expected, the deflections of both the front and back facesheets decrease with the increase of their thicknesses. Drastic reduction in displacements by increasing the facesheet thickness demonstrates its significance in suppressing the blast loading of the dual-meta panel. It is noted that in most cases, the displacement at the central point of the front facesheet is smaller than that of the back facesheet due to their boundary conditions. The four edges of the back facesheet are restrained in all directions while the edges of the front facesheet are free. The displacement of the overhanging portion of the front facesheet would counteract its central point displacement resulting in a reduction in the displacement amplitude. As shown in Figures 6-15c and 6-15d, with an increase in the thickness of the front facesheet from 4 mm to 12 mm, there is an increase in the reaction force and a substantial reduction in the total energy absorption. This phenomenon happens mainly because less deflection of the facesheet means less energy absorption through

its plastic deformation. In brief, the reaction force is highly sensitive to the front facesheet thickness and it is not beneficial to use a thick front facesheet in the design of sacrificial panels. Regarding the influence of the thickness of the back facesheet, when changing its thickness, the first peak displacement of the front facesheet is the same but the second peak displacement and the subsequent displacement responses vary. This is attributed to the stress waves generated by the blast load transfer from the front facesheet to the back facesheet. Regardless of the thickness (thus stiffness) of the back facesheet, the front facesheet will be the first component to resist the blast load, its first peak displacement, therefore, is not sensitive to the thickness of the back facesheet. However, its second peak displacement is affected by the stiffness of the back facesheet owing to the reflected stress and deformation of the back facesheet. It is observed that the second peak displacement occurs when the panel rebounds from its first peak and it moves back in the opposite direction.

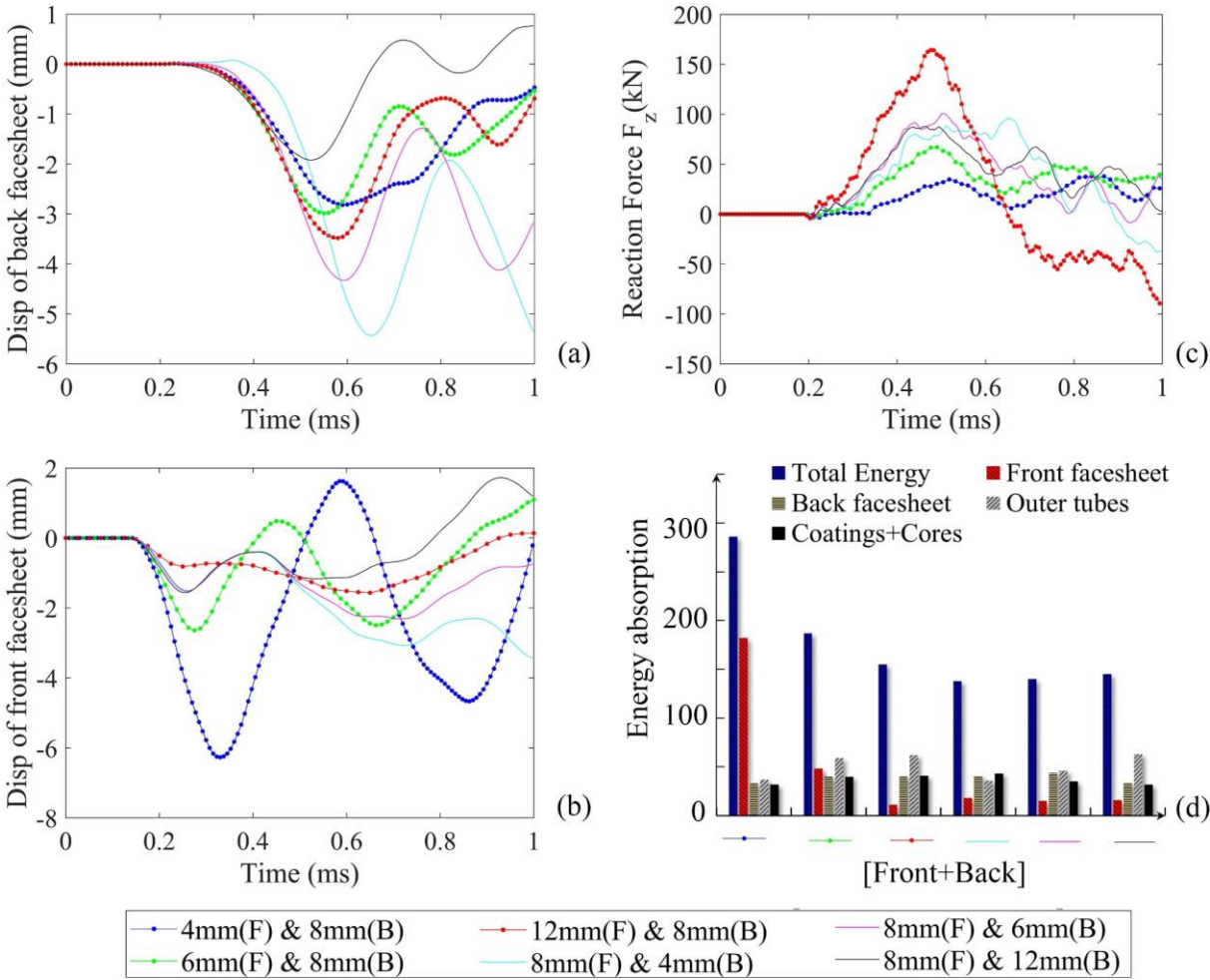


Figure 6-15. Effects of the facesheet thickness (a-b) displacements of the back and front facesheets, (c) reaction force, and (d) energy absorption

Meanwhile, the reaction force and the total energy absorption are not sensitive to the thickness of the back facesheet. In brief, the displacement of the facesheet is highly sensitive to the stiffness of the facesheet, due to the correlation between the stiffness and the displacement. While the thickness of the back facesheet only affects its displacement, reducing the front facesheet thickness results in smaller reaction forces and absorbing more energy. From Figure 6-15, it can be seen that the two good combinations are 4 mm (F) + 8 mm (B) and 8 mm (F) + 4 mm (B) since they absorb more energy compared to the total amount of materials. However, the combination of 8 mm (F) + 4 mm (B) exhibits a much higher reaction force than that of 4 mm (F) + 8 mm (B). Hence, the optimal design of the dual-meta panel as a sacrificial cladding should have a fairly thin front facesheet and a thick back facesheet to fully manifest its protective performance such as high energy absorption and less deflection of the back facesheet. It is noted that the effect of the facesheet's thicknesses on the blast mitigation of the dual-meta panel is similar to that of other blast-resistant sandwich panels [177].

6.4.5.2 Effect of boundary conditions

The boundary condition determination relies on how sacrificial claddings can be utilized in structural protection [192]. There are various ways that the protective panel can be attached to the main structure, namely, clamped or pinned at the edges allowing some clear space between the panel and the protected structure, or directly fixed against the system without a gap. In this chapter, these attachment methods are considered with three boundary conditions including all perimeter is clamped, simply pinned, and all the surface of the back facesheet is fixed, i.e., directly attaching the panel on the protected structure. The transient responses of the dual-meta panel with these selected boundary conditions subjected to the same blast loading (defined in Figure 6-5) are compared in Figure 6-16. As shown, the central displacement of the back facesheet of the panel with pinned boundary is 13.1% larger than that with clamped boundary condition. Meanwhile, the facesheets and the meta-cores of the pinned panel witness a decrease in energy absorption compared to the clamped panel by 16.7 % and 20.7 %, respectively. However, the energy absorbed by the truss bars of the clamped panel is lower than that of the pinned panel. Therefore, the total energy absorption of the panel with the pinned and fixed boundary conditions differs by only 1 %. As for the case with the fixed back surface, the energy absorbed by the trusses is higher compared to that of the other two boundary conditions because the constraints of the back facesheet result in more deformation of the trusses leading to more energy absorption. The total energy absorption of the fully fixed panel is comparable to that of

the panel with clamped boundary, implying the amount of energy absorbed by the back facesheet deformation is compensated by the larger plastic deformation of the outer tube of the truss bars. The reaction force in the Z-direction of the panel with the fully fixed back surface is two times higher than those of the panel with other boundary conditions, therefore, it is not recommended to apply the fixed back surface in practice. In summary, the displacement and the energy absorption by various parts of the panel are significantly affected by the boundary conditions while it exerts less influence on the total energy absorption of the panel. This conclusion is in good agreement with other blast-resistant sandwich panels such as aluminium foam-cored sandwich panels [193]. For practical applications, the dual-meta panel will perform better as a sacrificial cladding if there is a gap between it and the protected structure, with less blast force transferred to the protected structure, but concentrated at the supports. Directly attaching the panel on the protected structure also leads to larger plastic deformations of the outer tube of the truss bars, making the meta-cores less effective in absorbing blast energy.

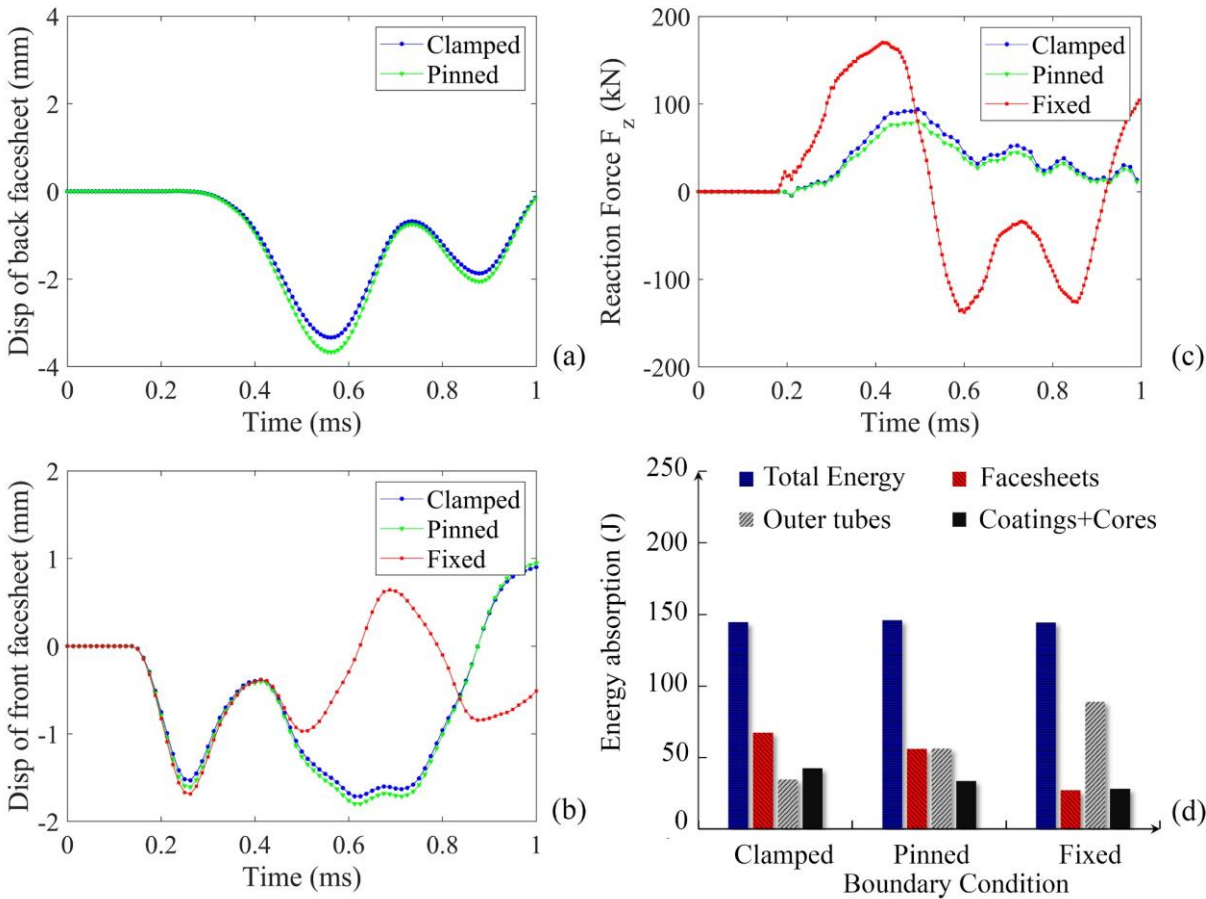


Figure 6-16. Effects of the boundary conditions (a-b) displacements of the back and front facesheets (c) reaction force, and (d) energy absorption

6.4.5.3 Effects of blast loading duration and intensity

To comprehend the influence of different levels of blast loading duration on a given dual-meta panel, four blast loading profiles (shown in Figure 6-17) with different duration but the same amplitude are considered. The blast loading profile is defined by using the modified Friedlander's equation [194]:

$$F = F_{\max} \left(1 - \frac{t-t_0}{t_d} \right) e^{-\frac{t-t_0}{t_d}}, t_0 \leq t < t_0 + t_d \quad (6-14)$$

$$F = 0, t < t_0 \text{ or } t \geq t_0 + t_d$$

where F_{\max} is the amplitude while the time constants t_0 and t_d are the blast initial time and blast duration, respectively.

In this chapter, the negative phase in the blast loading profile is neglected in the analysis [195]. For different loading regimes, durations t_d of 0.1 ms, 0.2 ms, 0.3 ms, and 0.4 ms are chosen in the analyses. It should be noted that the blast loading duration is purposely chosen relatively short to generate a wider loading frequency band for evaluating the performance of the dual-meta panel in mitigating the blast loading effect. In an explosion case, such short loading duration could be associated with contact and very close-in explosions. With the amplitude F_{\max} of 13.5 MPa, the corresponding impulses are 530 Ns, 1,027 Ns, 1,523 Ns, and 2,020 Ns, respectively with the four different duration.

It is obvious when varying the duration of the blast loading, the dominant frequency band of the blast loading would change accordingly. The corresponding blast loading energy in the three bandgaps of the current meta-truss bars can be calculated by the area (A_{bandgap}) enclosed by the FFT spectrum of the blast loading in each bandgap as illustrated in Figure 6-18b. The portion of the blast loading energy corresponding to each bandgap is calculated by dividing the energy in each bandgap by the total blast loading energy (A_{total}), and are given in Table 6-6. As shown, more proportion of energy from blast load with longer duration falls into the bandgaps of the dual-meta panel, i.e, 77.0%, 81.0%, 82.4%, and 83.4%, respectively for the four considered loading cases, implying the dual-meta panel is more effective in mitigating the blast loading with the longest duration.

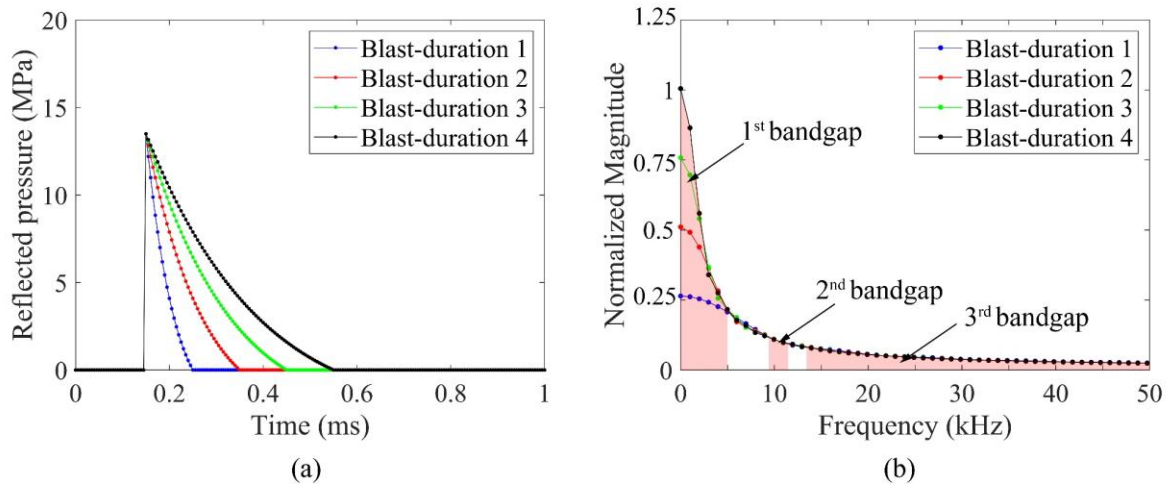


Figure 6-17. Blast loading with different duration, (a) Time histories and (b) FFT spectra

Table 6-6 gives the dynamic response of the dual-meta panel subjected to the assumed blast loads with different duration uniformly applied to the front facesheet of the panel. The results indicate that the dynamic responses of the dual-meta panel rely heavily on the blast loading impulse. The facesheet deflections, the reaction forces, and the energy absorption of the panel increase with the loading impulse. It is obvious that the effectiveness of the dual-meta panel in blast load mitigation depends on the frequency band of the blast loading, therefore, aside from the total energy absorption increases from loading case 1 to case 4 due to the increased blast loading energy imparted to the structure, the largest percentage of energy absorption by the coatings and the cores of the meta-truss bars corresponds to the loading case 4, which is $392/1,188=32.9\%$ as shown in Table 6-5, followed by 31.9%, 29.6%, and 28.7%, respectively for the loading cases 3 to 1. This is because the proportion of the blast energy of the loading cases considered in the analyses reduces from case 4 to case 1, implying the meta-truss bars can stop more blast loading energy transmission as shown in Figure 6-18b when more proportion of the blast loading energy falls into the bandgaps.

It should be noted that the percentage of energy absorption of the coatings and the cores in the dual-meta panel calculated from Table 6-6 is smaller than the corresponding values in Table 6-5. It is because the energy absorption of the dual-meta panel is constituted by four components, i.e., the facesheets, the truss bars, the coatings, and the cores. Only the meta-cores including the coatings and the cores have the bandgap-related mitigating capability, while the facesheets and trusses absorb energy through plastic deformation.

Table 6-5. Proportion of blast loading energy with different duration falling in the bandgaps of the single meta-truss bar

Blast loadings	1 st bandgap		2 nd bandgap		3 rd bandgap		Total %
	$\frac{A_{\text{bandgap}}}{A_{\text{total}}}$	%	$\frac{A_{\text{bandgap}}}{A_{\text{total}}}$	%	$\frac{A_{\text{bandgap}}}{A_{\text{total}}}$	%	
Blast-duration 1	$\frac{4,875}{15,340}$	31.7%	$\frac{927}{15,340}$	6.0%	$\frac{6,039}{15,340}$	39.3%	77.0%
Blast-duration 2	$\frac{7,746}{17,976}$	43.1%	$\frac{929}{17,976}$	5.1%	$\frac{5,903}{17,976}$	32.8%	81.0%
Blast-duration 3	$\frac{9,364}{19,580}$	47.8%	$\frac{929}{19,580}$	4.7%	$\frac{5,855}{19,580}$	29.9%	82.4%
Blast-duration 4	$\frac{10,570}{20,740}$	50.9%	$\frac{926}{20,740}$	4.4%	$\frac{5,835}{20,740}$	28.1%	83.4%

Table 6-6. Effect of blast loading duration on displacements, reaction force, and energy absorption

Blast loadings	Displacement (mm)		Reaction force (kN)	Energy absorption (J)			Total
	Front facesheet	Back facesheet	F_z	Face- sheet	Outer tubes	Coatings + Cores	
	Blast-duration 1	1.7	4.1	120	95	46	
Blast-duration 2	2.6	7.3	190	253	136	164	553
Blast-duration 3	3.1	9.7	230	392	212	283	887
Blast-duration 4	3.5	11.2	270	528	268	392	1188

To evaluate the effectiveness of the dual-meta panel subjected to blast load with different peaks but the same impulse, the responses of the dual-meta panel subjected to blast load with the impulse of 530.8 Ns but varying the peak pressure and duration. The blast loading duration of 0.1 ms, 0.2 ms, 0.3 ms, and 0.4 ms with the corresponding peak pressure of 13.5 MPa, 6.75 MPa, 4.5 MPa, 3.375 MPa, respectively are considered. Figure 6-18 shows the blast loading time histories and the corresponding FFT spectra of these blast loading. The portions of the blast loading energy in each bandgap of the meta-truss bars are given in Table 6-7. The corresponding percentages of the blast loading energy falling into the bandgaps of the panel are 77.0%, 80.9%, 82.2%, and 83.4%, respectively for blast loading case 1-4, shown in Table 6-7.

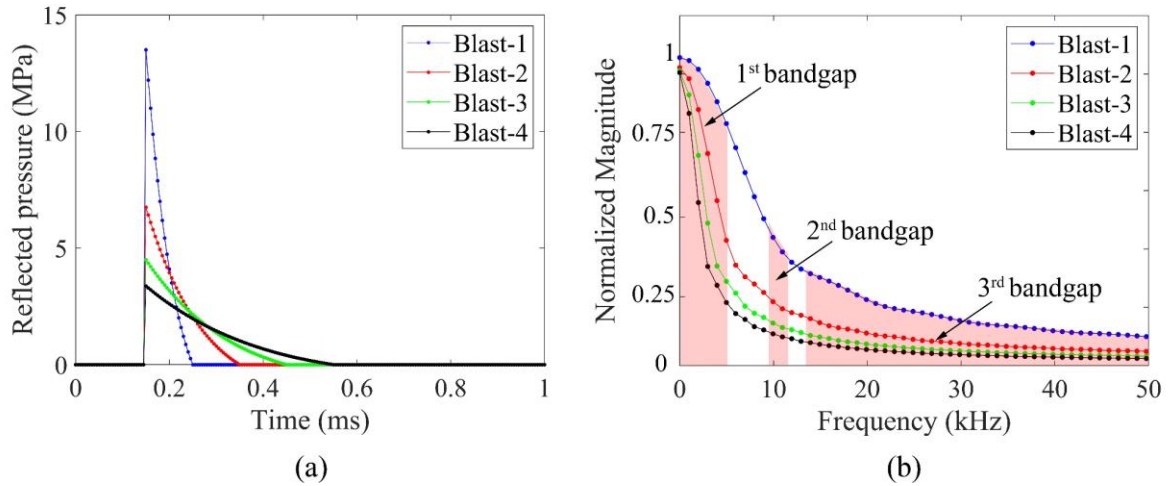


Figure 6-18. Blast loading profiles with different duration and intensities (a) Time histories, and (b) FFT spectra

The structural responses of the dual-meta panel under blast loading with different duration and intensities are given in Table 6-8 while Table 6-7 summarizes the proportion of blast loading energy falling in the bandgaps. As shown, increasing the blast duration while decreasing the blast intensity leads to more blast energy in the lower frequency range that fall into the low-frequency bandgap of the meta-panel. In particular, it is found that the blast loading with the highest intensity and shortest duration results in the least percentage of energy in the bandgaps, i.e., 77.0 %, followed by 81.0 %, 82.4 %, and 83.4 % respectively for the loading Blast-2 to Blast-4.

As shown in Table 6-8, the facesheet displacements and energy absorption of the dual-meta panel decrease with the reduction of the peak blast load given the same impulse. Also, the highest peak reaction force corresponds to the loading Blast-1, which is reasonable since it is associated with the highest peak blast load. As given in Table 6-8, although the total energy absorption increases from the loading Blast-4 to Blast-1 due to the increase of the peak blast load, the largest percentage of energy absorption by the coatings and the cores corresponds to Blast-4, which is $26/76=34.2\%$, followed by 32.5%, 30.1%, and 28.7%, for Blast-3 to Blast-1, respectively. It is again attributed to the proportion of the blast loading energy falling into the bandgaps given in Table 6-7. These results demonstrate that the transient responses of the dual-meta panel correlate with the peak blast load and its capacity to absorb energy in the bandgap ranges. Therefore, the proposed dual-meta panel can be designed to maximize its blast load mitigation efficiency for an expected blasting scenario.

Table 6-7. Proportion of blast loading energy with different duration and intensities falling in the bandgaps of the single meta-truss bar

Blast loadings	1 st bandgap		2 nd bandgap		3 rd bandgap		Total %
	$\frac{A_{\text{bandgap}}}{A_{\text{total}}}$	%	$\frac{A_{\text{bandgap}}}{A_{\text{total}}}$	%	$\frac{A_{\text{bandgap}}}{A_{\text{total}}}$	%	
Blast-1	$\frac{4,875}{15,340}$	31.7%	$\frac{927}{15,340}$	6.0%	$\frac{6,039}{15,340}$	39.3%	77.0%
Blast-2	$\frac{3,877}{9,010}$	43.1%	$\frac{465}{9,010}$	5.1%	$\frac{2,958}{9,010}$	32.8%	81.0%
Blast-3	$\frac{3,125}{6,543}$	47.8%	$\frac{310}{6,543}$	4.7%	$\frac{1,956}{6,543}$	29.9%	82.4%
Blast-4	$\frac{2,646}{5,198}$	50.9%	$\frac{232}{5,198}$	4.4%	$\frac{1,462}{5,198}$	28.1%	83.4%

Table 6-8. Effects of blast loading duration and intensities on displacements, reaction force, and energy absorption

Blast loadings	Displacement (mm)		Reaction force (kN)	Energy absorption (J)			Total
	Front facesheet	Back facesheet	F _z	Face- sheets	Outer tubes	Coatings + Cores	
	Blast- 1	1.7	4.1	120	95.0	46.0	
Blast- 2	1.3	3.6	109	63.2	34.0	41.8	139
Blast- 3	0.9	3.2	97	42.5	25.0	32.5	100
Blast- 4	0.8	2.8	87	30.8	19.2	26.0	76

6.5. Conclusions

The capability of the proposed dual-meta panel to attenuate the blast loading effect is examined in this chapter. Theoretical derivations and numerical simulations are carried out to investigate the mechanism and responses of the dual-meta panel against blast load. The proposed dual-meta panel is aimed to increase the blast resistance capacity, whilst maintaining a low base reaction force. The key points found in this chapter can be enumerated as follows:

1. Compared to the conventional sandwich panel with solid and hollow truss core, the panel with dual-meta truss core has smaller central peak deflections of the back facesheet (up to 20%

for the first peak and 52% for the second peak), smaller reaction force (up to 30% for the first peak and 78% for the second peak), and absorbs more blast loading energy, demonstrating that the dual-meta panel has the potential for significantly enhancing the dynamic performance of the cladding and outperforms its conventional counterparts.

2. The performance of the dual-meta panel on blast loading mitigation depends on the structural configurations. A relatively weak front facesheet and stronger back facesheet, and separating the sacrificial dual-meta panel from the protected structure with a small gap lead to better protective effectiveness of the panel in terms of energy absorption and the level of the load transmitted to the protected structure.

3. The performance of the dual-meta panel also depends on the blast loading profile and energy distribution. The dual-meta panel with bandgaps consistent with the primary blast loading energy distribution in the frequency domain is more effective in mitigating the blast loading effect.

The chapter proves that the dual-meta panel holds great potential for extensive applications in various engineering fields requiring blast load mitigation.

CHAPTER 7. EXPERIMENTAL AND NUMERICAL VALIDATION OF IMPACT MITIGATION CAPABILITY OF META-PANELS

Abstract⁶

The unique stress wave mitigation capacity of meta-materials and meta-structures has been extensively investigated by many analytical studies but there has been very limited experimental verification on their favourable properties and performances, particularly the excellent stress wave mitigation of meta-panels. To address this research gap, the impact mitigation performances of meta-panels were experimentally and numerically investigated in this chapter. Firstly, an instrumented hammer impact test was conducted to verify the ability of the meta-truss bar in filtering out the incident stress. Then, impact tests using the gas gun system were implemented to examine the effectiveness of the meta-panel consisting of meta-truss bars on impact mitigation. It is experimentally proven that the meta-panel exhibited better dynamic performances, i.e., reductions in force transmission to the protected structure as well as in the back facesheet displacement, and an increase in energy absorption compared to the traditional panels, namely hollow-truss panels and solid-truss panels. Furthermore, the effect of the impact velocity on the response of meta-panels was also experimentally investigated and discussed.

⁶ The related work in this chapter was submitted for Under Review with the bibliographic citation as follows:

N.H. Vo, T.M. Pham, K. Bi, W. Chen, H. Hao. Experimental and Numerical Validation of Impact Mitigation Capability of Meta-panels. *International Journal of Mechanical Sciences*. 2022;201:107591.

<https://doi.org/10.1016/j.ijmecsci.2022.107591>

7.1. Introduction

Damage to structures caused by terrorist bombing attacks, accidental explosions, or extreme natural events has motivated researchers and engineers to develop new and effective solutions for structure protections against those impulsive loads [196]. During a blast/impact event, critical load-bearing members may be severely damaged [116, 197], leading to substantial losses of human lives and economy. Hence, it is of significance to mitigate the effects of blast/impact loading on primary structures and guarantee their resilience by using various strengthening measures as well as protective structures such as sacrificial claddings [118, 119]. The objective of the sacrificial claddings, which are commonly attached to the exterior of the main structures, is to absorb energy during blast/impact events and reduce load transmission to the protected structures.

Sandwich panels comprising double facesheets and integrated cores are commonly used as sacrificial claddings [146, 198]. Much attention has been focused on the use of metallic foam core for sandwich panels due to its large deformation and thus high energy absorption capability [48, 156]. For example, an experimental study of the sandwich panel with aluminium foam core was conducted by Hanssen et al. [7] to demonstrate its effectiveness in energy absorption against blast loads while its analytical solution was presented in another study by Ma and Ye [122]. Besides, numerous innovative bio-inspired panels have also shown their excellent blast/impact resistance, e.g. honeycomb panels [26], thin-walled corrugated structures [27], and hierarchical multi-cell structures [29]. These structures have been proven to possess a high energy absorption efficiency and great ability to enhance their crashworthiness. For instance, various configurations of bionic multicellular tubes were proposed to investigate their crashworthiness under axial impact loads [199]. In addition to the conventional approaches for energy absorption, more innovative solutions are sought and a few concepts have been recently proposed for better energy absorption capability without the need for large plastic deformation, i.e. meta-materials [42, 83]. The locally resonant meta-panels which adopt metamaterial-based concepts have attracted tremendous interest. Meta-panels absorbing energy due to not only plastic deformation but also the local resonance of the resonators show exceptional properties due to the presence of specially designed resonators. The favourable properties of meta-panels stem from the capability of generating frequency regions namely “bandgap” where stress waves cannot propagate [41, 134]. It has been found that the meta-panel has a high energy absorption capacity and can effectively attenuate the impact/blast effect owing to the local resonance of

the internal resonators. Up to date, literature on the dynamic performance of the meta-panel is still very limited, particularly the experimental investigations are not yet available.

This chapter presents the experimental and numerical investigations on the effectiveness of the meta-panel acting as a sacrificial layer under impact loading (Figure 7-1). Firstly, the experimental results from the instrumented hammer impact tests are compared with the analytical predictions to validate the wave mitigation properties of the meta-truss bar in the bandgap regions. Afterwards, the dynamic performance of the meta-panel integrated by meta-truss bars as cores, was investigated under the pneumatic gas gun tests to examine its effectiveness in impact load mitigation. Finally, the effect of impact velocity on the effectiveness of the meta-panel is assessed through in-depth discussions. It is noted that the analytical derivations and the numerical models are respectively presented in Sections 3 and 4 while the experimental, analytical and numerical outcomes are discussed in Section 5.

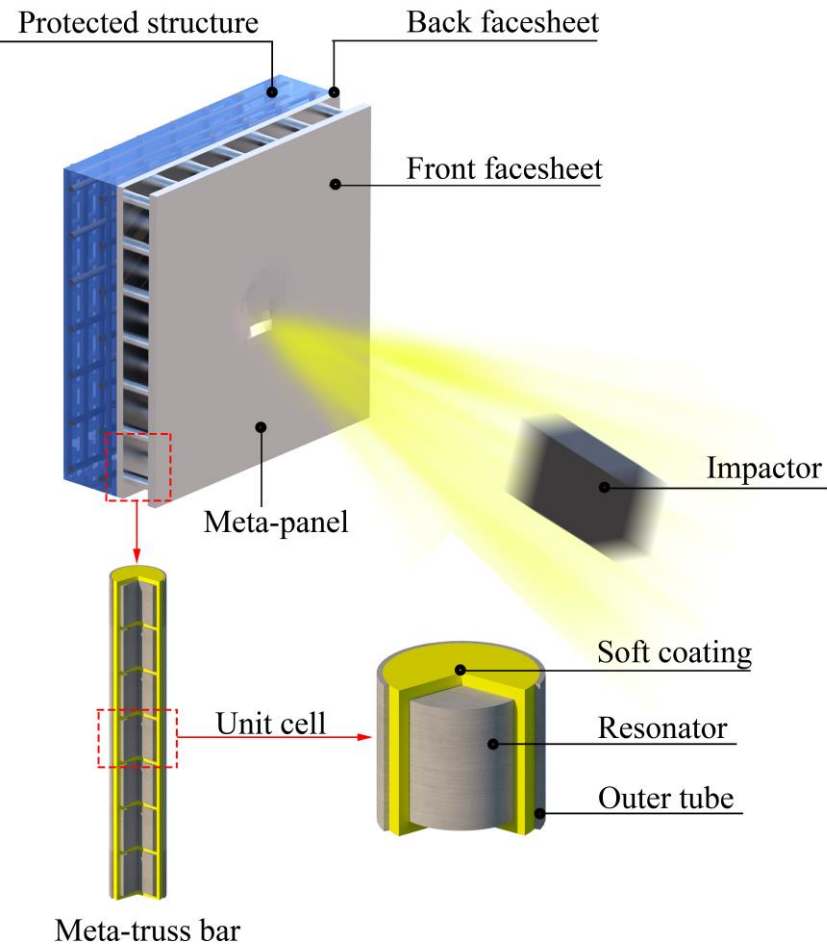


Figure 7-1. Schematic view of the meta-panel comprised of two thin facesheets and the meta-truss bars under impact loading

7.2. Experimental campaign

7.2.1 Testing programs

The dynamic performances of the meta-truss bar and meta-panel under impact loads are investigated by using non-destructive impact tests and gas gun impact tests, respectively. The instrumented hammer impact tests were carried out to experimentally confirm the bandgap formation of the meta-truss bar, which is its unique characteristic but was only demonstrated in analytical solutions and numerical simulations [41, 42]. Then, the gas gun tests on different panels, namely the meta-panel comprising meta-truss bars and the conventional panels comprising hollow-truss and solid-truss bars were carried out to demonstrate the effectiveness of the meta-panel in mitigating the impact loading effects. Furthermore, to investigate the effect of the impact velocity on the dynamic performance of the meta-panel, the projectile mass was kept unchanged while its velocity varied in the test. The impact force, back facesheet displacement, and reaction forces, i.e., the force transmitted to the protected structure, of the panels were recorded in the test to quantify the impact performance of these panels.

7.2.2 Fabrication process

Details of the specimen fabrication including the meta-truss bars and the meta-panels are briefly described in this section.

7.2.2.1 Meta-truss bars

To experimentally demonstrate the exceptional characteristics of the meta-truss bars in generating the bandgaps, a prototype of the meta-truss bar was fabricated for experimental testing. The manufacturing process of the meta-truss bar is schematically illustrated in Figure 7-2. As shown, the meta-truss bar was comprised of the outer tube embedded by soft-coated resonators. The metallic resonators were cut into the cylindrical shape of 14 mm height and 7 mm radius by a water-jet cutting machine, and embedded in the soft coating. The soft coats having 2 mm thickness were fabricated by the hot-press moulding method. The soft-coated resonators were then encased in the hollow tube which had 10 mm and 9 mm of outer and inner radii, respectively. In this chapter, the commercially available aluminium alloy was used to make the resonators and the outer tube while the soft coat was made of silicone rubber. These materials were chosen based on the design procedure in the previous study [134]. The mechanical properties of aluminium alloy 1060 are: density $\rho_a = 2,770 \text{ kg/m}^3$, modulus of

elasticity $E_a = 70 \text{ GPa}$, and Poisson's ratio $\nu_a = 0.39$ [25], which were given by the manufacturer; whereas silicone rubber has $\rho_s = 1150 \text{ kg/m}^3$, $\nu_s = 0.42$, and $E_s = 3.3 \text{ MPa}$ obtained from coupon tensile tests described in the following section.

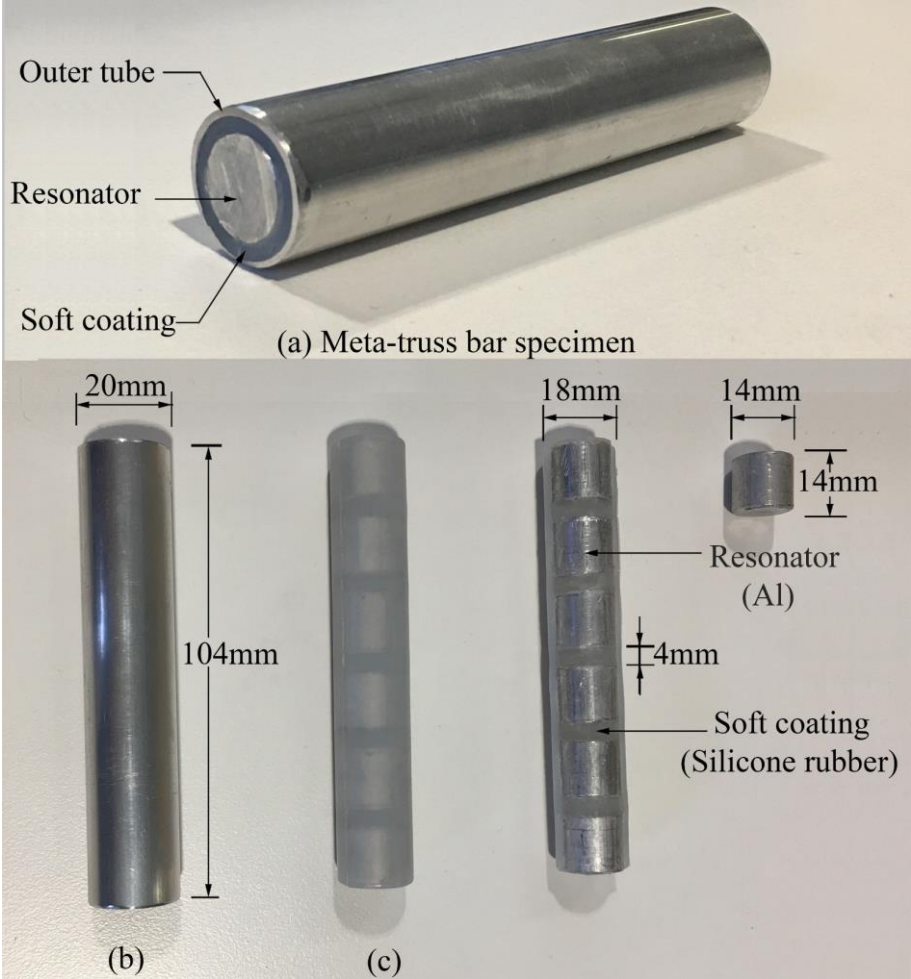


Figure 7-2. Schematic diagram of the meta-truss bars (a) meta-truss bar, (b) outer tube, (c) meta-cores with coating

7.2.2.2 Meta-panels

A total of four meta-panel specimens consisted of two solid facesheets made of aluminium alloy 1060 and the meta-truss bars were prepared (Figure 7-3). The facesheets were 4 mm thick with the dimension of 200 mm x 200 mm for the front facesheet and 300 mm x 300 mm for the back facesheet. The meta-truss bars were enclosed between the facesheets and bonded by the commercial two-component 3M impact-resistant structural adhesive (IRSA 07333). The bonding connection was adopted in this chapter due to small-scale specimens and for convenience. Other connection methods (e.g. welding or bolting) can be used in practical applications. Great attention was paid to achieving the perfect bonding between the facesheets

and the meta-truss bars for satisfactory structural performance. Oxide material and contaminants on the surface of facesheet were cleaned off using abrasive sandpaper and acetone.

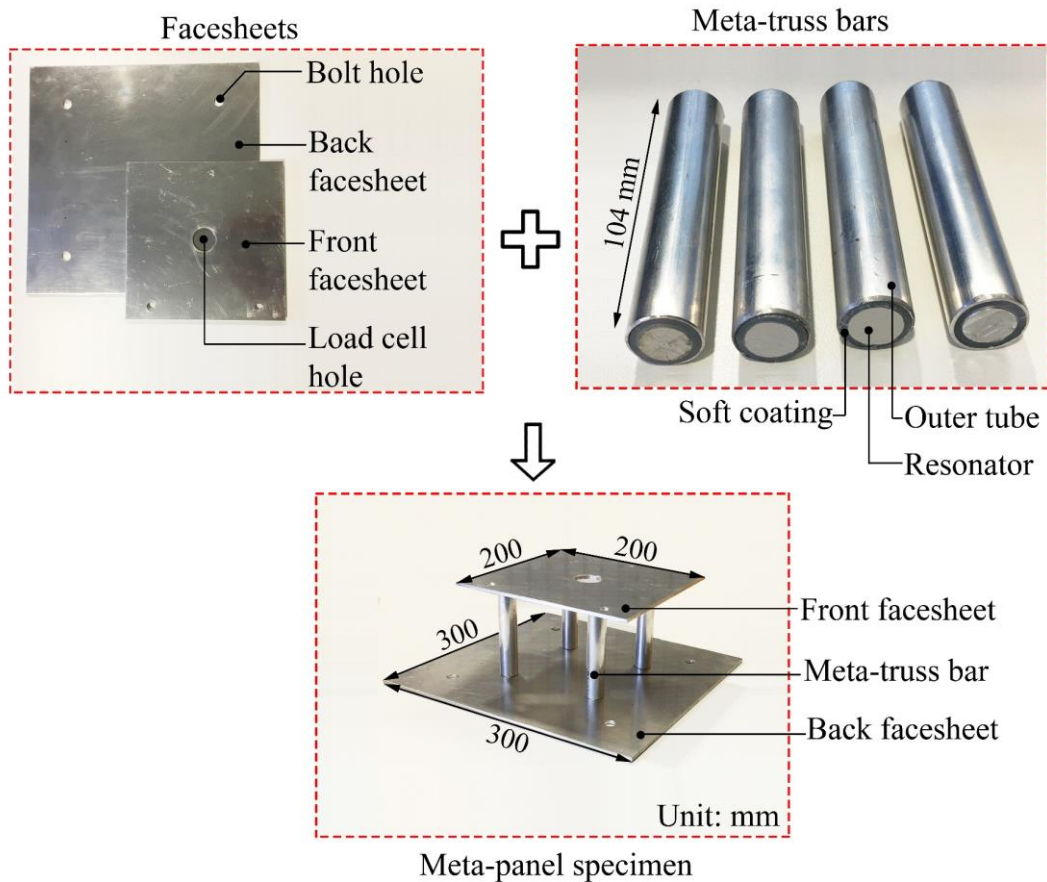


Figure 7-3. Schematic diagram of the meta-panel fabrication in which the two facesheets were bonded to the meta-truss bars by 3M impact-resistant adhesive

7.2.2.3 Material properties

Previous studies have reported that the elastic modulus of the soft coating layer significantly affects the wave attenuation performance of meta-materials and meta-truss bars [41, 84]. Therefore, it is important to accurately determine the mechanical properties of the coating material in the meta-truss bar for proper analysis and evaluation of the test results. The tensile test was set up with the same settings as described in the previous study [200] using a SHIMADZU testing machine (Figure 7-4a) with a 50 kN load cell. Three samples were tested at a fixed loading rate of 1 mm/s. The tensile test samples in dog-bone shape (Figure 7-4b) were designed according to ASTM standard D412 [201], in which the total length, L_0 , was 115 mm, and the widest width, W_0 , was 25 mm. The gauge length, G , was 33 mm, while the width at the middle, W , was 6 mm and the thickness, T , was 2 mm. The Young's modulus of the sample was

obtained from the stress-strain curve in Figure 7-4c and the average mechanical properties of the soft coating material are summarized in Table 7-1.

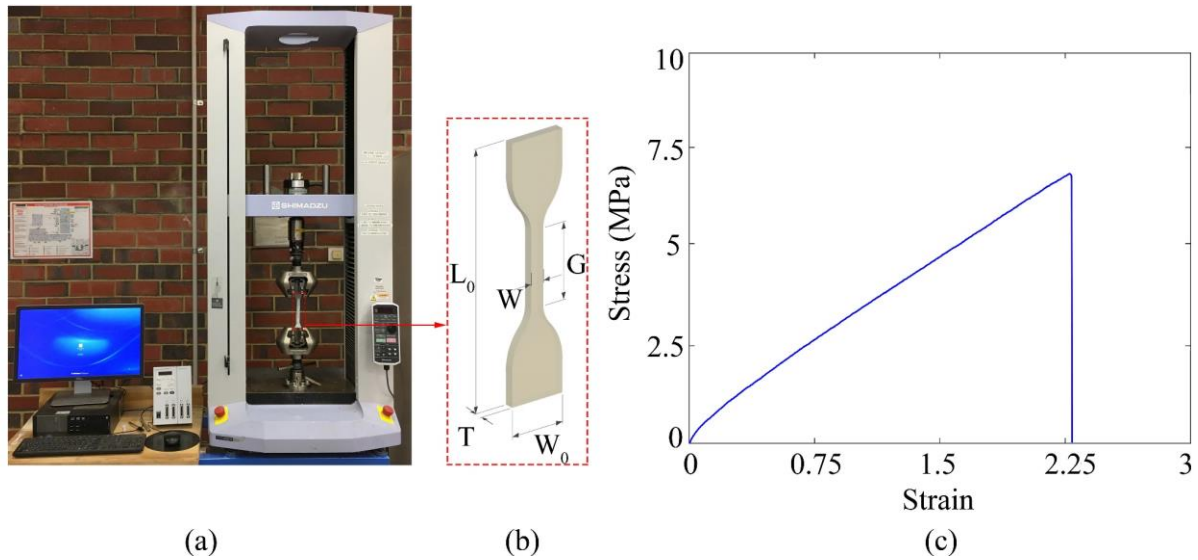


Figure 7-4. Schematic diagram of the meta-panel fabrication in which the two facesheets were bonded to the meta-truss bars by 3M impact-resistant adhesive

Table 7-1. Material properties of silicone rubber

Material	Material properties		
	Density ρ (kg/m ³)	Young's modulus E (MPa)	Poisson's ratio ν
Silicone rubber	1,150	3.3	0.42

7.2.3 Experimental setup

7.2.3.1 Instrumented hammer impact test on meta-truss bars

The instrumented hammer impact tests were carried out on the meta-truss bars to experimentally confirm its bandgap regions and validate the theoretical derivations. For the test setup, a vise was used to hold the specimen during the test, as illustrated in Figure 7-5. The vise was fixed to the workbench. Then, the specimen was clamped along its entire length by the vise. The instrumented hammer (Dytran 5800B3) equipped with the polyurethane head (6250PS) was used to strike the specimen and generate the stress wave propagation. The stress wave would activate the vibrations of the resonator, therefore, mitigating the impact energy being transmitted to the other end of the specimen. The impact force was measured using the DAQ system, i.e. QuantumX MX840B, with a sampling rate of 19.2 kHz. One accelerometer

was attached to one end of the specimen to record the input acceleration (ac_{in}), while another accelerometer was adhered to the other end to monitor the transmitted acceleration (ac_{out}). The signals from the accelerometers were amplified by a charge amplifier to improve the signal to noise ratio before sending to the DAQ system. The input and output signals were utilized to compute the transmission ratio of the meta-truss bar for evaluation of its wave mitigation ability. Details of the test setup are shown in Figure 7-5.

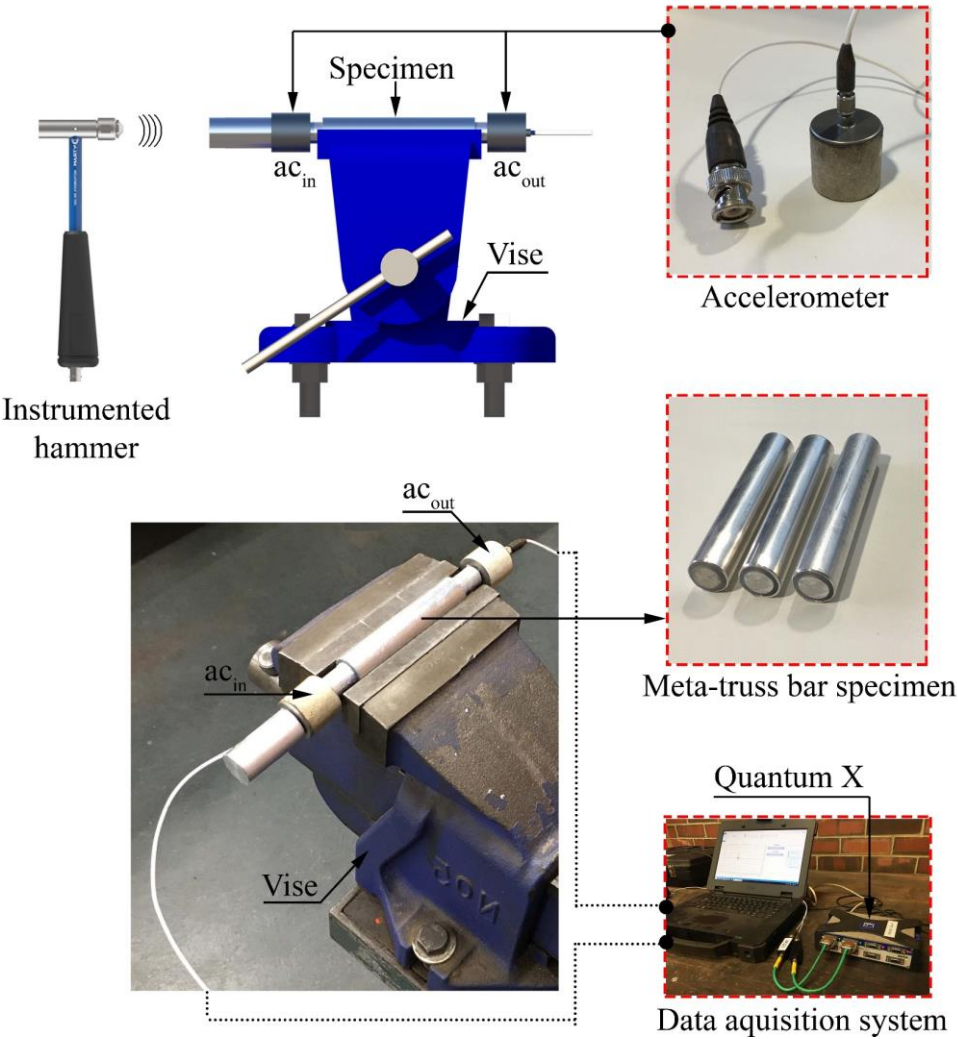


Figure 7-5. Setup of the instrumented hammer impact test

7.2.3.2 Gas gun impact test on meta-panels

The gas gun impact test was performed by a pneumatic gas gun system (see Figure 7-6). This system contained a launch tube and a pressure vessel in which the impact velocity can be controlled by adjusting the gas pressure and the projectile weight. The launch tube had a length of 2 m and an inner diameter of 115 mm while the dimension of the wooden projectile was 50 mm x 100 mm x 300 mm. The meta-panel specimens were fixed on a steel frame by 4 bolts, in

which four load cells were placed between the back facesheet and the steel frame to measure the reaction forces for quantifying the force transmission. Another load cell (100 mm x 100 mm) was mounted on the front facesheet and connected to the data acquisition system (DAQ) to record the impact force time history. The impact process was captured by the high-speed camera (Photron Fastcam SA5). The image processing technique was used to track the velocity of the projectile via tracking points attached to it. A laser triangulation sensor was set up at the back of the tested specimen to monitor the deformation of the back facesheet.

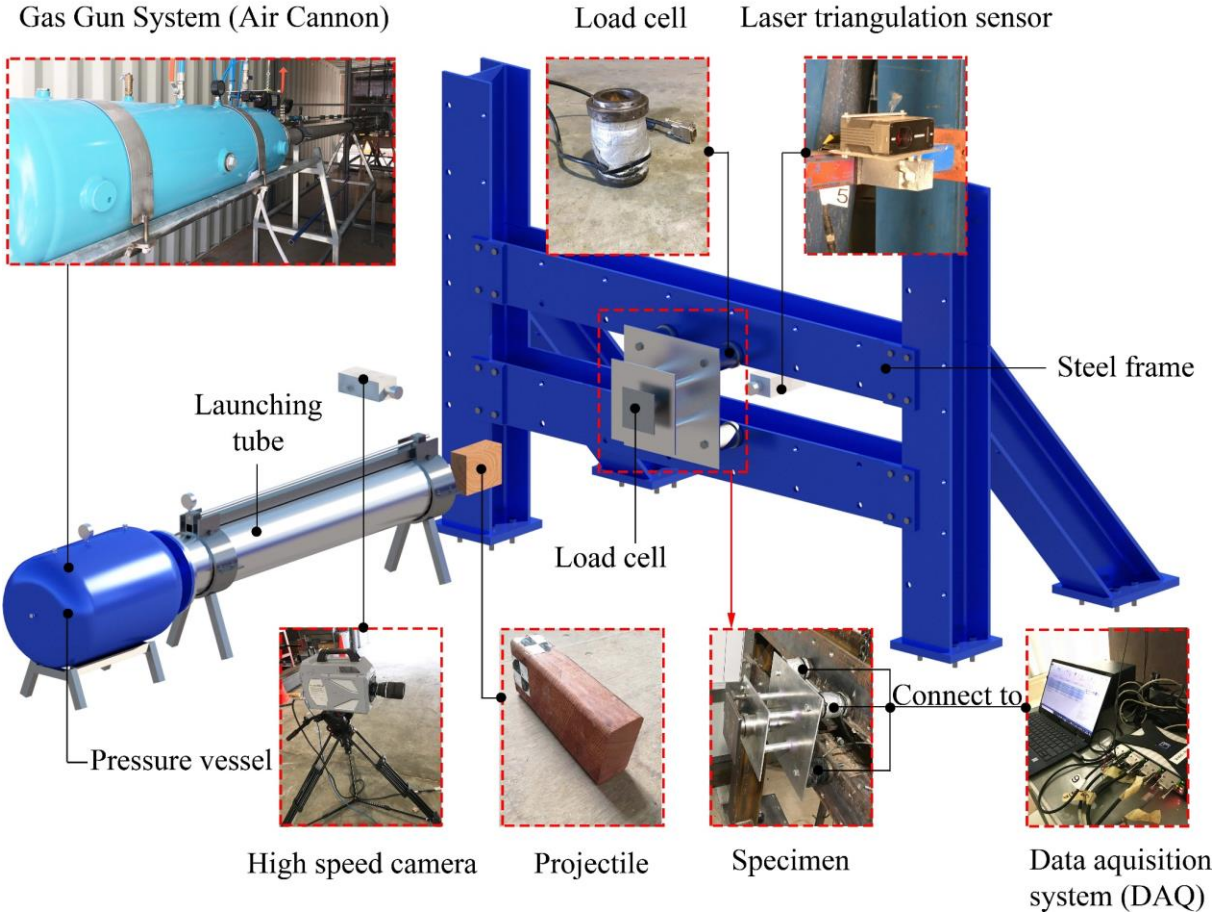


Figure 7-6. Setup of the gas gun test

7.3. Theoretical analysis

The spring-mass model [134] depicted in Figure 7-7 can be utilized to theoretically conceptualize the meta-truss bar configuration. In the model, the stiffness k_{a1} periodically connects two adjacent mass m which is restrained by shear stiffness k_{s1} at a spacing of L . The equation of motion for the j^{th} unit cell, in which u^j denotes the displacement, can be expressed as follows:

$$m_1 \frac{\partial^2 u_1^{(j)}}{\partial t^2} + k_{a1} (2u_1^{(j)} - u_1^{(j+1)} - u_1^{(j-1)}) + k_{s1} u_1^{(j)} = 0 \quad (7-1)$$

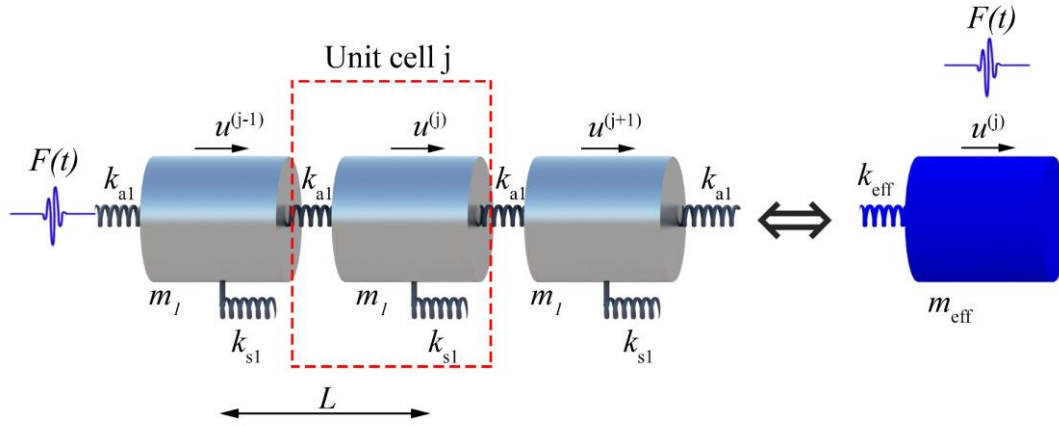


Figure 7-7. Illustration of the idealized spring-mass model for an infinite long meta-truss bar

The solution for the harmonic wave can be given as $u^{j+n} = Ue^{i(qx+nqL-\omega t)}$, in which U , q , and ω represent the displacement amplitude, wave number, and angular frequency, respectively. Then, the effective mass and effective stiffness of the lattice system can be respectively derived as [42, 134]:

$$m_{eff} = m_1 - \frac{k_{s1}}{\omega^2} \quad (7-2)$$

$$k_{eff} = k_{a1} - \frac{1}{4} \left(m_1 - \frac{k_{s1}}{\omega^2} \right) \omega^2 \quad (7-3)$$

where m_{eff} and k_{eff} are the effective mass and effective stiffness of the equivalent system.

The dispersion relation of the system in which each unit is regarded as an equivalent homogeneous material can be given as

$$\cos qL = 1 - \frac{m_1 \omega^2 - k_{s1}}{2k_{a1}} \quad (7-4)$$

To define the width of the passband, the dispersion in Eq. (7-4) is solved and the expression of the angular frequency can be obtained as follows

$$\omega = \sqrt{\frac{2k_{a1} (1 - \cos(qL)) + k_{s1}}{m_1}} \quad (7-5)$$

By substituting $qL = 0$ into Eq. (7-5) or setting the effective mass m_{eff} in Eq. (7-2) to zero, the starting point of the passband is

$$\omega = \sqrt{\frac{k_{s1}}{m_1}} \quad (7-6)$$

Similarly, the ending point of the passband can be calculated by setting Eq. (7-3) to zero or substituting $qL = \pi$ into Eq. (7-5) as

$$\omega = \sqrt{\frac{4k_{a1} + k_{s1}}{m_1}} \quad (7-7)$$

The transmission coefficients of the entire system, T , can be computed based on the ratio of displacements of the inner and end unit cells as

$$T = \left| \prod_{j=1}^N T^{(j)} \right| = \left| \prod_{j=1}^N \frac{u^{(j)}}{u^{(j-1)}} \right| \quad (7-8)$$

More information and discussions on the equivalent spring-mass model for the meta-truss bar were presented in previous studies [83, 134]. Based on Eqs. (7-2), (7-3), and (7-4), the analytical dispersion curve and the effective parameters including the effective mass and effective stiffness at a sweep frequency range for the considered meta-truss bar are obtained and presented in Figures 7-8a and 7-8b, respectively. It is shown that the theoretical passband of the meta-truss bar is in the frequency range of [1,200 – 2,800] Hz, where both the effective parameters are positive. Particularly, at other frequencies, when either the effective mass or the effective stiffness is negative, the bandgaps exist. The associated frequency regions where m_{eff} and k_{eff} become negative are termed as the 1st bandgap at [0 – 1,200] Hz and the 2nd bandgap at [$>2,800$] Hz, respectively. As shown, the bandgap prediction from the dispersive analysis agree well with the corresponding results from the negative effective parameters, indicating the existence of the two bandgaps of the meta-truss bar. It is evident that the bandgaps of the meta-truss bar with single local resonators are independently formed when the effective mass and effective stiffness become negative, respectively. It is worth mentioning that the interested frequency range in this chapter is only up to 5,000 Hz, covering the frequency band of common impact loads acting on structures [10].

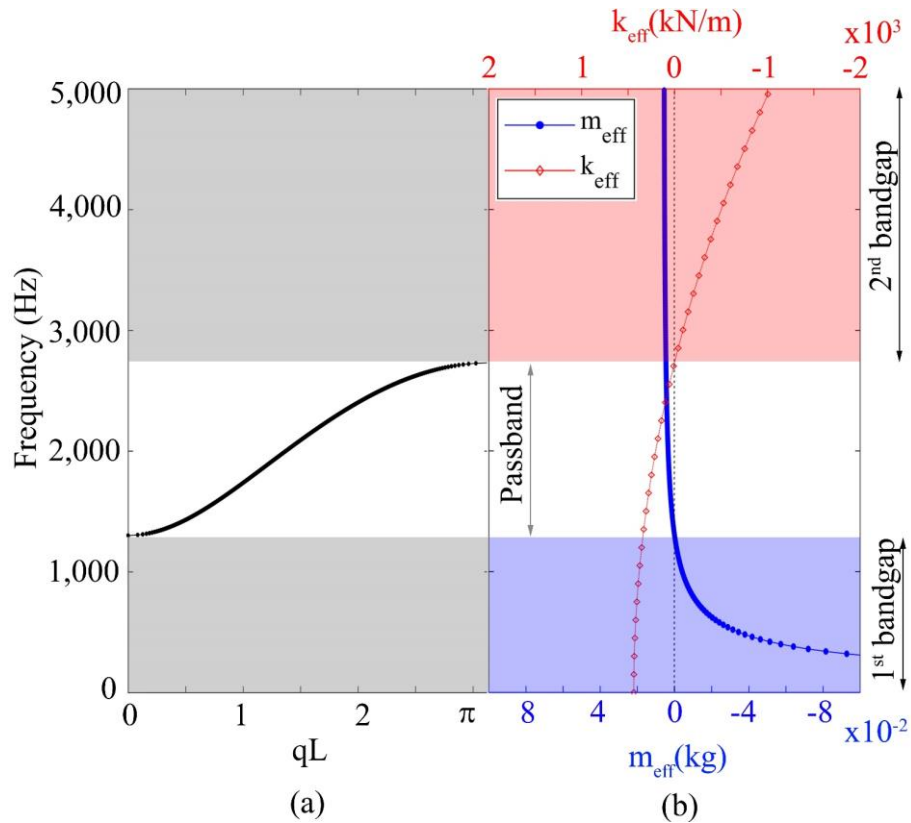


Figure 7-8. Theoretical bandgap regions of the meta-truss bar are determined by (a) dispersion curve and (b) effective parameters

7.4. Numerical simulation

The FE models of the meta-truss bar and the meta-panel are built to quantify the influences of some parameters which cannot be measured from the experiments, e.g. energy absorption of individual components and stress contours. Simulations are performed by utilizing an explicit dynamic FE software, LS-DYNA, to examine the dynamic characteristics of the meta-truss (Figure 7-2) and the meta-panel (Figure 7-9). The projectile is considered rigid by using the card *MAT_RIGID while the *MAT_ELASTIC material model is used to simulate the dynamic behaviour of silicone rubber. The contact between the projectile and the load cell is simulated by the contact algorithm *AUTOMATIC_SURFACE_TO_SURFACE. The outer truss bar and the two facesheets are assumed to be perfectly connected and modelled by the keyword *TIED_NODE_TO_SURFACE. The interfaces between the resonators and silicone coating are defined by the keyword *TIED_SURFACE_TO_SURFACE. An initial velocity is assigned to the projectile through the *INITIAL_VELOCITY_GENERATION card. The clamp condition at the load cell positions in the back facesheet is adopted by *BOUNDARY_SPC_SET option. All the elements are modelled using solid hexahedron

elements (SOLID 164) with a minimum mesh size of 1 mm. A reasonably fine mesh in the vicinity of the contact area is adopted after performing the convergence study, therefore, gradient mesh is chosen for both computing efficiency and accuracy consideration.

In addition, to numerically predict the bandgaps of the meta-truss bar (Figure 7-2), an input signal with a sweep frequency ranging from 0 – 5,000 Hz defined by the keyword *PRESCRIBED_MOTION_SET is applied to one end of the simulated meta-truss bar, and the output response at the other end is captured to calculate the transmission coefficient. All nodes along the perimeter of the outer tube are fixed in all directions using the *BOUNDARY_SPC_SET.

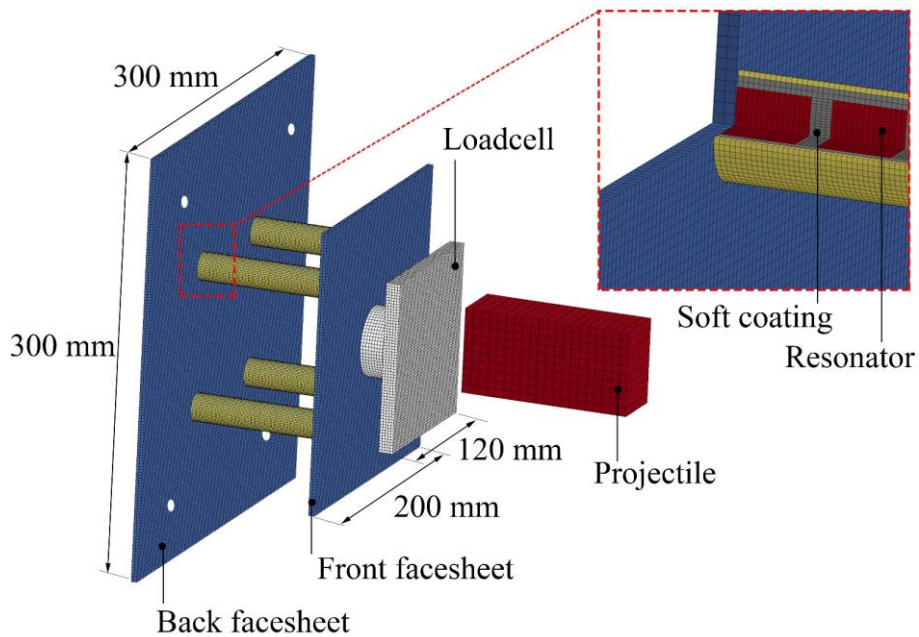


Figure 7-9. Schematic of finite element model used to investigate the dynamic response of the meta-panel in the impact test

Johnson-Cook material model with strain hardening is adopted for aluminium. The yield stress is, therefore, expressed as

$$\sigma_{eq} = \left[A + B \varepsilon_{eq}^n \right] \left[1 + C \ln \left(\frac{\dot{\varepsilon}}{\dot{\varepsilon}_0} \right) \right] (1 - T^{*m}) \quad (7-9)$$

where the yield stress and the equivalent plastic strain are denoted by σ_{eq} and ε_{eq} , respectively; $\dot{\varepsilon}$ is the plastic strain rate while $\dot{\varepsilon}_0$ is a reference strain rate and is generally set to 1.0 s^{-1} ; T^* is the nondimensional temperature ratio and is set to zero in this chapter [113]; A , B , C , n , and m are material constants and their values are given in Table 7-2.

Table 7-2. Material parameters of aluminium alloy 1060 for Johnson-Cook model [113]

Density (kg/m ³)	Poisson's ratio	Young's Modulus (GPa)	<i>A</i> (GPa)	<i>B</i> (GPa)	<i>C</i>	<i>m</i>	<i>n</i>
2,770	0.33	70	0.369	0.675	0.007	1.5	0.7

7.5. Results and discussions

7.5.1 Experimental verification of the bandgaps in meta-truss bar

The hammer impact tests described above were conducted to examine the wave mitigation characteristics of the meta-truss bar. The transmission ratio, TR , is a critical parameter for the design of the meta-truss bar, which is utilized to quantify the resonance-induced bandgaps in the experiments. It is also adopted to tailor the meta-core design to attenuate incident stress wave at targeted frequency ranges. By definition, TR is the ratio between the frequency-dependent amplitudes of the output and input signals. Firstly, the time-history acceleration responses from the two accelerometers, i.e. $ac_{in}(t)$ and $ac_{out}(t)$, are transformed into the frequency domain by using Fast Fourier Transform (FFT). For brevity, the details of the method are not presented herein and readers can refer to a previous study by Adesina et al. [202] for more details. Then, the transmission ratio in the frequency band structure can be calculated as follows [58, 82]:

$$TR = 20 \times \log \left[\frac{ac_{out}(f)}{ac_{in}(f)} \right] \quad (7-10)$$

where $ac_{in}(f)$ and $ac_{out}(f)$ are the frequency-dependent amplitudes of the input signal (i.e. incident acceleration) and the output signal (i.e. transmitted acceleration) through the test specimen recorded by two accelerometers in the frequency domain, respectively.

In this chapter, the meta-truss specimen described in section 7.2.2.1 was examined by conducting the non-destructive impact test with an instrumented impact hammer. The test setup was presented in Section 7.2.3.1. The specimen was impacted five times, and a total of ten acceleration time histories were analyzed to derive the experimental transmission ratio. Figure 7-10 illustrates the typical pair of input and output acceleration time histories recorded by the two accelerometers located at two ends of the meta-truss bar. As shown, wave attenuation was experimentally observed as expected.

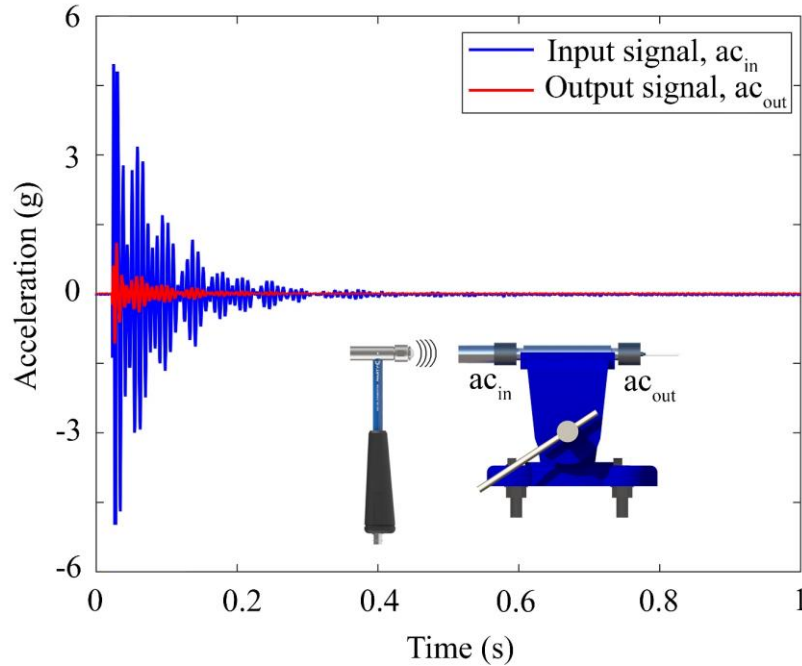


Figure 7-10. Input and output acceleration time histories at two ends of the meta-truss bar

To verify the mechanism and evaluate the width of the bandgaps, the experimental transmission ratio (TR) calculated from the test data is compared with the analytical and numerical transmission coefficients, as shown in Figures 7-11a, 7-11b, and 7-11c. The results of the three approaches show that the transmission profile of the meta-truss bar can be divided into three regions including two apparent bandgaps in the low and high-frequency ranges and one transmission band. The analytical and numerical bandgaps of the meta-truss bar are respectively marked by the red and grey-shaded areas in Figures 7-11a and 7-11b, respectively while the blue-shaded areas labelled in Figure 7-11c represent the experimental bandgaps, in which the negative TR values in the frequency band structure indicate the significant wave attenuation due to the local resonance effect. The bandgaps obtained from the experimental TR show a reasonably good agreement with those from the analytical and numerical results, which indicates the validity of the analytical derivation and numerical simulation, although a slight mismatch is also observed. In particular, the analytical derivations give two bandgaps in the red-shaded areas at the frequency ranges of $[0 - 1,200]$ Hz for the 1st region and $[>2,800]$ Hz for the 2nd region, while the corresponding ranges from the experimental results are $[0 - 950]$ Hz and $[>3,000]$ Hz in the blue-shaded areas. The possible reason for the slight variation is the assumption of the simplified analytical model. In particular, the meta-truss bar is assumed continuous with an infinite number of unit cells connected by springs in the analytical model while the experimental specimen had a finite length of 6 unit cells only. The bandgaps obtained

from the FE model are $[0 - 1,100]$ Hz and $[>2,940]$ Hz, which are closer to the experimental results since it contains the same number of unit cells as the tested specimen (i.e. 6 unit cells). The difference between the numerical and experimental results can be attributed to the finite element model discretization errors and the discrepancies in material properties used in the numerical model and the true material properties. Nonetheless, these results confirm the existence of bandgaps that reduce wave transmission in the meta-truss bar and verify that both the analytical solution and numerical model give reasonable predictions of the bandgaps.

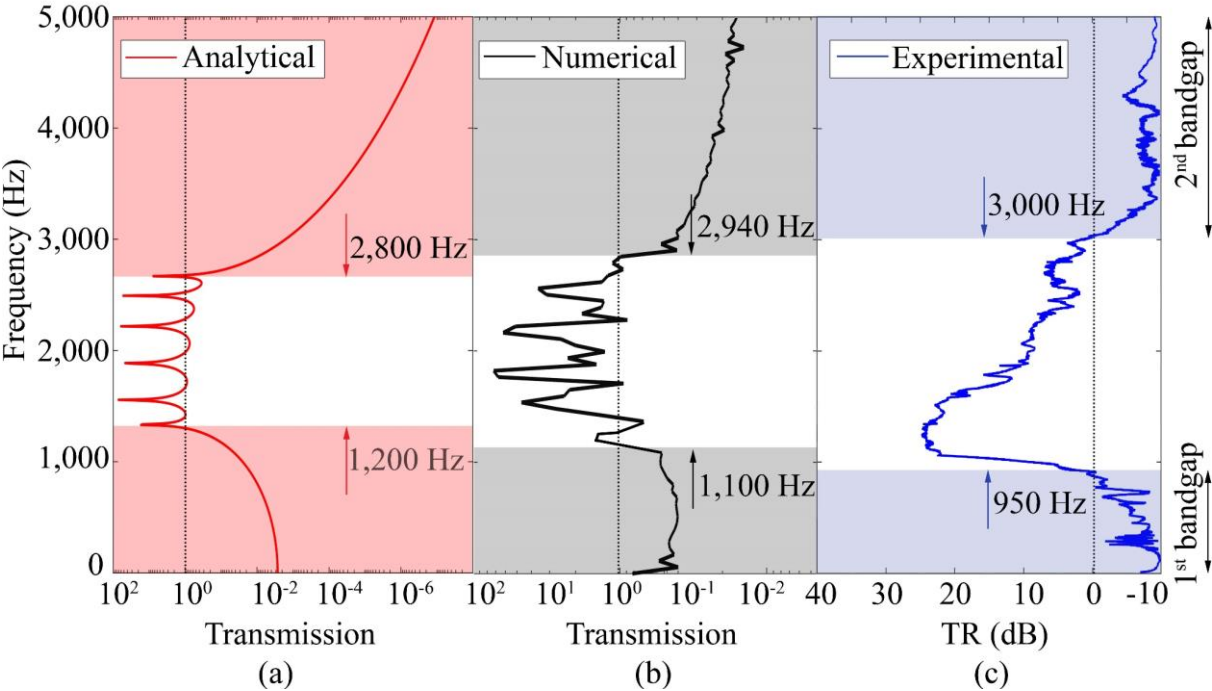


Figure 7-11. Comparison of the bandgaps based on wave transmission ratio of (a) analytical, (b) numerical and (c) experimental results

7.5.2 Transient responses of the meta-panel

To demonstrate the excellent performance of the meta-panel under dynamic loading, the transient responses of the three sandwich panels with different cores are compared in this section. The gas gun impact tests (Figure 7-6) were conducted to evaluate the transient performances of the three specimens including the meta-panel (Figure 7-3) and two reference panels, i.e. the hollow-truss panel (Figure 7-12a) and solid-truss panel (Figure 7-12b). The three specimens had the same dimensions and the sole difference lies in the configuration of the truss cores. In the test, a wooden projectile (Figure 7-6) weighing 1 kg with a velocity of 25.8 m/s impacted the specimens via a load cell at the centre point. It is worth mentioning that the weights

of the considered panels are different, in which meta-panel weighs 1.63 kg while the weight of the hollow-truss and solid-truss panels are 1.49 kg and 1.77 kg, respectively.

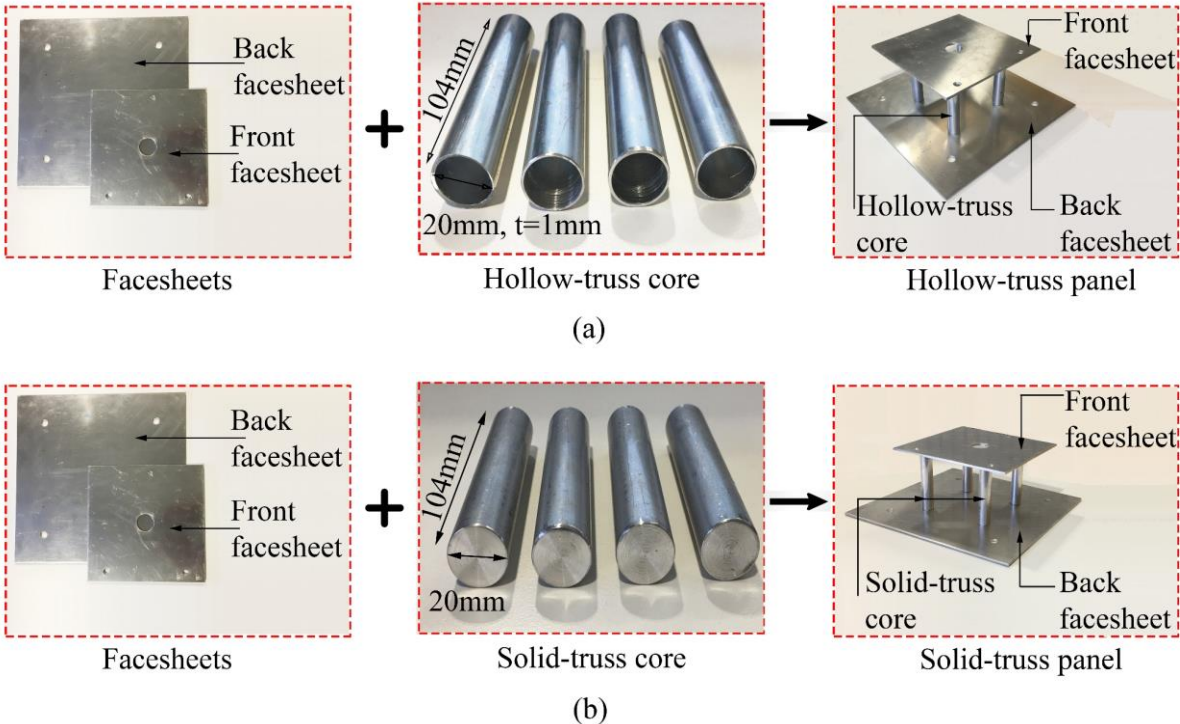
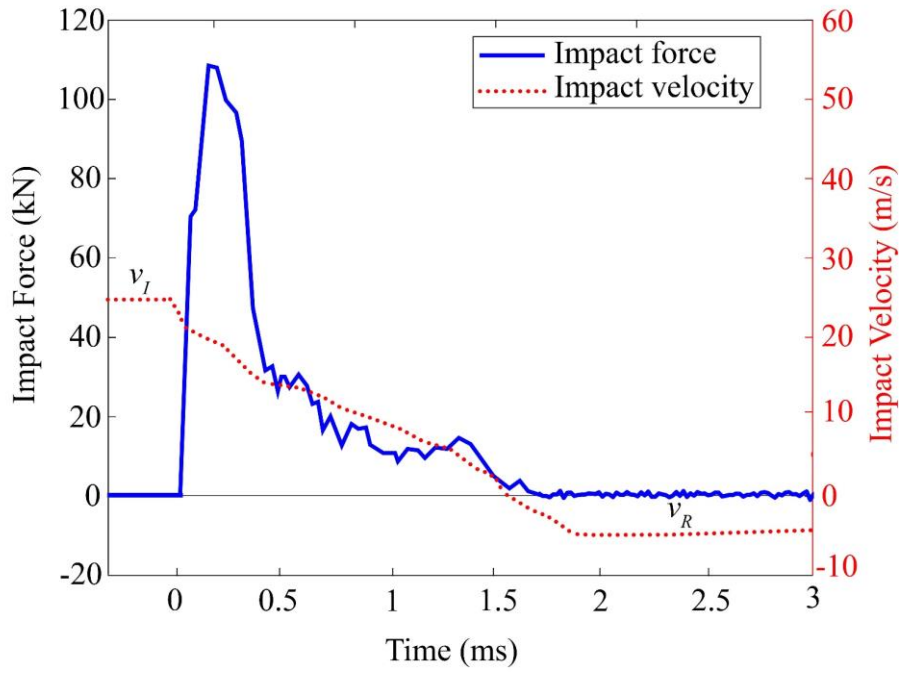


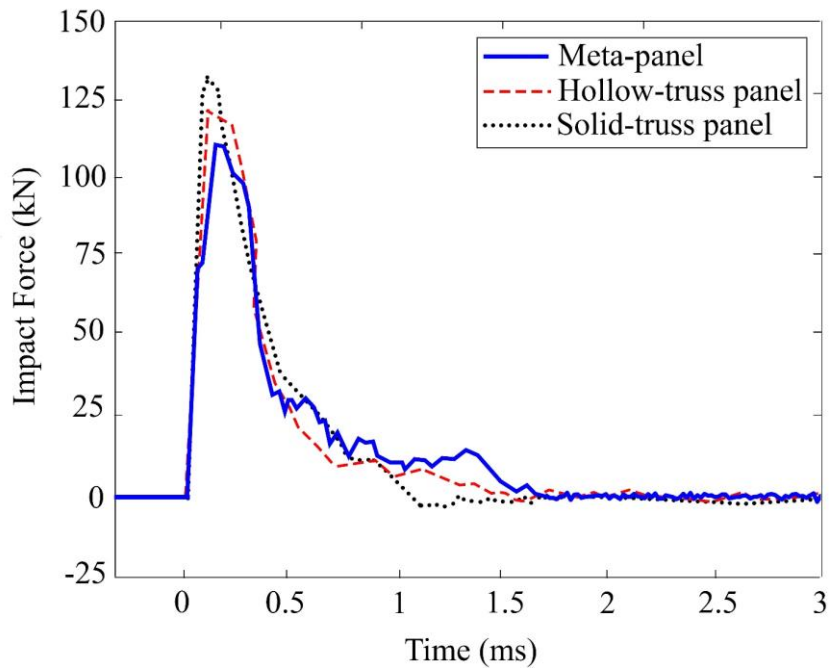
Figure 7-12. Schematic diagram of the referenced panels including (a) hollow-truss panel and (b) solid-truss panel

7.5.2.1 Impact response description

Generally, as shown in Figure 7-13, there are distinct stages during the impact process in which the interaction and energy absorption mostly occurred, namely the increasing-force stage, the decreasing-force stage, and the zero-force stage. The initial increase in impact force indicates the collision of the projectile and the specimen, after reaching its peak, it progressively decreases to zero. There was no penetration of the projectile because of the test setup. Meanwhile, the projectile experienced different motion phases including the decreasing-velocity phase, the rebounding-velocity phase, and the detaching-velocity phase. Initially, the velocity of the projectile decreased from $v_I = 25.8$ m/s to 0 m/s. After the projectile velocity became zero, it reincreased from zero to $v_R = -5.3$ m/s in the opposite direction. Finally, the projectile separated from the meta-panel with a rebound velocity and it resulted in a residual deformation on the front facesheet of the meta-panel. This experimental observation is consistent with those reported in the previous studies regarding the experimental impact response of conventional sandwich panels [203].



(a)



(b)

Figure 7-13. Impact force and impact velocity of the projectile under gas gun impact test of (a) meta-panel and (b) three different panels

The typical impact force time history measured under the impact velocity of 25.8 m/s on the meta-panel is presented in Figure 7-13a, while the impact forces time histories of the three panels are compared in Figure 7-13b. As shown, these impact force time histories were quite similar. A slight variation of the peak impact forces was observed. The stiffer specimen (solid-

truss panel) experienced a slightly higher peak impact force while its duration is marginally shorter. To examine the effectiveness of the meta-panel on mitigation of the impact force, the impact force time history is transformed into the frequency domain using FFT and shown in Figure 7-14. As shown, the impact force energy is distributed in a broad frequency band from 0 to 5,000 Hz. The bandgaps of the meta-truss bar obtained above from the hammer impact test is also shown in Figure 7-14. The impact force energy with frequencies coincident with the meta-truss bandgaps is expected to be substantially reduced when transmitting through the meta-truss bar. However, as shown, a large amount of impact force energy can also be transmitted through the meta-truss bar to the back facesheet because their frequencies fall into the passband of the meta-truss bar.

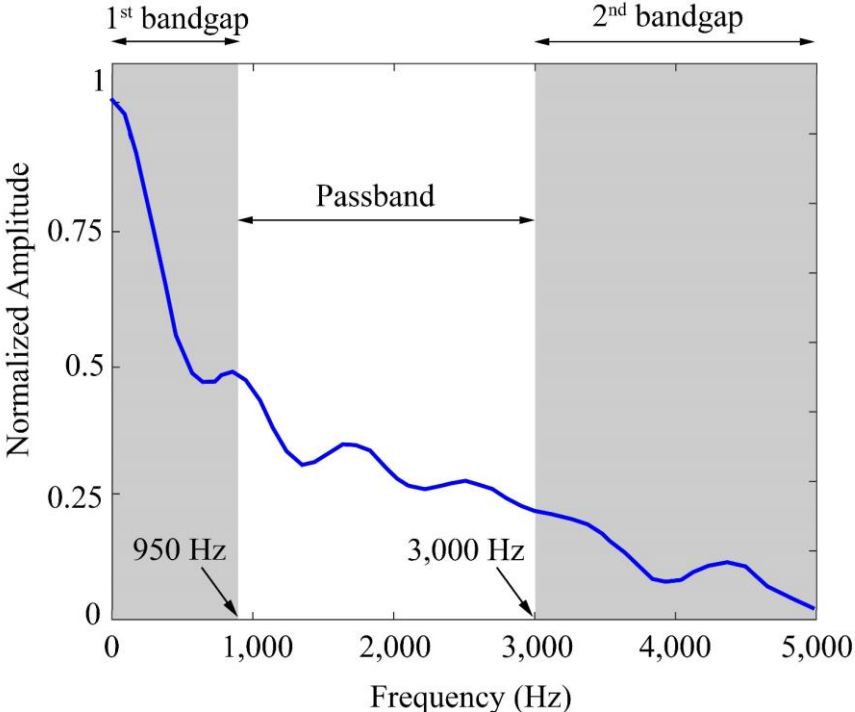


Figure 7-14. FFT spectrum of the impact force of the meta-panel recorded in the impact test

7.5.2.2 Deformation analysis

Predicted results from the numerical study and experimental data are compared to verify the numerical model. Figure 7-15 shows the comparison of the experimental and numerical deformation process of the meta-panel. As shown, the experiment and numerical prediction showed similar deformation patterns and the deformation process of the meta-panel. When the projectile hit the centre of the front facesheet of the panel with the impact velocity $v_I = 25.8$ m/s, the panel started to deform instantly to absorb the impact energy. The facesheets were mainly deformed in their central region and the indentation can be observed. The depth of the

indentation at the front facesheet depends on the impulse loaded on the panel while that of the back facesheet depends on the force transmitted to the back facesheet through the truss bars, which can be used to demonstrate the effectiveness of the proposed meta-panel for structure protection. The deformation of the meta-panel initially occurred at the impacted area of the front facesheet and then propagated to the remaining parts. The impact loading was also transferred from the front facesheet through the meta-core to the back facesheet and then the support. When the panel reached its maximum deflection, the projectile started bouncing back in the opposite direction. As shown, there was no perforation failure of the facesheets under the impact testing. It is worth mentioning that the circular hole in the front facesheet was intentionally designed to mount the load cell, which is also modelled in the numerical simulation to replicate the test. Finally, the projectile separated from the panel and the panel entered the free vibration phase.

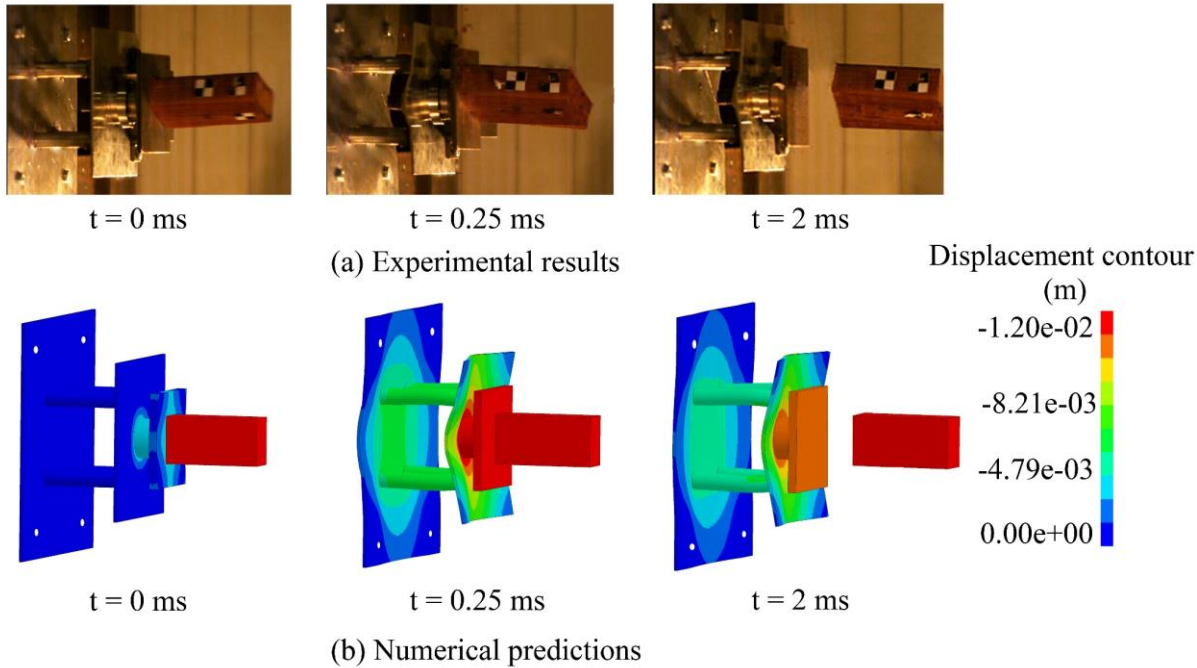


Figure 7-15. Comparison of deformation process of the meta-panel from (a) experimental results and numerical predictions

To demonstrate the effectiveness of the meta-panel in the impact mitigation, the experimental central displacement time histories of the back facesheet recorded by the laser triangulation sensor are shown in Figure 7-16. The numerical displacement at the center of the back facesheet of the meta-panel is also compared with that of the experimental data to further validate the numerical model. Generally, the simulation outcomes agree well with the experimental results,

indicating the reliability of the numerical model. The displacement of the meta-panel reached its peak at 7.9 mm in the experiment while the corresponding numerical prediction is 7.4 mm.

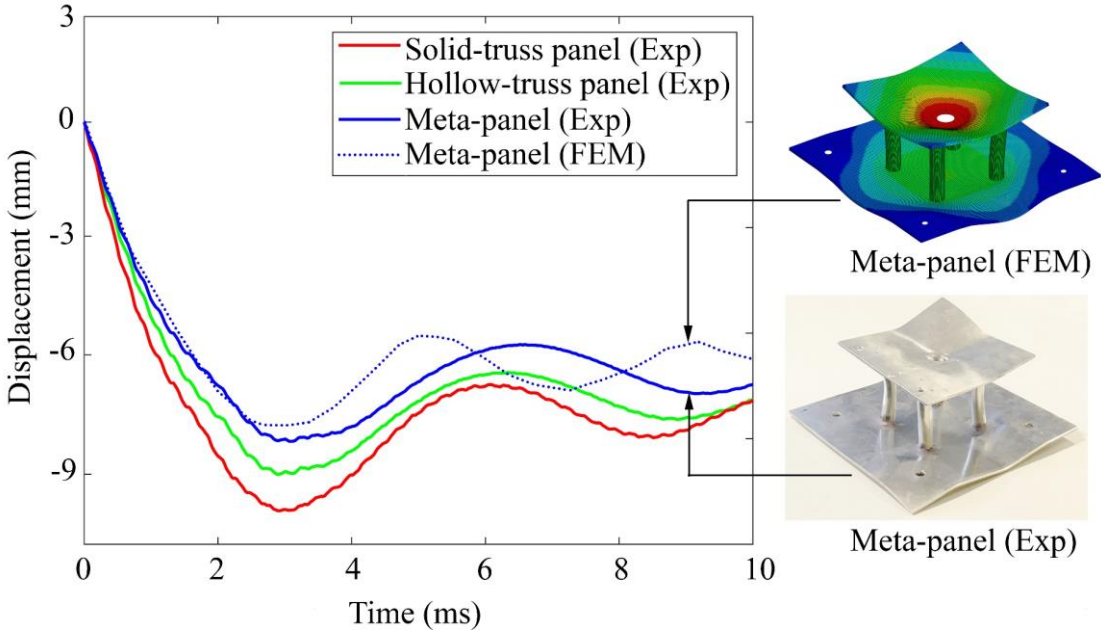


Figure 7-16. Displacement time histories of the back facesheet of the three panels

In particular, the maximum and residual deflection of the back facesheet of the meta-panel were 7.9 mm and 6.4mm, respectively (see Figure 7-17). It was observed that the solid-truss panel had the largest displacement (i.e. 10.1 mm), followed by the hollow-truss panel (i.e. 8.7 mm) and the meta-panel (i.e. 7.9 mm). The meta-panel experimentally demonstrated its effectiveness in mitigating the impact loading effect, the maximum displacement of the meta-panel back facesheet was 10.1 %, and 27.8 % lower than that of the hollow-truss panel and solid-truss panel, respectively. The meta-core mitigated the impact loading being transmitted to the back facesheet of the meta-panel compared to the other two reference panels. Furthermore, the plastic deformation of the meta-truss bar is relatively less intensive as compared to the other two reference panels as shown in Figure 7-17. This is because the local resonance of the meta-core absorbs a certain amount of impact energy, while the impact energy of the reference panels was absorbed mainly by plastic deformation, including the plastic deformation of the solid and hollow-truss bar. These results demonstrate the meta-panel had better capacity than the other two reference panels in resisting the repeated impact loads. It is worth noting that the total weights of these three structures are different. The sizes of the solid and hollow truss bars need to be adjusted to make the total weight of the three panels the same. Since the main objective of this chapter is to investigate the effectiveness of the meta-panel in mitigating the impact loading, the size of the truss bars is kept the same instead of the weight in the analysis. Besides,

the dynamic load resistant effectiveness of the meta-panel having the same mass as the conventional panels, i.e. hollow-truss and solid-truss panels, was proven in the previous study [41], which is therefore not repeated herein for brevity.

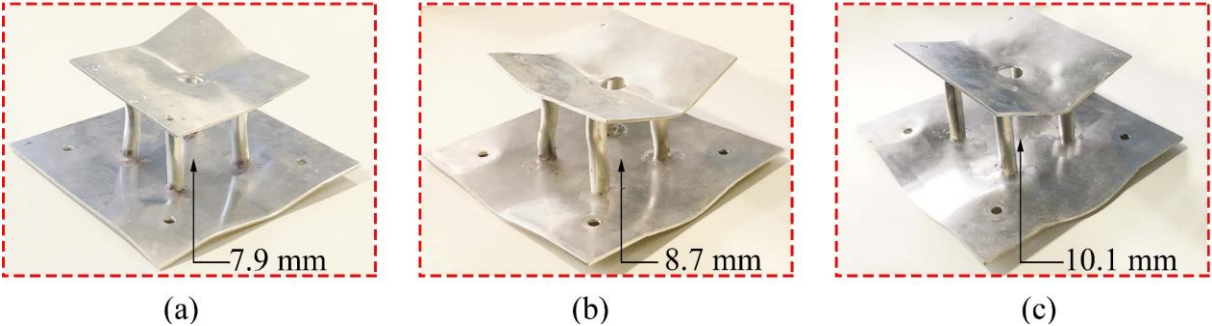


Figure 7-17. Deformed shapes with the maximum residual deformation of the back facesheet of (a) meta-panel, (b) hollow-truss panel, and (c) solid-truss panel

7.5.2.3 Reaction forces

The reaction force is another key parameter that is widely used to evaluate the effectiveness of the sandwich panel in an impact event as it represents the force being transmitted to the protected structure. Figure 7-18 illustrates the reaction force time histories of the three considered panels in the impact tests. The reaction force was calculated as the sum of all those recorded by the four load cells mounted to the back facesheet of the panel in the time domain. As shown, the lowest reaction force is observed for the meta-panel with a peak of 42.5 kN. In particular, the peak reaction force of the meta-panel was 19.1% and 31.3% lower than that of the hollow-truss and solid-truss panels, respectively, indicating its good capability in reducing the force transmission to the protected structure under impact loads. This phenomenon was expected and can be explained by the favourable bandgaps generated from the relative motions between the resonators and the silicone-rubber coatings. These bandgaps possess the ability to counteract the incident stress from the impact load, leading to a reduction in stress transmission from the impact point to the back facesheet and then the supports. It should be noted that the stress-filtering phenomenon only occurs when the stress waves of the impact load have frequencies falling into the bandgap ranges. To further examine the impact resistance, the reaction forces of the three considered panels in the time domain are transformed to the frequency domain, as shown in Figure 7-19. It can be seen that the reaction force of the meta-panel in the 1st bandgap is substantially smaller than those of the other two reference panels while there was no reduction occurring in the passband. It should be noted that the complete suppression of the force transmissions in the frequency bandgaps of the meta-truss bar could

not be achieved since the outer tube of the meta-truss bar could still transmit a certain amount of impact load. The testing results demonstrated the better protective performance of the meta-panel in terms of the back facesheet deformation and force transmission as compared to the other two reference cladding panels.

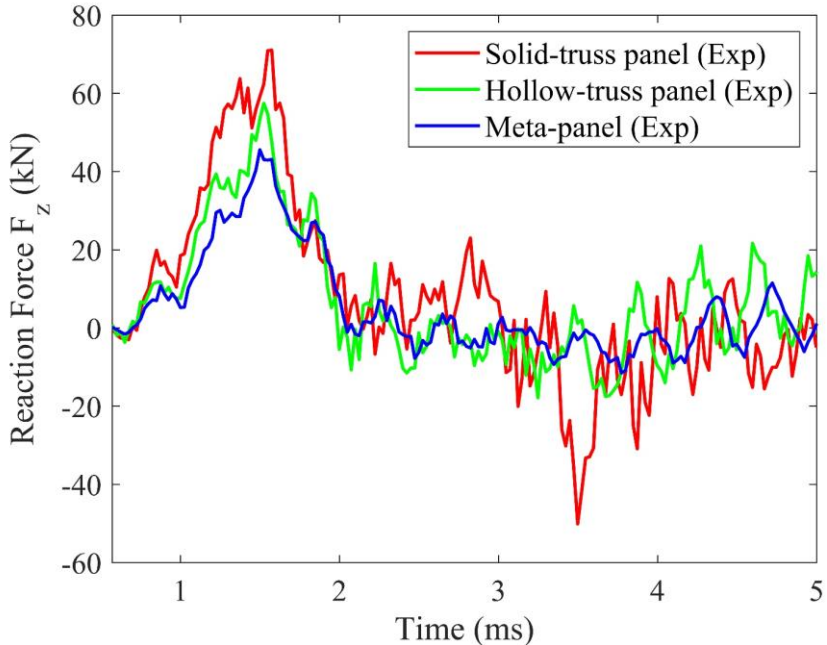


Figure 7-18. Measured reaction force time histories of the three considered panels

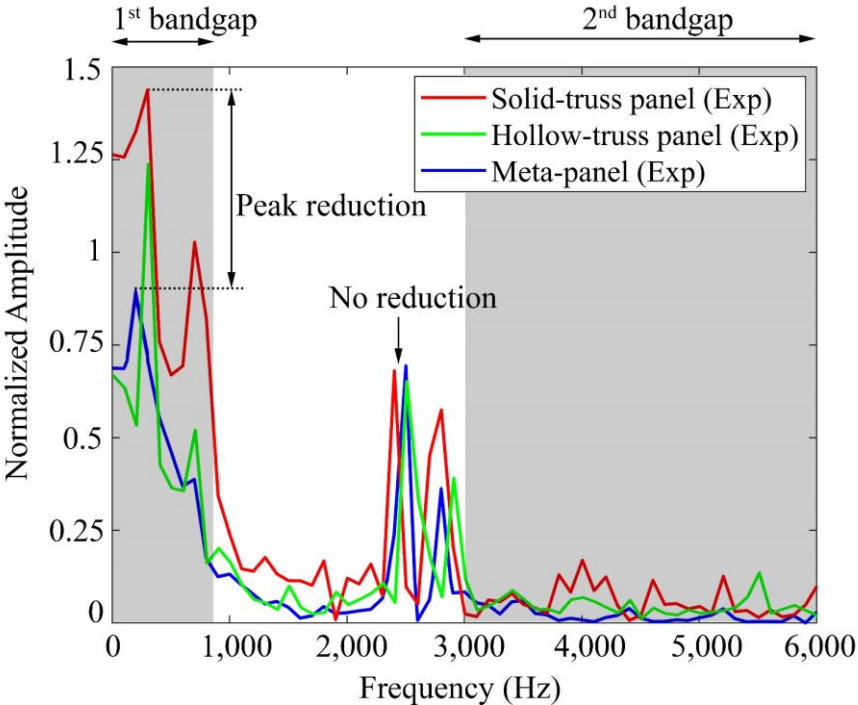


Figure 7-19. FFT spectra of the measured reaction forces of the three considered panels

7.5.2.4 Energy absorption characteristics

The energy absorption capacity is another critical index for evaluating the impact resistance of the sandwich panels under impact loading. Three important indexes including the total energy, the kinetic energy and the internal energy are adopted to evaluate the energy absorption performance of each component of the meta-panel. It is worth mentioning that the verified numerical model is used to evaluate the energy absorption of the sandwich panels subjected to impact loads. Regarding the conservation law of energy, the total energy of the system is constant throughout the impact event. In the impact process, the initial kinetic energy of the projectile is transformed into the internal energy and kinetic energy of the sandwich panels. Figure 7-20 illustrates the energy of the projectile and the energy absorption of each component of the meta-panel, i.e. facesheets, outer tube of the meta-truss bar, soft coatings, and resonators. Initially, the kinetic energy of the projectile decreases quickly after contacting with the meta-panel, which is transformed into the internal energy and kinetic energy of each meta-panel component. The kinetic energy of the projectile becomes zero at the lowest position before re-increasing again with the rebound of the impactor. At the end of the impact event, the projectile separated from the meta-panel with the rebound kinetic energy. Figure 7-20 shows the cores and the coatings absorbed approximately 33% of the impact energy. This explains the better impact resistance of the meta-panel.

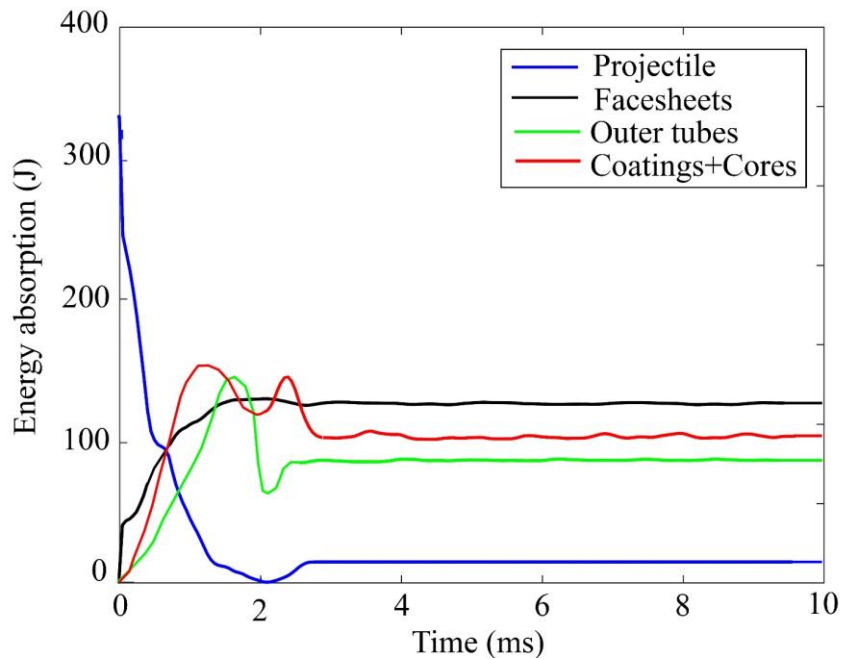


Figure 7-20. Time histories of energy compositions in the meta-panel (FEM)

As can be seen from Figure 7-21, among the energy absorption by each component, the facesheets (i.e. front and back facesheet) of each panel absorb the highest amount of energy (i.e. 120 J), followed by 110 J and 90 J respectively for the coatings + cores and the outer tube of the truss bar. It is worth mentioning that the energy absorption of the coatings + cores is composed of the kinetic energy of the resonators due to their relative movement and internal energy owing to the deformation of the coatings. As shown, the amount of energy absorbed by the coatings and resonators is higher than that of the outer tube of the meta-truss bar, which is associated with its plastic deformation. These results demonstrate less impact-induced damage to the truss bar because the local vibration of the resonators absorbs a considerable amount of the total impact energy. This is an advantage of the meta-panel since the less-deformed meta-truss bars can resist subsequent loads and absorb more impact energy. It also can be seen that the energy absorbed by the back facesheet is relatively small (i.e. 50 J), indicating the meta-panel possesses a high energy absorption ability through the local vibrations of the resonators, which not only reduce the damage to the truss bars but also protect its back facesheet hence the protected structures.

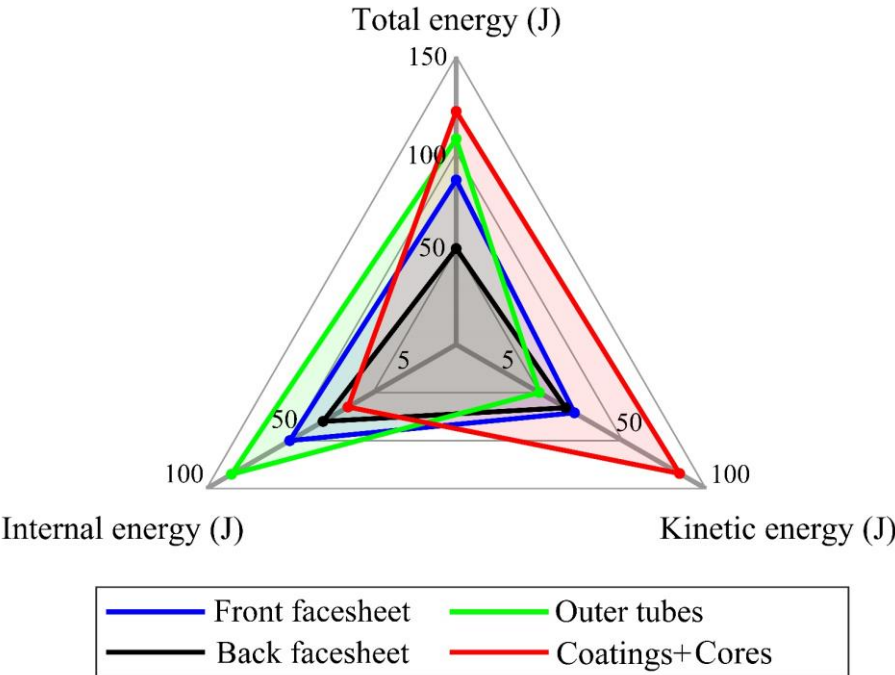


Figure 7-21. Energy absorption of each component of the meta-panel (FEM)

The energy absorption of different sandwich panels under impact loading is compared in Figure 7-22. Among the three panels, the meta-panel with the meta-core embedded inside the outer tube exhibits the highest total energy absorption (320 J) while the panel with the solid truss bars absorbs the least amount of energy (265 J). It is because the strong solid-truss bars experience

less plastic deformation as compared to the hollow-truss bars. Higher energy absorption of the meta-panel is attributed to the fact that more energy can be absorbed by a combination of plastic deformation and out-of-phase movement of the cores while the energy absorption of the two reference panels is solely due to the plastic deformation of the two facesheets and the truss bars. As shown, the energy absorption of the truss bars in the hollow-truss panel is the highest, indicating the largest plastic deformation, followed by those in the solid-truss panel and meta-panel, respectively. The outer tube of the meta-truss bar absorbs the least energy, implying the least damage to the meta-core. Overall, compared to the two reference panels, the meta-panel has the highest energy absorption capacity and suffered the least damage to its back facesheet and the truss bars, demonstrating its better performance in absorbing impact energy and mitigating damage to the protected structures. It should be noted that these results are based on the example meta-panel consisting of only four meta-truss bars. For a realistic protective sandwich panel, there are more meta-truss bars, hence more local resonators. Local vibrations of more resonators would absorb more impact energy, hence increasing the effectiveness of the structure protections in terms of the reduced force transmission and back facesheet deformation as compared to the example meta-panel with only four meta-truss bars.

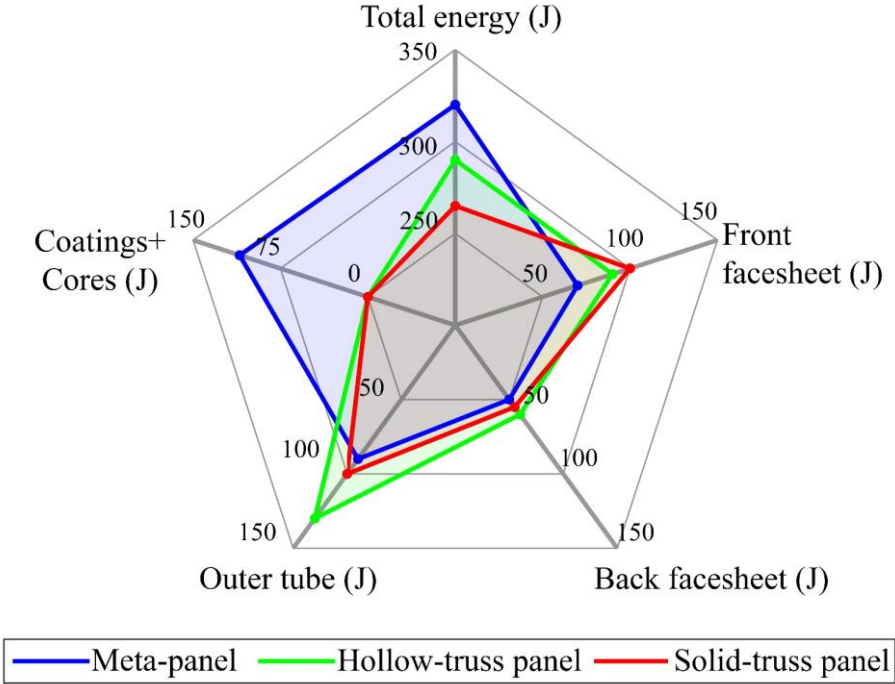


Figure 7-22. Energy absorption of different panels (FEM)

It is worth mentioning that the total mass of the three investigated panels are different. There need to be some modifications in terms of the sizes of the hollow-truss and solid-truss bars to make the total mass of the three panels the same. This study primarily focuses on the impact

load mitigation effect of the meta-panel, therefore, the size of the truss bars remains unchanged instead of the mass. Additionally, specific energy absorption (SEA) obtained by using the energy absorption of the investigated panel dividing its mass is utilized in this study to provide a straightforward comparison of the energy absorption capacity with respect to the mass of the panels. The results exhibit that SEA of the reference panels (i.e. 280 J/kg and 190 J/kg for panels with hollow-truss bar and solid-truss bar, respectively) are significantly smaller than that of the meta-panel (302 J/kg), indicating the better energy absorption capacity per unit mass of the meta-panel. Besides, the dynamic load resistant effectiveness of the meta-panel having the same mass as the traditional panels was proven in the previous study, which is therefore not repeated herein for brevity. In conclusion, it is proven that the meta-panel outperforms the conventional panels in resisting impact loading.

7.5.3 Effect of impact velocity

The influence of impact velocity on the dynamic performance of sandwich panels has been extensively studied over the last twenty years [204, 205]. However, no experimental testing has been conducted to evaluate the impact velocity effect on the newly proposed meta-panel. Therefore, the effect of impact velocity on the performance of the meta-panel was experimentally tested in this section. It should be noted that in the tests, the projectile had different impact velocities but the same mass of 1 kg. To gain an insightful understanding of the influence of impact velocity on the meta-panel, impact tests with three velocities, i.e. 25.8 m/s, 30.5 m/s, and 35.2 m/s, of the projectile on three identical specimens were conducted.

7.5.3.1 Impact response

The relationship between the duration and the peak amplitude of the impact force under different impact velocities is shown in Figure 7-23. The impact velocity significantly affected the peak impact force while it had a limited influence on the duration of the impact loading. Particularly, in this chapter, increasing the impact velocity from 25.8 m/s to 35.2 m/s led to the peak impact force almost doubled from 108.5 kN to 210.5 kN, but only slightly increased the loading duration from approximately 1.50 ms to 1.75 ms. This observation was consistent with those reported in the previous studies of the impact tests [56, 142].

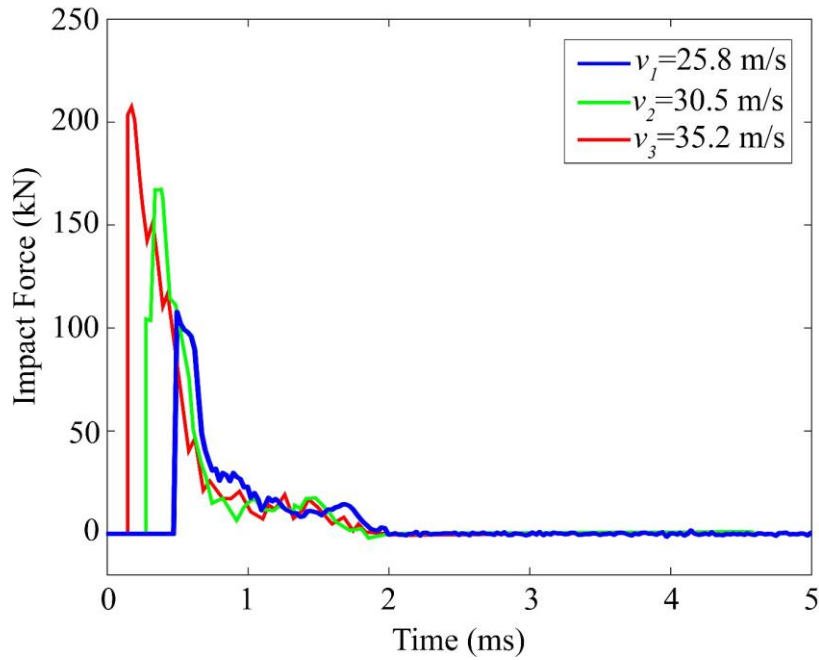


Figure 7-23. Impact force time histories with various impact velocities

The frequency profiles of the impact forces are illustrated with the normalized amplitudes in Figure 7-24 to investigate the effect of the impact velocity on the impact load characteristics in the frequency domain. It shows that the impact forces had broadband frequencies ranging from 0 to 5,000 Hz with high amplitudes in the low-frequency region and low amplitudes in the high-frequency region. When varying the impact velocity, the dominant frequency band of the impact loading slightly changed. However, it resulted in more impact energies falling into the passband, indicating less impact mitigation efficiency for the meta-panel. The areas enclosed by the FFT spectrum of the impact loading in Figure 7-24 are utilized to calculate the impact loading energy falling into each frequency band of the meta-truss bar. Details of estimation of the portion of the impact energy falling into each bandgap (Table 7-3) have been reported in the previous study [41], which is therefore not repeated herein for brevity. It was interesting to find that the impact force induced by a lower impact velocity led to more portion of energy falling into the bandgaps, i.e. 65.4%, 59.7%, and 53.2% respectively for the loadings induced by velocity v_1 , v_2 , and v_3 , implying that the lower velocity the projectile was, the more effective the meta-panel would be in mitigating the impact load. In another word, the impact mitigation efficiency of this meta-panel decreased when the impact velocity increased. It is noted that this observation is based on the bandgap structures and characteristics of the impact loading, therefore, it is not necessarily correct for other scenarios. This is because the impact duration from the projectile with relatively lower velocity is shorter, which makes the impact energy

more evenly distributed in a wider frequency band as shown in Figures 7-23 and 7-24. As a result, slightly more proportion of impact energy is distributed in the bandgap, resulting in the meta-panel being more effective in absorbing the impact energy.

Table 7-3. Proportion of impact energy with different velocities falling in the bandgaps of the meta-truss bar.

Impact velocity	1 st bandgap		2 nd bandgap		Total %
	$\frac{A_{\text{bandgap}}}{A_{\text{total}}}$	%	$\frac{A_{\text{bandgap}}}{A_{\text{total}}}$	%	
	v_1	$\frac{4,462}{11,532}$	38.7%	$\frac{3,079}{11,532}$	
v_2	$\frac{6,775}{18,264}$	37.1%	$\frac{4,127}{18,264}$	22.6%	59.7%
v_3	$\frac{7,637}{21,514}$	35.5%	$\frac{3,808}{21,514}$	17.7%	53.2%

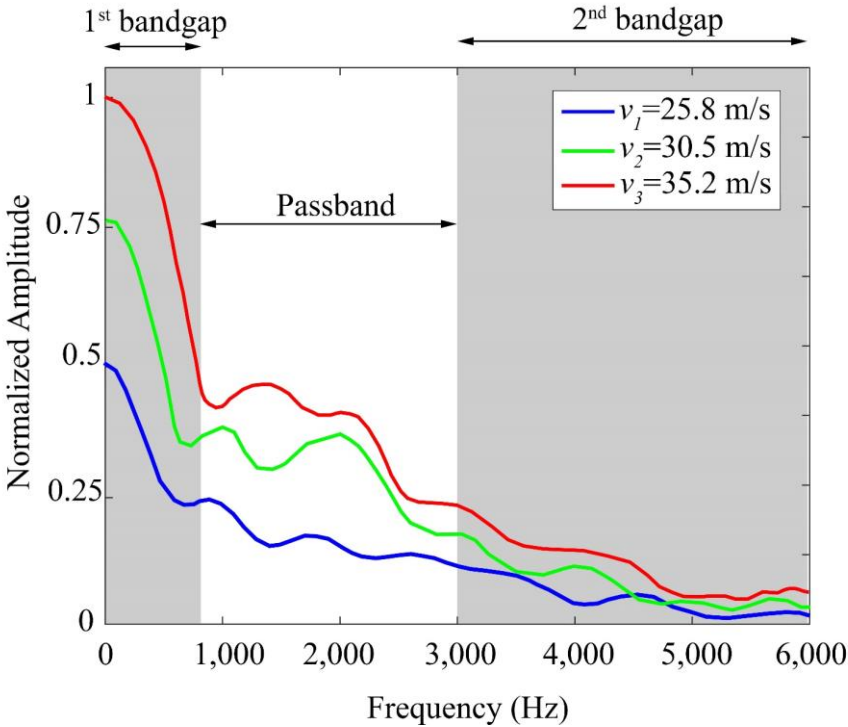


Figure 7-24. FFT spectra of impact forces with various impact velocities

7.5.3.2 Deformation, reaction force and energy absorption

Figure 7-25 shows the damage patterns of the back facesheet and reaction force of the meta-panels subjected to projectile with different velocities. The experimental results indicated that,

as expected, the projectile with higher velocity led to more severe damage to the back facesheet of the meta-panel. In the range of the investigated velocity, increasing impact velocity resulted in a substantial increase in deformation of the back facesheet and reaction force. Particularly, increasing the velocity from 25.8 m/s to 35.2 m/s enlarged the maximum deflection of the back facesheet from 7.9 mm to 15.4 mm and the corresponding reaction force from 42.5 kN to 72.9 kN, respectively. In the experimental program, penetration of the facesheets was not observed. The energy absorption characteristics of the meta-panel depend not only on the panel itself but also on the impulse and the frequency band of the impact loading. The verified FE models are used to quantify the energy absorption of the different components of meta-panels subjected to impact loads from different velocities, which cannot be comprehensively obtained from the experiments. In particular, the energy absorption of the panel increased with the loading impulse. Although the total energy absorption increased from 315 J to 601 J when varying the projectile velocity from 25.8 m/s to 32.5 m/s due to the increased impact energy imparted to the specimen, the largest percentage of the impact energy was absorbed by the coating + core (i.e. 31.7% of the total energy) when the velocity was 25.8 m/s as explained above and tabulated in Table 7-4, followed by 27.8% and 25.2% respectively for the impact cases with velocities 30.5 m/s to 35.2 m/s. It is attributed to the decrease in the proportion of the impact energies from the 25.8 m/s to 35.2 m/s impact falling in the bandgaps of the meta-panel.

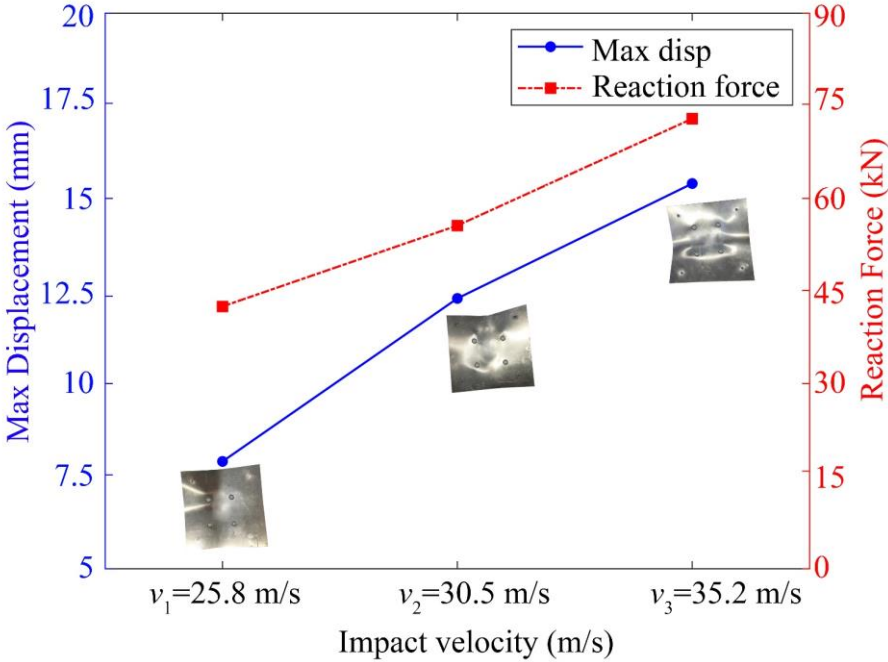


Figure 7-25. Effects of the impact velocity on the central displacement of the back facesheet and the reaction force of the meta-panel

This result indicates that the meta-panel is more effective in impact resistance when more proportion of the impact loading energy has the frequency range falling into its bandgaps. Therefore, to make the meta-panel more robust and more effective in mitigating impact energy, broadening the bandgap range of the meta-panel is the key design objective. Improved design to broaden the bandgap, e.g. using different sizes of resonators or different materials, was presented in the previous study [42]. These findings demonstrate that the performance of the meta-panel correlates with the frequency content and amplitude of the impact load which is projectile velocity dependent. It should be noted that the impact loading characteristics are also mass-dependent. The influences of the impact mass are however not tested in this chapter, which could be a future topic of study.

Table 7-4. Effect of impact velocities on energy absorption (FEM).

Impact velocity (m/s)	Energy absorption (J)				
	Front facesheet	Back facesheet	Truss	Coating + Core	Total
$v_1 = 25.8$	75 (23.8 %)	50 (15.8 %)	90 (28.7 %)	100 (31.7 %)	315
$v_2 = 30.5$	135 (30.0 %)	70 (15.5 %)	120 (16.7 %)	125 (27.8 %)	450
$v_3 = 35.2$	185 (30.7 %)	94 (15.6 %)	170 (28.5 %)	152 (25.2 %)	601

7.6. Conclusions

In this chapter, the impact mitigation performances of the meta-panel were experimentally, numerically and theoretically investigated. The main conclusions can be drawn as follows:

1. The stress wave attenuation capacity of the meta-truss bar comprising an aluminium tube and silicone-coated resonators were experimentally demonstrated for the first time. The experimentally measured bandgaps agreed well with the numerical and analytical predictions. The existence of two bandgaps in the meta-truss bar was experimentally verified.
2. Compared with the conventional sandwich panels, i.e. hollow-truss and solid-truss panels, the meta-panel exhibited excellent impact resistance in reducing the back facesheet deformation and force transmission to the protected structure, and had higher energy absorption capacity.
3. Increasing the impact velocity resulted in more concentrated distribution of impact energy in a narrower frequency band, hence less proportion of impact energy falling into the bandgaps of the meta-panel, leading to less effectiveness of the meta-panel in mitigating impact loading

effect. Widening the bandgaps of the meta-panel is the key objective in designing the meta-panel to enhance its protective effectiveness.

CHAPTER 8. CONCLUDING REMARKS

8.1 Findings

This dissertation comprehensively develops a new concept and design of a novel meta-panel for impact/blast-resistant applications as a protective structure. The primary goal is to minimize the force transmitted to the protected structures through mitigating the stress wave propagation by leveraging the coupled mechanisms of plastic deformation and local resonance. The dynamic responses of the proposed meta-panel subjected to blast and impact loads are theoretically, numerically and experimentally investigated. The theoretically derived bandgap formation is verified against the numerical simulation and experimental study in terms of transmission coefficient, which exhibits good agreement between the three approaches. Furthermore, the effects of designed parameters and installation conditions on the performance of the proposed meta-panel are systematically examined to maximize the dynamic performance of the proposed panels, followed by a design procedure for engineering applications. The primary findings of this dissertation are summarized as follows:

Analytical studies

1. The comprehensive approach including the effective properties (i.e. effective mass and effective stiffness), the wave dispersive curves, and transmission analysis is derived to analytically determine the meta-materials/meta-structures bandgaps. Particularly, the negative effective mass and the negative effective stiffness are collaboratively contributed to the 1st bandgap of the meta-concrete whilst the latter separately generates another high-frequency bandgap. In addition, the creation of the very low-frequency bandgap in the meta-truss bar, which is utmostly important for loads associated with low-frequency region such as earthquake, is governed by the shear stiffness between the resonators and the surrounding host matrix.

2. By taking the shear stiffness of the all coating layers into account, the proposed analytical model successfully captures a broader low-frequency bandgap which could not be predicted by the traditional model due to the negligence of the shear stiffness. It is found that the 1st and 2nd bandgaps are significantly influenced by the two masses. In particular, these bandgaps widen with the internal mass m_1 while they tend to narrow with the increasing value of external mass m_2 . Conversely, the 3rd bandgap remains unchanged regardless of m_2 but increases with m_1 . Regarding the effect of the stiffness, while the axial stiffnesses have limited influence on the

1st bandgap, it narrows the third bandgap. The shear stiffness is insensitive to the third bandgap, but it widens the other two bandgaps.

3. A detailed design procedure for the proposed meta-panel is proposed, which is programmable and can be employed to facilitate the meta-panel design for the attenuation of stress waves induced by dynamic loading.

Numerical simulations

1. The numerical model shows that the proposed meta-panel exhibits excellent impact-resistant performances compared to its conventional counterparts with a significant reduction in the facesheet deflection (33%) and the force transmission to the protected structure (47%) and substantial increase in the energy absorption. The meta-panel is the most effective in mitigating the impact loading effect with a fairly thin hollow truss and a properly selected soft coating. Furthermore, the impact velocity considerably affects the dominant frequency band of impact energy distribution, hence significantly influences the effectiveness of the meta-panel. A higher impact velocity triggers more impact energy distribution in the passband, therefore affecting the effectiveness of the meta-panel in the impact mitigation effect.

2. The proposed meta-panel consisting of multiple types of resonators made of different materials, sizes, and geometric designs considerably enhance its blast-resistant performances. A complete bandgap formation covering the entire range of dominant frequencies of the loading is obtained by using properly tailored arrangements of resonators. This design results in a remarkable wave attenuation and therefore better protection effectiveness. For practical design, the cylinder shape of resonator is recommended for meta-panels in terms of its excellent blast mitigation and easy fabrication process.

3. The new design of meta-panel with dual-resonators is proposed to significantly enhance its impact and blast resistance performance and is proven outperforming its conventional counterparts. The recommended design of the proposed panel should possess a relatively thin front facesheet and thick back facesheet. In addition, the protective effectiveness of the dual-meta panel depends on frequency contents of the impact or blast loads, and is the most effective if the bandgaps cover the dominant frequency band of the impact or blast loads. Therefore, the

bandgaps of the meta-panel should be designed to cover the primary frequency contents of the expected loads.

Experimental studies

1. The stress wave-filtering effect of the meta-truss bar consisting of an aluminium tube and silicone-coated resonators was experimentally verified. The obtained bandgaps from the experiment showed a good agreement with the numerical and analytical predictions, verifying the numerical models and analytical derivations.

2. It was experimentally proven that the proposed meta-panel exhibits excellent impact resistance as compared with the conventional sandwich panels, i.e. a substantial increase in the energy absorption, and a remarkable decrease in the facesheet displacement and reaction force transmission to the protected structure.

3. Increasing impact velocity resulted in more even distribution of impact energy in a wider frequency band, hence less proportion of impact energy falling into the bandgaps of the meta-panel, leading to less effectiveness of the meta-panel in mitigating impact loading effect. Therefore, one of the primary design target of meta-panels is to widen their bandgaps. Widening the bandgaps of the meta-panel is the key objective in the design to enhance the protective effectiveness of the meta-panels. This can be done by adopting the design procedure proposed in Chapter 1.

8.2 Recommendation for future directions

From the main findings in this dissertation, the recommendations for possible future works are given as follows:

1. Additional tests and numerical simulations for the meta-truss bar are recommended to investigate the influence of critical factors on its favourable bandgaps, e.g. vibration test with transverse loadings, vibration test without the outer tube.

2. In this research, only the meta-panel with single resonator was tested due to the complex fabrication process. More experimental tests should be carried out for meta-panels with various configurations, for instance, dual-meta panel, meta-panel with multitypes of resonators.

Besides, a wider range of impact loads which is impact mass and velocity-dependent should be carried out, especially with the low impact velocity, to examine the effectiveness of the meta-panel to resist impact loads of different loading scenarios. The pendulum test is recommended for this task.

3. In this study, manual fabrication process was carried out for the meta-truss bars due to the limitations of fabrication means. This issue would be addressed in the future work by leveraging the 3D printing method for manufacturing process. Improvements in accurate manufacture of the structures could be obtained if all layers are automatically printed simultaneously.

REFERENCES

- [1] R.E. Bartholomew, The Paris terror attacks, mental health and the spectre of fear, *Journal of the Royal Society of Medicine*, 109 (2016) 4-5.
- [2] H. Bardwell, M. Iqbal, The Economic Impact of Terrorism from 2000 to 2018, *Peace Economics, Peace Science and Public Policy*, 27 (2021) 227-261.
- [3] Z. Zong, Z. Sun, Y. Tan, C. Tian, L. Qu, L. Ji, Impact of an accidental explosion in Tianjin Port on enhanced atmospheric nitrogen deposition over the Bohai Sea inferred from aerosol nitrate dual isotopes, *Atmospheric and Oceanic Science Letters*, 13 (2020) 195-201.
- [4] J.P. Chalon, J.C. Famkhauser, P.J. Eccles, Structure of an Evolving Hailstorm, Part 1: General Characteristics and Cellular Structure, *Monthly Weather Review*, 104 (1976) 564-575.
- [5] D.K. Sahoo, A. Guha, A. Tewari, R.K. Singh, Performance of Monolithic Plate and Layered Plates Under Blast Load, *Procedia Engineering*, 173 (2017) 1909-1917.
- [6] A.N. Rotariu, C. Dima, E. Trană, C. Enache, F. Timplaru, L.C. Matache, Uninstrumented Measurement Method for Granular Porous Media Blast Mitigation Assessment, *Experimental Techniques*, 40 (2016) 993-1003.
- [7] A.G. Hanssen, L. Enstock, M. Langseth, Close-range blast loading of aluminium foam panels, *Int J Impact Eng*, 27 (2002) 593-618.
- [8] S.C.K. Yuen, G.N. Nurick, M.D. Theobald, G.S. Langdon, Sandwich Panels Subjected to Blast Loading, in: A. Shukla, G. Ravichandran, Y.D.S. Rajapakse (Eds.) *Dynamic Failure of Materials and Structures*, Springer US, Boston, MA, 2010, pp. 297-325.
- [9] Z. Xue, J.W. Hutchinson, Preliminary assessment of sandwich plates subject to blast loads, *Int J Mech Sci*, 45 (2003) 687-705.
- [10] T.M. Pham, W. Chen, H. Hao, Review on impact response of reinforced concrete beams: Contemporary understanding and unsolved problems, *Adv Struct Eng*, 24 (2021) 2282-2303.
- [11] P.-R. Wagner, V. Dertimanis, I. Antoniadis, E. Chatzi, *On the feasibility of structural metamaterials for seismic-induced vibration mitigation*, 2016.
- [12] R.M. Walser, *Electromagnetic metamaterials*, SPIE, 2001.
- [13] R. Grimberg, *Electromagnetic metamaterials*, *Materials Science and Engineering: B*, 178 (2013) 1285-1295.
- [14] D. Powell, Core Concept: Mechanical metamaterials bend the rules of everyday physics, *Proceedings of the National Academy of Sciences*, 115 (2018) 2545.
- [15] K.T. Tan, B. li, M. Mahfujul Khan, *Acoustic/Elastic Metamaterials: A Novel Solution to Impact Problems*, 2017.
- [16] L. Fan, Z. Chen, S.-y. Zhang, J. Ding, X.-j. Li, H. Zhang, An acoustic metamaterial composed of multi-layer membrane-coated perforated plates for low-frequency sound insulation, *Appl. Phys. Lett.*, 106 (2015) 151908.
- [17] Q. Chen, A. Elbanna, Emergent wave phenomena in coupled elastic bars: From extreme attenuation to realization of elastodynamic switches, 2017.
- [18] X. Zhou, X. Liu, G. Hu, Elastic metamaterials with local resonances: an overview, *Theoretical and Applied Mechanics Letters*, 2 (2012) 041001.
- [19] B. li, K.T. Tan, J. Christensen, *Investigation of Locally Resonant Nanophononic Metamaterials with Ultralow Thermal Conductivity*, 2017.
- [20] P. Sheng, *Coupled membranes with doubly negative mass density and bulk modulus*, 2013.
- [21] V. Richman, M.R. Santos, J.T. Barkoulas, *SHORT- AND LONG-TERM EFFECTS OF THE 9/11 EVENT: THE INTERNATIONAL EVIDENCE*, *International Journal of Theoretical and Applied Finance*, 08 (2005) 947-958.
- [22] S. Al-Hajj, H.R. Dhaini, S. Mondello, H. Kaafarani, F. Kobeissy, R.G. DePalma, *Beirut Ammonium Nitrate Blast: Analysis, Review, and Recommendations*, 9 (2021).

- [23] N.S. Ha, G. Lu, A review of recent research on bio-inspired structures and materials for energy absorption applications, *Compos Part B: Eng*, 181 (2020) 107496.
- [24] N.S. Ha, G. Lu, D. Shu, T.X. Yu, Mechanical properties and energy absorption characteristics of tropical fruit durian (*Durio zibethinus*), *Journal of the Mechanical Behavior of Biomedical Materials*, 104 (2020) 103603.
- [25] N.S. Ha, G. Lu, X. Xiang, High energy absorption efficiency of thin-walled conical corrugation tubes mimicking coconut tree configuration, *Int J Mech Sci*, 148 (2018) 409-421.
- [26] N.S. Ha, G. Lu, X. Xiang, Energy absorption of a bio-inspired honeycomb sandwich panel, *J. Mater. Sci.*, 54 (2019) 6286-6300.
- [27] N.S. Ha, G. Lu, Thin-walled corrugated structures: A review of crashworthiness designs and energy absorption characteristics, *Thin-Walled Structures*, 157 (2020) 106995.
- [28] N.S. Ha, T.M. Pham, W. Chen, H. Hao, G. Lu, Crashworthiness analysis of bio-inspired fractal tree-like multi-cell circular tubes under axial crushing, *Thin-Walled Structures*, 169 (2021) 108315.
- [29] N.S. Ha, T.M. Pham, H. Hao, G. Lu, Energy absorption characteristics of bio-inspired hierarchical multi-cell square tubes under axial crushing, *Int J Mech Sci*, 201 (2021) 106464.
- [30] V.G. Veselago, The Electromanatics of Substances with Simultaneously Negative Value of ϵ and μ , *Soviet Physics Uspekhi*, 10 (1968) 509-514.
- [31] C. Comi, L. Driemeier, Wave propagation in cellular locally resonant metamaterials, *Lat. Am. J. Solid. Struct.*, 15 (2018).
- [32] S. Lin, Y. Zhang, Y. Liang, Y. Liu, C. Liu, Z. Yang, Bandgap characteristics and wave attenuation of metamaterials based on negative-stiffness dynamic vibration absorbers, *J. Sound. Vib.*, 502 (2021) 116088.
- [33] X. Xiang, Z. Fu, S. Zhang, G. Lu, N.S. Ha, Y. Liang, X. Zhang, The mechanical characteristics of graded Miura-ori metamaterials, *Mater. Des.*, 211 (2021) 110173.
- [34] A. Banerjee, R. Das, E.P. Calius, Frequency graded 1D metamaterials: A study on the attenuation bands, *J. Appl. Phys.*, 122 (2017) 075101.
- [35] X. Xu, M.V. Barnhart, X. Li, Y. Chen, G. Huang, Tailoring vibration suppression bands with hierarchical metamaterials containing local resonators, *J. Sound. Vib.*, 442 (2019) 237-248.
- [36] C. Cai, Z. Wang, Y. Chu, G. Liu, Z. Xu, The phononic band gaps of Bragg scattering and locally resonant pentamode metamaterials, *J. Phys. D: Appl. Phys.*, 50 (2017) 415105.
- [37] T. Lee, H. Iizuka, Bragg scattering based acoustic topological transition controlled by local resonance, *Physical Review B*, 99 (2019) 064305.
- [38] Y. Xiao, J. Wen, G. Wang, X. Wen, Theoretical and Experimental Study of Locally Resonant and Bragg Band Gaps in Flexural Beams Carrying Periodic Arrays of Beam-Like Resonators, 2013.
- [39] A.O. Krushynska, M. Miniaci, F. Bosia, N.M. Pugno, Coupling local resonance with Bragg band gaps in single-phase mechanical metamaterials, *Extreme Mechanics Letters*, 12 (2017) 30-36.
- [40] M. Cenedese, E. Belloni, F. Braghin, Interaction of Bragg scattering bandgaps and local resonators in mono-coupled periodic structures, *J. Appl. Phys.*, 129 (2021) 124501.
- [41] N.H. Vo, T.M. Pham, K. Bi, W. Chen, H. Hao, Stress Wave Mitigation Properties of Dual-meta Panels against Blast Loads, *Int J Impact Eng*, 154 (2021) 103877.
- [42] N.H. Vo, T.M. Pham, H. Hao, K. Bi, W. Chen, N.S. Ha, Blast resistant enhancement of meta-panels using multiple types of resonators, *Int J Mech Sci*, 215 (2022) 106965.
- [43] G. Hu, L. Tang, R. Das, S. Gao, H. Liu, Acoustic metamaterials with coupled local resonators for broadband vibration suppression, *AIP Adv.*, 7 (2017) 025211.

- [44] L.-Z. Huang, Y. Xiao, J.-H. Wen, H.-B. Yang, X.-S. Wen, Analysis of underwater decoupling properties of a locally resonant acoustic metamaterial coating, *Chinese Physics B*, 25 (2016) 024302.
- [45] H. Meng, N. Bailey, Y. Chen, L. Wang, F. Ciampa, A. Fabro, D. Chronopoulos, W. Elmadih, 3D rainbow phononic crystals for extended vibration attenuation bands, *Sci. Rep.*, 10 (2020) 18989.
- [46] J.H. Oh, S.J. Choi, J.K. Lee, Y.Y. Kim, Zero-frequency Bragg gap by spin-harnessed metamaterial, *New J. Phys.*, 20 (2018) 083035.
- [47] Y.Y. Zhang, N.S. Gao, G.S. Xu, J.H. Wu, M. Cao, Z.T. Zhou, Low-frequency band gaps within a local resonance structures, *Mod. Phys. Lett. B*, 34 (2020) 2150014.
- [48] T.N.T. Cao, V.H. Luong, H.N. Vo, X.V. Nguyen, V.N. Bui, M.T. Tran, K.K. Ang, A Moving Element Method for the Dynamic Analysis of Composite Plate Resting on a Pasternak Foundation Subjected to a Moving Load, *International Journal of Computational Methods*, 16 (2018) 1850124.
- [49] P. Sheng, X.X. Zhang, Z. Liu, C.T. Chan, Locally resonant sonic materials, *Physica B: Condensed Matter*, 338 (2003) 201-205.
- [50] P. Wang, F. Casadei, S. Shan, J.C. Weaver, K. Bertoldi, Harnessing Buckling to Design Tunable Locally Resonant Acoustic Metamaterials, *Phys. Rev. Lett.*, 113 (2014) 014301.
- [51] A. Palermo, M. Vitali, A. Marzani, Metabarriers with multi-mass locally resonating units for broad band Rayleigh waves attenuation, *Soil Dynamics and Earthquake Engineering*, 113 (2018) 265-277.
- [52] G. Hu, L. Tang, J. Xu, C. Lan, R. Das, Metamaterial With Local Resonators Coupled by Negative Stiffness Springs for Enhanced Vibration Suppression, *Journal of Applied Mechanics*, 86 (2019).
- [53] M. Yang, P. Sheng, *Sound Absorption Structures: From Porous Media to Acoustic Metamaterials*, 2017.
- [54] G. Finocchio, O. Casablanca, G. Ricciardi, U. Alibrandi, F. Garescì, M. Chiappini, B. Azzerboni, Seismic metamaterials based on isochronous mechanical oscillators, *Appl. Phys. Lett.*, 104 (2014) 191903.
- [55] Y.Y. Chen, M.V. Barnhart, J.K. Chen, G.K. Hu, C.T. Sun, G.L. Huang, Dissipative elastic metamaterials for broadband wave mitigation at subwavelength scale, *Compos. Struct.*, 136 (2016) 358-371.
- [56] N.H. Vo, T.M. Pham, H. Hao, K. Bi, W. Chen, Impact load mitigation of meta-panels with single local resonator, *Eng. Struct.*, 265 (2022) 114528.
- [57] K.K. Reichl, D.J. Inman, Lumped mass model of a 1D metastructure for vibration suppression with no additional mass, *J. Sound. Vib.*, 403 (2017) 75-89.
- [58] Y. Liu, X. An, H. Chen, H. Fan, Vibration attenuation of finite-size metaconcrete: Mechanism, prediction and verification, *Composites Part A: Applied Science and Manufacturing*, 143 (2021) 106294.
- [59] J. Huang, Z. Shi, Attenuation zones of periodic pile barriers and its application in vibration reduction for plane waves, *J. Sound. Vib.*, 332 (2013) 4423-4439.
- [60] R. Zhu, X.N. Liu, G.K. Hu, C.T. Sun, G.L. Huang, A chiral elastic metamaterial beam for broadband vibration suppression, *J. Sound. Vib.*, 333 (2014) 2759-2773.
- [61] G. Hu, L. Tang, A. Banerjee, R. Das, Metastructure With Piezoelectric Element for Simultaneous Vibration Suppression and Energy Harvesting, *J. Vib. Acoust.*, 139 (2016) 011012-011012-011011.
- [62] Y. Yan, A. Laskar, Z. Cheng, F. Menq, Y. Tang, Y.L. Mo, Z. Shi, Seismic isolation of two dimensional periodic foundations, *J. Appl. Phys.*, 116 (2014) 044908.
- [63] Y. Yan, Z. Cheng, F. Menq, Y.L. Mo, Y. Tang, Z. Shi, Three dimensional periodic foundations for base seismic isolation, *Smart Mater. Struct.*, 24 (2015) 075006.

- [64] M. Miniaci, A. Krushynska, F. Bosia, N.M. Pugno, Large scale mechanical metamaterials as seismic shields, *New J. Phys.*, 18 (2016) 083041.
- [65] Z. Shi, Z. Cheng, H. Xiang, Seismic isolation foundations with effective attenuation zones, *Soil Dynamics and Earthquake Engineering*, 57 (2014) 143-151.
- [66] A.O. Krushynska, A. Amendola, F. Bosia, C. Daraio, N.M. Pugno, F. Fraternali, Accordion-like metamaterials with tunable ultra-wide low-frequency band gaps, *New J. Phys.*, 20 (2018) 073051.
- [67] Q. Zhang, K. Zhang, G. Hu, Tunable fluid-solid metamaterials for manipulation of elastic wave propagation in broad frequency range, *Appl. Phys. Lett.*, 112 (2018) 221906.
- [68] Y. Liu, X. Shen, X. Su, C.T. Sun, Elastic Metamaterials With Low-Frequency Passbands Based on Lattice System With On-Site Potential, *J. Vib. Acoust.*, 138 (2016) 021011-021011-021010.
- [69] S. Yao, X. Zhou, G. Hu, Experimental study on negative effective mass in a 1D mass-spring system, *New J. Phys.*, 10 (2008) 043020.
- [70] S.J. Mitchell, A. Pandolfi, M. Ortiz, Metaconcrete: designed aggregates to enhance dynamic performance, *J. Mech. Phys. Solids.*, 65 (2014) 69-81.
- [71] C. Xu, W. Chen, H. Hao, The influence of design parameters of engineered aggregate in metaconcrete on bandgap region, *J. Mech. Phys. Solids.*, 139 (2020) 103929.
- [72] C. Xu, W. Chen, H. Hao, K. Bi, T.M. Pham, Experimental and numerical assessment of stress wave attenuation of metaconcrete rods subjected to impulsive loads, *Int J Impact Eng*, 159 (2022) 104052.
- [73] C. Xu, W. Chen, H. Hao, H. Jin, Effect of engineered aggregate configuration and design on stress wave attenuation of metaconcrete rod structure, *International Journal of Solids and Structures*, 232 (2021) 111182.
- [74] C. Ding, L. Hao, X. Zhao, Two-dimensional acoustic metamaterial with negative modulus, *J. Appl. Phys.*, 108 (2010) 074911.
- [75] X. Zhou, G. Hu, Analytic model of elastic metamaterials with local resonances, *Physical Review B*, 79 (2009) 195109.
- [76] S.H. Lee, C.M. Park, Y.M. Seo, Z.G. Wang, C.K. Kim, Acoustic metamaterial with negative modulus, *J. Phys.: Condens. Matter*, 21 (2009) 175704.
- [77] S.H. Lee, C.M. Park, Y.M. Seo, Z.G. Wang, C.K. Kim, Composite Acoustic Medium with Simultaneously Negative Density and Modulus, *Phys. Rev. Lett.*, 104 (2010) 054301.
- [78] X.N. Liu, G.K. Hu, G.L. Huang, C.T. Sun, An elastic metamaterial with simultaneously negative mass density and bulk modulus, *Appl. Phys. Lett.*, 98 (2011) 251907.
- [79] Y.-F. Wang, Y.-S. Wang, V. Laude, Wave propagation in two-dimensional viscoelastic metamaterials, *Physical Review B*, 92 (2015) 104110.
- [80] A.O. Krushynska, V.G. Kouznetsova, M.G.D. Geers, Towards optimal design of locally resonant acoustic metamaterials, *J. Mech. Phys. Solids.*, 71 (2014) 179-196.
- [81] D. Lee, D.M. Nguyen, J. Rho, Acoustic wave science realized by metamaterials, *Nano Convergence*, 4 (2017) 3.
- [82] C. Xu, W. Chen, H. Hao, T.M. Pham, K. Bi, Damping properties and dynamic responses of metaconcrete beam structures subjected to transverse loading, *Constr. Build. Mater.*, 311 (2021) 125273.
- [83] N.H. Vo, T.M. Pham, K. Bi, H. Hao, Model for analytical investigation on meta-lattice truss for low-frequency spatial wave manipulation, *Wave Motion*, 103 (2021) 102735.
- [84] H. Jin, H. Hao, Y. Hao, W. Chen, Predicting the response of locally resonant concrete structure under blast load, *Constr. Build. Mater.*, 252 (2020) 118920.
- [85] M.M. Hajjaj, J. Tu, A seismic metamaterial concept with very short resonators using depleted uranium, *Archive of Applied Mechanics*, (2021).

- [86] S. Fujikura, M. Bruneau, Experimental Investigation of Seismically Resistant Bridge Piers under Blast Loading, *J. Bridge Eng.*, 16 (2011) 63-71.
- [87] S. Krödel, N. Thomé, C. Daraio, Wide band-gap seismic metastructures, *Extreme Mechanics Letters*, 4 (2015) 111-117.
- [88] C. Kettenbeil, G. Ravichandran, Experimental investigation of the dynamic behavior of metaconcrete, *Int J Impact Eng*, 111 (2018) 199-207.
- [89] S.J. Mitchell, A. Pandolfi, M. Ortiz, Investigation of elastic wave transmission in a metaconcrete slab, *Mech. Mater.*, 91 (2015) 295-303.
- [90] Y. Cheng, T. Yu, X. Zhou, Control of underwater acoustics using anisotropic solid metamaterials with continuously tuned material axes, *Extreme Mechanics Letters*, 32 (2019) 100544.
- [91] H. Wang, Y. Zhang, W. Lin, Q.-H. Qin, A novel two-dimensional mechanical metamaterial with negative Poisson's ratio, *Computational Materials Science*, 171 (2020) 109232.
- [92] H.H. Huang, C.T. Sun, Wave attenuation mechanism in an acoustic metamaterial with negative effective mass density, *New J. Phys.*, 11 (2009) 013003.
- [93] W. Witarto, S.J. Wang, C.Y. Yang, X. Nie, Y.L. Mo, K.C. Chang, Y. Tang, R. Kassawara, Seismic isolation of small modular reactors using metamaterials, *AIP Adv.*, 8 (2018) 045307.
- [94] Y. Zeng, Y. Xu, H. Yang, M. Muzamil, R. Xu, K. Deng, P. Peng, Q. Du, A Matryoshka-like seismic metamaterial with wide band-gap characteristics, *International Journal of Solids and Structures*, 185-186 (2020) 334-341.
- [95] Z. Lu, X. Yu, S.-K. Lau, B.C. Khoo, F. Cui, Membrane-type acoustic metamaterial with eccentric masses for broadband sound isolation, *Appl. Acoust.*, 157 (2020) 107003.
- [96] X. Xiang, X. Wu, X. Li, P. Wu, H. He, Q. Mu, S. Wang, Y. Huang, W. Wen, Ultra-open ventilated metamaterial absorbers for sound-silencing applications in environment with free air flows, *Extreme Mechanics Letters*, 39 (2020) 100786.
- [97] X. An, C. Lai, H. Fan, C. Zhang, 3D acoustic metamaterial-based mechanical metalattice structures for low-frequency and broadband vibration attenuation, *International Journal of Solids and Structures*, 191-192 (2020) 293-306.
- [98] P.F. Pai, H. Peng, S. Jiang, Acoustic metamaterial beams based on multi-frequency vibration absorbers, *Int J Mech Sci*, 79 (2014) 195-205.
- [99] E. Kim, J. Yang, H. Hwang, C.W. Shul, Impact and blast mitigation using locally resonant woodpile metamaterials, *Int J Impact Eng*, 101 (2017) 24-31.
- [100] M.H. Khan, B. Li, K.T. Tan, Impact load wave transmission in elastic metamaterials, *Int J Impact Eng*, 118 (2018) 50-59.
- [101] A. Hall, E. Calius, G. Dodd, E. Wester, Modelling and experimental validation of complex locally resonant structures, 2019.
- [102] S. Ning, F. Yang, C. Luo, Z. Liu, Z. Zhuang, Low-frequency tunable locally resonant band gaps in acoustic metamaterials through large deformation, *Extreme Mechanics Letters*, 35 (2020) 100623.
- [103] A. Madeo, P. Neff, I.-D. Ghiba, G. Rosi, Reflection and transmission of elastic waves in non-local band-gap metamaterials: A comprehensive study via the relaxed micromorphic model, *J. Mech. Phys. Solids.*, 95 (2016) 441-479.
- [104] I.L. Chang, Z.-X. Liang, H.-W. Kao, S.-H. Chang, C.-Y. Yang, The wave attenuation mechanism of the periodic local resonant metamaterial, *J. Sound. Vib.*, 412 (2018) 349-359.
- [105] M. Omelyanovich, V. Ovchinnikov, C. Simovski, A non-resonant dielectric metamaterial for the enhancement of thin-film solar cells, *Journal of Optics*, 17 (2015) 025102.
- [106] B. Li, S. Alamri, K.T. Tan, A diatomic elastic metamaterial for tunable asymmetric wave transmission in multiple frequency bands, *Sci. Rep.*, 7 (2017) 6226.

- [107] Y. Chen, F. Qian, L. Zuo, F. Scarpa, L. Wang, Broadband and multiband vibration mitigation in lattice metamaterials with sinusoidally-shaped ligaments, *Extreme Mechanics Letters*, 17 (2017) 24-32.
- [108] W. Milton, R. Willis, On modifications of Newton's second law and linear continuum elastodynamics, *Proceedings of the Royal Society A: Mathematical, Physical and Engineering Sciences*, 463 (2007) 855-880.
- [109] Y. Liu, X. Su, C.T. Sun, Broadband elastic metamaterial with single negativity by mimicking lattice systems, *J. Mech. Phys. Solids.*, 74 (2015) 158-174.
- [110] S. Alamri, B. Li, G. McHugh, N. Garafolo, K.T. Tan, Dissipative diatomic acoustic metamaterials for broadband asymmetric elastic-wave transmission, *J. Sound. Vib.*, 451 (2019) 120-137.
- [111] B. Li, Y. Liu, K.-T. Tan, A novel meta-lattice sandwich structure for dynamic load mitigation, *J. Sandw. Struct. Mater.*, (2017) 1099636217727144.
- [112] F. Farzbod, M. Leamy, Analysis of Bloch's Method and the Propagation Technique in Periodic Structures, *J. Vib. Acoust.*, 133 (2011) 031010.
- [113] P. Tran, S. Linforth, T.D. Ngo, R. Lumantarna, T.Q. Nguyen, Design analysis of hybrid composite anti-ram bollard subjected to impulsive loadings, *Compos. Struct.*, 189 (2018) 598-613.
- [114] L.-C. Alil, L.-C. Matache, S. Sandu, Numerical Simulation of a Ballistic Impact on Tensylon® UHMWPE Laminates Using the Plastic Kinematic Model in LS-Dyna®, *Journal of Military Technology*, 1 (2018) 43-50.
- [115] D.T. Tran, T.M. Pham, H. Hao, W. Chen, Numerical study on bending response of precast segmental concrete beams externally prestressed with FRP tendons, *Eng. Struct.*, 241 (2021) 112423.
- [116] T.T. Ngo, T.M. Pham, H. Hao, W. Chen, M. Elchalakani, Performance of monolithic and dry joints with GFRP bolts reinforced with different fibres and GFRP bars under impact loading, *Eng. Struct.*, 240 (2021) 112341.
- [117] T.V. Le, A. Ghazlan, T. Ngo, T. Nguyen, A. Remennikov, A comprehensive review of selected biological armor systems – From structure-function to bio-mimetic techniques, *Compos. Struct.*, 225 (2019) 111172.
- [118] N.S. Choudhary, M.D. Goel, S. Panchal, Numerical Analysis of Innovative Sacrificial Protection System under Blast Loading, *Practice Periodical on Structural Design and Construction*, 27 (2022) 04021075.
- [119] W. Van Paepegem, S. Palanivelu, J. Degrieck, J. Vantomme, B. Reymen, D. Kakogiannis, D. Van Hemelrijck, J. Wastiels, Blast performance of a sacrificial cladding with composite tubes for protection of civil engineering structures, *Compos Part B: Eng*, 65 (2014) 131-146.
- [120] P. Tran, A. Ghazlan, T.D. Ngo, Chapter 8 - Design and Modeling of Bio-inspired Lightweight Composite Panels for Blast Resistance, in: A.P. Mouritz, Y.D.S. Rajapakse (Eds.) *Explosion Blast Response of Composites*, Woodhead Publishing, 2017, pp. 201-231.
- [121] R. Codina, D. Ambrosini, F. de Borbón, New sacrificial cladding system for the reduction of blast damage in reinforced concrete structures, *Int J Prot Struct*, 8 (2017) 221-236.
- [122] G.W. Ma, Z.Q. Ye, Energy absorption of double-layer foam cladding for blast alleviation, *Int J Impact Eng*, 34 (2007) 329-347.
- [123] M.A. Hazizan, W.J. Cantwell, The low velocity impact response of an aluminium honeycomb sandwich structure, *Compos Part B: Eng*, 34 (2003) 679-687.
- [124] D.T. Queheillalt, H.N.G. Wadley, Pyramidal lattice truss structures with hollow trusses, *Materials Science and Engineering: A*, 397 (2005) 132-137.
- [125] J. Xiong, A. Vaziri, L. Ma, J. Papadopoulos, L. Wu, Compression and impact testing of two-layer composite pyramidal-core sandwich panels, *Compos. Struct.*, 94 (2012) 793-801.

- [126] G. Yang, C. Hou, M. Zhao, W. Mao, Comparison of convective heat transfer for Kagome and tetrahedral truss-cored lattice sandwich panels, *Sci. Rep.*, 9 (2019) 3731.
- [127] V.T. Le, N.S. Ha, N.S. Goo, Advanced sandwich structures for thermal protection systems in hypersonic vehicles: A review, *Compos Part B: Eng*, 226 (2021) 109301.
- [128] N. Abdolrahim, G. Liaghat, H. Askari, Experimental study of low velocity impact on Sandwich panels with honeycomb core and Comparison with the FEM results, 2013.
- [129] J. Liu, T. Chen, Y. Zhang, G. Wen, Q. Qing, H. Wang, R. Sedaghati, Y.M. Xie, On sound insulation of pyramidal lattice sandwich structure, *Compos. Struct.*, 208 (2019) 385-394.
- [130] S. Ehsan Moosavimehr, A. Srikantha Phani, Sound transmission loss characteristics of sandwich panels with a truss lattice core, *The Journal of the Acoustical Society of America*, 141 (2017) 2921-2932.
- [131] J.S. Chen, B. Sharma, C.T. Sun, Dynamic behaviour of sandwich structure containing spring-mass resonators, *Compos. Struct.*, 93 (2011) 2120-2125.
- [132] B. Sharma, C.T. Sun, Impact load mitigation in sandwich beams using local resonators, *J. Sandw. Struct. Mater.*, 18 (2015) 50-64.
- [133] V. La Salandra, M. Wenzel, O.S. Bursi, G. Carta, A.B. Movchan, Conception of a 3D Metamaterial-Based Foundation for Static and Seismic Protection of Fuel Storage Tanks, 4 (2017).
- [134] N.H. Vo, T.M. Pham, H. Hao, K. Bi, W. Chen, A reinvestigation of the spring-mass model for metamaterial bandgap prediction, *Int J Mech Sci*, 221 (2022) 107219.
- [135] J.J.L.S.T.C. Hallquist, *LS-Dyna Theory manual*, March 2006, (2012).
- [136] E.A. Flores-Johnson, L. Shen, I. Guiamatsia, G.D. Nguyen, Numerical investigation of the impact behaviour of bioinspired nacre-like aluminium composite plates, *Compos. Sci. Technol.*, 96 (2014) 13-22.
- [137] K. Lee, Effects on the various rubber fenders of a tripod offshore wind turbine substructure collision strength due to boat, *Ocean Engineering*, 72 (2013) 188-194.
- [138] M. Ramezani, Z.M. Ripin, R. Ahmad, Plastic bulging of sheet metals at high strain rates, *The International Journal of Advanced Manufacturing Technology*, 48 (2010) 847-858.
- [139] P. Chivapornthip, E.L.J. Bohez, Dependence of bulk viscosity of polypropylene on strain, strain rate, and melt temperature, *Polym. Eng. Sci.*, 57 (2017) 830+.
- [140] B. Aryal, E.V. Morozov, H. Wang, K. Shankar, P.J. Hazell, J.P. Escobedo-Diaz, Effects of impact energy, velocity, and impactor mass on the damage induced in composite laminates and sandwich panels, *Compos. Struct.*, 226 (2019) 111284.
- [141] J. Liu, W. Chen, H. Hao, Z. Wang, Numerical study of low-speed impact response of sandwich panel with tube filled honeycomb core, *Compos. Struct.*, 220 (2019) 736-748.
- [142] G.B. Chai, S. Zhu, A review of low-velocity impact on sandwich structures, *Proceedings of the Institution of Mechanical Engineers, Part L: Journal of Materials: Design and Applications*, 225 (2011) 207-230.
- [143] Z. Li, W. Chen, H. Hao, Blast mitigation performance of cladding using square dome-shape kirigami folded structure as core, *Int J Mech Sci*, 145 (2018) 83-95.
- [144] S. Yao, H. Zhu, M. Liu, Z. Li, P. Xu, Energy absorption of origami tubes with polygonal cross-sections, *Thin-Walled Structures*, 157 (2020) 107013.
- [145] J. Liu, Y. Li, X. Shi, W. Wang, Dynamic Response of Bird Strike on Aluminum Honeycomb-Based Sandwich Panels, *Journal of Aerospace Engineering*, 27 (2014) 520-528.
- [146] S. Cheng, B. Xiao, X. Zhao, Y. Xin, H. Li, Drop-weight impact test on an integrated composite sandwich panel of aluminum honeycomb and epoxy resin, *J. Mater. Res.*, 32 (2017) 2258-2265.
- [147] X.-k. Lan, Q. Huang, T. Zhou, S.-s. Feng, Optimal design of a novel cylindrical sandwich panel with double arrow auxetic core under air blast loading, *Defence Technology*, 16 (2020) 617-626.

- [148] G. Imbalzano, P. Tran, T.D. Ngo, P.V.S. Lee, A numerical study of auxetic composite panels under blast loadings, *Compos. Struct.*, 135 (2016) 339-352.
- [149] C.-C. Liang, M.-F. Yang, P.-W. Wu, Optimum design of metallic corrugated core sandwich panels subjected to blast loads, *Ocean Engineering*, 28 (2001) 825-861.
- [150] X. Li, Z. Wang, F. Zhu, G. Wu, L. Zhao, Response of aluminium corrugated sandwich panels under air blast loadings: Experiment and numerical simulation, *Int J Impact Eng*, 65 (2014) 79-88.
- [151] F.W. Zok, S.A. Waltner, Z. Wei, H.J. Rathbun, R.M. McMeeking, A.G. Evans, A protocol for characterizing the structural performance of metallic sandwich panels: application to pyramidal truss cores, *International Journal of Solids and Structures*, 41 (2004) 6249-6271.
- [152] L. Jing, L. Zhao, Blast resistance and energy absorption of sandwich panels with layered gradient metallic foam cores, *J. Sandw. Struct. Mater.*, 21 (2017) 464-482.
- [153] X. Ren, J. Shen, A. Ghaedizadeh, H. Tian, Y. Min Xie, Experiments and parametric studies on 3D metallic auxetic metamaterials with tuneable mechanical properties, *Smart Mater. Struct.*, 24 (2015) 095016.
- [154] X. Xiang, S. Zou, N.S. Ha, G. Lu, I. Kong, Energy absorption of bio-inspired multi-layered graded foam-filled structures under axial crushing, *Compos Part B: Eng*, 198 (2020) 108216.
- [155] Z. Li, W. Chen, H. Hao, Dynamic crushing and energy absorption of foam filled multi-layer folded structures: Experimental and numerical study, *Int J Impact Eng*, 133 (2019) 103341.
- [156] Z. Li, W. Chen, H. Hao, Numerical study of blast mitigation performance of folded structure with foam infill, *Structures*, 20 (2019) 581-593.
- [157] D.T. Queheillalt, H.N.G. Wadley, Cellular metal lattices with hollow trusses, *Acta Mater.*, 53 (2005) 303-313.
- [158] X. Cao, H. Hua, Acoustic responses of the composite sandwich plates with lattice truss core to the subsonic turbulent boundary layer, *Compos. Struct.*, 153 (2016) 176-192.
- [159] S. Yin, L. Wu, L. Ma, S. Nutt, Pyramidal lattice sandwich structures with hollow composite trusses, *Compos. Struct.*, 93 (2011) 3104-3111.
- [160] G. Qi, L. Ma, Experimental investigation of composite pyramidal truss core sandwich panels with lightweight inserts, *Compos. Struct.*, 187 (2018) 336-343.
- [161] E.C. Clough, J. Ensberg, Z.C. Eckel, C.J. Ro, T.A. Schaedler, Mechanical performance of hollow tetrahedral truss cores, *International Journal of Solids and Structures*, 91 (2016) 115-126.
- [162] J.-H. Lim, K.-J. Kang, Mechanical behavior of sandwich panels with tetrahedral and Kagome truss cores fabricated from wires, *International Journal of Solids and Structures*, 43 (2006) 5228-5246.
- [163] U.K. Vaidya, M.V. Hosur, D. Earl, S. Jeelani, Impact response of integrated hollow core sandwich composite panels, *Composites Part A: Applied Science and Manufacturing*, 31 (2000) 761-772.
- [164] X. Liu, X. Tian, T.J. Lu, D. Zhou, B. Liang, Blast resistance of sandwich-walled hollow cylinders with graded metallic foam cores, *Compos. Struct.*, 94 (2012) 2485-2493.
- [165] I. Elnasri, H. Zhao, Impact Response of Sacrificial Cladding Structure with an Alporas Aluminum Foam Core Under Blast Loading, *International Journal of Applied Mechanics*, 12 (2020) 2050094.
- [166] H.B. Rebelo, C. Cismasiu, Robustness assessment of a deterministically designed sacrificial cladding for structural protection, *Eng. Struct.*, 240 (2021) 112279.
- [167] Z. Liu, C.T. Chan, P. Sheng, A.L. Goertzen, J.H. Page, Elastic wave scattering by periodic structures of spherical objects: Theory and experiment, *Physical Review B*, 62 (2000) 2446-2457.

- [168] L. D'Alessandro, A.O. Krushynska, R. Ardito, N.M. Pugno, A. Corigliano, A design strategy to match the band gap of periodic and aperiodic metamaterials, *Sci. Rep.*, 10 (2020) 16403.
- [169] X. An, F. Sun, P. Yu, H. Fan, S. He, D. Fang, Negative Effective Mass Density of One-Dimensional Hierarchical Metacomposite, *Journal of Applied Mechanics*, 82 (2015).
- [170] B. Li, K.T. Tan, Asymmetric wave transmission in a diatomic acoustic/elastic metamaterial, *J. Appl. Phys.*, 120 (2016) 075103.
- [171] C. Xu, W. Chen, H. Hao, H. Jin, Effect of engineered aggregate configuration and design on stress wave attenuation of metaconcrete rod structure, *International Journal of Solids and Structures*, (2021) 111182.
- [172] X. Chen, Q. Ji, J. Wei, H. Tan, J. Yu, P. Zhang, V. Laude, M. Kadic, Light-weight shell-lattice metamaterials for mechanical shock absorption, *Int J Mech Sci*, 169 (2020) 105288.
- [173] Z.-Y. Li, T.-X. Ma, Y.-Z. Wang, F.-M. Li, C. Zhang, Vibration isolation by novel meta-design of pyramid-core lattice sandwich structures, *J. Sound. Vib.*, 480 (2020) 115377.
- [174] Z. Liu, X. Zhang, Y. Mao, Y.Y. Zhu, Z. Yang, C.T. Chan, P. Sheng, Locally Resonant Sonic Materials, *Science*, 289 (2000) 1734.
- [175] P.A. Shirbhate, M.D. Goel, A Critical Review of Blast Wave Parameters and Approaches for Blast Load Mitigation, *Archives of Computational Methods in Engineering*, (2020).
- [176] G. Imbalzano, S. Linforth, T.D. Ngo, P.V.S. Lee, P. Tran, Blast resistance of auxetic and honeycomb sandwich panels: Comparisons and parametric designs, *Compos. Struct.*, 183 (2018) 242-261.
- [177] W. Chen, H. Hao, Numerical study of blast-resistant sandwich panels with rotational friction dampers, *Int. J. Struct. Stab. Dyn.*, 13 (2013).
- [178] C.-Y. Lee, M.J. Leamy, J.H. Nadler, Frequency band structure and absorption predictions for multi-periodic acoustic composites, *J. Sound. Vib.*, 329 (2010) 1809-1822.
- [179] H. Yasuda, J.J.J.-I.A.f.S. Yang, S. Structures, Tunable Frequency Band Structure of Origami-Based Mechanical Metamaterials, 58 (2017) 287-294.
- [180] P.R. Villeneuve, M. Piché, Photonic band gaps in two-dimensional square lattices: Square and circular rods, *Phys Rev B Condens Matter*, 46 (1992) 4973-4975.
- [181] N.T. Lam, I. Howard, L. Cui, Path planning for the Platonic solids on prescribed grids by edge-rolling, *PLOS ONE*, 16 (2021) e0252613.
- [182] N.T. Lam, I. Howard, L. Cui, A Literature Review on Path Planning of Polyhedrons with Rolling Contact, in: 2019 4th International Conference on Control, Robotics and Cybernetics (CRC), 2019, pp. 145-151.
- [183] W. Chen, H. Hao, Numerical Simulations of Stiffened Multi-arch Double-layered Panels Subjected to Blast Loading, *Int J Prot Struct*, 4 (2013) 163-188.
- [184] M. Li, L. Wu, L. Ma, B. Wang, Z. Guan, Structural design of pyramidal truss core sandwich beams loaded in 3-point bending, *Journal of Mechanics of Materials and Structures*, 6 (2011) 1255-1266.
- [185] Z. Li, W. Chen, H. Hao, Blast resistant performance of cladding with folded open-top truncated pyramid structures as core, 2018.
- [186] H. Wadley, K. Dharmasena, Y. Chen, P. Dudt, D. Knight, R. Charette, K. Kiddy, Compressive response of multilayered pyramidal lattices during underwater shock loading, *Int J Impact Eng*, 35 (2008) 1102-1114.
- [187] A. Silva, F. Monticone, G. Castaldi, V. Galdi, A. Alù, N. Engheta, Metastructures for signal manipulation, in: 2013 USNC-URSI Radio Science Meeting (Joint with AP-S Symposium), 2013, pp. 231-231.
- [188] W. Cai, V. Shalaev, Introduction, in: W. Cai, V. Shalaev (Eds.) *Optical Metamaterials: Fundamentals and Applications*, Springer New York, New York, NY, 2010, pp. 1-10.

- [189] J.-S. Hwang, T.-G. Choi, D. Lee, M.-Y. Lyu, D.G. Lee, D.-Y. Yang, Dynamic and static characteristics of polypropylene pyramidal kagome structures, *Compos. Struct.*, 131 (2015) 17-24.
- [190] Y. Shen, W. Cantwell, R. Mines, Y. Li, Low-velocity impact performance of lattice structure core based sandwich panels, *J. Compos. Mater.*, 48 (2013) 3153-3167.
- [191] F. Qin, A. Tong, C. Na, Strain rate effect and Johnson-Cook models of lead-free solder alloys, 2008.
- [192] R. Alberdi, J. Przywara, K. Khandelwal, Performance evaluation of sandwich panel systems for blast mitigation, *Eng. Struct.*, 56 (2013) 2119-2130.
- [193] C. Qi, S. Yang, L.-J. Yang, Z.-Y. Wei, Z.-H. Lu, Blast resistance and multi-objective optimization of aluminum foam-cored sandwich panels, *Compos. Struct.*, 105 (2013) 45-57.
- [194] F.G. Friedlander, G.I. Taylor, The diffraction of sound pulses I. Diffraction by a semi-infinite plane, *Proceedings of the Royal Society of London. Series A. Mathematical and Physical Sciences*, 186 (1946) 322-344.
- [195] H.N.G. Wadley, K.P. Dharmasena, M.Y. He, R.M. McMeeking, A.G. Evans, T. Bui-Thanh, R. Radovitzky, An active concept for limiting injuries caused by air blasts, *Int J Impact Eng*, 37 (2010) 317-323.
- [196] S. Palanivelu, W. van Paeppegem, J. Degrieck, B. Reymen, E. Segers, J.M. Ndambi, J. Vantomme, J. Van Ackeren, J. Wastiels, D. Kakogiannis, D. Van Hemelrijck, Performance of Sacrificial Cladding Structure Made of Empty Recyclable Metal Beverage Cans under Large-Scale Air Blast Load, *Applied Mechanics and Materials*, 82 (2011) 416-421.
- [197] T.T. Ngo, T.T. Tran, T.M. Pham, H. Hao, Performance of geopolymer concrete in monolithic and non-corrosive dry joints using CFRP bolts under cyclic loading, *Compos. Struct.*, 258 (2021) 113394.
- [198] G. Sun, E. Wang, H. Wang, Z. Xiao, Q. Li, Low-velocity impact behaviour of sandwich panels with homogeneous and stepwise graded foam cores, *Mater. Des.*, 160 (2018) 1117-1136.
- [199] L. Zhang, Z. Bai, F. Bai, Crashworthiness design for bio-inspired multi-cell tubes with quadrilateral, hexagonal and octagonal sections, *Thin-Walled Structures*, 122 (2018) 42-51.
- [200] Y. Staudt, C. Odenbreit, J. Schneider, Failure behaviour of silicone adhesive in bonded connections with simple geometry, *Int. J. Adhes. Adhes.*, 82 (2018) 126-138.
- [201] A.D.J.A.b.o. standards, Standard test methods for vulcanized rubber and thermoplastic elastomers-tension, in, ASTM West Conshohocken, PA, 2006.
- [202] A. Adesina, I. Alzaharnah, B. Yilbas, Effects of Laser Welding Parameters on the Flexural Characteristics of Laser Welded AISI 316L Stainless Steel Plates, *Lasers in Engineering*, 33 (2016) 31-51.
- [203] D. Zhang, Q. Fei, P. Zhang, Drop-weight impact behavior of honeycomb sandwich panels under a spherical impactor, *Compos. Struct.*, 168 (2017) 633-645.
- [204] R.A.W. Mines, A.M. Roach, N. Jones, High velocity perforation behaviour of polymer composite laminates, *Int J Impact Eng*, 22 (1999) 561-588.
- [205] W. Hou, F. Zhu, G. Lu, D.-N. Fang, Ballistic impact experiments of metallic sandwich panels with aluminium foam core, *Int J Impact Eng*, 37 (2010) 1045-1055.

APPENDIX I. STATEMENTS OF CONTRIBUTION OF CO-AUTHORS

To whom it may concern,

I, Hoang Nhi Vo, conducted analytical derivations, numerical simulations, experimental tests, data processing & analysis, and wrote manuscripts of the papers titled as follows, which were revised and edited by the co-authors. They also provided insights on conceptualization, experimental preparation, data processing, and data analysis.

- 1. A Reinvestigation of the Spring-Mass Model for Metamaterial Bandgap Prediction**
- 2. Model for Analytical Investigation on Meta-lattice Truss for Low-frequency Spatial Wave Manipulation**
- 3. Impact Load Mitigation of Meta-panels with Single Local Resonator**
- 4. Blast Resistant Enhancement of Meta-panels Using Multiple Types of Resonators**
- 5. Blast Resistant Enhancement of Meta-panels Using Multiple Types of Resonators**
- 6. Experimental Validation of Impact Mitigation Capability of Meta-panels**

Hoang Nhi Vo

I, as a co-author, endorse that this level of contribution by the candidate indicated above is appropriate.

Prof. Hong Hao

Dr. Thong Pham

A/Prof. Kaiming Bi

A/Prof. Wensu Chen

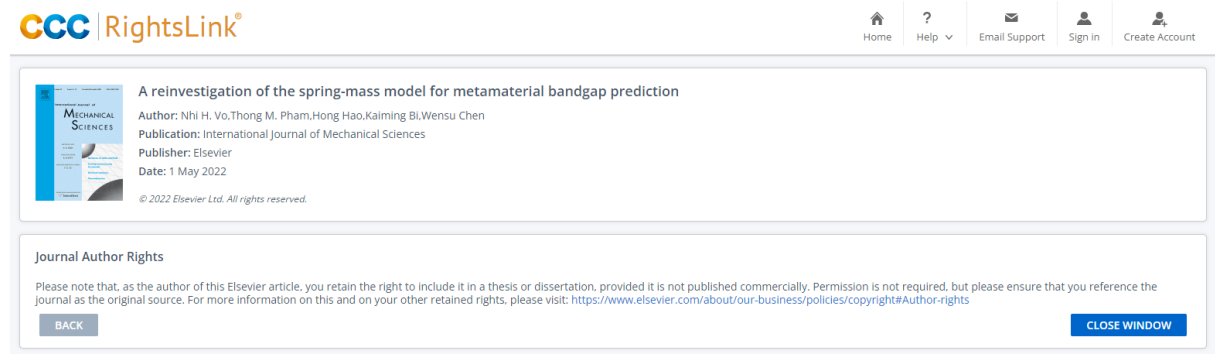
Dr. San Ha

APPENDIX II. COPYRIGHT CLEARANCE

The proof of the rights, granted by publisher for the publication that form the chapters of this dissertation are attached below.

Chapter 2. N.H. Vo, T.M. Pham, H. Hao, K. Bi, W. Chen. A reinvestigation of the spring-mass model for metamaterial bandgap prediction. *International Journal of Mechanical Sciences*. 2022;221:107219

<https://doi.org/10.1016/j.ijmecsci.2022.107219>



CCC | RightsLink®

Home ? Email Support Sign in Create Account

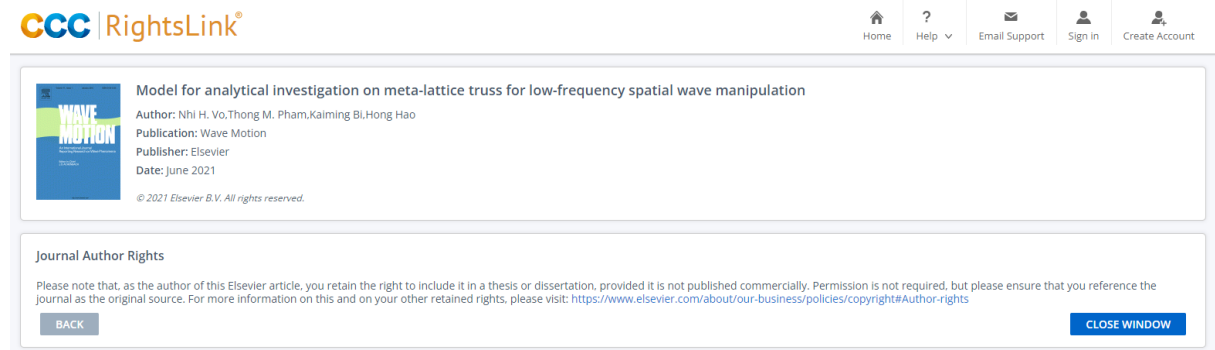
A reinvestigation of the spring-mass model for metamaterial bandgap prediction
Author: Nhi H. Vo, Thong M. Pham, Hong Hao, Kaiming Bi, Wensu Chen
Publication: International Journal of Mechanical Sciences
Publisher: Elsevier
Date: 1 May 2022
© 2022 Elsevier Ltd. All rights reserved.

Journal Author Rights
Please note that, as the author of this Elsevier article, you retain the right to include it in a thesis or dissertation, provided it is not published commercially. Permission is not required, but please ensure that you reference the journal as the original source. For more information on this and on your other retained rights, please visit: <https://www.elsevier.com/about/our-business/policies/copyright#Author-rights>

BACK CLOSE WINDOW

Chapter 3. N.H. Vo, T.M. Pham, K. Bi, H. Hao. Model for analytical investigation on meta-lattice truss for low-frequency spatial wave manipulation. *Wave Motion*. 2021;103:102735.

<https://doi.org/10.1016/j.wavemoti.2021.102735>



CCC | RightsLink®

Home ? Email Support Sign in Create Account

Model for analytical investigation on meta-lattice truss for low-frequency spatial wave manipulation
Author: Nhi H. Vo, Thong M. Pham, Kaiming Bi, Hong Hao
Publication: Wave Motion
Publisher: Elsevier
Date: June 2021
© 2021 Elsevier B.V. All rights reserved.

Journal Author Rights
Please note that, as the author of this Elsevier article, you retain the right to include it in a thesis or dissertation, provided it is not published commercially. Permission is not required, but please ensure that you reference the journal as the original source. For more information on this and on your other retained rights, please visit: <https://www.elsevier.com/about/our-business/policies/copyright#Author-rights>


BACK CLOSE WINDOW

Chapter 4. N.H. Vo, T.M. Pham, H. Hao, K. Bi, W. Chen. Impact Load Mitigation of Meta-panels with Single Local Resonator. *Engineering Structures*. 2022; 265: 114528.

<https://doi.org/10.1016/j.engstruct.2022.114528>

CCC | RightsLink®

Home ? Help Email Support Sign in Create Account

 **Impact load mitigation of meta-panels with single local resonator**
Author: Nhi H. Vo,Thong M. Pham,Hong Hao,Kaiming Bi,Wensu Chen
Publication: Engineering Structures
Publisher: Elsevier
Date: 15 August 2022
© 2022 Elsevier Ltd. All rights reserved.

Journal Author Rights
Please note that, as the author of this Elsevier article, you retain the right to include it in a thesis or dissertation, provided it is not published commercially. Permission is not required, but please ensure that you reference the journal as the original source. For more information on this and on your other retained rights, please visit: <https://www.elsevier.com/about/our-business/policies/copyright#Author-rights>


BACK CLOSE WINDOW

Chapter 5. N.H. Vo, T.M. Pham, H. Hao, K. Bi, W. Chen, N.S. Ha. Blast resistant enhancement of meta-panels using multiple types of resonators. *International Journal of Mechanical Sciences*. 2022;215:106965.

<https://doi.org/10.1016/j.ijmecsci.2021.106965>

CCC | RightsLink®

Home ? Help Email Support Sign in Create Account

 **Blast resistant enhancement of meta-panels using multiple types of resonators**
Author: Nhi H. Vo,Thong M. Pham,Hong Hao,Kaiming Bi,Wensu Chen,Ngoc San Ha
Publication: International Journal of Mechanical Sciences
Publisher: Elsevier
Date: 1 February 2022
© 2021 Elsevier Ltd. All rights reserved.

Journal Author Rights
Please note that, as the author of this Elsevier article, you retain the right to include it in a thesis or dissertation, provided it is not published commercially. Permission is not required, but please ensure that you reference the journal as the original source. For more information on this and on your other retained rights, please visit: <https://www.elsevier.com/about/our-business/policies/copyright#Author-rights>


BACK CLOSE WINDOW

Chapter 6. N.H. Vo, T.M. Pham, K. Bi, W. Chen, H. Hao. Stress Wave Mitigation Properties of Dual-meta Panels against Blast Loads. *International Journal of Impact Engineering*. 2021;154:103877.

<https://doi.org/10.1016/j.ijimpeng.2021.103877>

CCC | RightsLink®

Home ? Help Email Support Sign in Create Account

 **Stress Wave Mitigation Properties of Dual-meta Panels against Blast Loads**
Author: Nhi H. Vo,Thong M. Pham,Kaiming Bi,Wensu Chen,Hong Hao
Publication: International Journal of Impact Engineering
Publisher: Elsevier
Date: August 2021
© 2021 Elsevier Ltd. All rights reserved.

Journal Author Rights
Please note that, as the author of this Elsevier article, you retain the right to include it in a thesis or dissertation, provided it is not published commercially. Permission is not required, but please ensure that you reference the journal as the original source. For more information on this and on your other retained rights, please visit: <https://www.elsevier.com/about/our-business/policies/copyright#Author-rights>

BACK CLOSE WINDOW

Chapter 7. N.H. Vo, T.M. Pham, K. Bi, W. Chen, H. Hao. Experimental and Numerical Validation of Impact Mitigation Capability of Meta-Panels. *International Journal of Mechanical Sciences*. 2022;231:107591.

<https://doi.org/10.1016/j.ijmecsci.2022.107591>

CCC RightsLink

Home ? Email Support Sign in Create Account



Experimental and numerical validation of impact mitigation capability of meta-panels

Author: Nhi H. Vo,Thong M. Pham,Hong Hao,Kaiming Bi,Wensu Chen

Publication: International Journal of Mechanical Sciences

Publisher: Elsevier

Date: 1 October 2022

© 2022 Elsevier Ltd. All rights reserved.

Journal Author Rights

Please note that, as the author of this Elsevier article, you retain the right to include it in a thesis or dissertation, provided it is not published commercially. Permission is not required, but please ensure that you reference the journal as the original source. For more information on this and on your other retained rights, please visit: <https://www.elsevier.com/about/our-business/policies/copyright#Author-rights>

BACK

CLOSE WINDOW

BIBLIOGRAPHY DISCLAIMER

Every reasonable effort has been made to acknowledge the owners of the copyright material. I would be pleased to hear from any copyright owner who has been omitted or incorrectly acknowledged.